COMPUTATIONAL FLUID DYNAMICS MODELING AND SIMULATION OF ACID JETTING ON LIMESTONE CARBONATES

A Dissertation

by

VANESSA CHRISTELLE MPON A NDONHONG

Submitted to the Office of Graduate and Professional Studies of
Texas A&M University
in partial fulfillment of the requirements for the degree of

DOCTOR OF PHILOSOPHY

Chair of Committee,	Ding Zhu
Co-Chair of Committee,	A. Daniel Hill
Committee Members,	Hisham Nasr El Din
	Mahmoud El Halwagi
Head of Department,	Jeff Spath

December 2018

Major Subject: Petroleum Engineering

ABSTRACT

Acid jetting is a well stimulation method for carbonate reservoirs, with promising outcomes for the production enhancement in horizontal wells. It is a process where an acid solution is injected at a high rate via relatively smaller localized nozzles. The flow out of the nozzles is designed to be a fully turbulent jet which impinges on the porous surface of the rock, leading to a dissolution structure. That structure is of great interest as it determines the quality of the well stimulation job, and correlates directly to the well productivity. Preliminary experimental acid jetting studies, aiming to understand the acid jetting mechanism on carbonate cores and its key parameters, revealed the recurring creation of a large dissolution structure at the impingement location in the shape of a cavity and, depending on injection conditions, the propagation of wormholes through the core. The objective became to model/describe acid jetting from a mathematical standpoint. A computational fluid dynamics model was thus developed to simulate acid jetting.

A core-scale model was developed to simulate cavity and wormhole growth during acid jetting. It is a three-dimensional model which alternates between the two fundamental aspects of the overall acid jetting process. Firstly, it models the fluid mechanics of the turbulent jet exiting the nozzle and continuously impinging on the porous media transient surface. The jet fluid dynamics are implemented using a transient finite volume numerical solver using Large Eddy Simulations with the Dynamic Smagorinsky-Lilly sub-grid model to solve the Navier-Stokes and continuity equations.

The results of this simulation include velocity and pressure distributions at the porous media surface. Secondly, it models an irreversible chemical reaction with dissolution and transport at the impingement location between the fluid and the rock matrix. This two-step model successfully replicates experimental results and observations. When coupled with a wormhole growth model, it can represent the entire experimental acid jetting outcome.

The tool developed in this study builds the understanding for the upscaling and integrated dynamic modeling of acid jetting in the field and can therefore lead to the establishment of a standard for predicting and improving field applications of acid jetting.

DEDICATION

To my parents, Sara and Joseph Ndonhong.

ACKNOWLEDGEMENTS

I would like to thank my committee co-chairs, Dr. Zhu and Dr. Hill, as well as my committee members, Dr. El Halwagi, Dr. Nasr El Din, for their patience, guidance and support throughout the course of this research.

Thanks also go to my friends and colleagues and the department faculty and staff for making my time at Texas A&M University a great experience.

Finally, thanks to my support system for their encouragement and to my husband, Remy Gael for his patience and love.

CONTRIBUTORS AND FUNDING SOURCES

This work was supported by a dissertation committee consisting of Professor Zhu [advisor], Professor Hill [co-advisor] and Professor Nasr El Din of the Department of Petroleum Engineering and Professor El Halwagi of the Department of Chemical Engineering. Graduate study was supported by a fellowship from Texas A&M University and Exxon Mobil.

NOMENCLATURE

A	Area
Cs	Arbitrary constant for the Smagorinsky-Lilly
C_{tip}	Acid concentration at the wormhole tip
C_0	Initial acid concentration
CFD	Computational fluid dynamics
d*	Non-dimensional standoff distance
d	Standoff distance expressed in inches or meters
d_{nozzle}	Nozzle inner diameter expressed in inches or meters
D	Nozzle diameter at the exit
F	Objective function in the optimization
L_{wh}	Current wormhole length
N_{AC}	Acid capacity number
Nu	Nusselt number
Nu_o	Stagnation Nusselt number
p	Instantaneous pressure
P	Acid placement efficiency defined for optimization
PVbt	Estimated pore volumes of acid used to reach acid breakthrough for a core, or to reach a specific axial length of stimulation

q	Volumetric flowrate, L^3/ T
r	Radial distance from centerline
$r_{1/2}$	Radial distance where velocity falls to half of centerline speed
R	Nozzle radius
Re	Reynolds number
r, θ, z	Three coordinate axes in cylindrical system
s	Skin factor
S_{ij}	Strain rate
t	Time in seconds
U	Average velocity at the exit of the nozzle
<U>	Statistically-averaged velocity as function of distance x along jet and radial distance from centerline r
¯Ui	Resolved velocity vector
ui	Instantaneous velocity vector
u/i	Unresolved velocity vector
Uj	Jet velocity at nozzle;
Uo	Jet velocity along centerline, function of x
v (r,t)	Jet inlet velocity profile
V(r)	Time-averaged jet inlet velocity profile
V_1	Time-averaged jet centerline velocity
V_2	Time-averaged jet co-flow velocity

$v_{dissolved}$	Dissolution growth rate L/t; cm/min
v_i	Interstitial velocity in cm/min
$v_{i,tip}$	Interstitial velocity at the tip, L/t, cm/min
v_{jet}	Jet velocity, expressed in m/s
v_{node}	Node velocity at the acid/rock boundary
W	Wormhole efficiency defined for optimization
x	X or z represents the distance along jet's centerline, axial length/depth
z	Axial direction x or z represents the distance along jet's centerline,
Z	Nozzle to plate spacing, standoff distance

Subscript

i	Index of coordinate direction
a	Axisymmetric excitation
h	Helical excitation
e	Excitation

Superscript

+	Nondimensional quantity in wall coordinates

Greek Symbols

α	Represents the extent of the reaction of calcite with a solution of 15 wt.% HCl per unit time at a given fluid pressure at 75 degrees Fahrenheit
α_1, α_2	Weights of outcomes used in the optimization definition
β_{100}	Acid dissolving power, m/m, kg/kg
ρ	Density
ρ_{acid}	Acid density, m/L³, lbm/ ft³
ρ_F	Density of the fast reacting mineral, m/L³, lbm/ ft³
μ_{SGS}	SGS eddy viscosity
ν	Kinematic viscosity
ν	Fluid kinematic viscosity in $m^2.s$
τ_{ij}	Sub grid stress
θ_m	Momentum thickness
φ	Porosity
χ_{100}	Volumetric dissolving power, L³/ L³, ft³/ft³

TABLE OF CONTENTS

LIST OF FIGURES

Figure Page

Figure Page

Figure Page

Figure Page

Figure Page

LIST OF TABLES

CHAPTER I

INTRODUCTION

1.1 BACKGROUND

In the oil and gas industry, strong acids such as hydrochloric acid are a preferred choice for the stimulation of carbonate reservoirs. There are two general approaches based on the acid injection rate. The stimulation could either be an acid fracturing job, where the acid injection pressure is above the rock fracture pressure or it could be a matrix acidizing job where the injection pressure is below the fracture pressure. The objective of matrix acidizing is to improve the transport of hydrocarbons to the well, by creating highly conductive paths called wormholes. Figure 1.1 depicts a projection of a portion of a reservoir with a horizontal well, where the unaltered reservoir region (Reservoir) is shown, as well as the damaged zone, and the mudcake or filtercake around the wellbore. Figure 1.2 shows wormholes obtained after a radial large-scale matrix acidizing experiment conducted by McDuff et al. (2010), where wormholes can be seen extending from the borehole into the surrounding reservoir.

The desired wormholes resulting from the stimulation would bypass the damage zone, thus creating an "easier" path for the hydrocarbons flowing to the wellbore and improving the well productivity. Numerically, the long wormholes would lead to a reduction of the skin factor, s, a non-dimensional parameter introduced by Van

Everdingen and Hurst (1949), which accounts for the additional pressure drop in the near wellbore region due to the reduced permeability in the damaged zone.

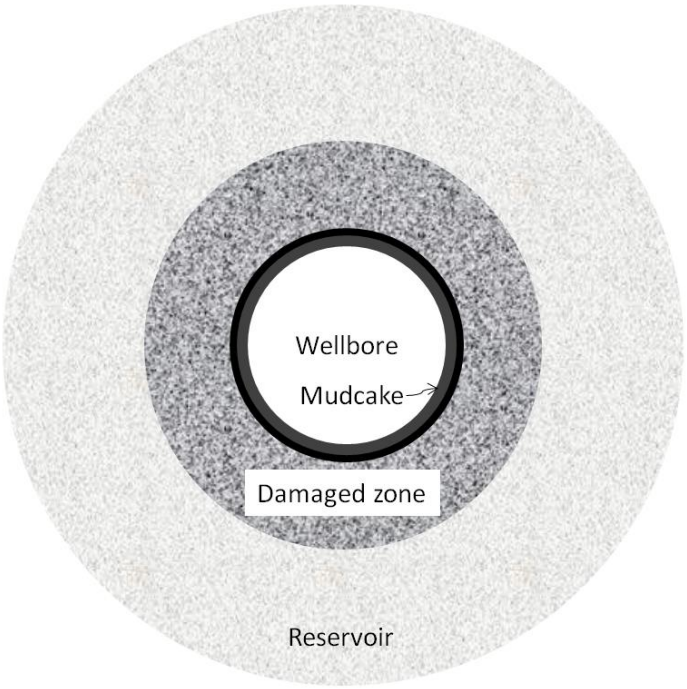

Figure 1.1: Projection of a horizontal wellbore with a damaged zone in a reservoir

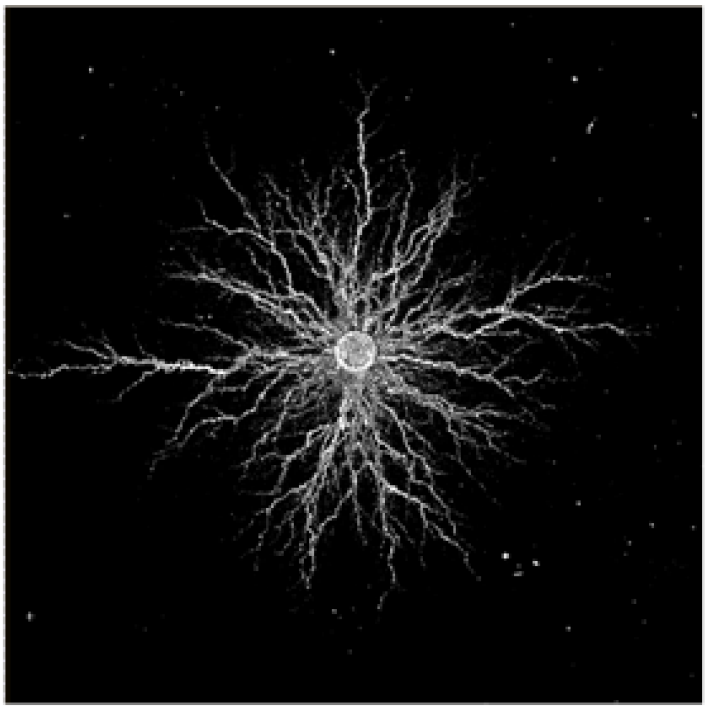

Figure 1.2: Wormholes after a radial matrix acidizing experiment. Reprinted from McDuff et al. 2010

Acid jetting is a process where acid is injected into the formation below the fracture pressure, through tiny nozzles at rates corresponding to turbulent flow. It leads to a turbulent jet of acid impinging on the rock surface. This stimulation method has shown optimistic results for long horizontal wells in carbonate formations, especially when accomplished using limited entry liners, coiled tubing or the controlled acid jet technology.

There are many publications reporting successful field implementations of controlled acid jet, acid tunneling and acid jetting. These reports hint that acid jetting could become an established successful well stimulation method for carbonate

formations. In order to confirm that idea, several experimental studies were conducted. Mikhailov (2007) and Zhang (2009) have studied the effect of jetting on filter cake removal and stimulation; they have both shown that water and acid jetting could effectively remove filter cake. Furthermore, they showed that wormholes could be created and propagate through the rock when using 15 weight% hydrochloric acid solutions at jetting speeds above 10 ft/s. Several sets of acid jetting experiments were run without a filter cake and have indicated the creation of a bulb-shaped dissolution structure around the location of impingement. The experiments have also shown an ability to lead to the creation of wormholes under specific injection conditions. Water jetting at similar injection conditions resulted in no change to the rock, indicating that the dissolution/erosion can only be achieved with the use of acid given our current design parameters (Holland 2014, Beckham 2015, Ndonhong et al. 2017, Ridner et al. 2018). Despite all those studies, there is still a gap of knowledge to be filled, when it comes to a theoretical understanding of the acid jetting process. It is necessary to investigate the benefits of turbulent jets to well simulation, in order to potentially guarantee successful stimulation jobs with acid jetting. The experimental work has shown several optimistic trends; however, these benefits of jetting are still limited to field or experimental observations, with no predictability. This research therefore aims at providing a thorough theoretical understanding of acid jetting for the purpose of treatment optimization. That theoretical understanding would combine studying and modeling turbulent jets impingement and reactive flow on porous media.

1.2 MOTIVATION

Due to the high reactivity of calcite with strong acids, the acidizing of limestone carbonate using hydrochloric acid has been extensively studied and applied in the oil and gas industry. It follows the chemical Equation 1.1. Several experimental investigations have been conducted, with various settings. Generally, in experimental linear and radial acid matrix treatment of limestone carbonates, several types of dissolution structures are created, depending on the flowrate, due to the mass-transfer limited nature of the process. Figure 1.3 shows experimental results from matrix acidizing in a radial geometry, where the wormhole efficiency curve indicates the presence of optimal injection conditions, where the least amount of acid (measured in acid pore volumes to breakthrough, indicated on the y-axis) is used to stimulate the same core volume. The top image corresponding to the left star on the curve shows an enlarged wormhole, at low acid flux. The middle image, corresponding to the middle star, shows an optimal wormhole at both optimum acid volume and optimum flux. The bottom image, corresponds to the star on the right and shows a more branched wormhole, at high flux.

$$2HCl + CaCO_3 \rightarrow H_2O + Ca^{2+} + CO_2 + 2Cl^- \quad (1.1)$$

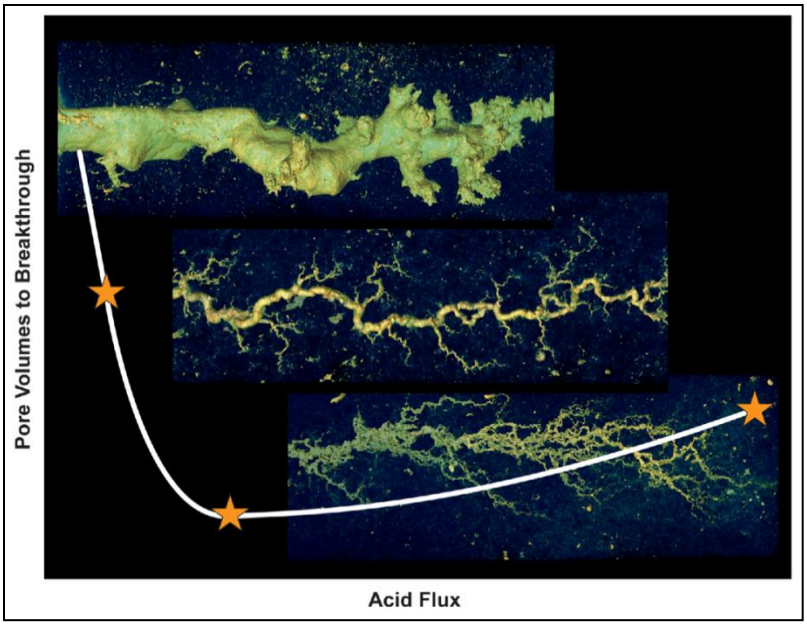

Figure 1.3: Dissolution structures in experimental radial acid matrix stimulation, Reprinted from McDuff et al. 2010

Matrix acidizing has been studied extensively and following laboratory experiments and theoretical modeling, guidelines for successful field jobs have been tested and established as industry standards. (Hung et al., 1989, Fredd and Fogler, 1999, Wang et al., 1993, Panga et al., 2005, Glasbergen et al., 2009, Furui et al. 2012)

Acid jetting is a process where limited entry devices lead to the creation of turbulent jets of acid impinging on the surface of a reactive rock. It is a very complex transient process, occurring in all three dimensions. It combines the science of turbulence, specifically for turbulent jets impingement, and reactive transport through porous media. It is of considerable interest in the oil and gas industry because it has the potential to enhance the effectiveness of acid stimulation jobs. For a long time, water

jetting has been an industry standard for wellbore cleaning, and scale removal (Johnson, et al., 1998) meanwhile abrasive water jets have been considered for drilling. Well stimulation with acid or water jetting has gained a lot of interest for carbonate formations. (McDaniel et al., 2006, Surjaatmadja et al., 2008).

Acid jetting, as a well stimulation method for carbonate reservoirs, is designed to promote acid placement mechanically in the wellbore via multiple strategically located jetting nozzles and limited entry completions. (Hansen and Nederveen, 2002, Denney, 2002, Carpenter, 2013). The mechanical action is created by the injection of high velocity fluids through high differential pressure orifices. Acid jetting is similar to matrix acidizing in that acid is injected below the formation fracture pressure and wormholes propagate into the formation to potentially bypass the damage zones. Additionally, it was shown that acid jetting can also effectively remove mud filter cakes along wellbore walls, when the high velocity fluid impinges on the wellbore area (Mikhailov, 2007).

Regular acid jetting treatments in the field are achieved through coiled tubing, drill pipe or a controlled acid jet. The effectiveness of jetting depends on stand-off distance, fluid velocity, jet stream profile and the pulsation effect from a rotating jet as compared to a stationary jet (Aslam, 2000, Holland, 2014). In the field, a rotary action is required for perforation coverage, as well as screen or open hole coverage. (Kofoed et al., 2012) Early acid jetting jobs were achieved with simple coiled tubing and a nozzle. Recently, more sophisticated methods have been designed and implemented, to achieve larger jobs and reach more complex targets.

Recent successful applications of acid jetting in carbonates are acid tunneling and the use of limited entry liners. Acid tunneling is a modified method of the selective stimulation using coiled tubing, which uses a combination of chemical drilling and acid stimulation. The acid tunneling process involves constructing some highly stimulated lateral tunnels in the original well. (Portman et al, 2002, Stanley et al. 2010, Siddiqui, et al., 2013). Limited entry liners are stationary completions to distribute acid in extended-reach horizontal wells. They are engineered to force greater volumes of acid into the low permeability zones using zonal isolation packers and adjusting the frequency of jetting nozzles in low or high permeability compartments. (Beckham, et al., 2015).

Turbulent jets are chaotic in nature, yet also self-similar with repeatable/common average properties. Pope (2009) gives ample descriptions of turbulent jets, especially free jets, Lee and Chu (2003) have also presented a description of turbulent jet in stagnant, co-flow and cross-flow using a Lagrangian approach. Hanjalic and Launder (2011) provide extensive modeling recommendations for free turbulent jets. Impinging turbulent jets offer several benefits in terms of localized heat or mass transfer and are thus found in a variety of engineering applications and disciplines. Several experimental and computational studies have been conducted to further understand and predict that transport mechanism. Cooper et al. (1993) provided an extensive set of hydrodynamics experimental data of a turbulent jet impinging orthogonally onto a large plane surface, with standoff distances ranging from two to six nozzle diameters. Jambunathan et al. (1992) and Viskanta (1993) collected experimental data for the rate of heat transfer from impinging turbulent jets for a wide range of Reynolds numbers and standoff distances.

Tummers et al. (2011) carried out detailed measurements of the turbulent flow in the near field of an impinging jet. Zuckerman and Lior (2006) provided guidelines for the numerical modeling of the heat transfer occurring during jet impingement. Wilke and Sesterhenn (2015) and Uddin et al (2013) thoroughly described some computational fluid dynamics approaches for simulating turbulent jet impingement. In the oil and gas industry, turbulent jets have been considered for the transport of both reactive and non-reactive fluids. Reactive transport with impinging turbulent jets is used for acid tunneling (Stanley et al., 2010, Ashkanani et al. 2012; Siddiqui, 2013; Livescu and Craig, 2017), controlled acid jet (Hansen and Neverdeen, 2002; Mogensen and Hansen, 2007) and acid jetting (Ritchie, 2008; Kofoed, 2012; Rajes et al. 2014). Turbulent jets of non-reactive fluids are used for wellbore cleaning or drilling (Pekarek et al, 1963; Johnson et al. 1998; Nasr-El-Din et al. 2005; Marin et al. 2013).

1.3 OBJECTIVES

The objective of this research is five-fold. The initial goal is to get a scientific and consistent understanding of acid jetting with respect to matrix stimulation. The questions to answer here would be: What happens to the rock during acid jetting? What is the outcome of an acid jetting experiment? How is the dissolution structure? How does the dissolution structure changes with the design parameters? How can we quantify and qualify the extent of the matrix stimulation after acid jetting? The second objective would be to identify the parameters controlling the outcome of acid jetting. For this section, sensitivity studies on design parameters could help identify trends and

dependencies between these parameters and the acid jetting results. These first two goals could be achieved with an experimental investigation. Some details about the experimental investigation will be provided in Chapter IV. The third objective is to establish a theoretical model to test the parameters roles and identify the best scenario for the most beneficial jetting method. It would require an extensive literature review and a consideration for interdisciplinary studies on turbulent jets of reactive flow impinging on porous media. The theoretical model would provide guidelines for the optimization of the acid jetting results, which would lead to the fourth objective. This objective is to establish a method for the numerical simulations of acid jetting, via model validation and verification via experimental data followed by numerical case studies to extend beyond the experimental limitations and answer more questions. Some of those questions include: Does acid jetting provide a near or far-field benefit to the matrix stimulation? How does acid jetting results compare to conventional matrix acidizing results? Is there a point where acid jetting becomes detrimental to the matrix stimulation? Is there a sweet spot for acid jetting design conditions where the benefits are optimal? If yes, how can it be achieved? The last objective would be to establish an optimized procedure for a maximum benefit of acidizing via jetting, which could lead to an industry standard for acid jetting jobs after upscaling efforts.

1.4 ORGANIZATION

This dissertation is organized into six (6) chapters. **Chapter I** described the motivation and objective of this research; it also introduces the approach used. **Chapter II** presents a broad literature review as it delves into the details of the theory of the turbulent flows, turbulent jets and impingement of reactive flows on porous media, it also describes the modeling of wormholes. It provides an overview of acid stimulation of carbonate reservoirs, a literature review on well stimulation generally, followed by matrix acidizing and acid jetting specifically. Acid jetting jobs in the oil and gas industry are described, as well as turbulent jets and their use in other engineering disciplines. That chapter also aims to present the theory on the computational fluid dynamics side of acid jetting. It offers a description and comparison of the various approaches **Chapter III** presents the CFD model developed for experimental acid jetting. It covers the general methodology, the model's assumptions, and a detailed description of the modeling procedure and sample results. **Chapter IV** presents an analysis of the simulations results and discusses the model's strengths and limitations. **Chapter V** introduces the upscaling of the computational approach, for radial flow on larger rock sample. **Chapter VI** summarizes and concludes the work with recommendations for model improvement and suggestions for further studies.

CHAPTER II

LITERATURE REVIEW

2.1 THEORY OF ACID JETTING

A flow can characterized as turbulent or laminar, depending on the dimensionless Reynolds number, Re, which compares the inertia and viscous forces, for pipe flow, it is expressed as shown in Equation 2.1.

$$Re = \frac{inertia\ force}{viscous\ force} = \frac{DV\rho}{\mu} = \frac{DV}{\nu} \tag{2.1}$$

where D is the pipe diamter expressed in units of length, V is the flowing fluid velocity expressed as length over time, ρ is the density of the flowing fluid with units of mass over length to the third power, μ is the dynamic viscosity of the flowing fluid and ν is the kinematic viscosity in units of length square and time.

A large Renolds number represents a dominance of the inertial forces, which could lead to chaotic eddies, vortices and other flow instabilities. On the other hand, a dominance of the viscous forces would correspond to a more stable or laminar flow and a smaller Reynolds number value. The characterization of a flow by the Reynolds number depends on the type of flow and is obtained experimentally. Experimental results indicate that, for pipe flow a Reynolds number below 2,300 would imply laminar flow, while a Reynolds number value above 4,000 would imply a turbulent flow. For

Reynolds number values between 2,300 and 4,000 the flow would be considered transitional, a mixture of laminar and turbulent.

Turbulent flow are observed in countless cases: from the smoke form a chimney to a waterfall. The key observation in turbulent flow is the unsteadiness, irregularity and the apparently unpredictability of the flow. It appears to be chaotic and generally turbulent motions of several scales can be observed. For turbulent flows, the fluid velocity velocity field varies significantly and irregularly with respect to position and time. The velocity field is therefore denoted as **U**(x,t), where x is the position and t is the time. Turbulence provides an incomparable benefit for the transport and mixing of fluid. Compared with laminar flow, rates of heat and mass tranfer of turbulent flows at interfaces (solid-fluid or liquid-gas) are much more enhanced.

2.2 TURBULENT JETS

A jet is a shear flow generated by a continuous and instantaneous source of momentum with no buoyancy, in a stationary environment of uniform density. There are two types of jets, the planar jet where fluid flows out of a planar aperture bounded by two parallel plates, and the round or slot jet, where fluid flows out of a round hole or nozzle. Turbulent jets mentioned in this work correspond to turbulent round jets or slot jets in the conventional fuid mechanics approach. The turbulent planar jets have not yet found a use in petroleum engineering, and would therefore not require a thourough distinction. The Reynolds number of a jet is defined by Equation 2.2.

$$Re = \frac{d_{nozzle} * V_{jet}}{\nu} \tag{2.2}$$

where d_{nozzle} is the nozzle inner diameter expressed in inches (or meters), ν is the fluid kinematic viscosity in $m^2.s$, Re is the Reynolds number, and V_{jet} is the jet velocity, expressed in m/s.

Experiments have indicated that if the Reynolds number exceeds 2000, then the jet flow becomes turbulent (Lee and Chu, 2000). Figure 2.1 shows a turbulent jet, where turbulent eddies of various sizes are observed due to the presence of smoke as a tracer for the turbulent motion in air. The general trend is the increase in the length scale as eddies move along the jet. Turbulent entrainment is also observed, where due to the motion of eddies, fluid from the surrounding environment is drawn into the jet. The jet in Figure 2.1 produces enough power to launch a rocket engine. Jets are widely used across engineering disciplines for mixing of the source fluid with the ambient fluid. Experimental observations from free jets described by Lee and Chu (2000) have indicated that the entrainment process and the spreading rate of a turbulent jet is determined by the large and dominant eddies which extend across the entire width of the jet. The small eddies that circulate around the dominant eddies are responsible for the mixing of the entrained fluid with the source fluid.

Another observation is that there is a mixing layer zone at the edge of the jets contains the initial development of the jet. There is also the presence of a core region, about 6 nozzle diameters in length close to the source, where there is an irrotational fluid not affected by the jet diffusion. Beyond that region, the source fluid is mixed with the ambient fluid, with a fully established mean flow. Figure 2.2 presents a 2D conceptual

view of a jet with the various regions mentioned. The potential core region is the isosceles triangle with the two dashed lines and the base of length D.

For the turbulent jet defined in Figure 2.2, the flow can be described as a point source of momentum flux, with source velocity u_0 and centerline velocity u_m. The source strength and dimensions are presented in Equation 2.3. The volume flux is expressed in Equation 2.4.

$$\frac{M_0}{\rho_0} = \frac{\pi}{4} D^2 w_0^2 \sim \frac{L^4}{T^2} \tag{2.3}$$

where, M_0 is the source momentum, D is the diameter of the point source, w_0 is the source velocity, and ρ_0 is the density. L and T respectively represent the length and time dimensions. The expression for the volume flux Q is deduced by dimensional analysis.

$$Q \sim z \sqrt{\frac{M_0}{\rho_0}} \tag{2.4}$$

where, M_0 is the source momentum, D is the diameter of the point source, w_0 is the source velocity, and z is the vertical co-ordinate above source.

Figure 2.1: High Reynolds number turbulent jet produced by the test of a rocket by Lockheed in Redland, CA. Reprinted from Lockheed Martin, 1968

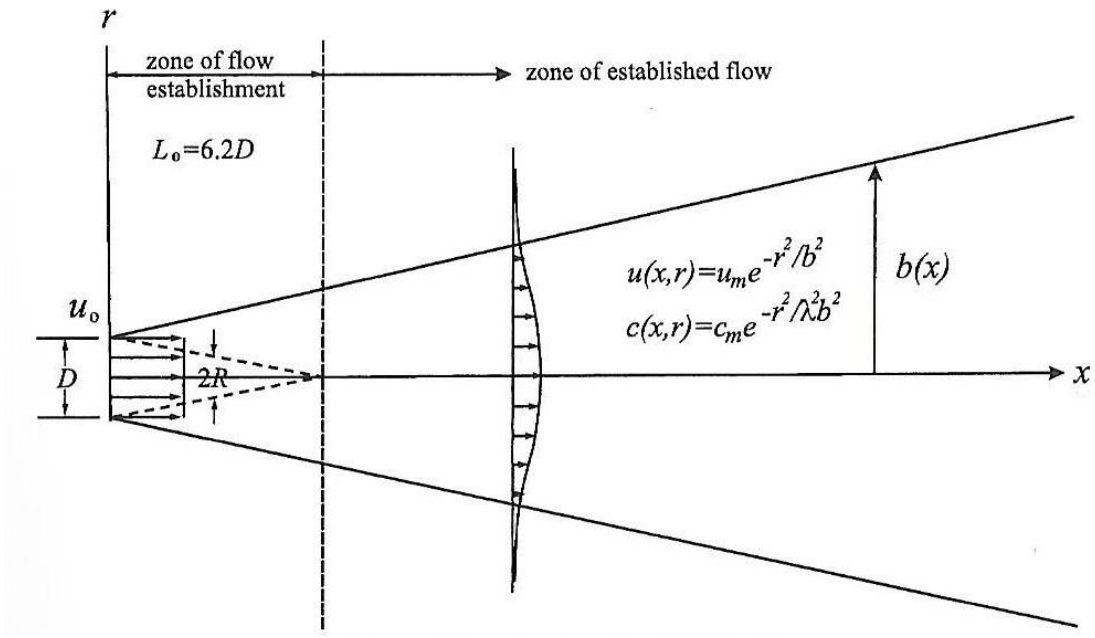

Figure 2.2: Free turbulent jet. Reprinted from Lee and Chu, 2000

For the mean flow structure, the velocity and concentration profiles across the jet are Gaussian or bell-shaped which could be expressed as a normal distribution, from a statistical sense. Mass and momentum in the turbulent jet move back and forth, and left and right, by the random action of the turbulent motion. The profile for the velocity is Gaussian as well, since momentum transport is equivalent to mass transport, and the velocity is momentum per unit mass of the fluid. The typical mean velocity profile in the fully developed region of the jet is Gaussian. The diffusion thickness spreads linearly, the static pressure is approximately constant. In the axisymmetric case, the length of the potential core is 6.2D; the mean axial velocity and concentration profiles are found to attain self-similarity beyond the potential core.

- In the zone of flow establishment (ZFE), $x \leq 6.2D$; the axial velocity can be computed using Equation 2.5 or 2.6.

$$u = u_0; \qquad r \leq R \tag{2.5}$$

$$u = u_0 \exp\left[-\frac{(r-R)^2}{b^2}\right]; \qquad r \leq R \tag{2.6}$$

- In the zone of established flow (ZEF), $x \geq 6.2D$, the axial velocity is self-similar and Gaussian and is can be computed using Equation 2.7.
-

$$u = u_m \exp\left[-\left(\frac{r}{b}\right)^2\right]; \qquad r \leq R \tag{2.7}$$

where x and r represent the streamwise and radial coordinates, respectively, while $u_m(x)$ is the centerline maximum velocity.

- The turbulent round jet spreads linearly following Equation 2.8.

$$b = \beta x \tag{2.8}$$

where β is a proportionality constant

The jet properties adopted for this work, stem from experimental observations summarized in Table 2.1.

It is important to note that for a turbulent jet in stagnant flow, the velocity is observed to be inversely proportional to the distance from the source, while the volume flux increases linearly with distance. The total amount of entrained flow depends only on the momentum flux M_0 and the axial distance z. All the kinetic energy would be ultimately dissipated (case of the discharge from an orifice into an infinite reservoir) and the local Reynolds number is equal to a constant. During experimental acid jetting, the flow through the core can be induced by imposing a constant pressure differential across the core. It will lead to a situation of jet in a coflowing fluid. Given the problem we are trying to describe, it is important to describe turbulent jets in a co-flow.

For a turbulent jet in co-flow, the jet is issued from a circular nozzle of diameter D at a velocity of U_0 in a fluid with a co-flow velocity U_a. The ratio of those velocities R' is defined in Equation 2.16 and it determines the strength of the jet with respect to the surrounding flow.

$$R' = \frac{U_0 - U_a}{U_0} = \frac{\Delta U}{U_0} \tag{2.16}$$

For strong jets in co-flow, the relationship can be approximated as presented in Equation 2.17.

$$U_0 \gg U_a \leftrightarrow R' \sim 1 \quad (2.17)$$

On the other hand, for weak jets in co-flow, the relationship can be expressed as Equation 2.18.

$$U_0 \sim U_a \leftrightarrow R' \sim 0 \quad (2.18)$$

The effect of the co-flow velocity can be neglected in the near field of a strong jet, when $R' \sim 1$, as the initial development of the strong jet would be very similar to the case of a jet in stagnant fluid. Far from the source, the jet velocity is considerably reduced and once it becomes comparable in magnitude to the co-flow velocity, R' approaches zero and the co-flow velocity dominates the process. The jet velocity would then only matter for its contribution to the spreading process. In the case of this study, the jet is strong, which means that the shape of the concentration contour and the mixing characteristics are similar to those of a jet in stagnant flow. The jet spread, on the other hand, is no longer linearly related to the axial distance z. For the same discharge, the half-width of the co-flowing jet is less than that of a jet in stagnant flow and depends on R'.

Table 2.1: Jet Properties from Lee and Chu (2000)

Properties		
Jet width	$b = 0.114z$	(2.9)
Centerline velocity	$u_m/u_0 = 6.2\left(\frac{z}{D}\right)^{-1}$	(2.10)
	$u_m = 7.0M_0^{\frac{1}{2}}z^{-1}$	(2.11)
Centerline concentration	$c_m/c_0 = \frac{5.26}{\left(\frac{z}{D}\right)^{-1}}$	(2.12)
Centerline dilution	$S = 0.19z/D$	(2.13)
Average dilution ratio	$\bar{\bar{S}} = 0.32z/D$	(2.14)
	$Q = 0.286M_0^{\frac{1}{2}}z$	(2.15)

2.3 LABORATORY OBSERVATIONS OF TURBULENT JETS

The turbulent jet can be uniquely described by two input variables: the nozzle diameter and the velocity of the exiting fluid. Along with the fluid viscosity, the parameters can be combined into a single dimensionless number, namely the Reynolds number previously described. Figure 2.3 presents the polar coordinate system used for the description and Figure 2.4 presents radial profiles of mean axial velocity for a turbulent jet. It can be observed that the bell shape curve still prevails, despite the increased spreading with the increased standoff.

The velocity along the centerline of the jet, expressed in Equation 2.19 is very important as it may uniquely characterize the jet flow, given the recurrent bell shape distribution, which only differs in height equivalent to the jet's centerline velocity.

$$U_o(x) = \bar{u}(x, r = 0) \tag{2.19}$$

The **jet self-similarity** property is observed as all the velocity profiles appear identical in shape, except for a stretching factor. If the velocity and the radial distance were made dimensionless with the centerline velocity and the half-width, respectively, then all the profiles would collapse on a single curve as shown in Figure 2.5.

The centerline velocity is inversely proportional to the axial distance along the jet, as shown in Equation 2.20

$$U_o(x) = U_J \frac{B}{(x - x_0)/d} \tag{2.20}$$

where B is a constant determined experimentally, usually around 6.

Laboratory investigations of jets penetrating into a quiescent fluid of the same density consistently reveal that the envelope containing the turbulence caused by the jet adopts a nearly conical shape. It implies that the radius of the jet, R, is proportional to the distance z downstream from the discharge. The opening angle is always the same, at 11.8 degrees, regardless of any parameter, which yields a ratio radius-to-axial-distance of 1-to-5. Therefore, the coefficient of proportionality between r and z is approximately 1/5 (since tan (11.8 degrees) ~0.2). The constant behavior of the half-width of the profiles yields Equations 2.21 to 2.23.

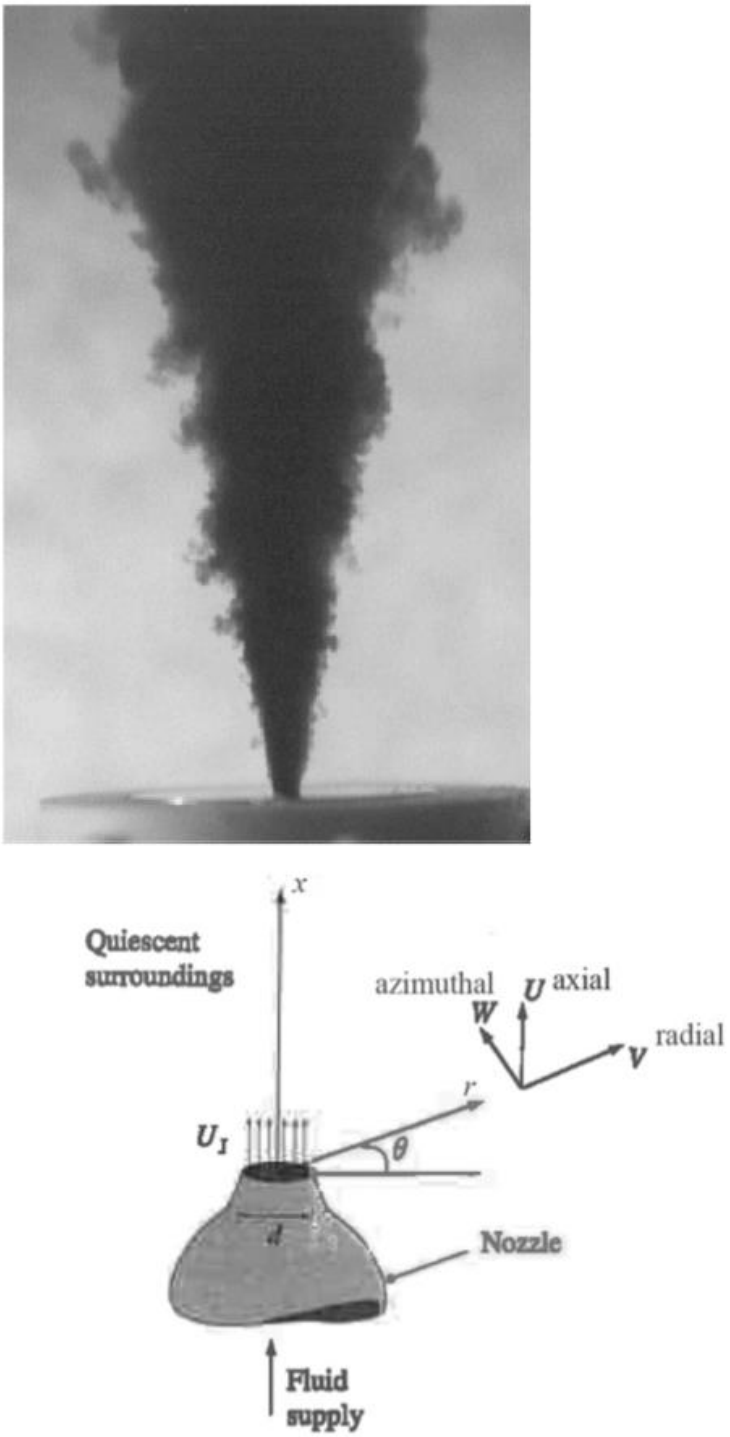

Figure 2.3: The polar-cylindrical coordinate system considered. Reprinted from Cushman-Roisin, 2013

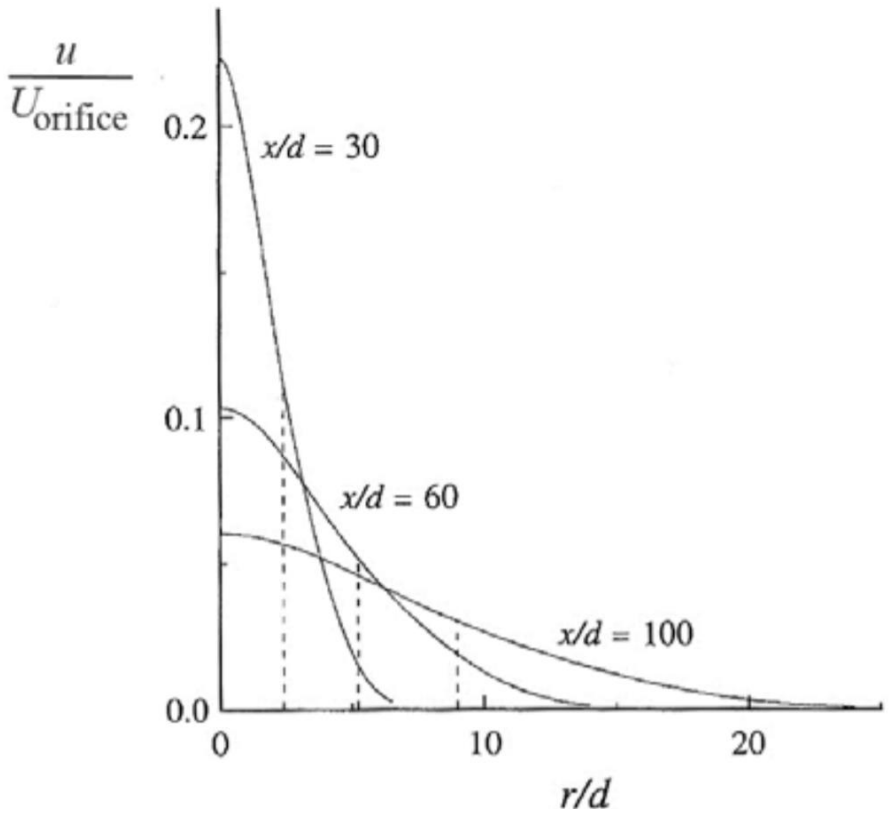

Figure 2.4: Radial profiles of mean axial velocity in a turbulent jet for Re=95,500. The dashed lines indicate the half-width of the profiles adapted from Pope (2009)

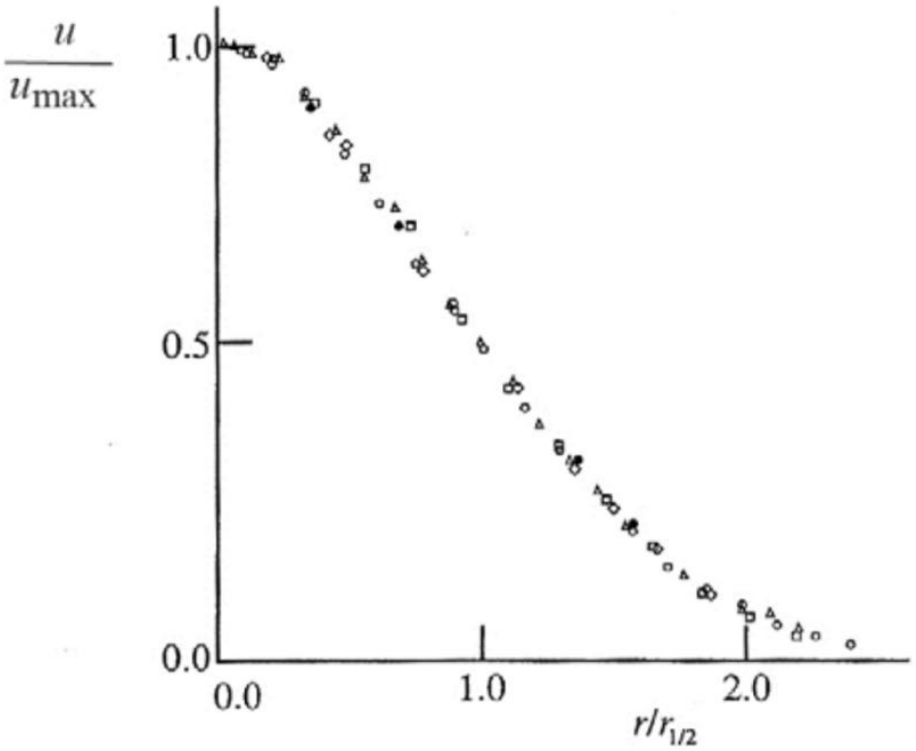

Figure 2.5: Mean axial velocity against radial distance in a turbulent round jet, Re~10^5; measurements of Wygnanski and Fiedler (1969). Symbols: ∘ corresponds to x/d=40; △ corresponds to x/d=50; ⊡ corresponds to x/d=60; ⋄ corresponds to x/d=75; ■ corresponds to x/d=97.5. Reprinted from Pope, 2009

$$\frac{dr_{1/2}}{dx} = constant = S \tag{2.21}$$

$$r_{\frac{1}{2}}(x) = S(x - x_0) \tag{2.22}$$

$$S = 0.094 \tag{2.23}$$

It is important to note that since the initial jet radius is not zero, but is given by the finite nozzle radius which is equal to half the nozzle diameter, the axial distance x

must be counted not from the orifice but from a virtual source at a distance 5d/2 into the nozzle, opposite the flow, as indicated in Figure 2.6.

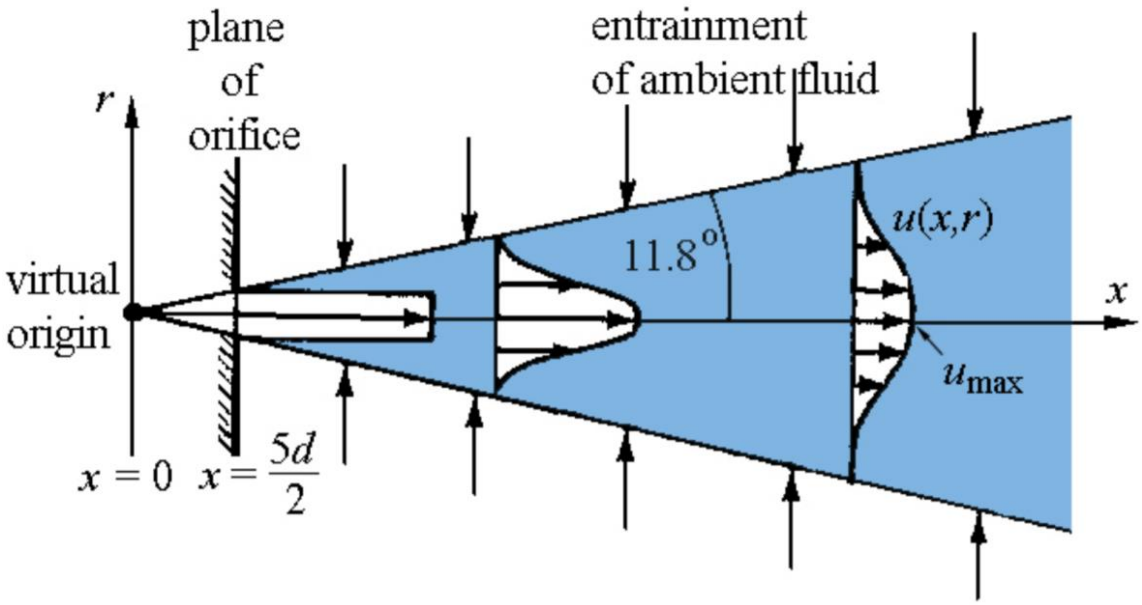

Figure 2.6: 2D axisymmetric geometry of a turbulent jet. Reprinted from Pope, 2009

Schlichting (1933) proposed a solution for the axial velocity scaled by the centerline velocity, presented in Equations 2.24 to 2.26.

$$\frac{\bar{u}(x,r)}{U_o(x)} = f(\eta) \tag{2.24}$$

$$f(\eta) \sim \frac{1}{(1+a\eta^2)^2} \tag{2.25}$$

$$\eta = \frac{r}{x - x_0}$$

(2.26)

Figure 2.7 shows the self-similar profile of the mean axial velocity obtained from that solution.

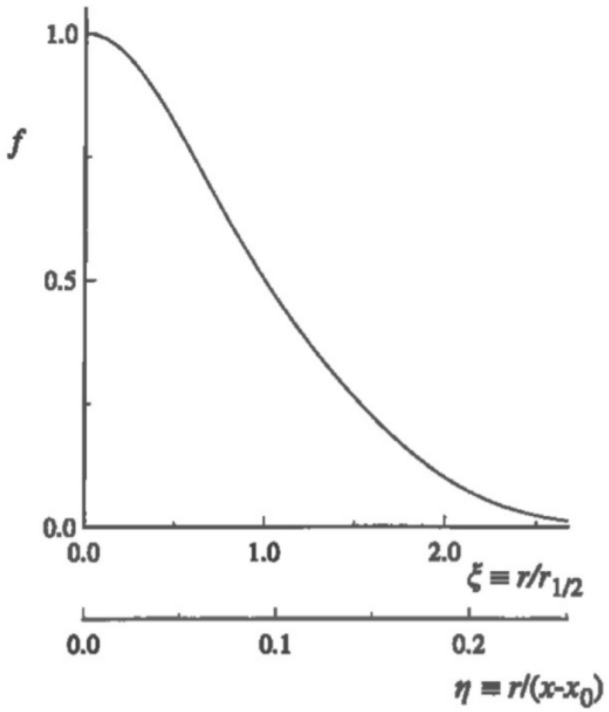

Figure 2.7: The self-similar profile of the mean axial velocity in the self-similar jet, adapted from Schlichting (1933)

The radial velocity scaled by the centerline velocity is obtained from Equation 2.27:

$$\frac{\partial \bar{u}}{\partial x} + \frac{1}{r}\frac{\partial (r\bar{v})}{\partial r} = 0 \tag{2.27}$$

The profile from that solution is shown in Figure 2.8.

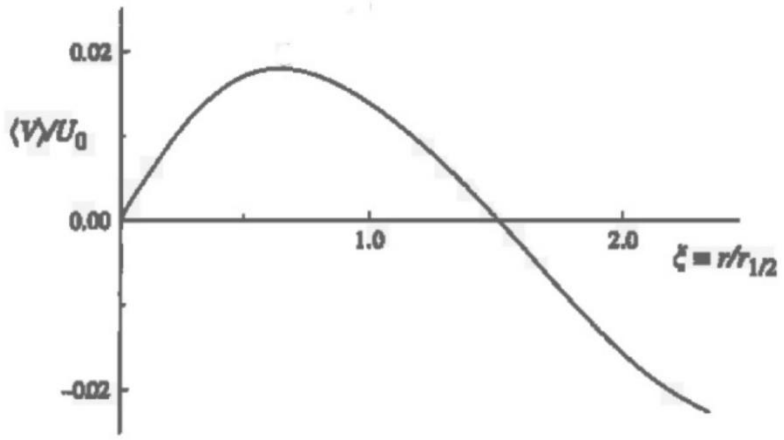

Figure 2.8: The self-similar profile of the mean radial velocity in the self-similar jet adapted from Schlichting (1933)

It is important to note that the radial velocity is no more than 3% of the axial velocity. For instance, at its maximum, the radial velocity normalized by the jet velocity is inward and approximately 0.025 whereas the axial velocity normalized by the jet velocity is approximately 0.75 at the same location.

The Reynolds stress is the component of the total stress tensor in a fluid obtained from the averaging of the Navier-Stokes equations to account for turbulent fluctuations in fluid momentum. The Reynolds stress tensor is anisotropic, as expressed in Equation 2.28 and yields self-similar profiles are presented in Figure 2.9. It further indicates the strong dependence to the radial and axial directions. It is therefore necessary to consider these two directions in studies on turbulent flow.

$$R_{st} = \begin{bmatrix} \overline{u'u'} & \overline{u'v'} & 0 \\ \overline{u'v'} & \overline{v'v'} & 0 \\ 0 & 0 & \overline{w'w'} \end{bmatrix} \tag{2.28}$$

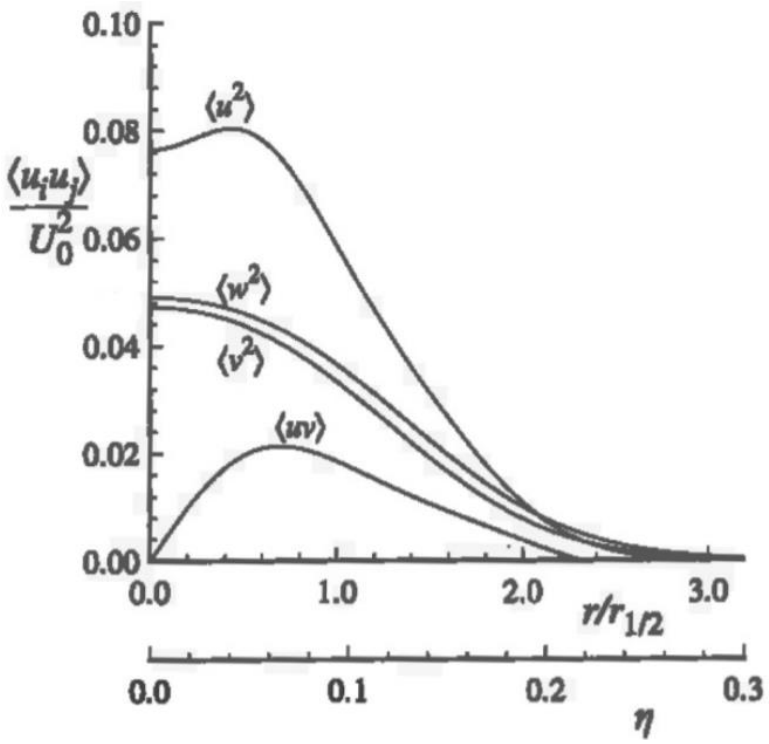

Figure 2.9: Profiles of Reynolds Stresses in the self-similar jet. Reprinted from Pope, 2009

The local turbulence intensity is another indicator of the spatial variation in jets, as shown in Figure 2.10, it reaches a minimum at the centerline, and increases indefinitely away from the centerline.

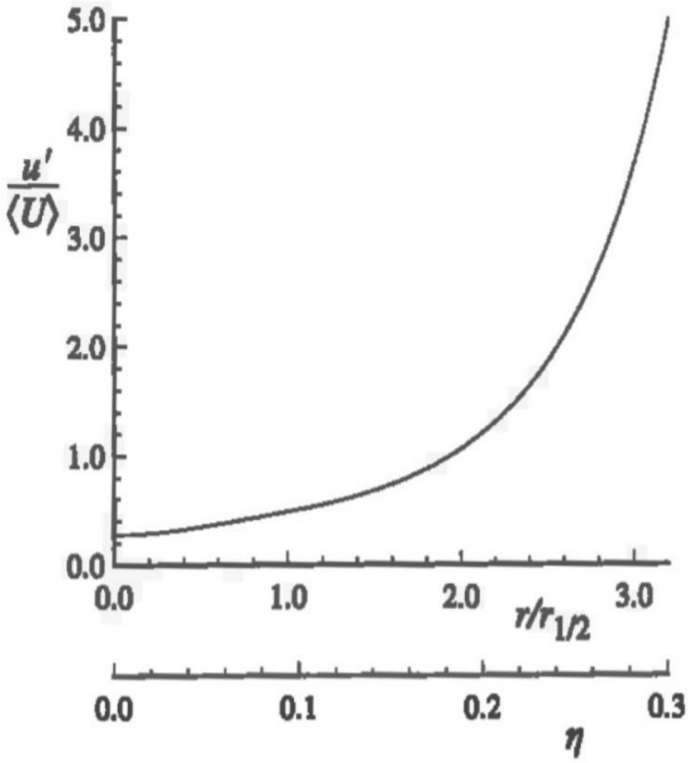

Figure 2.10: Profile of local turbulence intensity in the self-similar jet. Reprinted from Pope, 2009

With all these considerations, an analytical solution to the velocity distribution in a turbulent jet could be approximated. For a specific axial location (especially along the centerline) the velocity profile inside the jet can be expressed as a standard bell curve profile with standard deviation σ and maximum value as u_{max}:

$$u(r) = u_{max} \exp\left(-\frac{r^2}{2\sigma^2}\right) \tag{2.29}$$

We know that the width of the jet is approximately a fifth of the axial distance x hence the half width equivalent to the standard deviation σ is a tenth of the axial distance. Equation 2.29 could then be expressed as Equation 2.30.

$$u(x,r) = u_{max} \exp\left(-\frac{50r^2}{x^2}\right) \tag{2.30}$$

In order to determine the centerline velocity u_{max}, we consider the conservation of momentum between an axial position x and the nozzle tip which yields Equation 2.31.

$$\int_0^\infty \rho u \, 2\pi \, u \, r dr = \rho U_J \, U_J \frac{\pi d_{nozzle}^2}{4} \tag{2.31}$$

The integral of the left-hand side of Equation 2.31 using the expression of $u(x,r)$ from Equation 2.0 yields Equation 2.32.

$$u_{max} = \frac{5 d_{nozzle}}{x} U_J \tag{2.32}$$

which goes along with the fact that the centerline speed of a jet varies inversely with the distance along the jet.

The average velocity is computed as shown in Equation 2.33 and follows the same trend rom gaussian curves where the average value is equal to half of the maximum value.

$$\bar{u} = \frac{1}{\pi R^2}\int_0^{\infty} u\, 2\pi r dr = \frac{5d_{nozzle}}{2x}U_J = \frac{u_{max}}{2} \tag{2.33}$$

When considering the mass conservation, we observe that the mass carried by the jet increases with distance as shown in Equation 2.34, and it is due to the fact that the jet entrains ambient fluid, and therefore grows in size while maintaining the same momentum.

$$\dot{m} = \rho Q = \int_0^{\infty} \rho u\, 2\pi\, r dr = \frac{\pi}{50}\rho u_{max} x^2 = \frac{\pi}{10}\rho U dx \tag{2.34}$$

The entrainment rate can therefore be defined as shown in Equation 2.35.

$$E = \frac{change\ in\ volumetric\ flux}{distance} = \frac{dQ}{dx} = \frac{\pi dU}{10} \tag{2.35}$$

We observe that the rate of entrainment is constant down the jet. It is important to note that for cases of dilution or jet of a concentrated fluid into a less concentrated fluid zone, the fluid concentration as a function of axial and radial coordinates would

also follow a bell shape curve. It can also be shown that the Peclet number, a dimensionless number comparing the rates of advection and the rate of diffusion, is always very high, therefore accounting for the highly advective flow generated by the turbulent jet.

2.4 TURBULENT JETS IMPINGEMENT

Turbulent jet impingement flow can be fully defined by the jet Reynolds number, and the impingement conditions, which include the dimensionless standoff distance and the impingement wall shape and type. The dimensionless standoff distance, d^*, is a dimensionless axial distance between the jet nozzle and the impingement wall, characterized by the nozzle diameter as indicated by Equation 2.36.

$$d^* = \frac{z}{d_{nozzle}} \tag{2.36}$$

where z is the axial distance between the jet nozzle and the impingement plate, and d_{nozzle} is the nozzle diameter.

The jet impingement on a flat impermeable wall is characterized by three different regions, highlighted in Figure 2.11.

- Free jet region
- Stagnation region
- Wall jet region

2.4.1 The Free Jet Region

The free jet region is analogous to the free jet presented in Section 2.2. In that region, the central part of the jet, also called the potential core, about four to five nozzle diameters long, is an irrotational flow region which is unaffected and keeps a constant velocity equal to the initial jet velocity at the nozzle outlet. The shear-layer between the jet and the ambient fluid grows away from the nozzle due to the roll-up of vortices. The vortices induce a reduction in axial velocity, as they entrain large quantities of fluid. Past the potential core, the centerline velocity starts decaying as indicated in Table 2.1. That region can be considered as the jet development region or the decaying jet region, up to eight nozzle diameters away from the nozzle. (Hallqvist, 2006) After that region the fully developed jet is observed where the jet velocity has a Gaussian profile and follows the self-similarity rule. The existence of the three flow regimes is contingent upon the jet standoff distance, for instance, if it is less than three nozzle diameters, then only the potential core, within the free jet, region will be observed.

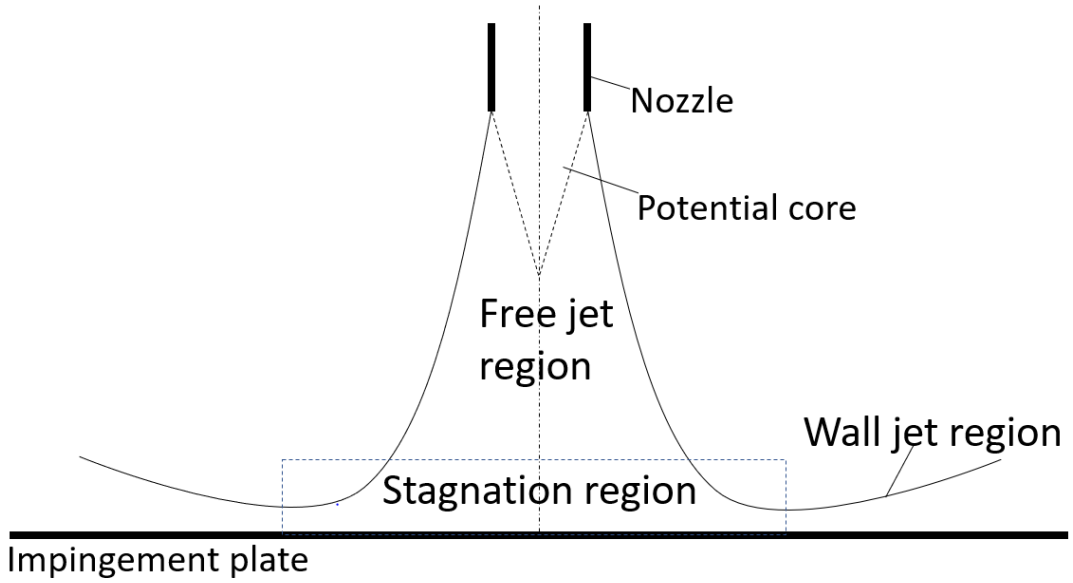

Figure 2.11: Regions of a jet impingement flow, adapted from Dewan et al. (2012)

2.4.2 The Stagnation Region

As the jet approaches the impingement plate, it turns in the transverse direction while simultaneously losing its axial velocity. These two effects lead to a spike in static pressure, which characterize the stagnation region. In this region high values for both the normal and shear stresses, as the jet is being deflected in that region. Nishino et al. (2008) reported a negative turbulence kinetic energy in that region, a complication which makes gridding very complex during numerical simulations.

2.4.3 The Wall jet

After deflecting at the stagnation region, the jet ends up moving parallel to the wall in the wall jet region. It leads to a velocity profile similar to the flat plate boundary-layer profile, except that it now consists of two distinct shear layers, a layer with the wall at the bottom, and a layer with the ambient fluid at the top. As a consequence, the turbulence levels in the wall jet are larger than in the boundary layer. (Hadziabdic and Hanjalic, 2008) The wall jet will also reach a self-similar behavior away from the stagnation region radially. Experiments by Knowles and Myszko (1998) indicate that the mean velocity of the wall jet attains self-similarity at a radial distance of 2.5 nozzle diameters, regardless of the initial standoff and jet velocity.

2.4.4 Key Parameters in Impingement Flows

2.4.4.1 The Standoff (or Nozzle to Plate) Distance Influence on Heat/Mass Transfer

The Nusselt number is a dimensionless number comparing the convective heat transfer across a boundary to the conductive heat transfer across that same boundary. Its mass transfer equivalent is the Sherwood number. They are both defined in details in section 2.7. The impingement of a developing or a fully developed jet (d*> 5) yields a peak in the Nusselt number, at the stagnation region and decreases sharply in the radial direction as the wall jet develops. Gardon and Akfirat (1965) achieved maximum stagnation Nusselt number (Nu_o) at a dimensionless standoff distance of 8. In their experiment, this length corresponded to the decaying jet region. They explained that the

reduction in Nu_o beyond this length was due to the reduction in axial velocity, while a reduction in Nu_o before this length was caused by less turbulence in the jet. Ashforth-Frost and Jambunathan (1996) have reported that the stagnation point Nusselt number reaches a maximum value at a distance of approximately 110% of the potential core length from the nozzle. The shape of the radial Nusselt number profile is also affected by the standoff distance. For small values while the jet is still within the potential core region, the Nusselt number produces a local minimum at the stagnation point and two maximums in the radial directions.

Several approaches have been proposed to explain the reasons behind this odd Nusselt number distribution. Goldstein and Timmers (1982), for instance, attributed this local minimum in the stagnation point Nusselt number to the low turbulence levels in the potential core. Gardon and Akfirat (1965) attributed the first peak to the flow acceleration in the wall jet region and the second peak to the transition from laminar to turbulent flow in the wall jet.

Huber and Viskanta (1994) justified the inner peak in the Nusselt number as a result of both the shallowness of the boundary layer due to the fluid accelerating out of the stagnation region and the influence of the turbulence generated at the shear layer around the jet circumference. Lytle and Webb (1994) explained that the outer peak was due to the transition to turbulent flow in the boundary layer; however, Chung and Luo (2002) have shown that the secondary peak also exists even for laminar jet impinging flows, where transition to turbulence does not exist. Chung and Luo (2002), credited the secondary peak to the vortical characteristics of the flow. The location and the amplitude

of these two maxima also depend on others parameters such as the Reynolds number and inlet flow conditions.

2.4.4.2 The Reynolds Number

Viskanta (1993) classified the flow regions for impinging flows based on the Reynolds number (Re) as laminar for Re < 1000, turbulent for Re > 3000, and laminar to turbulent transition for 1000 < Re < 3000. The jet Reynolds number was defined in Equation 2.2. The stagnation Nusselt number is related to the Reynolds number as expressed in equation 2.37.

$$Nu_0 \propto Re^k \tag{2.37}$$

The relation is stronger, and yields larger k values, for turbulent flows compared to laminar impingement. Shadlesky (1983) theoretically found a value of k = 0.5 for small nozzle to plate distance in a laminar flow. Chung and Luo (2002) also reported a similar value of k. Tawfek (1996) found a value of k = 0.691 for a dimensionless standoff distance d* between 6 and 58 and Reynolds number ranging from 3,400 to 41,000. The length of the potential core also depends on the Reynolds number. Beaubert and Viazzo (2003) reported that the potential core length varies in the Reynolds number range of 3000–7500; however, it attains a constant value of 4 for Reynolds number greater than 7500.

2.4.4.3 Semi-Confinement

A confinement of the flow affects the entrainment of the surrounding fluid into the jet. Ashforth-Frost et al. (1997) showed that the potential core becomes longer due to the confinement because of the less entrainment and corresponding lower levels of turbulence. Obot et al. (1982) reported a smaller value of Nusselt number in a confined impinging jet compared to that in an unconfined impinging jet for $2 < d^* < 12$.

2.4.4.4 Effects of Large Vortical Structures

The most recent interest in the impinging jet studies is on the vortex dynamics and the resulting unsteady behavior of the flow and surface heat transfer. Popiel and Trass (1991) using flow visualization, Yu et al. (2005) using LES, and others have visualized the formation, development, merging, and breakup of vortices in impinging flows. These studies show that pairing of small roll-up vortices produce large, so called primary vortices. These primary vortices induce secondary vortices in the wall jet region. O'Donovan (2005) (experimentally) and Hadziabdic and Hanjalic (2008), using LES, studied the possible effects of these structures on the surface heat transfer for small nozzle to plate distances. Their studies showed that the second peak in the Nusselt number is associated with the generation of secondary vortices in the wall jet.

2.5 TURBULENT JETS IMPINGING ON POROUS MATERIAL

The governing equations for the flow and energy of an incompressible fluid are given by the continuity equation in Equation 2.38, the momentum equation, the energy equations for the fluid phase and the solid porous matrix presented in Equations 2.40 and 2.41 respectively.

$$\nabla \cdot \boldsymbol{u} = 0 \tag{2.38}$$

$$\rho\left[\frac{\partial \mathbf{u}}{\partial \mathrm{t}} + \nabla \cdot (\boldsymbol{u}\boldsymbol{u})\right] = -\nabla p + \mu \nabla^2 \boldsymbol{u} \tag{2.39}$$

$$\left(\rho c_p\right)_f \left[\frac{\partial \mathrm{T_f}}{\partial \mathrm{t}} + \nabla \cdot (\boldsymbol{u}\mathrm{T_f})\right] = \nabla \cdot (k_f \nabla T_f) + S_f \tag{2.40}$$

$$\left(\rho c_p\right)_s \frac{\partial \mathrm{T}_s}{\partial \mathrm{t}} = \nabla \cdot (k_s \nabla T_s) + S_s \tag{2.41}$$

where the subscript f and s correspond to fluid and solid phases, respectively, T represents the temperature and k is the thermal conductivity, c_p is the specific heat and S is the heat generation term.

de Lemos (2012) designed a series of experiments and simulation of turbulent impinging flow unto a porous foam. A numerical simulation was also performed to address the limitations of the experimental work. The geometry for their design will be described, as well as the main results.

The geometry description is as follows: A fluid jet enters a cylindrical chamber through an aperture in an upper disk, Figure 2.12 shows a trimetric view of the setup with red arrows indicating the flow direction. An annular clearance between the cylinder lateral wall and the disc allows fluid to flow out of the enclosure. The geometry and simulation properties are listed in Table 2.2. Figure 2.13 shows a 2D projection of the geometry while indicating the simulation properties.

The two-dimensional planar cases detailed in Figure 2.14 are also considered. In Figure 2.14a, a turbulent jet with uniform velocity v_o enters through a gap into a channel with height H and length 2L. Fluid impinges normally against the bottom plate yielding a two-dimensional confined impinging jet configuration. The width of the inlet nozzle is B. In a different configuration, the bottom surface is covered with a porous layer of height h (Figure 2.14b). In both cases, the flow is assumed to be two-dimensional, turbulent, incompressible and steady. The porous medium is considered homogeneous, rigid and inert. Fluid properties are constant and gravity effects are neglected. The effect of the porous layer material, effectively representing a change in its permeability is highlighted in the fact that for the porous foam with the highest permeability, a secondary recirculation develops with a considerable size close to the cylinder wall. For the less permeable foams, this recirculation decreases due to the reduction of the porous layer permeability, so that the porous layer tends to act as a solid obstacle being hit by a jet, as it was the case for the solid wall impingement. The foams (porous layer) had porosities larger than 97% and permeabilities larger than 1E+8 mD.

Table 2.2: Geometry and simulation details for turbulent jets impinging on porous media from de Lemos (2012)

Parameter		Value
Incoming jet diameter	Dj	0.019 m
Inner cylinder diameter	D	0.39 m
Clearance width	W	0.005m
Height of fluid column	H	0.05 m 0.1 m 0.15 m
Porous layer thickness	Hp	0.05 m 0.1 m
Jet average velocity	Vj	1 m/s (Re = 18,900) 1.6 m/s (Re = 30,000) 2.5 m/s (Re = 47,000)

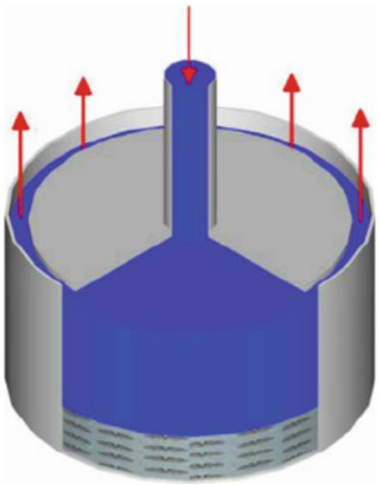

Figure 2.12: Axisymmetric flow of a confined jet impinging against a porous layer. Reprinted from de Lemos, 2005

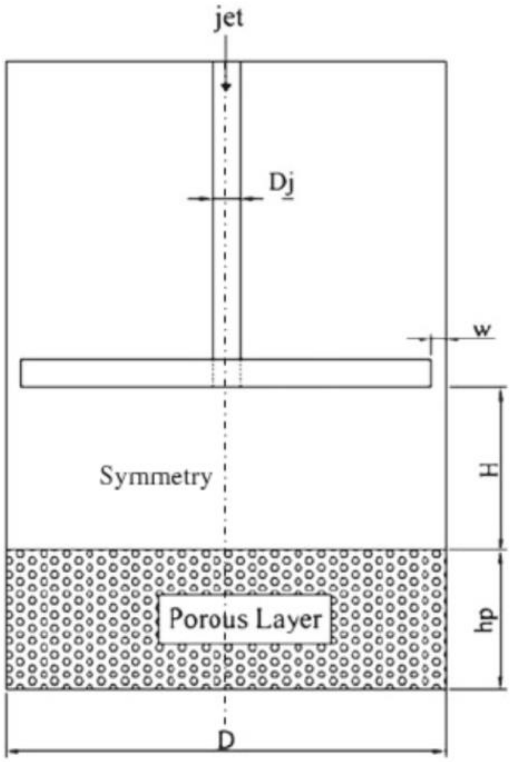

Figure 2.13: Cross section view and nomenclature of an axisymmetric flow of a confined jet impinging against a porous layer. Reprinted from de Lemos, 2005

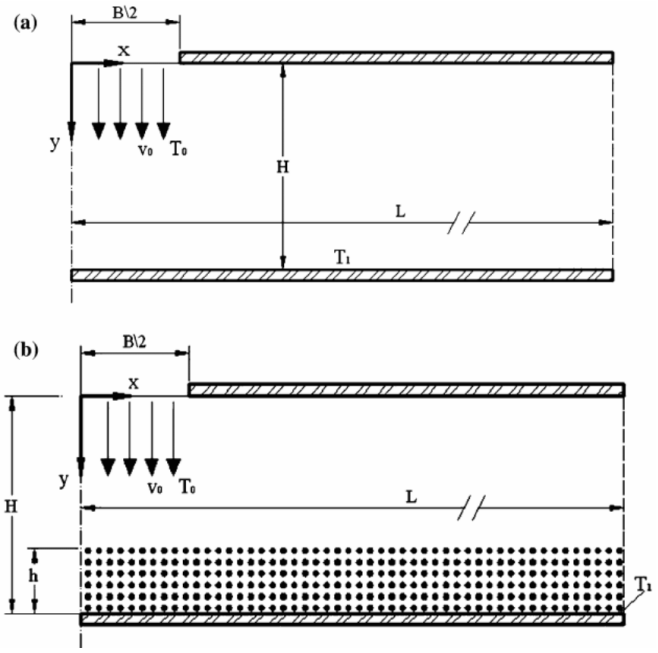

Figure 2.14: Two-dimensional planar flows: a) confined impinging jet on a flat plate; b) confined impinging jet on a plate covered with a layer of porous material. Reprinted from de Lemos, 2012

A turbulence field can be observed when the turbulent flow penetrates into the porous medium, as can be noticed by the contour lines going inside the porous bed. As the jet penetrates the foam, calculated turbulence intensities indicate that turbulence is damped almost completely at the interface.

2.6 ACIDIZING

2.6.1 Matrix Acidizing Modeling Approaches

There have been numerous modeling and numerical studies investigating wormhole initiation and growth. The most notable ones can be grouped in seven main categories.

- **Capillary Tube** Approach (Schechter and Gidley, 1969; Hung et al., 1989; Wang et al. 1993; Huang et al. 1997; Gdanski, 1999): The wormhole is assumed to be a cylindrical tube, which already exists and has a predetermined shape. A fundamental limitation of this approach is the assumption of the initial formation of the wormhole, which therefore requires a microscopic pore distribution at the surface where acid is injected in order to set up the model.

- **Damköhler Number** Approach (Hoefner and Fogler, 1988; Fredd and Fogler, 1998; Fredd, 2000): the Damköhler number is the ratio of the net rate of acid dissolution to the rate of transport of acid by convection. For mass-transfer limited systems the mass transfer rate is the net rate of dissolution. Models based on this approach do not independently predict wormhole growth and thus need to be combined with other models to predict skin evolution. Since the Damköhler number only applies to a single wormhole for a linear coreflood test, therefore the wormhole density and dimensions are required. Also, the approach does not translate directly to field scale.

- **Transition Pore Theory** (Wang et al, 1993; Huang et al., 1997): It postulates that there exists a critical pore cross-sectional area on the face of the rock for the formation of wormholes. Microscopic pore description is required for implementation. This method alone cannot be applied for monitoring skin evolution during treatment. The method incorrectly predicts than an increase in acid concentration will decrease the optimal acid flux.

- **Network Model** Approach (Hoefner and Fogler, 1988; Fredd and Fogler, 1998): This approach is used to describe processes in porous media where the important structural property of pore interconnectedness must be included. 3D extensions of this model require enormous computational power for field or laboratory scale.

- **Péclet Number** Approach (Daccord et al., 1989; Frick et al., 1994): It postulates that the propagation of wormhole is a function of the Péclet number, the injection volume and a fractal dimension.

- **Semi-Empirical** Approach (Buijse and Glasbergen, 2005; Furui et al., 2012): Here coreflood tests results for the fluid/mineral will yield an optimum acid velocity and pore volume to breakthrough. These two parameters will yield two constants which incorporate other parameters such as permeability, mineralogy, temperature and acid concentration. The results from this approach depend on the efficiency of the coreflood experiments.

- **Averaged Continuum (Two-Scale)** Models (Liu et al., 1997; Golfier et al., 2002; Panga et al., 2004; Kalia and Balakotaiah, 2007; Maheshwari et al. 2012): An approach based on continuum equations written at Darcy's scale. To describe the dissolution of carbonates, in a mass-transfer controlled regime, Golfier et al. coupled the pore scale phenomena to the Darcy's scale by using a mass transfer coefficient calculated from a pore scale simulation at each stage in the simulation of the model. These models give a good prediction of the dissolution pattern and

estimation of the optimum injection rate at laboratory scale. They will require enormous computational power for field scale simulations. It is important to describe the models' theory, as it also provides a theoretical understanding to the process.

2.7 MASS AND HEAT TRANSFER ANALOGY

Most of the engineering problems about impinging flows are considering both mass and heat transfer and there is a limited number of studies strictly on mass transfer. It is therefore important to understand how the analysis and results obtained from heat transfer studies of impinging jets could be translated to useful results for mass transfer. Here the mass and heat transfer analogy will be presented.

This theory was developed by Schmidt and Nusselt based on the conservation equations for momentum, heat and mass transfer of a constant property fluid in order to transfer information from a heat transfer process to physically and geometrically similar mass transfer process and vice versa. For instance, similarity would be expected/required for boundary conditions such as:

- Heat transfer: Reynolds number Re, Prandtl number Pr, a constant fluid temperature T_w or flow rate q_w, and identical model shape.
- Mass transfer: Reynolds number Re, Schmidt number Sc, fluid concentration cw or mass mw, and identical model shape.

It is important to distinguish in the description of a model between its size and its shape. The size is characterized by a prescribed length and appears in the Reynolds

number. The shape is described by all dimensionless lengths and is combined in the Nusselt and Sherwood numbers. The Nusselt number Nu, is a dimensionless expression of the heat transfer coefficient and the Sherwood number Sh is the equivalent expression for the mass transfer coefficient. They also represent the dimensionless temperature and mass concentration gradients, respectively, at the model surface. Equations 2.42 and 2.43 give their common definition.

$$Nu = \frac{\partial(T/\Delta T)_w}{\partial(n/C)_w} \tag{2.42}$$

$$Sh = \frac{\partial(c/\Delta c)_w}{\partial(n/C)_w} \tag{2.43}$$

where n is the normal to surface and C is the chord length.

The two processes are analogous (i.e. the Nusselt number equals the Schmidt number) for the two fluids when the Prandtl number and the Schmidt number are equal, which expresses the heat/mass transfer analogy.

A common difficulty arises when the Prandtl number, characterizing the heat transfer fluid is different from the Schmidt number characterizing the mass transfer fluid. In that case the heat/mass analogy is not fulfilled as previously described and now has to be presented as Equation 2.44, an analogy factor F has been included.

$$Nu = F \cdot Sh \text{ when } Pr \neq Sc \tag{2.44}$$

That analogy factor will be a function of the boundary conditions and will only be useful if simple relations can be found for it.

For an extended analogy, Eckert et al. (2001) presented some relationships which can be deduced from the Navier-Stokes, the heat transfer and the mass transfer equations. Two of these relationships are presented here.

a) The Navier-Stokes equations with their boundary conditions can be solved for a constant property fluid without information on heat and mass transfer processes, the flow field in dimensionless form is independent of either the Prandtl or the Schmidt numbers of the fluid and depends only on the Reynolds number and the model shape. The velocity field influences the temperature or concentration filed without itself being influenced.

b) For a specified flow process, the functional relationship between the temperature field and the concentration field in the differential equations describing a heat or mass transfer process such that the equation for a mass transfer process can be converted into an equation for the heat transfer process by replacing the Schmidt number by the Prandtl number and vice-versa.

This section shows that the scarcity of literature on mass transfer during a turbulent impinging jet of reactive fluid could be overcome with the inclusion of literature on thermal studies of turbulent impinging jets, which are more numerous. The conclusions

reached in the heat transfer studies could therefore be considered analogous in the equivalent mass transfer studies.

2.8 COMPUTATIONAL FLUID DYNAMICS (CFD) OF ACID JETTING

During acid jetting, a high-velocity stream of reactive fluid is injected to a carbonate rock surface. It leads to two processes as the turbulent acid stream reaches the porous medium surface: there ensues a physical impact and a chemical reaction. It leads to a turbulence-enhanced erosion at the location of impingement and wall-jet. This process combines turbulent impinging flows and reactive flow through porous media. Fundamental analysis of impinging turbulent flows is exceedingly difficult due to their intrinsic properties: chaotic, time-dependent and three-dimensional. Scientists and engineers have to resort to statistical methods based on a combination of experimental and theoretical approaches for analysis. (Deen, 2012) Experimentally, turbulent jets have displayed some common properties: 1- The existence of a zone of flow establishment up to a distance of approximately six times the nozzle diameter axially, 2- That zone is followed by the zone of established flow where the axial velocity is self-similar and gaussian, and 3- The jet propagates at an angle of 11.8^0 from the z-axis in the flow. The dominant flow direction is in the axial direction, with a relatively smaller lateral velocity. The flow spreads gradually and the axial gradients are smaller than the lateral gradients. (Pope, 2009) Turbulent jet impingement yields mass and energy transfer. The physics of the transfer change depending on the impingement location. The governing

equations for the steady flow of a free jet in the (z, r) co-ordinate system are the continuity equation (Equation 2.45) and the z-momentum equation (Equation 2.46).

$$\rho \frac{\partial u}{\partial z} + \rho \frac{1}{r} \frac{\partial}{\partial r}(rv) = 0 \tag{2.45}$$

$$\rho u \frac{\partial u}{\partial z} + \rho v \frac{\partial u}{\partial r} = -\frac{1}{r} \frac{\partial}{\partial r}(r\rho \overline{u'v'}) \tag{2.46}$$

where *z* is the axial direction, *r* is the radial direction, u is the axial velocity, *v* is the radial velocity, and ρ is the fluid density. Figure 2.15 displays a geometric representation of the coordinate system, from the nozzle tip.

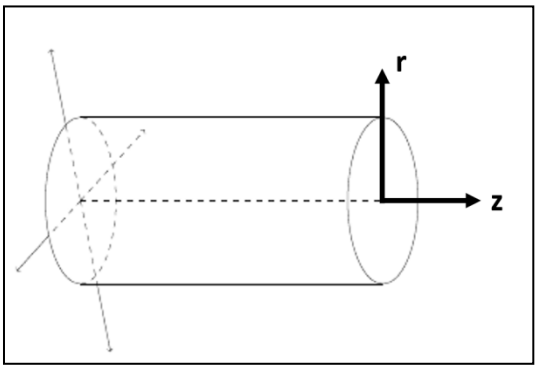

Figure 2.15: Geometric representation of the axial (z) and radial (r) directions mentioned.

It can be proven that the momentum flux in a turbulent jet is preserved, as expressed in Equation 2.47.

$$\frac{d}{dz}\int_0^\infty \rho u^2 2\pi r dr = 0 \tag{2.47}$$

where ρ is the density and u represents the fluid velocity

For free turbulent jets in stagnant flow, it is seen that the fluid velocity is inversely proportional to the distance from source, while the volume flux increases linearly with time. (Lee and Chu 2003)

For constant-property Newtonian fluid flow (laminar or turbulent), the Navier-stokes equations, embody the governing laws. Nonetheless for turbulent flows the equations describe every detail of the turbulent velocity field, which includes time and length scales from the largest to the smallest scales. This extremey large amout of information makes it very tough and almost impossible to perform direct numerical simulation (DNS), the other alternative is to follow a statistical approach, given that statistical fields generally have a smoother variation. In this case, for example rather than describing the flow in terms of the velocity **U**(x,t), the mean velocity field <**U**(x,t)> could be considered for calculations. The statistical approaches include the turbulent viscosity models such as the k-epsilon model, the Reynold stress models, models based on the probability density function (PDF), and large-eddy-simulations (LES).

2.8.1 Computation of a Normal Jet Impingement on a Flat Surface

Most practical impinging flows are turbulent in nature. In contrast to laminar flows, turbulent flow consists of a large spectrum of scales, inducing a higher level of complexity in computation. There are several computational approaches to solve for turbulent impinging flows. The most popular and recommended approach is the Large Eddy Simulation (LES) which now dominates computational methods based on the Reynolds averaged Navier-Stokes (RANS) approach. (Dewan et al., 2012)

2.8.1.1 Large Eddy Simulation (LES)

For a fundamental investigation of impinging flows, three-dimensional instantaneous flow fields are required, coupled with high Reynolds numbers, it makes the LES approach the most appropriate, as reaching a solution with the high-resolution direct numerical simulation (DNS) would become too demanding computationally and realistically unreachable. Several studies were conducted using LES of impinging flows with different objectives, from the testing a new sub grid scale (SGS) model to the investigation of complex physical phenomena too difficult to achieve experimentally.

A major parameter in the computational approach is the selection of the turbulence model. The LES approach allows for a detailed analysis of the larger eddies, responsible for most of the transport, mixing and the wall effects (impingement and wall jet) at the interface. The larger eddies would also carry most of the weight on the dissolution structure. The smaller 000000010eddies, in this case could be modeled using an SGS model. The LES is implemented via filtering of the time-dependent Navier-

Stokes equation in Fourier/configuration space. Equation 2.48 and 2.49 present the filtered Continuity and Navier-Stokes equations.

$$\frac{\partial \rho}{\partial t} + \frac{\partial}{\partial x_i}(\rho \bar{u}_\iota) = 0 \tag{2.48}$$

$$\frac{\partial}{\partial t}(\rho \bar{u}_\iota) + \frac{\partial}{\partial x_j}(\rho \bar{u}_\iota \bar{u}_\jmath) = \frac{\partial}{\partial x_j}\left(\mu \frac{\partial \sigma_{ij}}{\partial x_j}\right) - \frac{\partial \bar{p}}{\partial x_i} - \frac{\partial \tau_{ij}}{\partial x_j} \tag{2.49}$$

where, $\bar{u}_\iota$ is the filtered velocity. σ_{ij} is the stress tensor due to molecular viscosity, defined by Equation 2.50.

$$\sigma_{ij} = \left[\mu\left(\frac{\partial \bar{u}_\iota}{\partial x_j} + \frac{\partial \bar{u}_\jmath}{\partial x_i}\right)\right] - \frac{2}{3}\frac{\partial \bar{u}_\iota}{\partial x_i}\delta_{ij} \tag{2.50}$$

And τ_{ij} is the sub grid-scale stress defined by Equation 2.51.

$$\tau_{ij} \equiv \rho\overline{u_\iota u_\jmath} - \rho \bar{u}_\iota \bar{u}_\jmath \tag{2.51}$$

The Boussinesq hypothesis is used for computing sub grid-scale turbulent stresses, as shown in Equation 2.52.

$$\tau_{ij} - \frac{1}{3}\tau_{kk}\delta_{ij} = -2\mu_t \bar{S}_{ij} \tag{2.52}$$

where μ_t is the sub grid-scale turbulent viscosity and $\bar{S}_{ij}$ is the rate-of-strain tensor for the resolved scale.

2.8.1.2 The Smagorinsky Sub-grid Scale model

In the Smagorinsky SGS model, the eddy viscosity, which is a product of a length scale and a velocity scale, can be expressed as shown in Equation 2.53:

$$\mu_{SGS} = (C_s\Delta)^2\sqrt{2S_{ij}S_{ij}} \tag{2.53}$$

where Δ denotes the grid size, and C_s is an arbitrary constant which has to be provided as an input.

There are several limitations to the Smagorisnky model. The constant Cs changes with the flow configuration studied, and given that it cannot be negative, it would not be able to show the backscatter of the flow. The model does not reproduce the near-wall behavior of the SGS eddy viscosity, which implies that damping functions have to be used to resolve that issue. In order to go beyond these limitations, other SGS models have been developed. In a dynamic Smagorinsky model (Germano et al., 1991), the value of Cs is calculated at each time step by double filtering of the flow variables. All the limitations of the Smagorinsky model can be overcome by using a dynamic Smagorinsky model. However, it yields some instabilities in the field, which need to be overcome. In a wall-adapting eddy viscosity model (WALE) (Nicoud and Ducros,

1999), the expression for the sub grid-scale eddy viscosity is changed so as to automatically take care of the zero value at the wall. The similarity SGS model of Bardina et al. (1980) does not use the Boussinesq hypothesis and assumes the scale invariance. However, because of its non-dissipative nature, similarity models are often used with an eddy viscosity term. Such models are called mixed similarity models.

2.8.1.3 The Smagorinsky-Lilly Sub-grid Scale Model

The Smagorinsky-Lilly model is a sub grid scale model which could be used to compute μ_t. In this model, the eddy-viscosity is modeled by Equation 2.54 and 2.55.

$$\mu_t = \rho L_s^2 |\bar{S}| \tag{2.54}$$

$$|\bar{S}| \equiv \sqrt{2\bar{S}_{ij}\bar{S}_{ij}} \tag{2.55}$$

where L_s is the mixing length for sub grid scales, as defined in Equation 2.56.

$$L_s = min\left(\kappa d,\ C_s V^{\frac{1}{3}}\right) \tag{2.56}$$

where κ is the von Karman constant, d is the distance to the closest wall, C_s is the Smagorisnky constant as approximated in Equation 2.57, and V is the volume of the computational cell.

$$C_s \sim 0.1 \tag{2.57}$$

A more detailed description of the LES approach and the S-L sub grid model is provided by Sagault (2001) and Kim (2004).

2.8.1.4 Summary of Some LES Studies on Turbulent Impinging Jets

Olsson and Fuchs (1998) performed a study at Re of 10,000 with the objective to assess different sub grid scale models to study the dynamics near the wall and their key finding was that the stress-similarity model gave better results for the specific grid they considered. Also, the variation in turbulence intensity was less than 10% among different SGS models. They performed four different simulations; two without any explicit SGS models, one with dynamic models, and one using stress similarity model. For spatial discretization, they used a third order upwind biased scheme for the convective term, and fourth-order central finite difference for the other terms. For temporal discretization, they used a third order multistage Runge-Kutta method.

Cziesla et al. (2001) wanted to understand the flow phenomena and to accurately predict the stagnation heat transfer, for Reynolds number between 2000 and 10,000. They well predicted a negative production of turbulence at the stagnation point, which resulted in an accurate prediction of the stagnation Nusselt number. They used a dynamic Smagorinsky SGS. For the spatial discretization they used a second-order finite difference scheme in a staggered grid. For the temporal discretization, they used the explicit Adams–Bashforth scheme for the convective terms and the implicit Crank–Nicholson scheme for the viscous terms, and both are second-order accurate.

Beaubert and Viazzo (2003) wanted to assess the ability of LES to predict impinging flows. The dependence on the Reynolds number was also studied by comparing results at Reynolds number values of 3000, 7500 and 13500. They found that for Reynolds number values above 7500, the jet structure became independent of the Reynolds number and had an asymptotic behavior. They used a dynamic Smagorinsky SGS. For spatial discretization, they used the Fourth-order compact finite difference schemes in the inhomogeneous directions and Fourier pseudo-spectral scheme in the homogeneous direction and a staggered grid. They used the same temporal discretization as Cziesla et al. (2001).

Hallqvist (2006) studied the effect of different inflow conditions on the accuracy of the computation for Re=20,000. He concluded that the inflow conditions had a significant effect on the accuracy of the computations for standoff distances. He used no explicit SGS model, but rather a dissipative numerical scheme. For the spatial discretization, he used the finite difference with third-order upwind biased scheme for the advection equation and other terms using a fourth-order central difference. The three-step Runge–Kutta method was used for the temporal discretization. He justified not using an SGS model by arguing that using an SGS model, known to be incapable of account for anisotropy and backscatter would be more harmful than the expected error from neglecting the SGS terms.

Rhea et al. (2009) compared LES and RSM for plane impinging jets at Re =10,000 and found that the RANS computations lead to some discrepancies, especially in the free and wall jet regions. They used a dynamic Smagorinsky SGS for the LES

simulations. A finite volume with second-order discretization was used for the spatial coordinates, and an implicit Gear method, which is second-order accurate was used for temporal discretization.

Lodato et al. (2009) conducted a study of the prediction capabilities of a new WALE mixed similarity SGS model for Reynolds number at 23,000 and 70,000. They showed that a correct representation of the backscatter by SGS models is the key to accurate predictions, especially in the under-resolved near wall region. They used a mixed similarity model combined with WALE, a standard WALE, and a Lagrangian dynamic Smagorinsky model. They used a finite volume with fourth-order scheme for spatial discretization, and a third order Runge-Kutta scheme for the temporal discretization. Along with Ollson and Fuchs (1998), they found that all the SGS models yielded the same information for the mean velocity, they only slightly (<10%) differed in the prediction of the turbulence statistics.

2.8.1.5 Impact of Spatial and Temporal Numerical Schemes:

In LES, the choice of a numerical scheme can impact the accuracy of the computations because numerical schemes and SGS models are interrelated. Several different methods have been investigated such as: finite-difference, finite-volume, and spectral methods, for LES studies of impinging jet. In general, finite difference methods and spectral methods are more accurate than the corresponding finite-volume methods for simple geometries. A downside of the spectral methods is that they are only applicable in homogeneous directions. Prior efforts in LES of impinging flows used

either finite-difference or a combination of finite-difference and spectral methods. However, a recent tendency is to use the finite-volume method in all three directions. This trend could be a result of the confirmed usefulness of finite-volume methods in handling complex geometries and the availability of finite-volume packages in different institutions as well as commercially. In LES, dissipative schemes (upwind-based schemes) sometimes provide numerical dissipation which is more than the SGS dissipation, and the higher order central difference schemes result in numerical instabilities. Therefore, the selection of an appropriate scheme for a particular geometry also depends on other factors such as the SGS model. For time discretization, both implicit and explicit schemes and their combinations have been explored.

2.8.1.6 Impact of the Distribution of Grid

The grid spacing in LES must be chosen so that the cutoff filter falls in the inertial subrange, while also resolving the small streaks in the near wall regions with a minimum of grid stretching.

2.8.1.7 Impact of Near-Wall Treatment in LES

The standard no-slip condition is commonly used without any near-wall modeling. The grid size in the near-wall region has to be sufficiently fine and of the same order as in the DNS, as a consequence only small Reynolds number can be studied with LES for wall-bounded flows. Therefore, in order to use LES in the design of practical impinging systems modeling of the near-wall region is a priority. Two standard

methods have been reported in the literature for the near-wall modeling. In the first method the instantaneous wall functions are set at the first grid point, which is typically placed in the logarithmic region. The standard law-of-the-wall is used as the wall function. However, this method is failing for impinging flows, because the standard law-of the- wall is not valid in both the wall jet and in the stagnation regions. The second approach is the zonal two-layer strategy, where a separate modeling process applied near the walls supplies the wall shear stress for LES. The boundary layer equations or Reynold's Averaged Navier-Stokes (RANS) equations are solved in a coarse mesh in the near-wall region. When RANS equations are solved in the near-wall region the procedure is called the hybrid RANS/LES model. Another near-wall treatment of impinging flows has been reported by De Langhe et al. (2008), who studied a normal round jet impingement with a hybrid RANS/LES model and found a better prediction of Nusselt number profiles compared to the results with a detached eddy simulation (DES), another hybrid RANS/LES model.

2.8.1.8 Direct Numerical Simulation (DNS) of Normal Jet Impingement

Chung and Luo (2002) performed DNS to study the unsteady behavior of flow and heat transfer in an impinging jet and found that the unsteady behavior of the stagnation heat transfer is caused by the impingement of the primary vortices that originate at the exit of the jet nozzle. Tsubokura et al. (2003) performed DNS to study the differences in three-dimensional eddy structures in jet impingements. Satake and

Kunugi (1998) obtained mean velocity, turbulence profiles, pressure distribution, and turbulence kinetic energy budgets at various radial locations for a round jet impingement using DNS. Recently, Tsujimoto et al. (2009) performed DNS and studied the effect of active forcing using two types of excitations. Although these DNS studies are limited to low Reynolds number, they provide results detailed enough to construct a new useful turbulence model.

As in the LES studies, different researchers have used varied inflow conditions in their DNS studies. Satake and Kunugi (1998) and Hattori and Nagano (2004) used precursor simulations to generate inflow conditions. Tsujimoto et al. (2009) used a top-hat velocity profile given by Equation 2.58 and added random fluctuations of 1% of the mean velocity to it.

$$V = \frac{V_1 + V_2}{2} - \frac{V_1 - V_2}{2} \tanh\left[\frac{R}{4\theta_m}\left(\frac{r}{R} - \frac{R}{r}\right)\right] \tag{2.58}$$

where V_1 and V_2 are the jet centerline velocity and the co-flow velocity respectively, while θ_m represents the momentum thickness at the inlet. Here $\frac{R}{\theta_m}$ is equal to 20.

2.8.1.9 Reynolds-Averaged Navier-Stokes (RANS) Equation Modeling

Zuckerman and Lior (2006) compared the suitability of different RANS-based models in predicting the average Nusselt number distribution as well as the location and

magnitude of the secondary peak in Nusselt number. Their comparisons showed that shear-stress transport (SST) k-ω models would accurately predict both the Nu distribution and the secondary peaks, while the standard k-ε and k-ω models would not. Generally, the complexity of the flow in the stagnation region leads to poor prediction of stagnation Nusselt number by RANS-based models. For instance, Ashforth-Frost and Jambunathan (1996) have found severe exaggeration of the stagnation point heat transfer. A major reason for this deviation is the assumption of isotropy of eddy viscosity-based models, which is not valid in the stagnation region. Reynolds stress models (RSM) overcome this problem by solving transport equations for each of the Reynolds stress components. However, modeling the pressure-strain term in RSM is tough in the stagnation region, and it is the reason behind the poor prediction of the stagnation Nusselt number.

RANS-based models are also problematic because they include several arbitrary coefficients which have been optimized for a certain flow region and would not provide accurate results in a different flow region. For example, the standard k-ε model shows excellent agreement in the free jet region but is incorrect in the stagnation and the wall jet regions. Similarly, the standard k-ω model is well adjusted for the near-wall flows but performs poorly (compared to the k-ε model) in free-shear flows. Poor performance of the wall functions and damping functions in the stagnation as well as the wall jet region is also a reason for poor performance of the RANS-based models. Wall functions are used with high Reynolds number formulation and damping functions are used in low

Reynolds number formulation of RANS-based models to treat the near-wall behavior of flows.

The time averaging approach is another issue with the RANS-based models. It assumes that the flow is statistically stationary. However, recent studies show that quasi-periodic impingement of largescale coherent structures makes the flow and heat transfer in the impingement plate highly unsteady.

Le Song and Prud'homme (2007) used unsteady RANS (URANS) equations with steady boundary conditions to predict the coherent structures in jet impinging flows. It is an approach where an unsteady time averaging scheme of the Navier–Stokes equations is combined with a RANS model. Because of the unsteady averaging, URANS can resolve vortices in the flow at lesser computational cost in comparison to LES and DNS. The Reynolds number of the study was 6000. The results showed that this method accurately reproduces coherent structures of the impinging flow. Kubacki and Dick (2009) used an improved k-ω model for the computation of round impinging jet. The k-ω model was modified based on the length-scale correction and an impingement detector. They reported improvements in the prediction of stagnation flow region with this approach.

2.8.2 CFD of Carbonate Acidizing ad Flow Through Porous Media

After a careful review of the impingement flow CFD models, it is necessary to review the models accounting for the chemical reaction at the impingement location and the subsequent flow through the rock.

2.8.2.1 The Furui et al. (2010) Model

This wormhole propagation model argues that the velocity at the tip of the propagating wormhole drives the wormhole propagation rate. That tip velocity is also significantly higher than the average interstitial velocity. The model estimates the wormhole growth rate, as presented in Equation 2.59.

$$v_{wh} = v_{i,tip}\, N_{Ac} \left(\frac{v_{i,tip} PV_{bt,opt} N_{Ac}}{v_{i,opt}}\right)^{-\gamma} \left[1 - \exp\left[-4\left(\frac{v_{i,tip} PV_{bt,opt} N_{Ac} L_{core}}{v_{i,opt}}\right)^{2}\right]\right]^{2} \quad (2.59)$$

where v_{wh} is the wormhole growth rate, $v_{i,tip}$ is the interstitial velocity at the tip in cm/min, N_{AC} is the acid capacity number, $v_{i,opt}$ and $PV_{bt,opt}$ represent the empirical optimum interstitial velocity and optimum pore volumes to break through, respectively, and L_{core} is the core length.

2.8.2.2 3D Two-Scale Continuum Model

In this model, the dynamic changes of porosity and permeability due to dissolution of minerals are considered. In addition, nonlinear chemistry at the solid–fluid interface is considered. The governing equations are the continuity equation. The acid mass balance equation and the solid mass balance equation listed as Equation 2.60, 2.61 and 2.62 respectively.

$$\frac{\partial \phi}{\partial t} + \nabla \cdot V = 0 \tag{2.60}$$

$$\frac{\partial(\phi\, Cf)}{\partial t} + \nabla \cdot (V\, Cf) = \nabla \cdot (\boldsymbol{D}^* \cdot \nabla Cf) - k_c a_v (C_f - C_s) \tag{2.61}$$

$$\frac{\partial \phi}{\partial t} = \frac{(R\,(Cs)\alpha\, a_v)}{\rho_s} \tag{2.62}$$

where t is an independent variable, V is the Darcy velocity, D^* is the dispersion tensor, C_f and C_s are the acid concentration in the bulk of fluid phase and in the solid-liquid interface, respectively. φ is the porosity of the reservoir, k_c is the local mass-transfer coefficient, a_v is the interfacial area defined as the fluid–solid interfacial area per unit volume of the medium, α is the dissolving power of the acid, defined as grams of solid dissolved per mole of acid reacted, R(Cs) represents the rate of the dissolution reaction, and ρs is the density of the solid phase.

The auxiliary equation is the Darcy Equation

:

$$\nabla P - \rho g = -\mu\, K^{-1} \cdot V \tag{2.63}$$

where P is the reservoir pressure, K is the permeability tensor, μ and γ represent the viscosity and specific gravity of fluid. Moles of acid in the solid–liquid interface that

react with the solid phase are coming from the bulk of liquid phase with concentration C_f . The driving force for this transport is $(C_f - C_s)$.

It can be thus written that:

$$k_c\,(C_f - C_s) = R\,(C_s) \tag{2.64}$$

The term R(Cs) represents the rate of dissolution reaction, which is considered to be nonlinear and is defined as:

$$R\,(Cs) = k_s\,C_s^n = k_o exp\left(-\frac{\Delta E}{RT}\right) C_s^n \tag{2.65}$$

The constant k_s varies with temperature according to the Arrhenius' law, and the coefficient n varies with temperature for dolomite. In Equation 20, T is temperature, R is the universal gas constant, and constants for limestone are given in Table 2.3. In Table 2.3, concentrations are expressed in gram-mol per cubic centimeter and all rates are moles produced per square centimeter per second. In addition, some equations are required to represent the relations between pore scale and petrophysical properties in the porous media. The modified Kozeny-Carman relations (Kalia et al., 2007) can be used as shown:

$$\frac{K}{K_o} = \frac{\phi}{\phi_o}\left[\frac{\phi(1 - \phi_o)}{\phi_o(1 - \phi)}\right]^{2\beta} \tag{2.66}$$

$$\frac{r_p}{r_o} = \sqrt{\frac{K\phi_o}{\phi K_o}} \tag{2.67}$$

and

$$\frac{a_v}{a_o} = \frac{\phi r_{po}}{\phi_o r_p} \tag{2.68}$$

where, K_o, r_{po}, and a_o are the initial values of permeability, average pore radius, and interfacial area, respectively, and β is an exponent, which can be experimentally obtained. β is a tuning parameter calculated by matching the skin obtained from the field data with that obtained from the simulation. In the model, acid is assumed to be injected at constant rate into a well with the following boundary and initial conditions:

$$u_i = -\frac{K}{\mu}\frac{\partial P}{\partial r}\,, \qquad C_f = C_i\,, \qquad r = r_w \tag{2.69}$$

$$P = P_e, \qquad C_f = 0, \qquad r = r_e \tag{2.70}$$

Table 2.3: Constants for the reaction of Hydrochloric Acid and Calcite (Williams et al., 1979)

Mineral	n	$k_0 \left[\frac{kg\ mol\ HCl}{m^2 s \left(\frac{kg\ mol\ HCl}{m^3\ acid\ solution}\right)^n}\right]$	$\frac{\Delta E}{R}\ (K)$
Calcite ($CaCO_3$)	0.63	7.291×10^7	7.55×10^3

CHAPTER III

CFD MODEL OF EXPERIMENTAL ACID JETTING*

3.1 PREAMBLE

A core-scale CFD model has been developed to simulate cavity and wormhole growth in acid jetting. Presently the model is twofold, namely a 3D two-step model using commercial software (ANSYS Fluent) to solve for the turbulent impinging flow, combined with a computer code to simulate the dissolution due to impingement, wall jet and acid flux through the core.

The two-step model alternates between the two fundamental aspects of the overall acid jetting process. Firstly, it studies the fluid mechanics of the turbulent jet exiting the nozzle and continuously impinging on the porous media transient surface. Secondly it focuses on the inclusion of an irreversible chemical reaction with dissolution and transport at the impingement location between the fluid and rock matrix. The jet fluid dynamics are implemented using a 3D transient finite volume numerical solver using Large Eddy Simulations (LES) with the Dynamic Smagorinsky-Lilly sub-grid model to solve the Navier-Stokes and continuity equations. The results of this simulation include a velocity and pressure distribution at the porous media surface. The reactive transport is modeled after the conventional kinetics of the dissolution of calcite by

* Part of the data reported in this chapter is reprinted with permission from "Acid Jetting on Carbonate Rocks: A Computational Fluid Dynamics Study at Laboratory Scale" by Ndonhong, V., Zhu, D., and Hill, A.D. 2018, Paper SPE-190849, Copyright 2018, Society of Petroleum Engineers.

hydrochloric acid. This two-step model successfully replicates experimental results and observations for the cavity growth.

3.2 METHODOLOGY AND MODEL FORMULATION

The model described in this work is the coupling of a transient finite volume model for the turbulent flow from the jet nozzle to the rock/fluid interface and a model of dissolution by chemical reaction at that interface. The turbulent flow finite volume model is run using the commercial software ANSYS Fluent 15 to solve the transport equations for diffusion and convection of acid from the turbulent jet. The second part of the model focuses on the dissolution at the contact region between the acid and the rock surface and the subsequent change in geometry due to mass and momentum transfer; another finite-volume numerical code is used to process the results from Fluent and combine with the chemical reaction parameters to estimate the volumes and geometry of the dissolution structure.

In this modeling effort, the goal is to first match experimental work, then extend beyond the experimental limitations and possibly answer the questions about the extent of the turbulent jet effect on the stimulation from a single injection point in linear flow. These observations could lead to a better understanding of the additional benefit that the turbulent jet could add to conventional matrix acidizing.

3.3 EXPERIMENTAL ACID JETTING

Multiple linear acid jetting experiments were conducted in the Texas A&M University Acid Jetting Laboratory in the department of Petroleum Engineering. The reader interested in the objective, experimental procedure, and results from that study is encouraged to review the publications by Holland (2014), Ndonhong (2014), Belostrino (2016), Frick (2018) and Ridner (2018). The experimental observations are the foundation of this study; they revealed the outcome from acid jetting, a bulb-shaped cavity at the impingement location and wormholes if there was some acid flux trough the core. These observations helped understand the physical processes at play. The experimental data will also be considered for model validation and trend verification.

The cores used for the experiments were 4 inches in diameter and 16 inches in length. The nozzle inner diameter was set at 0.0225 inches and the initial standoff distance was always set at 4 nozzle diameters, which is equivalent to 0.09 inches. The parameters set prior to every experiment are the jetting velocity (expressed in ft/s, and 1 ft/s ~ $3.5 * 10^{-1}$ m/s) and the initial acid flux through the core, referred to as the initial interstitial velocity (initial v_i, volumetric flow rate over the normal cross-sectional porous area, q/Af in cm/min, and 1 cm/min ~ $1.7 * 10^{-4}$ m/s). The choice of jetting velocities was guided by prior field applications (Beckham et al., 2015), for that reason 3 jetting velocities were selected (107 ft/s ~ 33 m/s, 150 ft/s ~ 46 m/s and 200 ft/s ~ 61 m/s).

Holland (2014) and Beckham (2015) established the experiment design, and observed that the outcome of every acid jetting experiment was a bulb-shaped

dissolution structure from the initial impingement location, which could be followed by wormholes when acid flux through the core was induced by a pressure differential across the core. No wormholes would occur for conditions of no acid flux through the core.

3.4 MODEL ASSUMPTIONS

The model assumptions stem from experimental observations and literature recommendations. The system has several components including the geometry, the equipment, the fluid system, the rock and the dissolution structure made of the cavity and wormholes. The assumptions are made as follows:

3.4.1 Geometry

The study of turbulent jet impingement flows requires a full 3D domain to completely account for the eddies generated. For that reason, the turbulent jet flow is studied in all three cylindrical polar coordinates. The impingement process may be considered axisymmetric, given the expected regular gaussian curve for the velocity and pressure distribution, as described in Chapter II. These results are independent of the tangential (θ) component, as the jet dissipates in the axial direction and spreads axisymmetrically in the radial direction where the stagnation and wall jets occur. For that reason, the dissolution will only be studied and estimated in the radial (r) and axial (z) directions, as indicated in Figure 18, then the results will be revolved along the jet centerline to get the entire 3D dissolution geometry. This approach will considerably

save computational effort as it will reduce the geometry for the analysis from 3D to 2D polar coordinates.

3.4.2 Equipment

The simulation uses the same nozzle inner diameter and initial standoff distance at four times the nozzle inner diameter. The experimental apparatus was constrained by the core holder which could only accommodate cores with a diameter of 4 inches, as indicated in Figure 3.1, and a maximum length of 16 inches. Those restrictions were not imposed on the simulated cases, the core diameter was allowed to vary from a minimum value of 4 inches. The core length was also unconstrained, given the fact that the simulations only considered the free fluid (excluding fluid in the pores) domain within the acid jetting equipment.

In this computation, the kinetics of the chemical reaction are considered, with a major assumption that the overall fluid concentration is not considerably altered during the reaction. The assumption is based on the consideration of the continuous high jetting velocity, correlating with fast mixing and fluid entrainment. This assumption becomes obsolete once the velocity drops considerably, as the standoff distance (approximately inversely proportional to the velocity) increases during the dissolution process.

The jetting fluid is a 15wt% HCl solution at 25^{o}C. It is assumed that the continuous flow and uniform mixing with the turbulent eddies lead to a constant acid concentration at 15wt% HCl in most parts of the computational domain, namely in the headspace above the core and in the cavity.

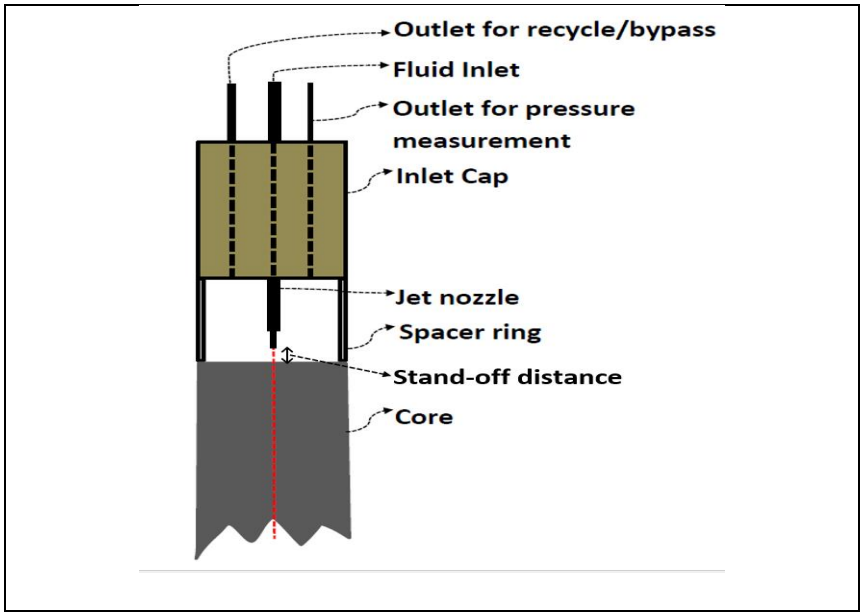

Figure 3.1: Description of parameters in the core holder upper section

3.4.3 Fluid System

On the other hand, the constrained flow through the wormholes makes that assumption counterintuitive, for that reason the change in concentration in the flow through the wormholes will be considered differently and modeled.

3.4.4 Porous Media

The rock is considered to be 100% calcite. A simplistic assumption is made to consider the porous media as a continuum with imbedded porosity of 15% and permeability of 5 mD. This assumption makes the rock fully homogeneous. In reality the rock is heterogeneous, which has been shown to be a basis for the propagation of a dominant wormhole. Nevertheless, for this preliminary study, it will be assumed that

despite the rock homogeneity, a single dominant wormhole would propagate as a result of acid flux through the core.

3.4.5 Chemical Reaction

The chemical reaction presented in Equation 1.1 is considered. Reaction kinetics data from literature are considered for a hydrochloric acid solution with a maximum concentration of 15 wt.% at room temperature, and at pressures above 1000 psi. The last condition would ensure that the produced CO_2 remains in solution and leaves the dissolution process unaltered. The reaction is considered of first order kinetics, irreversible and mass-transfer limited (Lund et al., 1975). The dissolution process is considered to happen via three different mechanisms: 1- The acid transport to the rock matrix, 2- The chemical reaction, 3- The transport of reaction products away from the surface. (Golfier et al., 2000). In the case of HCl reacting with calcite the chemical reaction is considered faster than the other two mechanisms.

The extent of the reaction is defined here as the percentage of acid volume reacted to dissolve a specific volume of calcite per time is a transient function of the fluid pressure at the onset of the reaction as shown in Figure 3.2. It shows that the reaction completion is dependent on the fluid pressure. Lower pressures achieve larger reaction extent quicker. Concurrently, at low fluid fluxes, mass-transfer or diffusion dominated features are expected to lead to a reduced or slowed dissolution through the rock, Similarly, at high fluid fluxes the dissolution through the rock is expected to be

enhanced. These observations indicate the strong influence of the fluid velocity and pressure on the dissolution process.

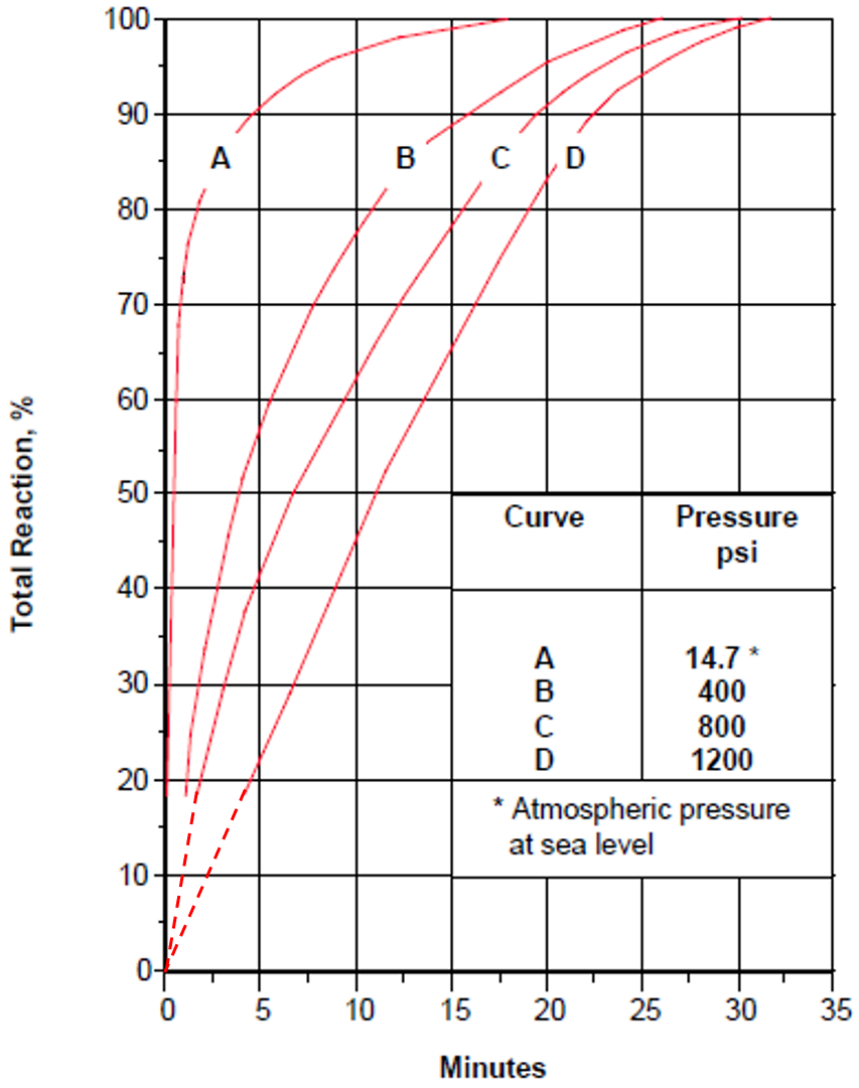

Figure 3.2: Relative Reaction Rates of 15% HCl with Limestone Formations at 75 degrees Fahrenheit; adapted from Tata (2016), the dashed lines result from the linear interpolation between the times at 0% total reaction and 18%.

3.4.6 Dissolution Structure

From Belostrino (2016) observations, we can assume that both the cavity and the wormhole propagate simultaneously, which would thus require a simultaneous computation of growth from the two types of dissolution structures.

Cavity: From experimental observations, the cavity grows to be bulb-shaped. Conditions of axisymmetry described in the geometry assumptions allow to build the cavity from a 360^{-}degrees revolve feature imposed on a 2D drawing of a planar projection of half a cavity.

Wormhole: Following Holland (2014), Ndonhong (2014) and Beckham (2015) observations, no wormhole forms at conditions of no acid fluid flux, equivalent to an interstitial velocity of zero. When the interstitial velocity is non-zero, it is assumed that a single wormhole propagates from the cavity from the location of largest axial velocity, which is along the jet centerline. The cylindrically shaped wormhole propagates in the axial direction, away from the injection point, with a minimum diameter set by the convergence limits of the computations.

3.5 MODEL FLOWCHART

Figure 3.3 presents a drawing of the model flowchart. The initial step is the design of the initial geometry, presented here using ANSYS 15 embedded Design Modeler. Initially the impingement surface (rock surface) is flat, therefore the

computational domain appears to be a 4 inches diameter and 2.25 inches tall cylinder with a 2.14 inches long nozzle at its center. After setting the initial geometry, the turbulent jet impingement model is implemented using ANSYS Fluent 15 for a predetermined time interval, initially 10 seconds. Details about the setup are provided in Section 3.6. The output from the turbulent jet impingement model, namely the velocity and pressure distribution at the acid/rock interface, is sent as an input to the chemical dissolution model, which is described in details in section 3.7. The model will turn the velocity (vector) distribution on that interface into an equivalent dissolution structure shape and volume. The output from this stage will lead to a new geometry for the acid/rock interface which will in turn modify the computational domain which would become the new input for the turbulent jet impingement model. After each round of simulation, the change in dissolution structure volume will be recorded and compared against a threshold value which will indicate when the dissolution has considerably slowed down, and trigger an increase in the time step size in increments of 10 seconds up to a maximum of 100 seconds to capture longer simulation times while saving computational cost and time. The length of a time increments will determine the percentage of the total reaction achieved based on Figure 3.2 data. When no significant dissolution (compared against the threshold value) occurs over the 100 seconds interval, then the dissolution is considered to have stopped and the simulation will end. The simulations could be stopped at earlier times to study the dissolution structure at specific times, as it is the case for the model validation data points presented in Chapter IV.

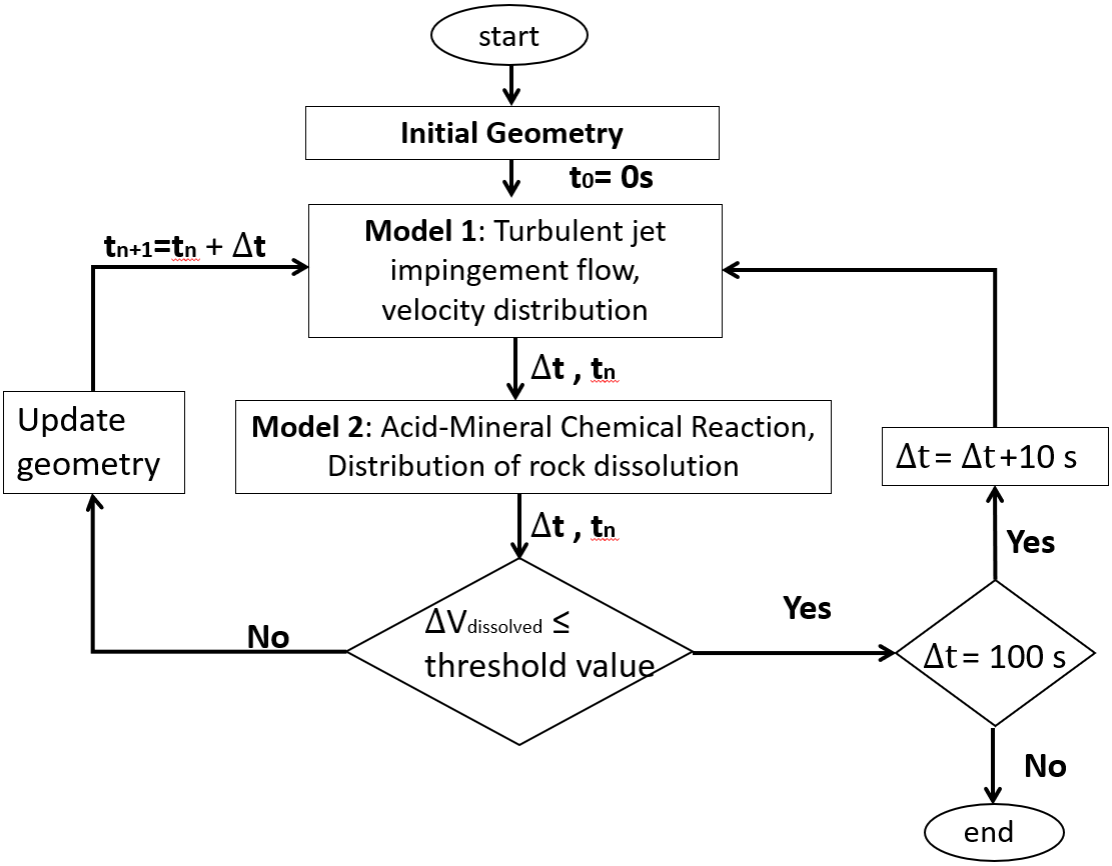

Figure 3.3: Model Flowchart

3.6 TURBULENT JET IMPINGING MODEL

3.6.1 Computational Space

The experimental apparatus, described by Holland (2014), Ndonhong (2014, 2017) and Belostrino (2016), is considered for the computational simulations. The results from that previous study are considered here for model validation purposes in Chapter IV. The computational domain is the fluid volume between the inlet cap and the top surface of the core, as presented in Figure 23.

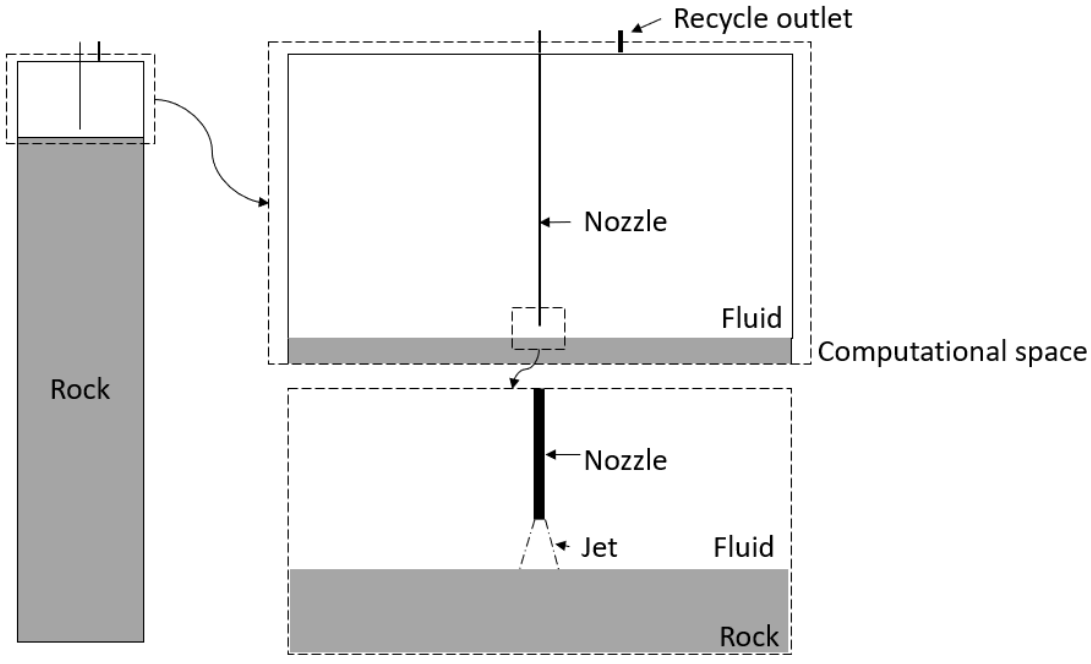

Figure 3.4: Close-up front view of the computational space from the experimental setup within the core holder

The nozzle initial standoff distance is set as four times the nozzle inner diameter. The distance from the inlet cap to the top core surface is 2.25 inches. The injection is considered to occur in the axial (z) direction. The interface between the fluid space and the porous medium will be modified transiently during the acid injection as a result of the chemical reaction in Equation 1.1. For every time step, the initial geometry is designed using ANSYS Design Modeler, with a careful designation of all the boundaries. Details about the entire ANSYS procedure for one round of simulation is provided in Appendix G.

The focus of the analysis is mainly on the free fluid region which implies that the fluid initially within the porous medium is not expressly included in the computation. The porous medium is treated as a continuum with averaged rock and flow properties.

For the linear jetting case, the computational domain geometry is built as follows: Initially a polyline is constructed as indicated in Figure 3.5 with the dimensions and constraints included in Table 3.1, followed by a 360 degrees revolve feature on the direction indicated by the red arrow in figure 3.5, to generate the 3D cylindrical geometry shown in Figure 3.6.

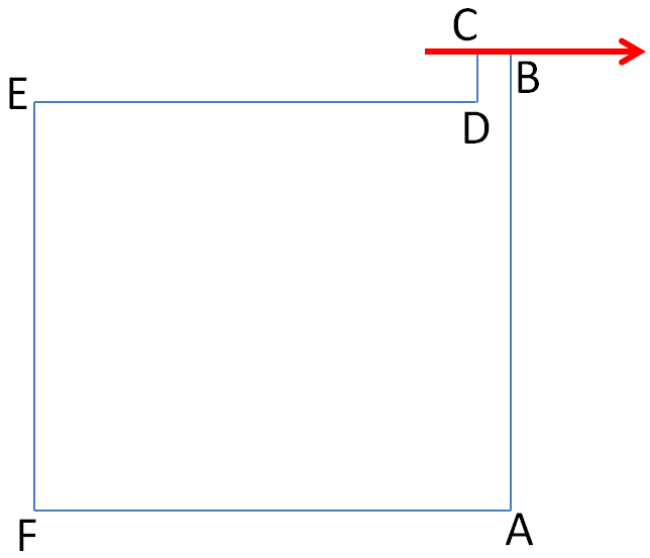

Figure 3.5: Polyline representing a planar projection of the computational domain, with the axis of revolution in red.

Table 3.1:Dimensions and constraints on polyline in Figure 3.5.

Segment	Physical meaning	Dimensions (in)	Constraints
AB	Headspace radius	2	∥ : CD, EF ⊥:BC, DE, FA
BC	standoff	0.09	Coincident with axis of revolution
CD	Nozzle radius	0.01125	
DE	Nozzle length	2.16	
EF			
FA	Headspace height	2.25	

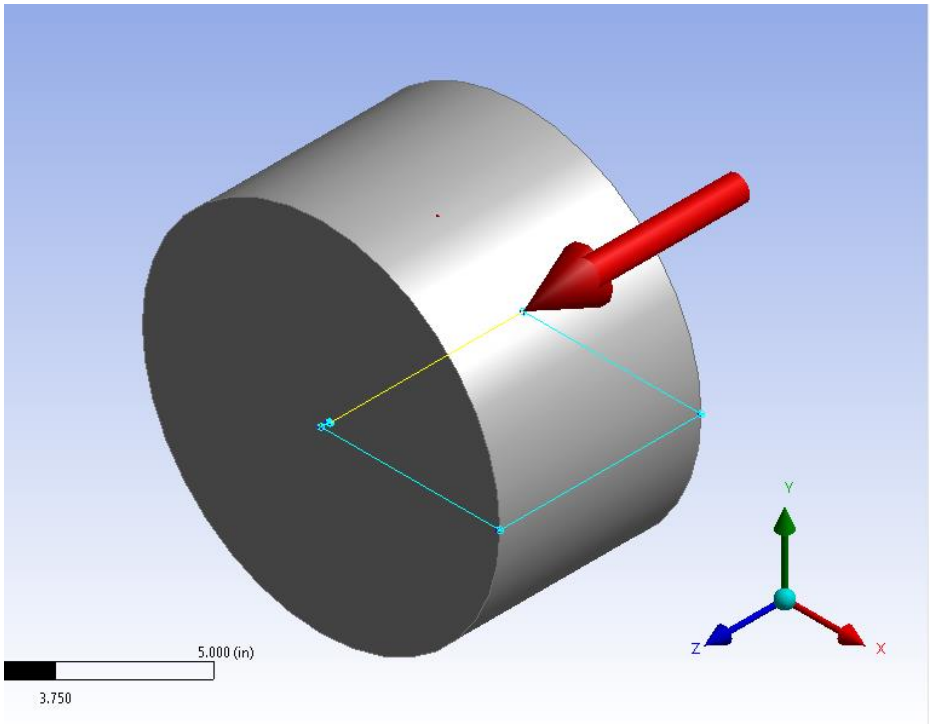

Figure 3.6: 3D representation of the initial computational domain

As chemical dissolution data is being generated, the standoff disance, represented by segment BC becomes longer and a spline A'B is added as indicated in Figure 3.7. The standoff is now the length of A'C. The spline follows the values generated from the dissolution simulation. The evolution of the section AB can be observed and it corresponds to the dissolution happening at the acid rock interface, for one acid jetting simulation. The "360 degrees Revolve" feature is used to generate the assumed 3D geometry used for the new simulation. It is important to note that, at the intersection of the segment and the spline, the angle should be smoothed as much as possible to avoid divergence in the calculations.

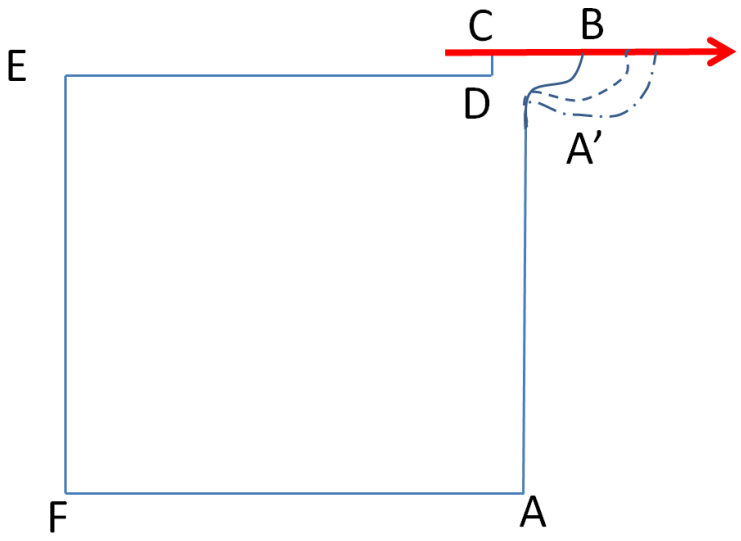

Figure 3.7: How the dissolution phenomena changes the planar projection of the computational domain

In the case of linear experimental acid jetting, the computational domain could be reduced to a 2D system, assuming axisymmetry tangentially and across the vertical midsection, as indicated in Figure 3.5 and 3.7. In that case, the dissolution will only computed from x=0 inches to x=2 inches on the velocity distribution data. In this case, considering tangential symmetry, only the axial and radial velocities will be considered. The total pressure distribution is also considered to account for potential mechanical changes in the system.

3.6.2 Meshing

Figure 3.8 displays a trimetric 3D view of the computational space as well as the resulting mesh after meshing the computational space before an acid jetting simulation. The mesh is refined near the nozzle and the impingement plate.

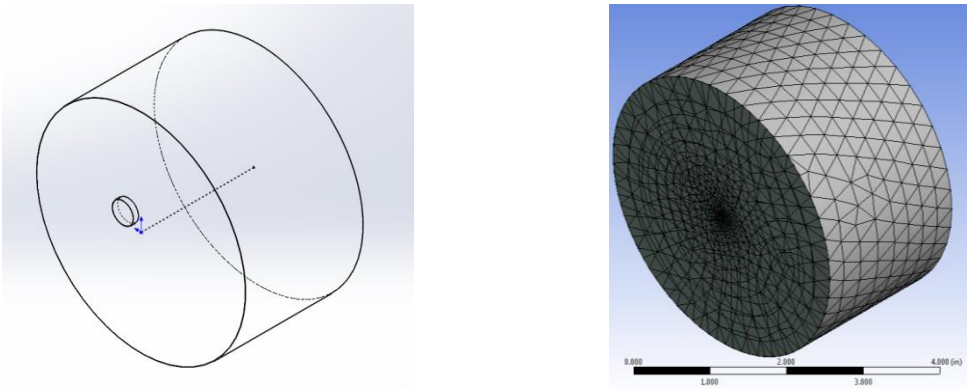

Figure 3.8: Initial computational space: trimetric view (left) and mesh (right)

3.6.3 Boundary Conditions

The fluid volume is surrounded by the headspace walls, the nozzle walls, the jet inlet boundary (nozzle tip), the fluid recycling outlet and the interface between the fluid and the porous volumes, in this case considered as the fluid outlet boundary.

a) Inlet

The inlet is represented by the nozzle tip area. There are four types of inlet boundary conditions available in the ANSYS Fluent 15 package, as indicated in Figure 3.9.

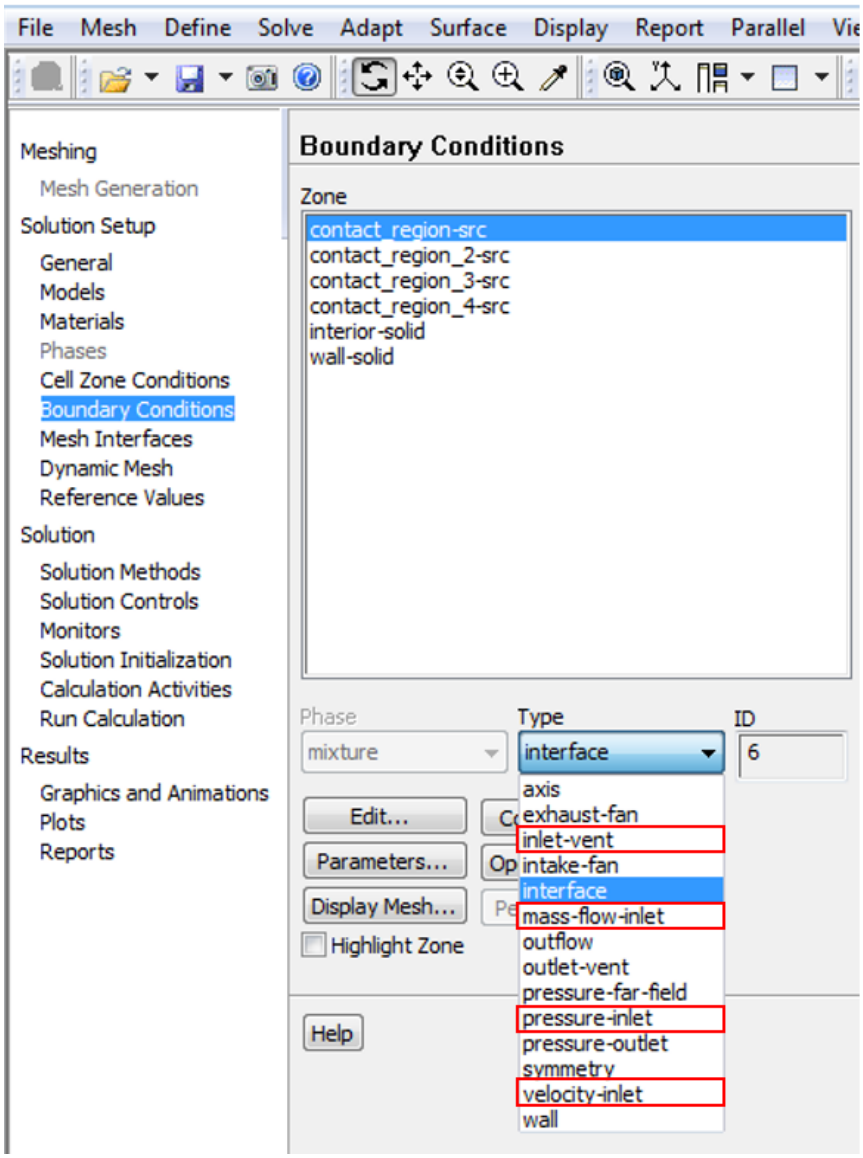

Figure 3.9: ANSYS Fluent platform highlighting the four inlet boundary types in the red rectangles

In our case, acid jetting at room temperature, the fluid is incompressible, the flow is continuous and the inlet velocity (magnitude and direction) is known. The inlet pressure can be estimated from the experimental design considerations. Therefore the

"velocity-inlet" type is the most appropriate choice. The inlet velocity magnitude is the specified jet velocity and the flow direction is normal to the inlet surface. The inlet pressure is defined as the pressure assigned by the upstream back-pressure regulator during experimental acid jetting. The downstream back pressure regulator is always set at 1000 psi to maintain the produced CO2 (from Equation 1.1) in solution. The upstream back pressure regulator is set at a pressure equal to 1000 psi plus an additional pressure differential equivalent to the desired flux or the desired interstitial velocity across a specific core. In ANSYS Fluent, the pressure is entered in Pascals and the velocity is entered in m/s, as shown in Figure 3.10.

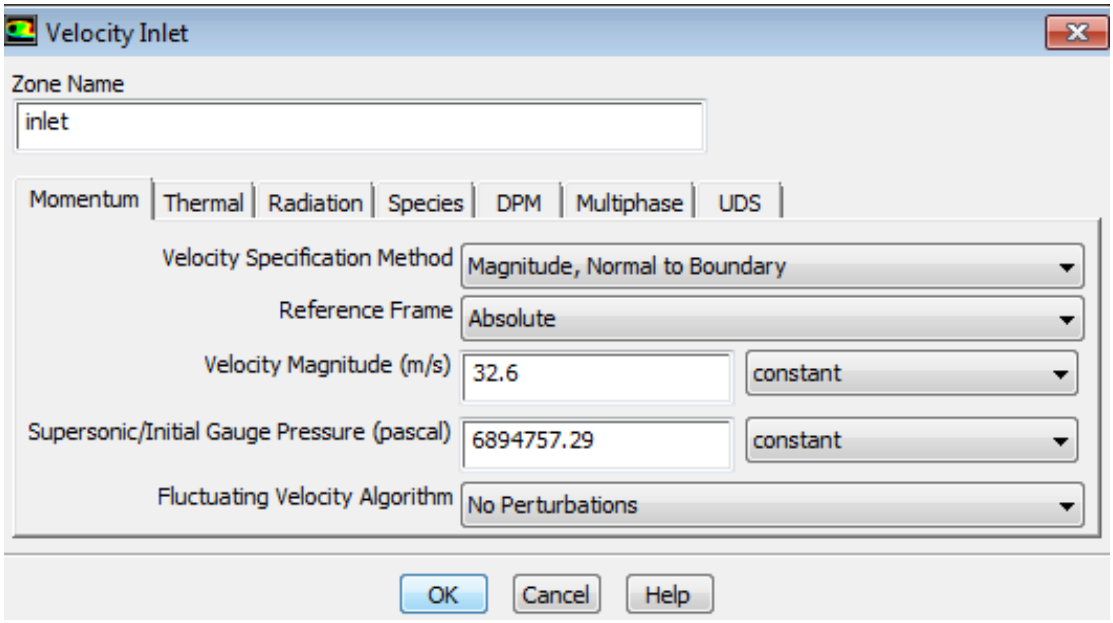

Figure 3.10: ANSYS Fluent 15 velocity-inlet panel

b) Outlet

The outlet is represented by the fluid/rock interface, where the impingement would happen. There are three types of outlet boundary conditions available in the ANSYS Fluent 15 package, as indicated in Figure 3.11.

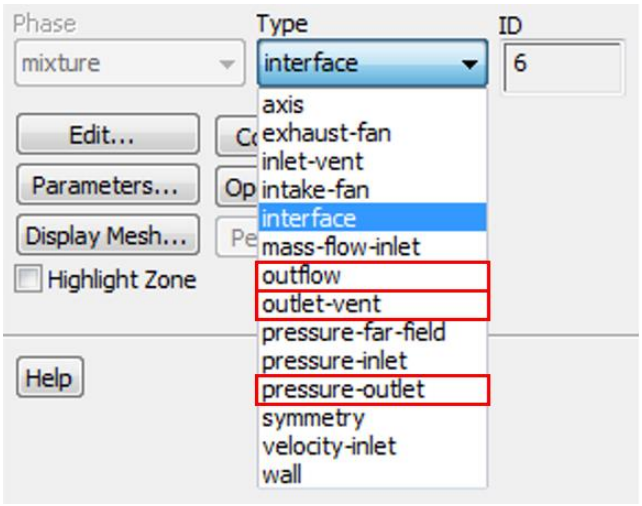

Figure 3.11: ANSYS Fluent 15 panel highlighting the three outlet boundary types in the red rectangles

The outlet surface is the interface between the fluid and the porous media. From De Lemos (2005, 2012) observations, when the jet reaches the porous wall, the impingement would occur to some extent, as a fraction of the fluid would flow axially through the porous media while the remaining fluid volume would proceed with the impingement and subsequent recirculation and entrainment in the eddies. No pressure or velocity information is available for that boundary. The fraction of fluid allowed to pass

through the interface can be approximated from the assigned flux through the porous media. With all these considerations it appears that the most appropriate boundary condition is the "Outflow" boundary condition. For this boundary type, the only parameter needed is a flow rate weighting scalar between 0 and 1 to represent the fraction of fluid allowed to flow through that boundary (the porous media). Appendix D shows a sample estimation of the flow rate weighting fraction. The outflow panel in ANSYS Fluent 15 is displayed in Figure 3.12.

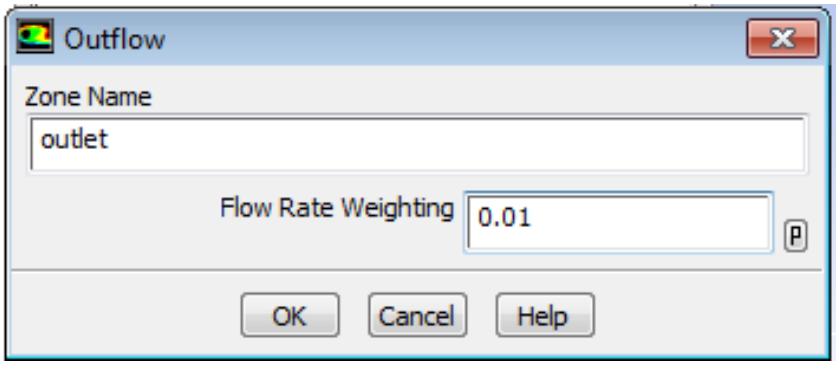

Figure 3.12: ANSYS Fluent 15 Outflow panel

c) Recycle outlet

The recycle outlet surface replicates the recycle line in the experimental design. The surface would operate as a vent to prevent extreme pressure build up due to the accumulation of fluid in the core holder's headspace. It is important to note that the preliminary mass balance on the system suggested that less than 10% of the injected

fluid is propagating through a core with 10mD permeability and 15% porosity when high flux values are considered (v_i~4cm/min). The outlet vent boundary type best fits this boundary, it is presented in Figure 3.13. The gauge pressure is set to 0 to assume atmospheric pressure at that outlet.

d) Walls

There are two walls in the geometry, the circumferential wall around the computational domain and the nozzle inner wall. They are both no-slip and stationary walls. The designation of the nozzle walls as such appeared to improve the model convergence compared to when it was not explicitly defined but instead assumed by the model.

e) Solid interior

The computational domain interior is set as a fluid region, initially filled with water, as indicated in Figure 3.14. The entire analysis is performed on the fluid region and the only solid regions are the walls, which in reality represent interfaces between the fluid and the experimental equipment interior. Table 3.2 summarizes the general conditions imposed on the boundaries. More details about the setup in ANSYS Fluent are provided in Appendix B and F.

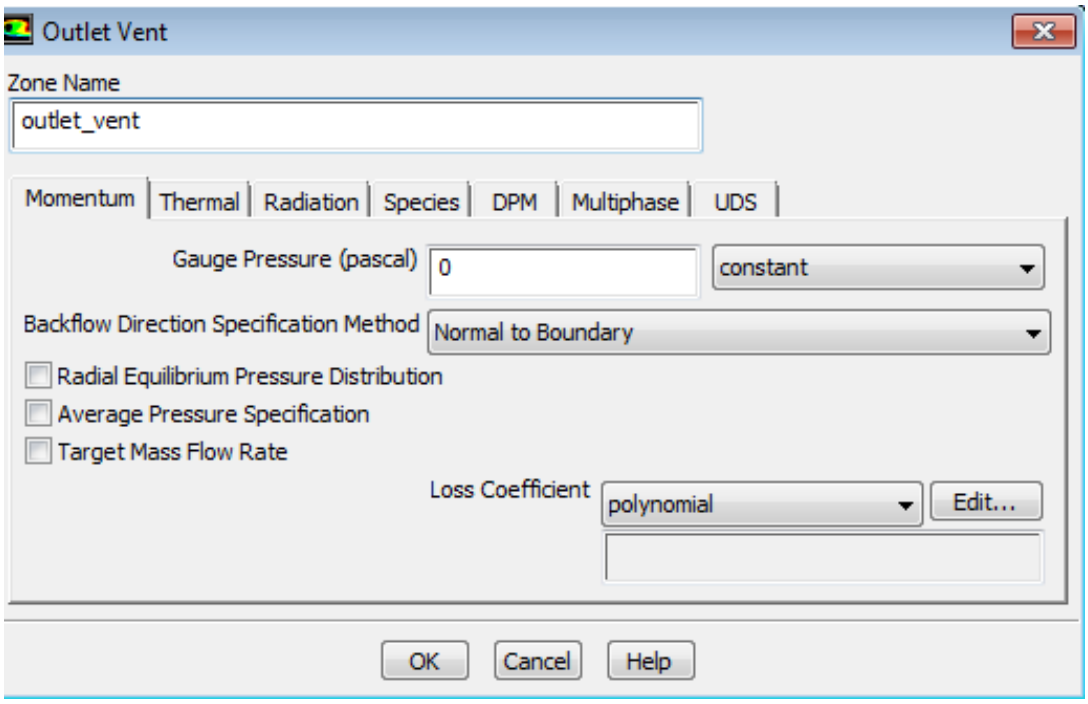

Figure 3.13: ANSYS Fluent 15 Outlet Vent panel

Table 3.2: General boundary conditions for model implemented in ANSYS Fluent 15

Surface	Condition
Interior	Fluid
Inlet (Nozzle Tip)	Velocity inlet, requires velocity magnitude, and initial gauge pressure, velocity normal to boundary
Inlet Walls	Stationary wall with no slip
Nozzle Walls	Stationary wall with no slip
Recycle Outlet	Outlet vent
Outlet	Outflow, requires flow rate weighting value.

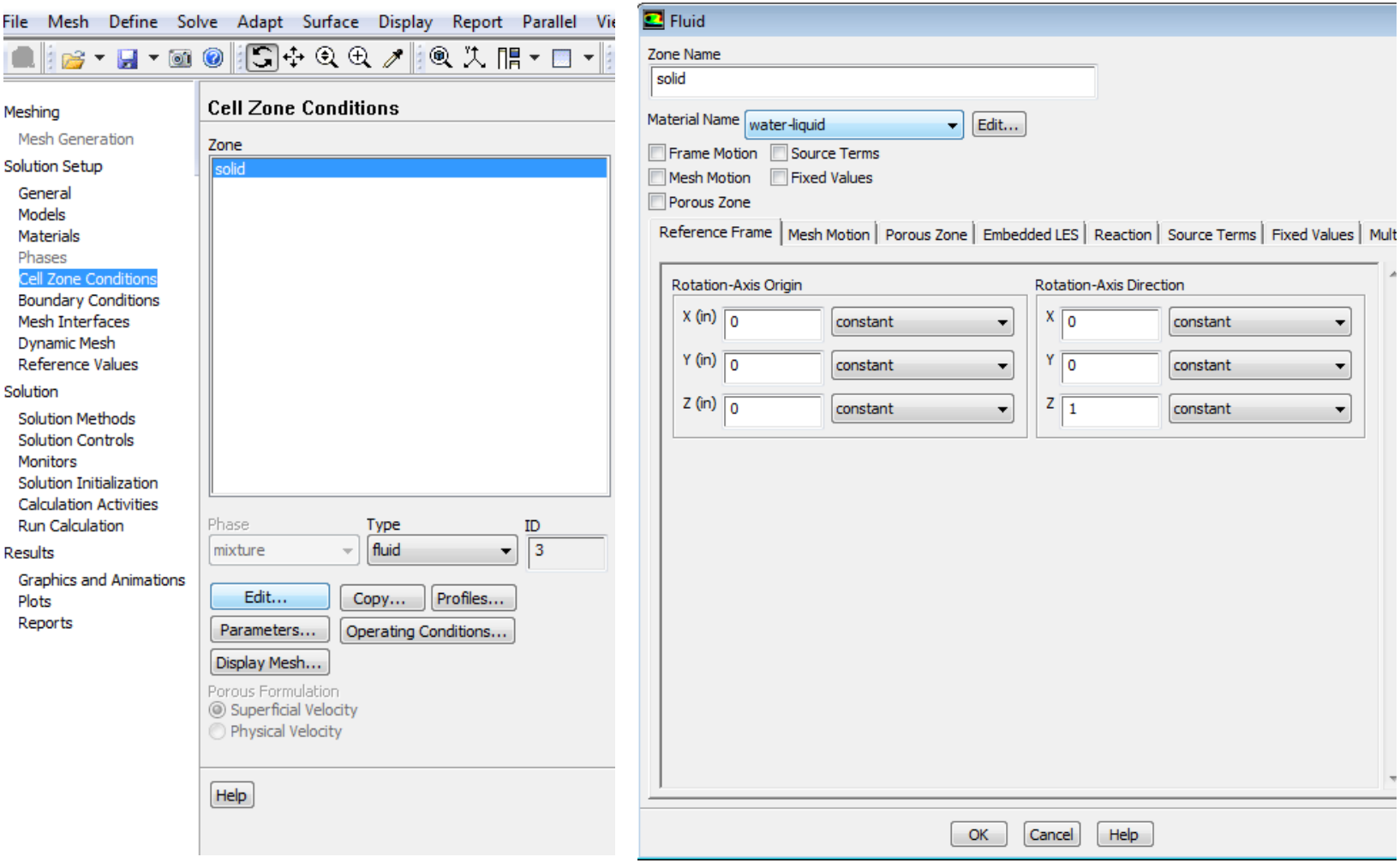

Figure 3.14: Definition of the computational space interior in ANSYS Fluent 15

The fluid inlet and outlet are the boundaries with changing conditions for every simulation. The inlet pressure and jetting velocity are selected for the inlet, meanwhile a flow weighting fraction value is selected for the outlet boundary. The flow weighting fraction is a value that indicates the volume of fluid "allowed" to flow through the boundary. It is thus a value that combines several flow properties of that interface (fluid properties: flux or interstitial velocity and rock properties: porosity and permeability) Appendix D shows a sample estimation of a flow weighting fraction for a specific set of conditions. Table 3.3 presents a summary of the flow rate weighting fractions considered for the simulations presented in this paper for the model validation. For set rock properties, these flow weighting values may correlate with the initial interstitial velocity of the experiment.

Table 3.3: Initial jetting properties considered for simulations, for a 15wt% HCl solution at 25^{o}C jetted on a porous calcite core of 15% porosity and a permeability of 5 mD.

Jetting velocity (ft/sec)	Jetting velocity (m/s)	Re	d*	Flow rate weighting fraction at fluid/rock interface	Interstitial velocity (cm/min)
107	32.61	$1.82 * 10^4$	4	10^{-4}	O (0)
				10^{-3}	O (10^{-1})
				10^{-2}	O (1)
200	60.96	$3.39 * 10^4$	4	10^{-4}	O (0)
				10^{-3}	O (10^{-1})
				10^{-2}	O (1)

At the end of the turbulent flow simulation, the pressure and velocity distribution data are extracted at the fluid/porous media interface. Specifically, the radial and axial components of the velocity are extracted to estimate the dissolution resulting from the wall jet and the impingement, respectively (Beckham et al. 2015, Hanjalic and Launder, 2011). After the dissolution volume is computed for each volume cell at the fluid/rock interface, a new interface/outlet boundary is constructed, by integrating and combining the dissolution volumes in the radial and axial directions (the system is considered axisymmetric). A new computational domain is thus constructed. The old and new computational domain volumes are compared against a change threshold value and if the change is considerable, then a new turbulent jetting flow simulation is run using the new computational domain geometry. The computation stops once the volume change reaches less than one percent of the largest dissolution volume change after the time increments described in the model flowchart section. Therefore, the dissolution growth is considered stopped when the dissolution volume after an iteration with a 100 seconds time increment is less than 1% of the largest dissolution volume achieved in a single iteration throughout the entire simulation.

3.6.4 Turbulence Model

As indicated in the literature review, the choice of a turbulent modle is highly critical for the accuracy of the turbulent jet impingement simulation results. The various avalaible turbulence models included in the ANSYS Fluent 15 package are listed in Figure 3.15. As discussed in Chapter II, the recommended approach is the Large Eddy

simulation (LES) approach with the additional consideration of the dynamic stress, rather than the constatnt dynamic subgrid scale version of the Smagorinsky-Lilly SGS model.

Figure 3.16 indicates how to select the appropriate subgrid scale model. By selecting the Large Eddy Simulation (LES) option in the display shown in Figure 3.15, the display shown in Figure 3.16 appears. then the user will select the Smagorisnky-Lilly Model in the Subgrid-Scale Model section.

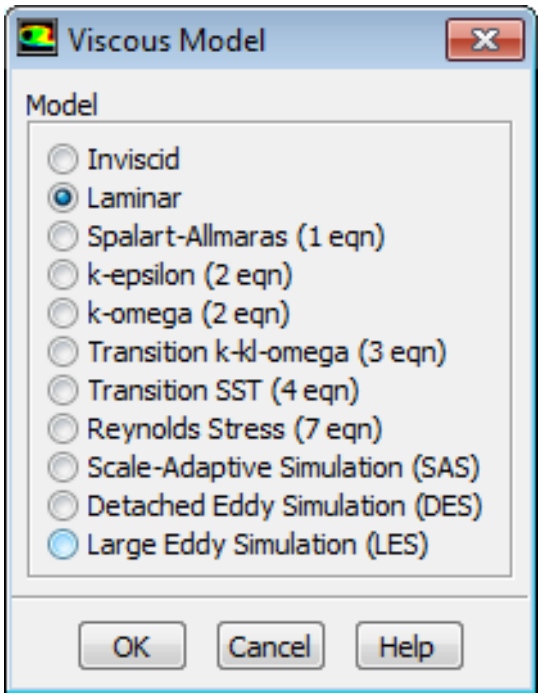

Figure 3.15: Turbulence Models Available Using ANSYS Ffuent 15

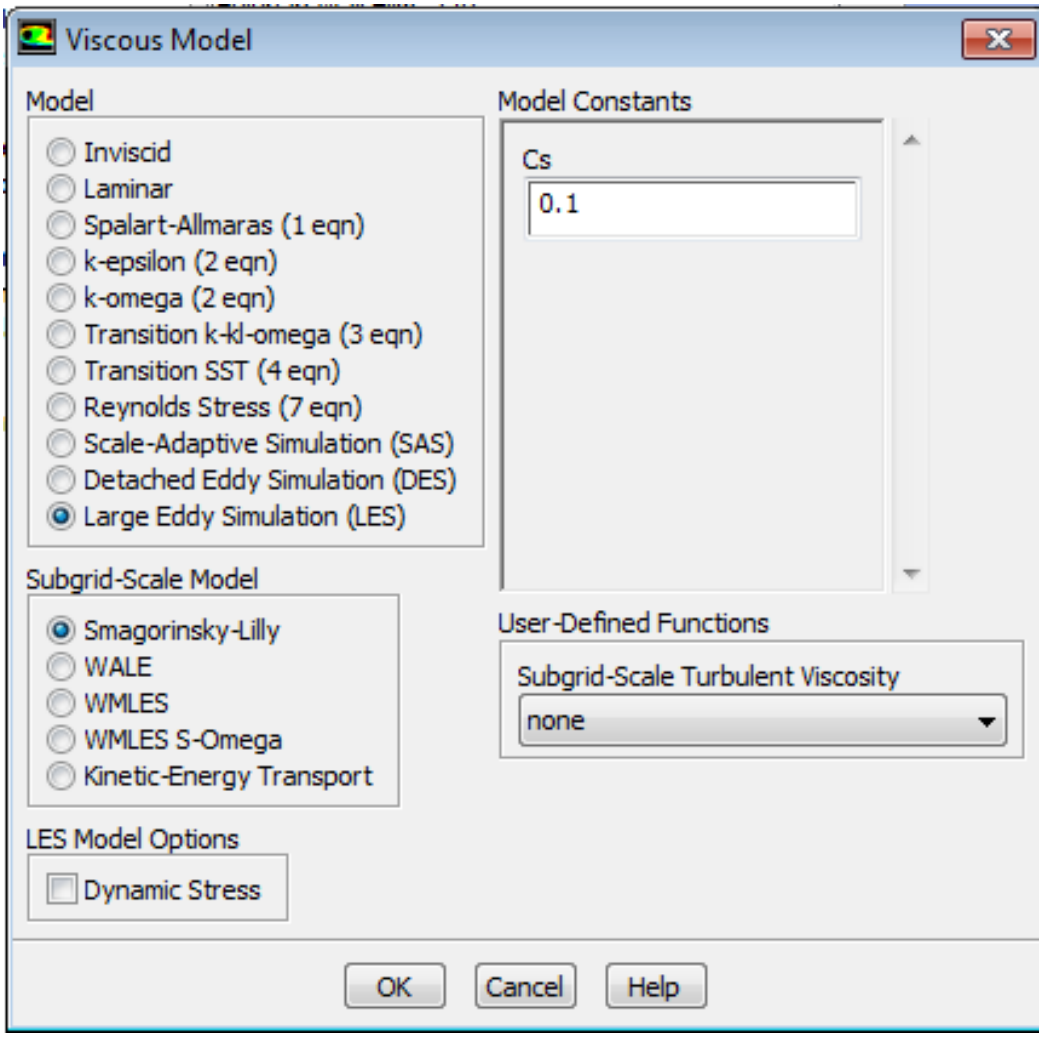

Figure 3.16: Display after selection of the LES with the Conventional Smagorinsky-Lilly model as the SGS model

By checking the Dynamic Stress box in the LES Model options, it will lead to the display shown in Figure 3.17, where it activates the dynamic Smagorinsky-Lilly model and eliminates the fixed C_S constant from the conventional Smagorinsky-Lilly model, as discussed in Chapter II.

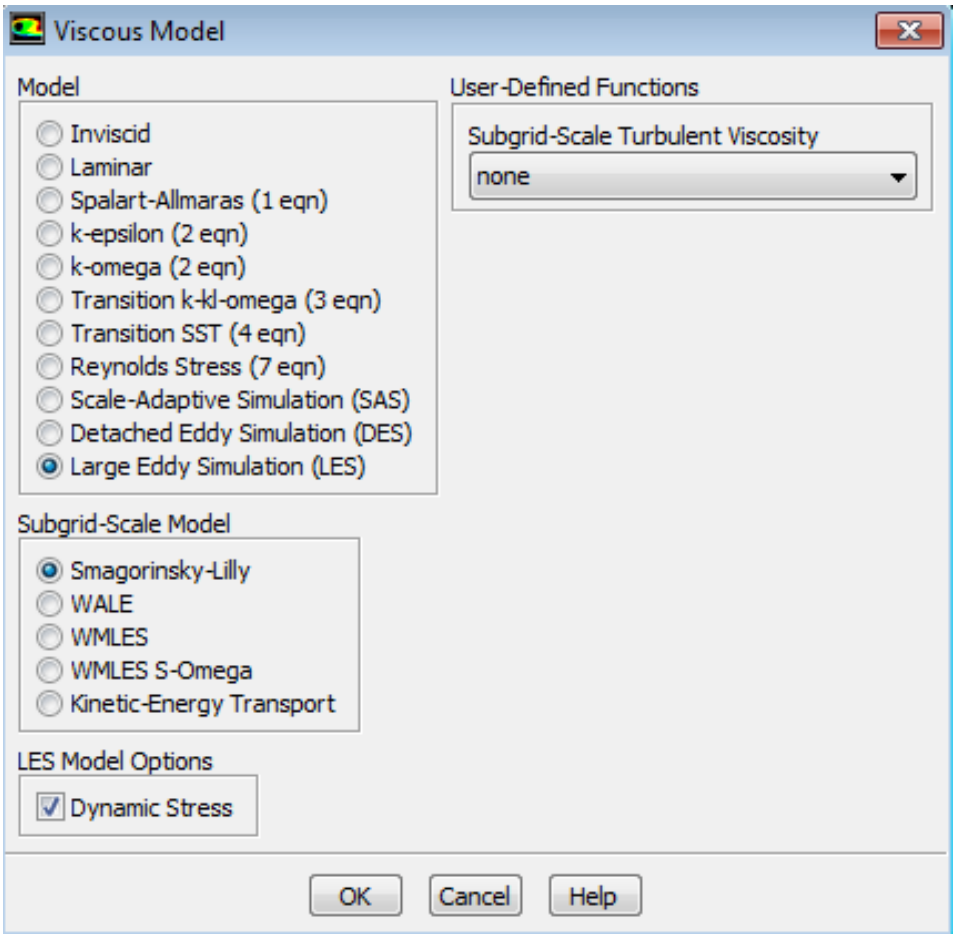

Figure 3.17: Display after selection of the LES model with the Dynamic Smagorinsky-Lilly model as the SGS model.

3.6.5 Numerical Solver

The Navier-Stokes equations are to be solved using a finite volume solver. The use of a LES turbulence model requires the use of the bounded second order implicit transient formulation. The spatial discretization is kept standard as a Least Squares Cell Based for the gradient, with computations of second order for the pressure and Bounded Central Differencing for the momentum. Figure 3.18 displays the ANSYS Fluent 15

interface for the selection of the solver parameters. The implicit transient computation requires a careful determination of the initial condition for convergence. For that reason it is recommended to initially run at least five hundred iterations at the initial time in order to converge to the right initial conditions prior to the actual transient calculations. Figure 3.19 shows the recommended setup for those preliminary calculations.

The time step size is recommended at a maximum value of 0.01 seconds, after observing a strong correlation between convergence and time step size larger 0.01 seconds, due to the implicit nature of the transient formulation. For larger time steps, the continuity and velocity monitors consistently diverged. Once covergence or the maximum number of iterations is achieved at a timestep of zero, the number of time steps is set at 1000. (equivalent to 10 seconds) which corresponds to the minimum time step size for the turbulent jet impingement flow model.

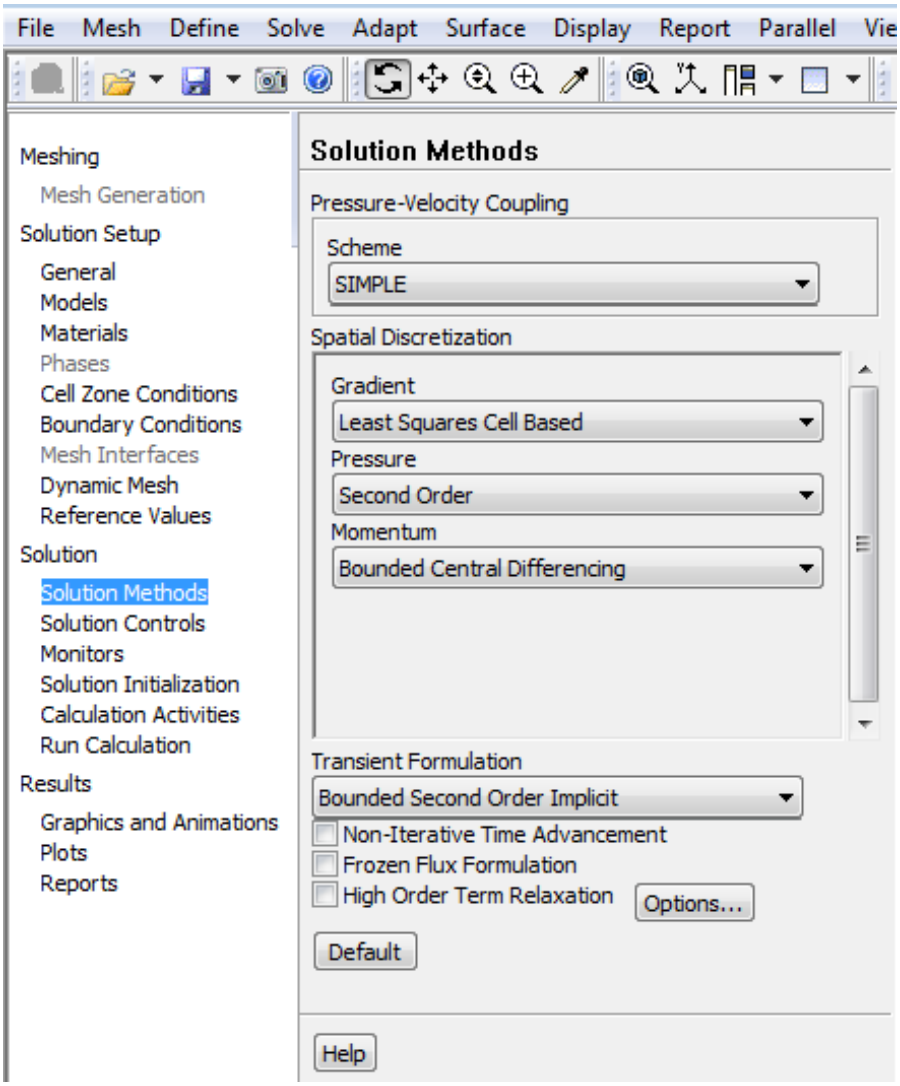

Figure 3.18: Selection of a finite volume solver for turbuent jet impingement flow computations

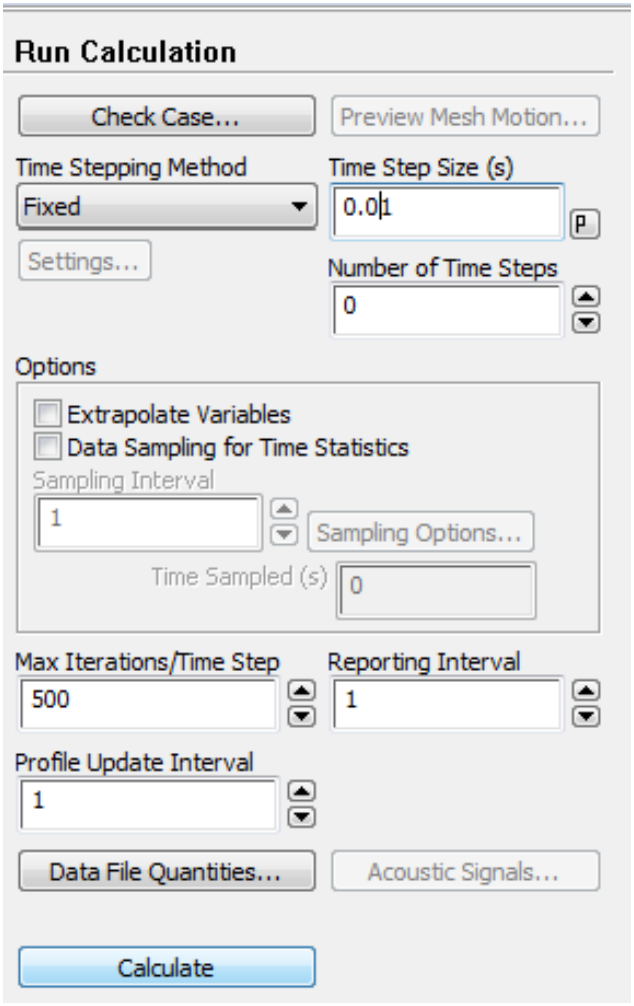

Figure 3.19: Time step size, number of time steps and maximum number of iterations for the computation of the initial conditions.

3.6.6 Numerical Convergence

Convergence is a critical parameter of the simulations would non-convergent calculations would yield misleading estimates. Monitors for residuals stemming from the continuity and the Navier stokes equations are set up as indicated in Figure 3.20 to observe the convergence of the computations as shown in Figure 3.21.

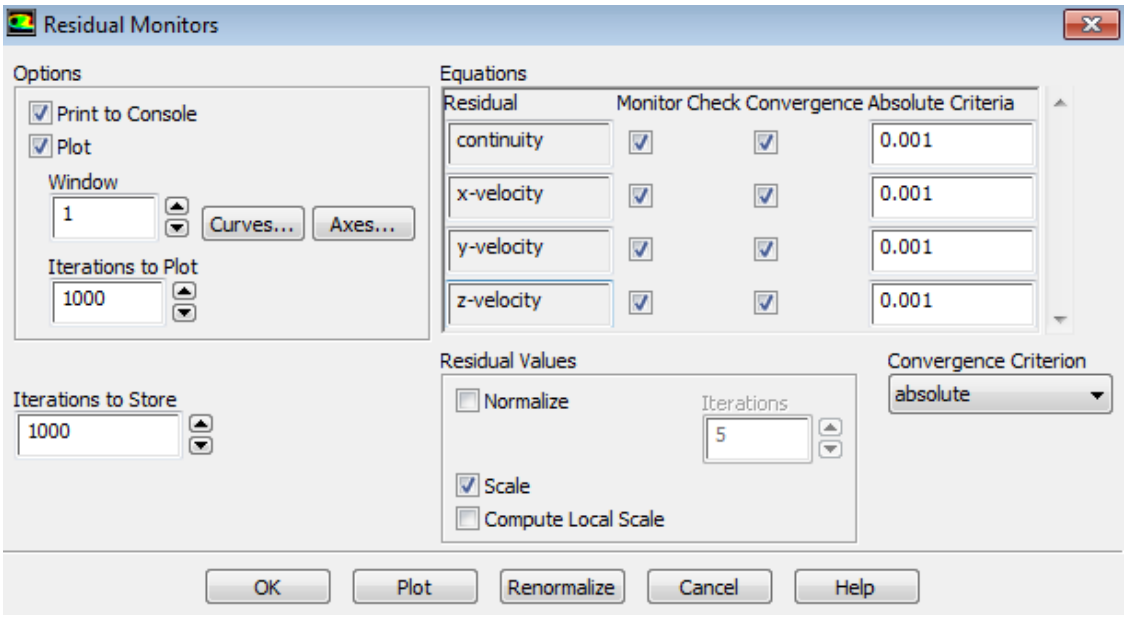

Figure 3.20: Residual monitor setup for computation convergence

As mentioned in Section 3.6.4 the time step size is highly critical to the speed of convergence and to convergence itself. Convergence is reached when all four convergence residuals reach the corresponding absolute criteria.

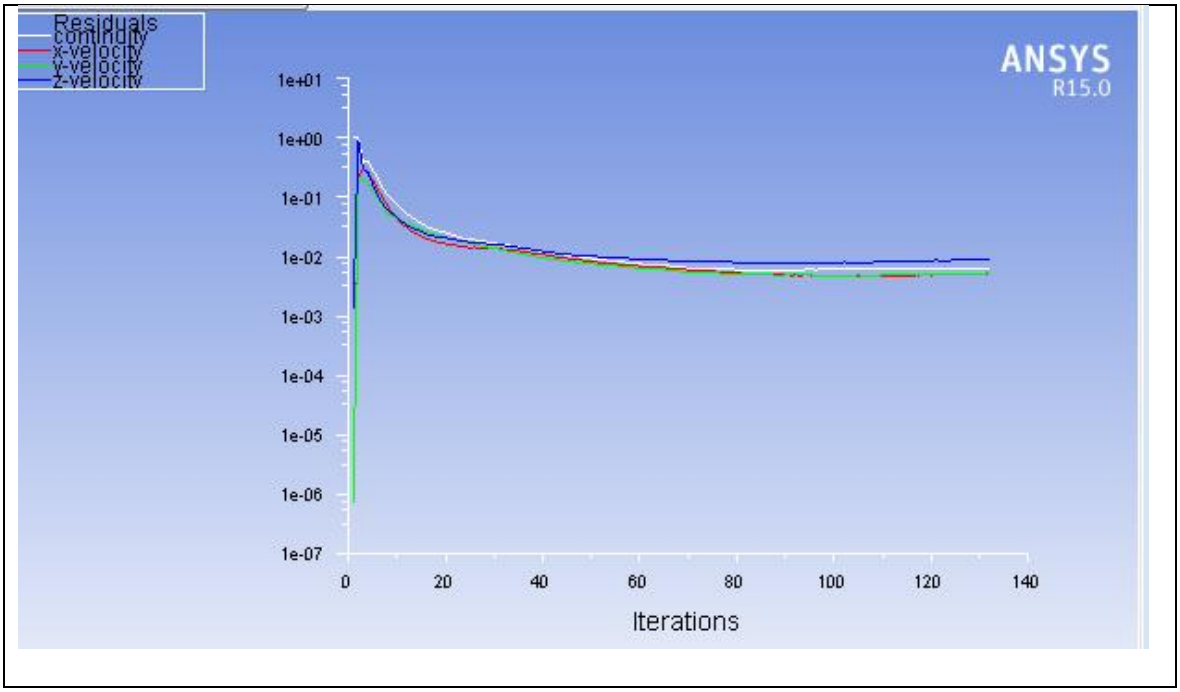

Figure 3.21: Residual monitoring during computations

3.6.7 Results and Processing

Once the desired time step change is achieved, the results can then be processed. ANSYS Fluent provides several avenues to process the results. It is possible to visualize the contours, vectors or pathlines. Figure 3.22 displays the interface where the visualizations types could be selected. The contour graphics provide a variety of options for the physical properties including the pressure and the velocity distribution. These options are highlighted in Figure 3.23. Once a physical property is selected, it can be further defined by a type such as the static and dynamic pressures for the pressure contours or the axial, radial and tangential velocities for the velocity contours. Figure 3.24 and 3.25 highlight the various types of pressure and velocity contours, respectively.

The contours are best observed with filled nodes in a 2D plane. For that reason, a plane has to be set up for the visualization. The most common ones are the mid-planes of the impingment such as the planes xz and yz. The velocity magnitude countour for a plane xz after a round of jetting simulation is shown in Figure 3.26

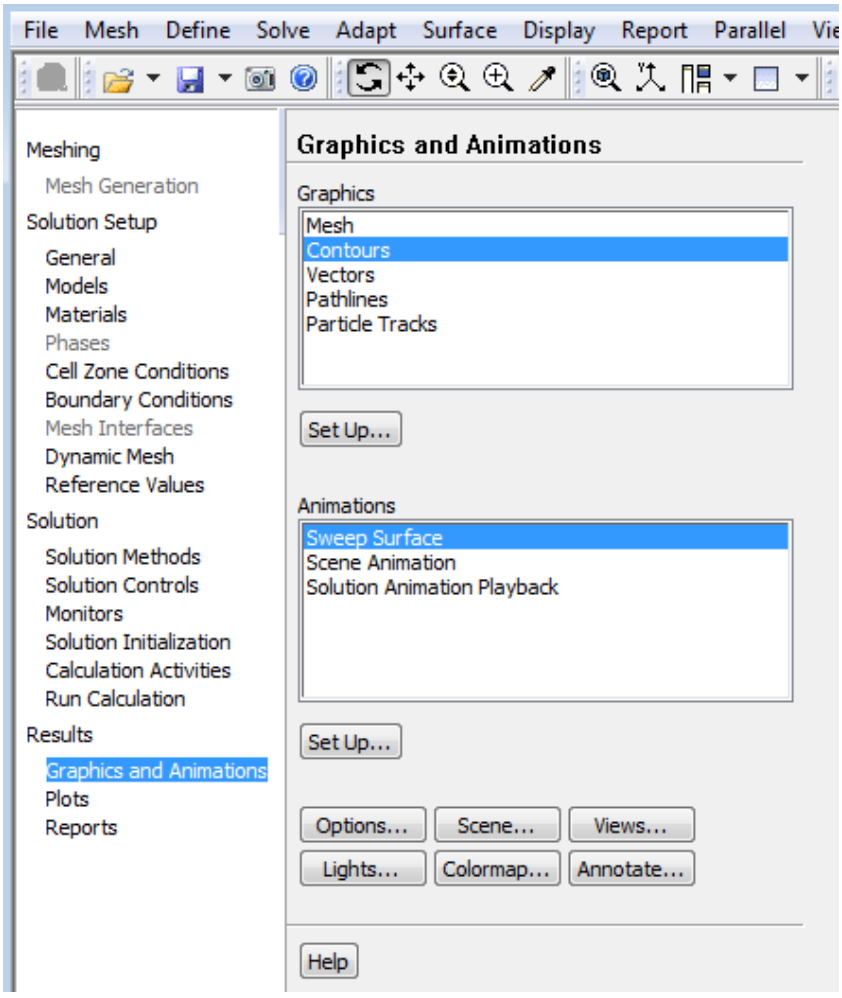

Figure 3.22: Results analysis capabilities in ANSYS Fluent 15

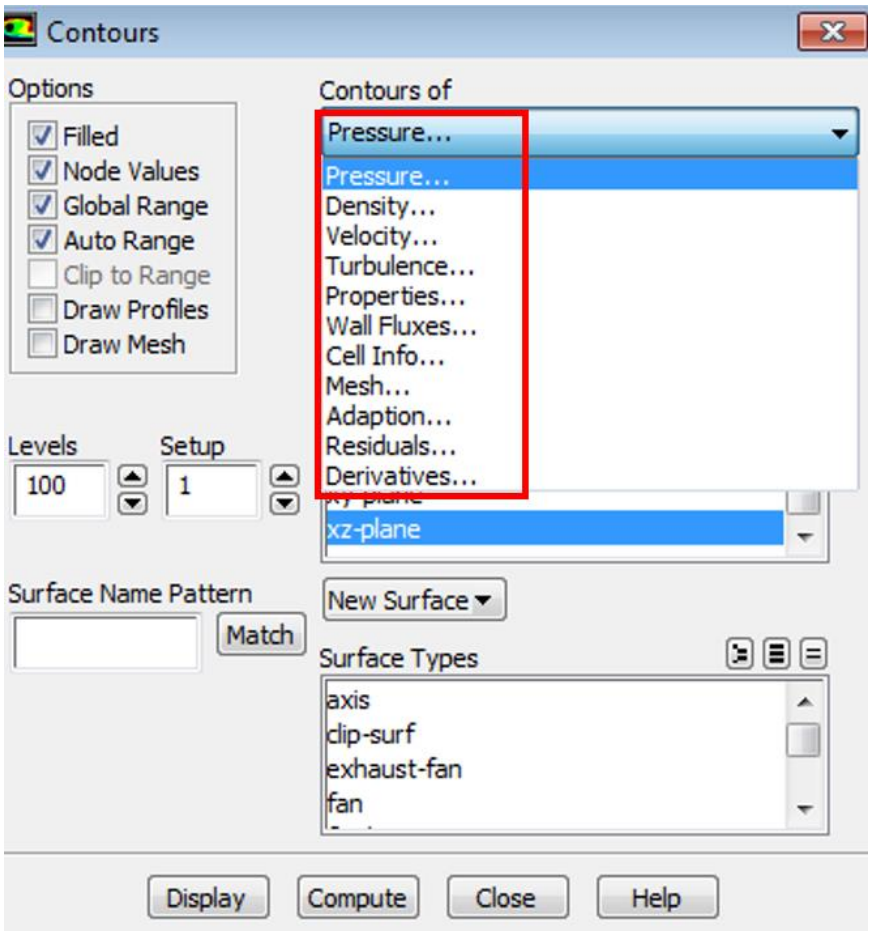

Figure 3.23: Physical properties which can be represented as Contours in ANSYS Fluent 15

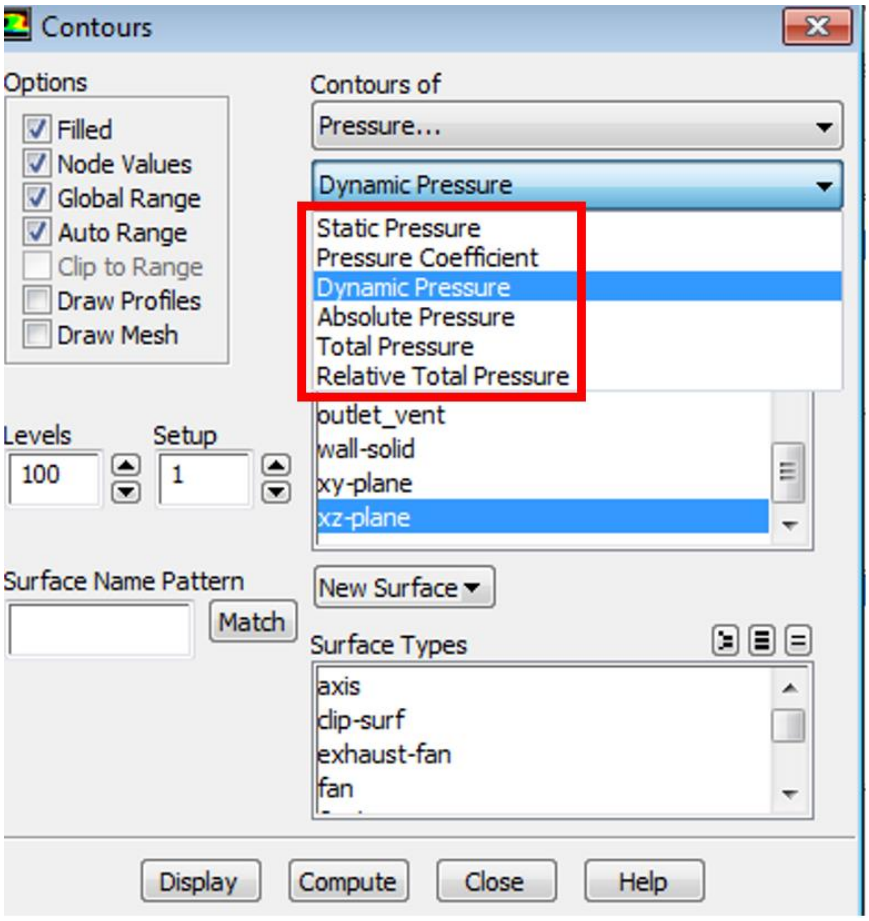

Figure 3.24: Types of Pressure contours in ANSYS Fluent 15

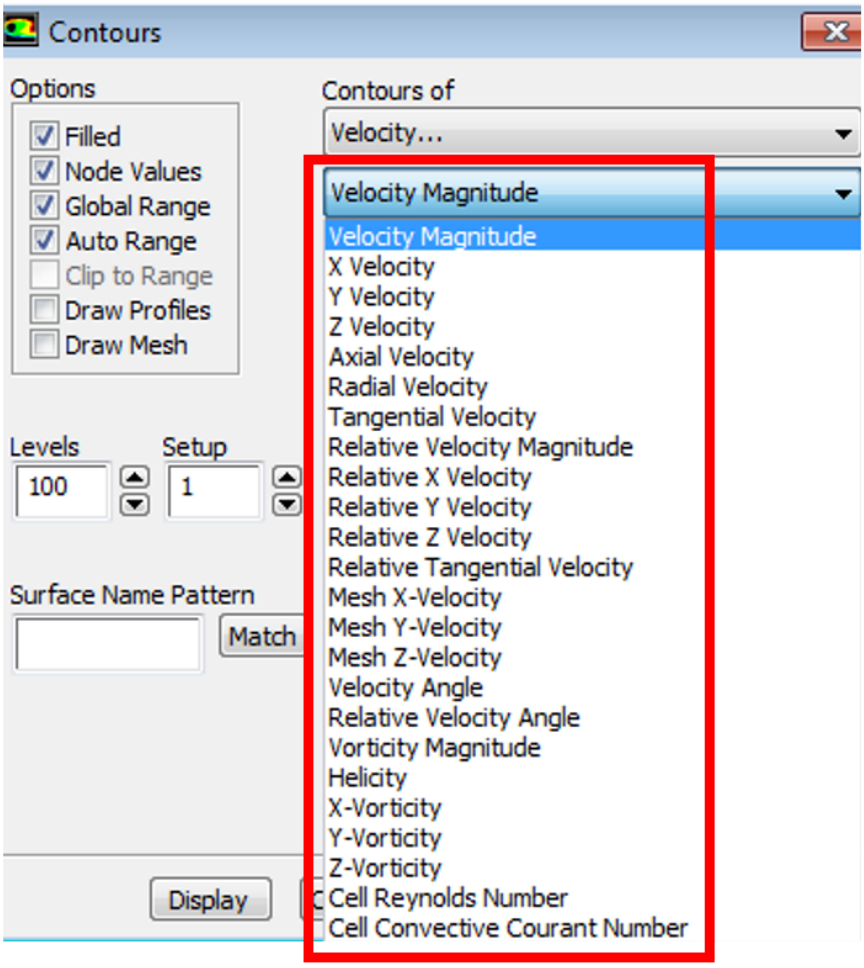

Figure 3.25: Types of Velocity contours in ANSYS Fluent 15

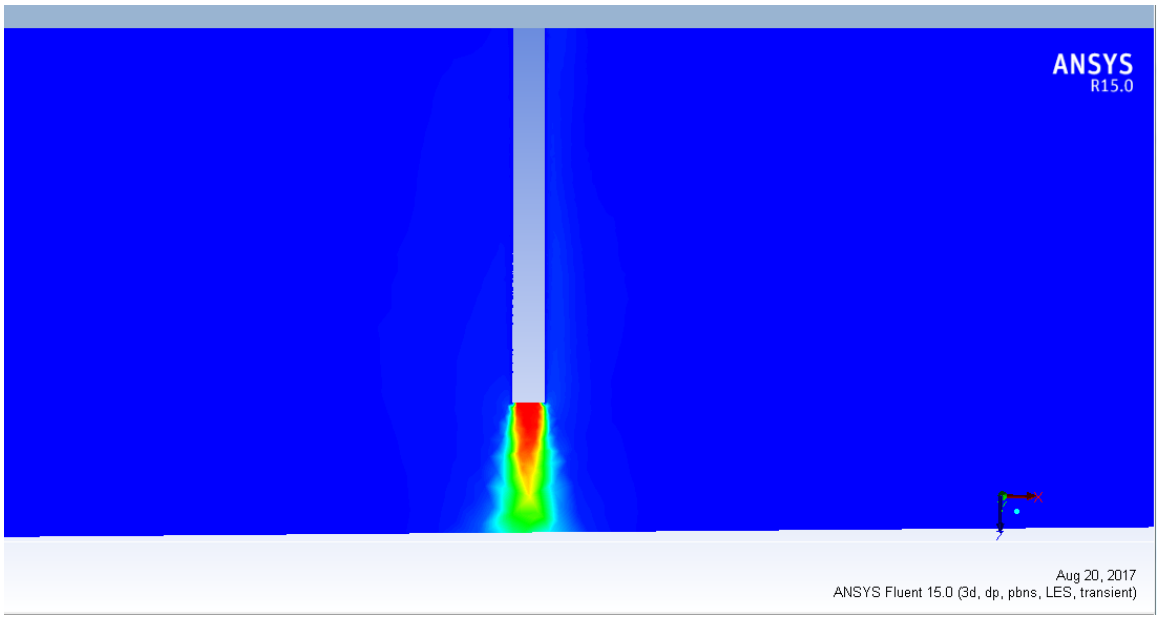

Figure 3.26: Close-up of contour of velocity magnitude after a round of jet impingement flow simulation at 107 ft/sec (32.6 m/s)

Some 2D results plots could also be extracted from the planar projection of the resulting physical properties distributions after a simulation. These plots would help in observing the shape of the distribution, to confirm if it matches with the theory. It will also be beneficial for the case of dissolution, where it would give an early indication of the dissoution structure shape. In our case, given the axisymmetry assumption, a plane yz or xz could be selected for the analysis of velocity distribution then revolved along the z axis to generate the estimated distribution in the entire 3D domain. Figure 3.27 and 3.28 indicate how an XY plot for the average velocity distribution could be produced within and Figure 3.29 shows how the generated data could be exported as a txt file for further processing with tools as simple as an Excel spreadsheet. The anticipated bell-

shape distribution is observed in Figure 3.28b, thus providing further reassurance that the results go along with theory.

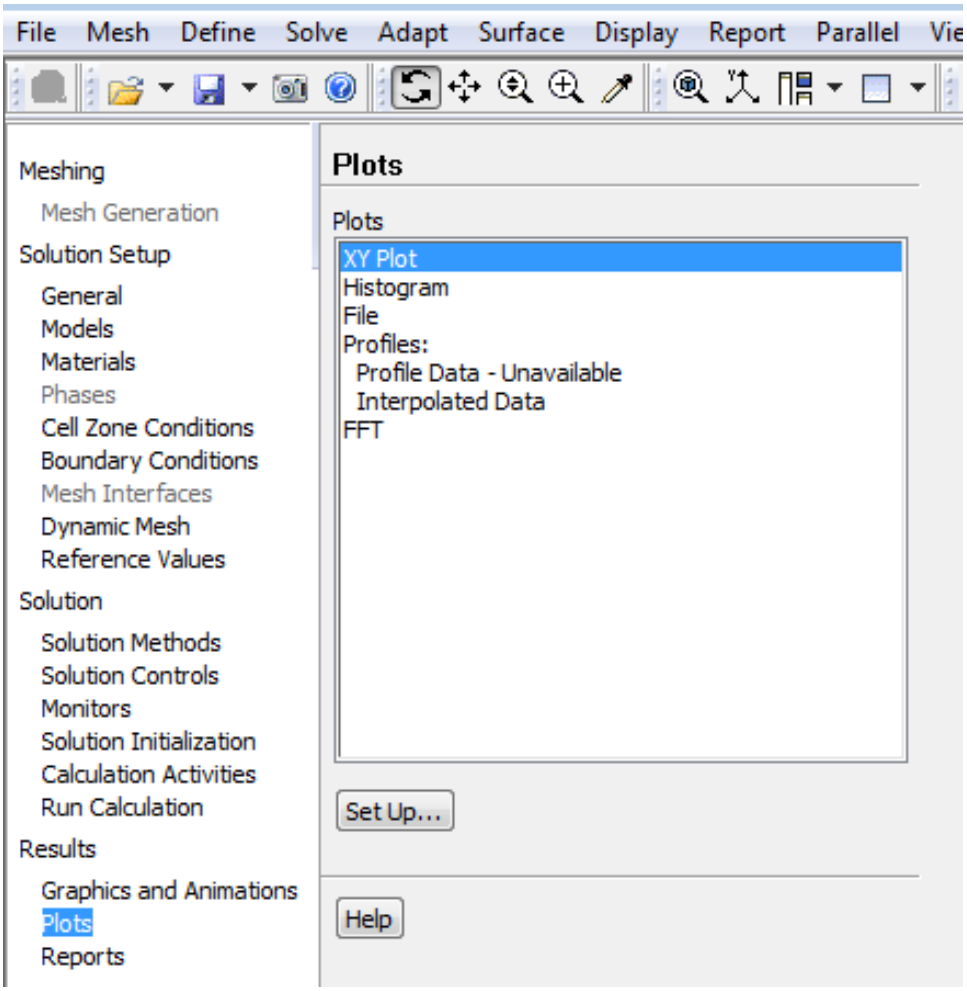

Figure 3.27: Interface for plots of results in ANSYS Fluent 15

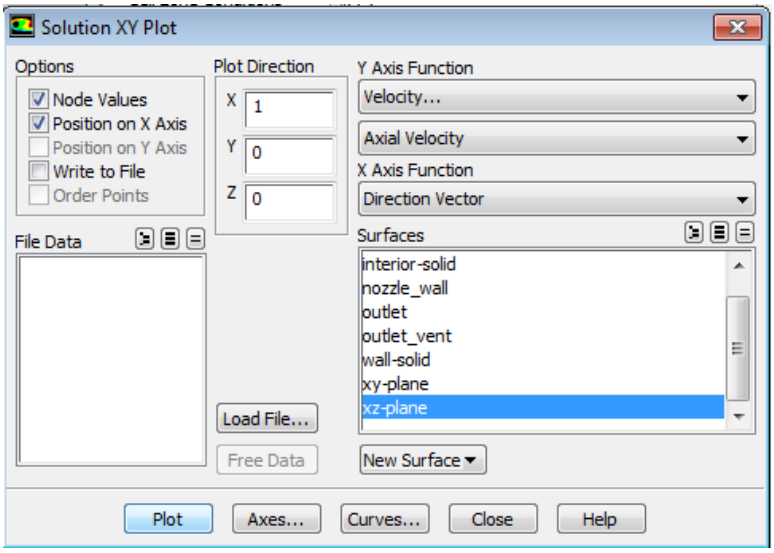

a)

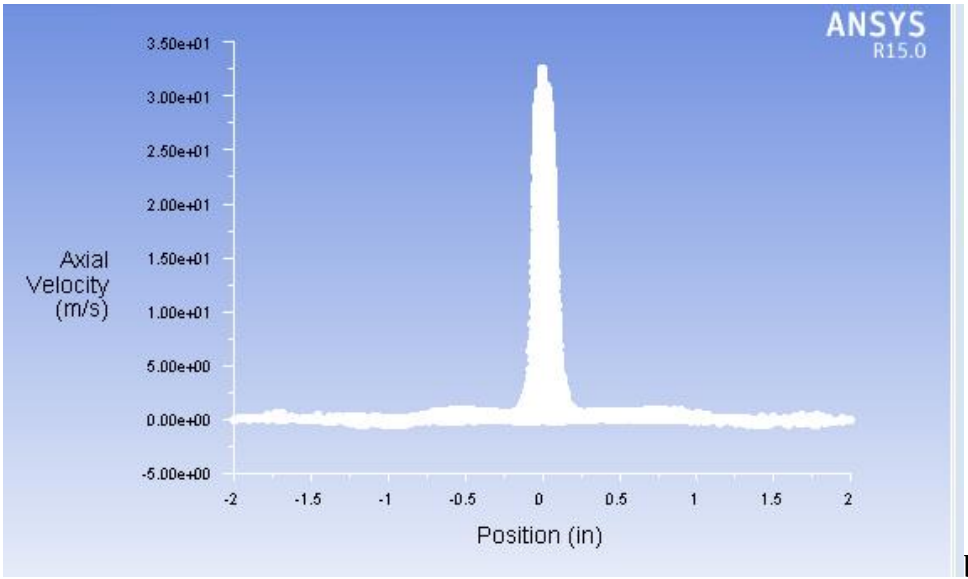

b)

Figure 3.28: Plots of axial velocity distribution on the xz-plane after a round of turbulent jet impingment flow simulation. a) interface to select the parameters in the plot, b) resulting plot

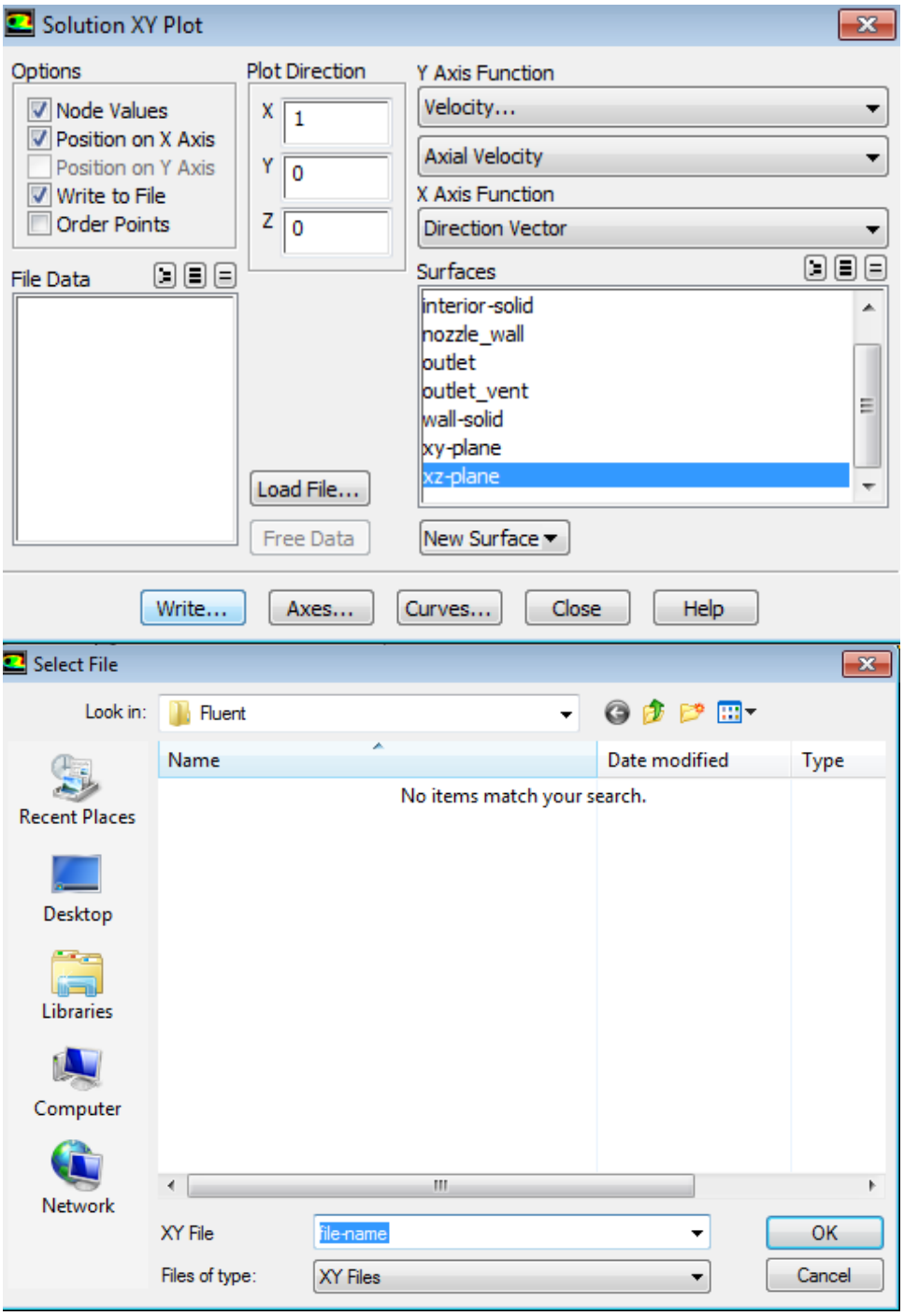

Figure 3.29: Exporting plots of axial velocity distribution on the xz-plane after a round of turbulent jet impingment flow simulation. Interface to select the parameyters in the plot (top), exporting the resulting plot (bottom)

3.7 REACTIVE FLOW AND DISSOLUTION MODEL

3.7.1 Description and Code

This model is a reactive flow model where the dissolution growth is simulated. It uses the velocity and pressure distribution results from the turbulent impinging flow model in order to estimate the volume, shape, and distribution of the dissolution at the rock/fluid interface. The goal of this convert velocity distribution data to dissolution data in 3D, considering the fluid pressure and time for the transient process. Some simplifying assumptions are made, such a treatment of the velocity data in 2D assuming axisymmetry. A pseudo-code for this chemical dissolution model is shown in Table 3.4

Table 3.4: Pseudo code for chemical dissolution model

```
{
For each time step,
        {
        Scan the velocity distribution data in a specific direction
        Scan the pressure distribution data in a specific direction
                {
                  Estimate the extent of reaction α for each pressure value at every node
point
                  Generate a vector adjacent to the velocity distribution to store the α
values
```

Table 3.4 Continued

```
        Identify the different cross sections of the finite volumes from the node data
            {
            Compute the equivalent dissolution volume, in the direction considered,
            for every volume area:
                Dissolution in cavity
                Dissolution in wormhole
            Add all the volumes to determine the volume dissolved in the time step
            }
        Determine the furthest propagation axially and radially and the approximate
        locations for both the cavity and the wormhole
        }
Return the dissolved volume, new wormhole length, cavity depth, cavity radius at initial
impingement surface and largest cavity width and corresponding location.
}
```

3.7.2 Approach

This dissolution propagation model follows the approach by Hung et al. (1989) and Furui et al. (2012). It is a reactive transport model with fluid loss from a single dissolution zone. The velocity of propagation of the dissolution structure in a single direction is given by Equation 3.1 and the acid capacity number is defined in Equation

3.2. The empirical matrix acidizing optimum parameters ($v_{i,opt}$ and $PV_{bt,opt}$) are also needed.

$$v_{dissolved} = v_{i,tip}\left(\frac{C_{tip}}{C_0}\right)N_{AC} \tag{3.1}$$

$$N_{AC} = \frac{\varphi\beta_{100}C_0\rho_{acid}}{(1-\varphi)\rho_F} = \frac{\varphi\chi_{100}C_0}{(1-\varphi)} \tag{3.2}$$

where $v_{dissolved}$ is the dissolution growth rate in cm/min, $v_{i,tip}$ is the interstitial velocity at the tip in cm/min, C_{tip} is the acid concentration at the wormhole tip, C_0 is the initial acid concentration, N_{AC} is the acid capacity number, φ is the rock's porosity, β_{100} is the acid dissolving power, ρ_{acid} is the acid density in lbm/ ft³, ρ_F is the density of the fast reacting mineral in lbm/ ft³, and χ_{100} is the volumetric dissolving power in ft³/ft³.

For this study, the terms in Equation 3.2 may carry different meanings depending on whether we are considering the dissolution in the cavity or the dissolution in the wormhole.

3.7.3 Dissolution in Cavity

$v_{dissolved}$ represents the rate of dissolution. In this case the dissolution is assumed to occur in both the radial and axial directions, which are the respective directions of the wall jet and the free jet regions, meanwhile the stagnation region

combines both directions. This reduction from 3D to 2D flow is assuming axisymmetry for the azimuth (tangential) direction. The expression $v_{i,tip}$ here means interstitial velocity at the onset of the dissolution, and it is also considered in the radial and axial directions as indicated in Equation 3.3 and 3.4

$$v_{i,tip,axial} = \frac{v_{node,axial}}{\phi} \tag{3.3}$$

$$v_{i,tip,radial} = \frac{v_{node,radial}}{\phi} \tag{3.4}$$

where, v_{node} is the node velocity at the acid/rock boundary, obtained from the turbulent jet impingement flow simulation results. The expression $\frac{C_{tip}}{C_0}$ represents the ratio of the concentration at the acid/rock interface location and the initial/bulk concentration.

Following the strong mixing approximation, those two concentrations can be considered almost identical, thus leading to an estimate of the ratio as indicated in Equation 3.5. Hence the vector components for the velocity of the dissolution propagation can be approximated by Equation 3.6 and 3.7.

$$\frac{C_{tip}}{C_0} \approx 1 \tag{3.5}$$

$$v_{dissolved_{rad}} = v_{node,radial} \frac{\chi_{100} C_0}{(1-\varphi)} \tag{3.6}$$

$$v_{dissolved_{axi}} = v_{node,axial} \frac{\chi_{100} C_0}{(1-\varphi)} \tag{3.7}$$

The corresponding dissolution vectors in the (r, z) configuration are expressed in Equation 3.8 and they represent the actual quantity dissolved. The factor α_{node} represents the extent of the reaction per unit time at a given fluid pressure and system temperature for each node, it was adapted from the data from Tata (2016) presented in Figure 3.2 at 75 degrees Fahrenheit assumed to be room temperature.

$$\begin{pmatrix} r_{dissolved} \approx (\alpha_{node}\, \Delta t) v_{dissolved_{rad}}\, \Delta t \\ z_{dissolved} \approx (\alpha_{node}\, \Delta t) v_{dissolved_{axi}}\, \Delta t \end{pmatrix} \tag{3.8}$$

where the value for α_{node} can be estimated from Figure 3.30 and the polynomial trendline indicated.

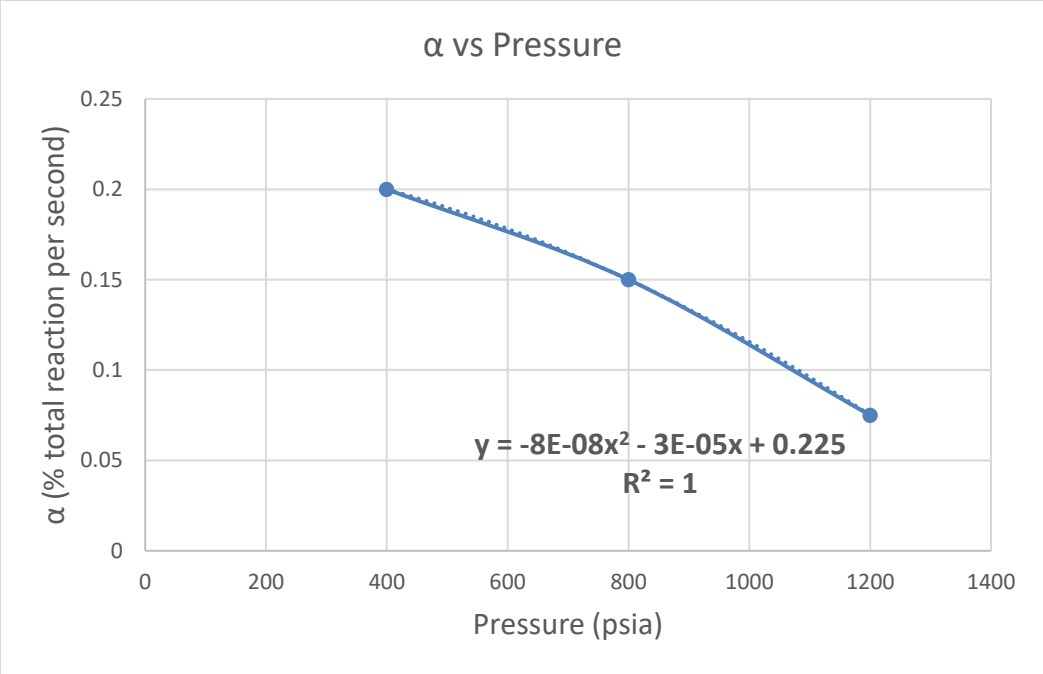

Figure 3.30: Extent of total reaction of 15 wt.% HCl with calcite per unit time, as a function of pressure, estimated from the data from Tata (2016).

The dissolution in the cavity for each node point in the planar projection of the velocity and pressure distribution can therefore be expressed in the radial direction by Equation 3.9 and in the axial direction by Equation 3.10, which will account for all the regions issuing from the turbulent jet impingement flow.

$$r_{dissolved} \approx v_{node,radial} \frac{\chi_{100} C_0}{(1-\varphi)} \alpha_{node} (\Delta t)^2 \tag{3.9}$$

$$z_{dissolved} \approx v_{node,axial} \frac{\chi_{100} C_0}{(1-\varphi)} \alpha_{node} (\Delta t)^2 \tag{3.10}$$

3.7.4 Dissolution in Wormhole

In this case, $v_{dissolved,wh}$ represents the rate of dissolution for the wormhole, expressed in Equation 3.11, and the dissolution is assumed to only occur in the axial direction z.

$$v_{dissolved,wh} = v_{i,tip,wh}\left(\frac{C_{tip}}{C_0}\right)N_{AC} \tag{3.11}$$

where the expression $v_{i,tip,wh}$ represents the interstitial velocity at the onset of the dissolution.

This expression has two components as indicated in Equation 3.12. The first one is the additional velocity provided by the turbulent jet impingement flow. That additional velocity is obtained from the impingement results. These relationships imply that additional velocity is estimated to decrease as the wormhole propagates further in the formation away from the impingement location. The second expression is the interstitial velocity issuing from the fluid flux through the core caused by the pressure differential across the core.

$$v_{i,tip,wh} = \frac{v_{node,axial}}{\phi} + v_i \tag{3.12}$$

where, v_i is the interstitial velocity.

The expression $\frac{C_{tip}}{C_0}$ represents the ratio of concentration at dissolution location and initial/bulk concentration. It can be approximated by the expression shown in Equation 3.13 from Furui et al. (2012).

$$\frac{C_{tip}}{C_0} \approx \left[1 - \exp\left[-4\left(\frac{v_i}{v_{iopt}}\right)^2\right]\right]^2 \tag{3.13}$$

where, v_{iopt} is the semi-empirical optimal interstitial velocity

The wormhole growth rate can therefore be estimated as indicated in Equation 3.14.

$$v_{dissolved,wh} = \left(\frac{v_{node,axial}}{\phi} + v_i\right)\left[1 - \exp\left[-4\left(\frac{v_i}{v_{iopt}}\right)^2\right]\right]^2 \frac{\varphi\chi_{100}C_0}{(1-\varphi)} \tag{3.14}$$

Similar to the cavity dissolution, the axial length dissolved can be estimated as shown in Equation 3.15.

$$z_{dissolved,wh} \approx (\alpha_{node}\,\Delta t)v_{dissolved_{wh}}\,\Delta t \tag{3.15}$$

Combining Equation 3.14 and Equation 3.15 yield Equation 3.16.

$$z_{dissolved,wh} \approx \alpha_{node}(\Delta t)^2 \left(\frac{v_{node,axial}}{\phi} + v_i\right)\left[1 - \exp\left[-4\left(\frac{v_i}{v_{iopt}}\right)^2\right]\right]^2 \frac{\varphi \chi_{100} C_0}{(1-\varphi)} \quad (3.16)$$

This equation correctly predicts that there will not be any wormhole growth when the interstitial velocity is set a zero, indicating no flux through the core.

Note: the 1D wormhole dissolution model requires another dimension of information to match the 2D cavity dissolution model, and that information is the wormhole diameter which is assumed constant at its lowest possible value set by computational limitations. We observed the presence of singularities and divergence whenever the wormhole diameter was set at values below 0.1 inches. Figure 3.31 and Figure 3.32 show the discrepancy in the velocity magnitude observed at the entrance of the wormhole at the bottom of a cavity when the wormhole diameter is set at 0.01 inches and 0.02 inches respectively, the continuity equation was unable to converge. The velocity spikes up to almost 10 orders of magnitude above the jet velocity. For that reason, the wormhole diameter was set at 0.1 inches.

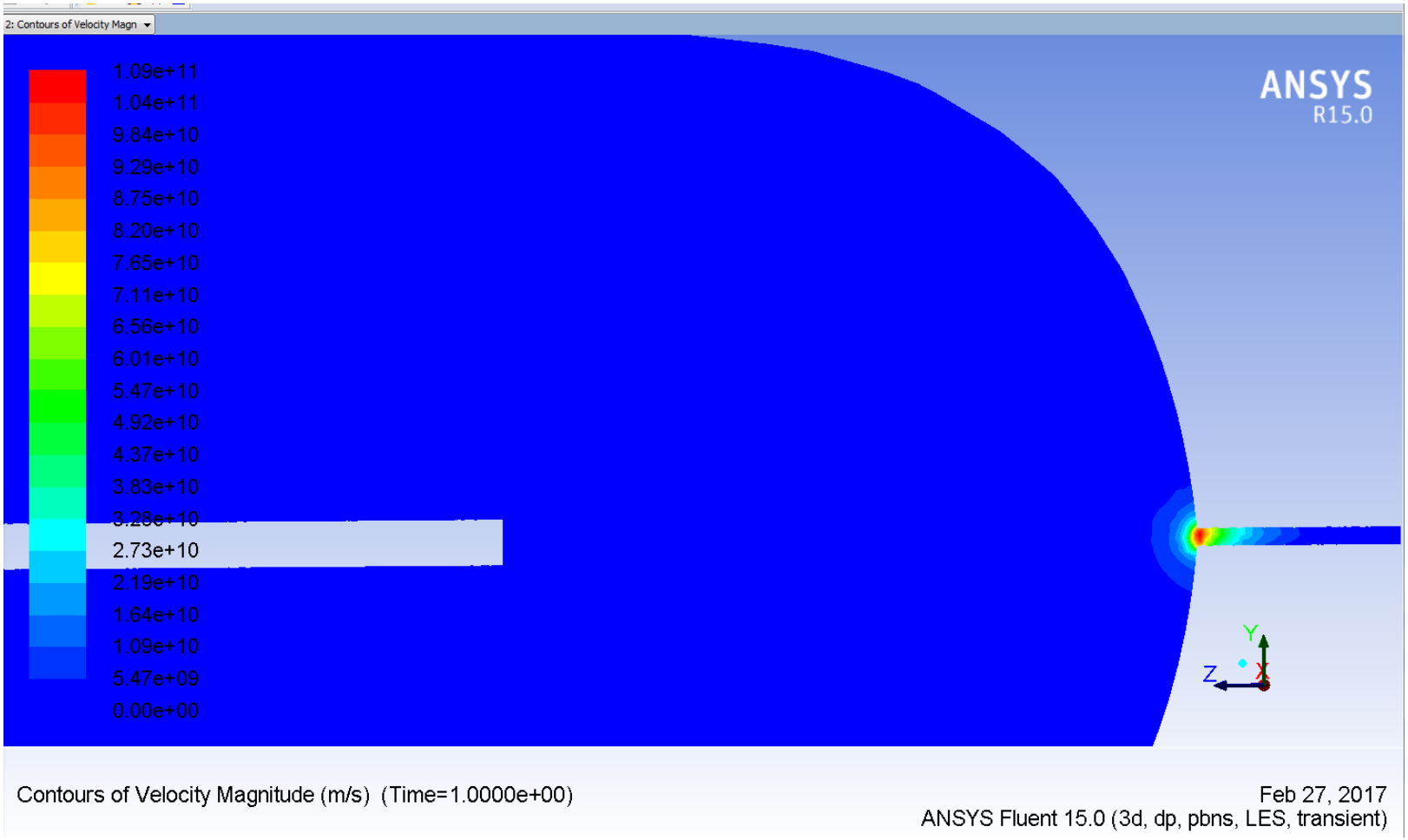

Figure 3.31: Singular region at the wormhole entrance, observed on contour of velocity magnitude on plane yz, for a wormhole diameter of 0.01 inches

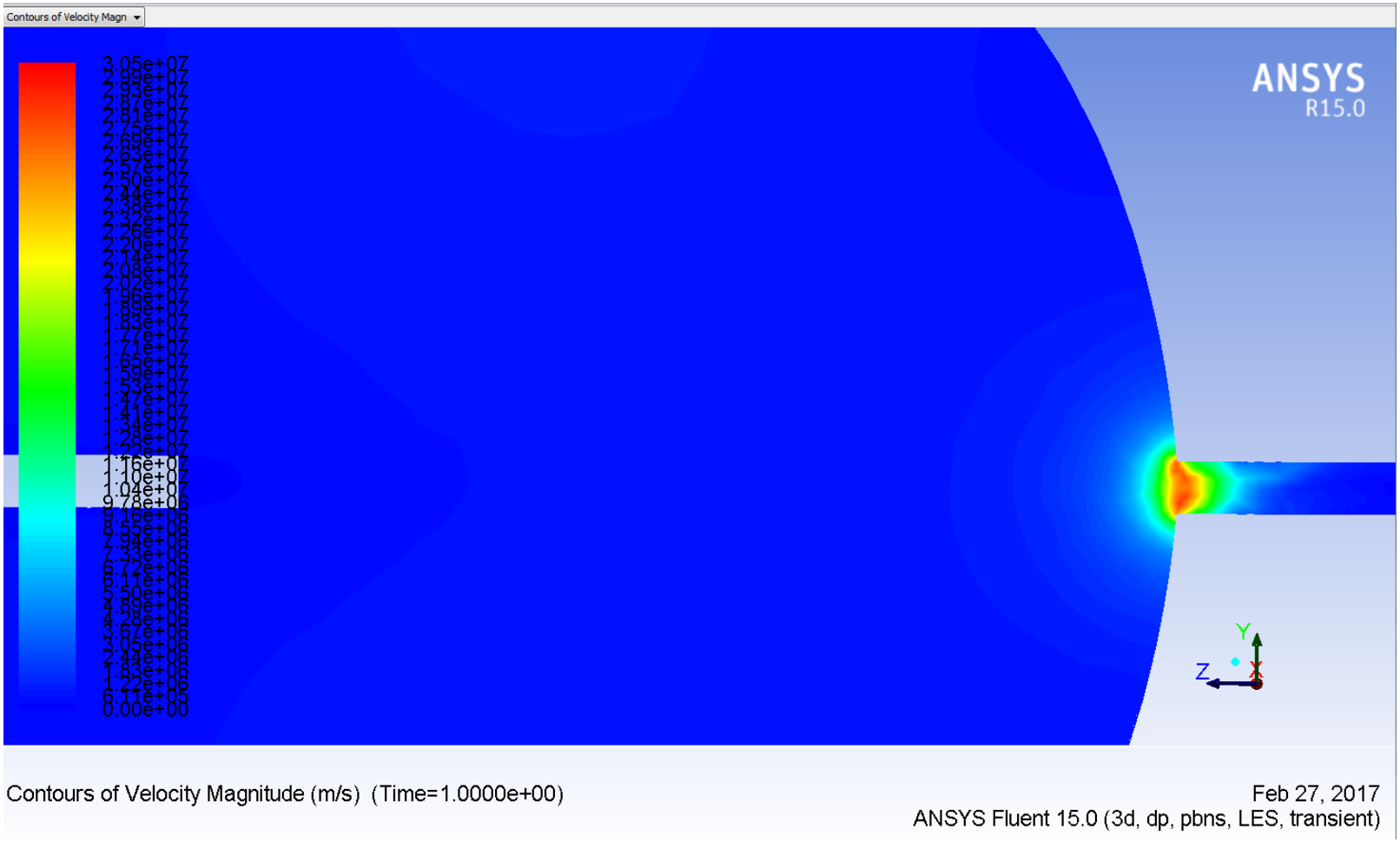

Figure 3.32: Singular region at the wormhole entrance, observed on contour of velocity magnitude on plane yz, for a wormhole diameter of 0.02 inches

3.8 SAMPLE SIMULATION RESULTS

Figure 3.33 to 3.41 show the transient evolution of the cavity during a simulation with no flux through the core.

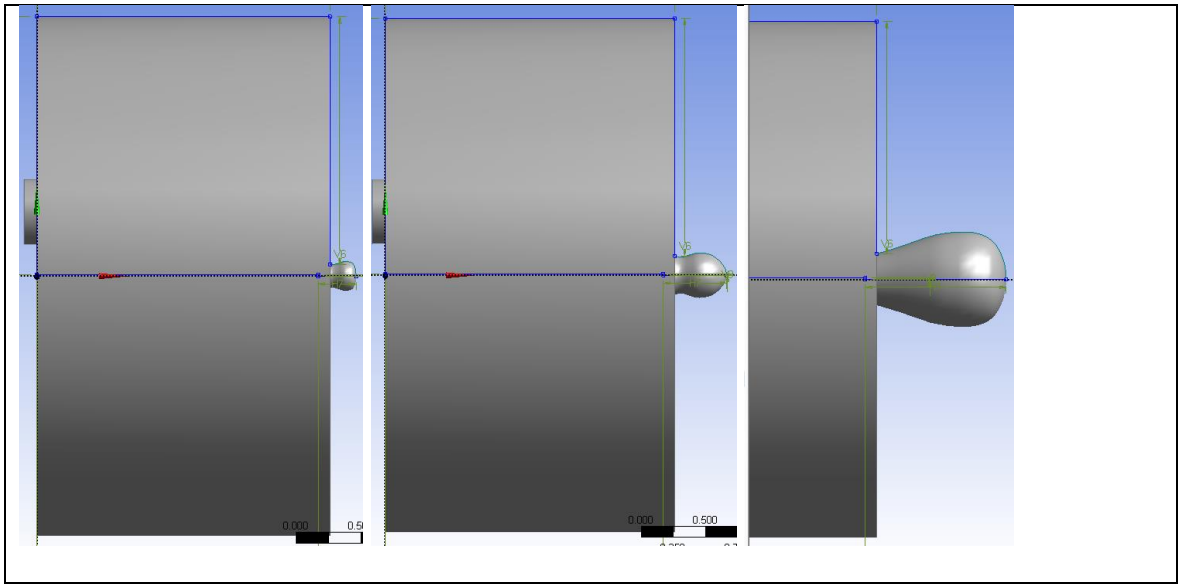

Figure 3.33: Computational domain at t= 90 seconds (1.5 minutes) (Left), t= 120 seconds (2 minutes) (Center), t= 240 seconds (4 minutes) (Right)

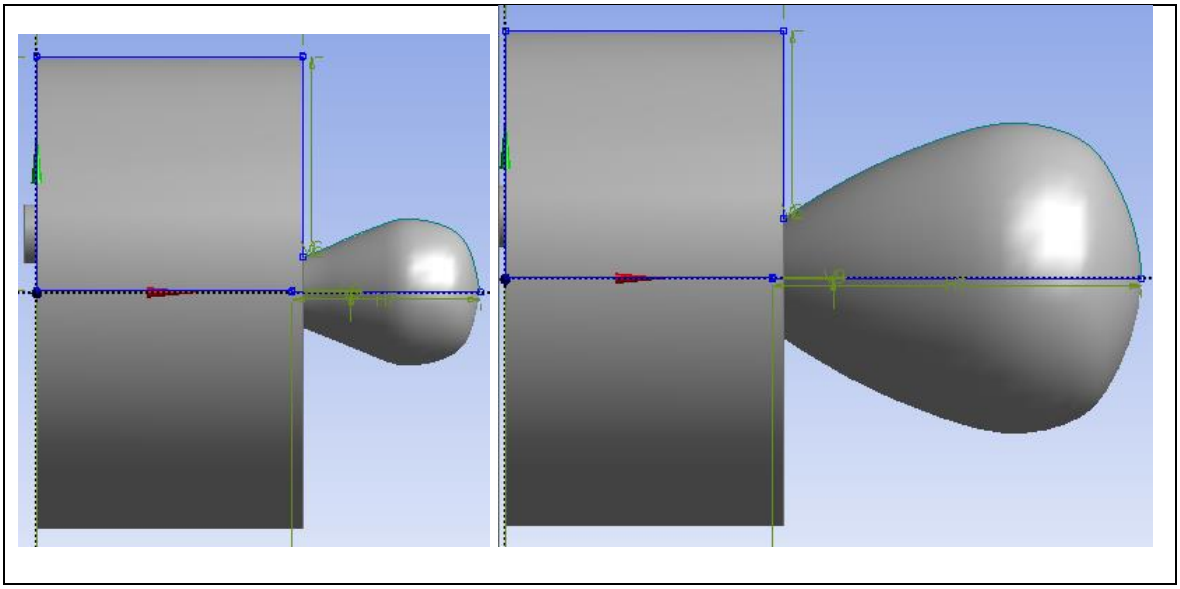

Figure 3.34: Computational domain at t= 300 seconds (5 minutes) (Left) t= 600 seconds (10 minutes) (Right)

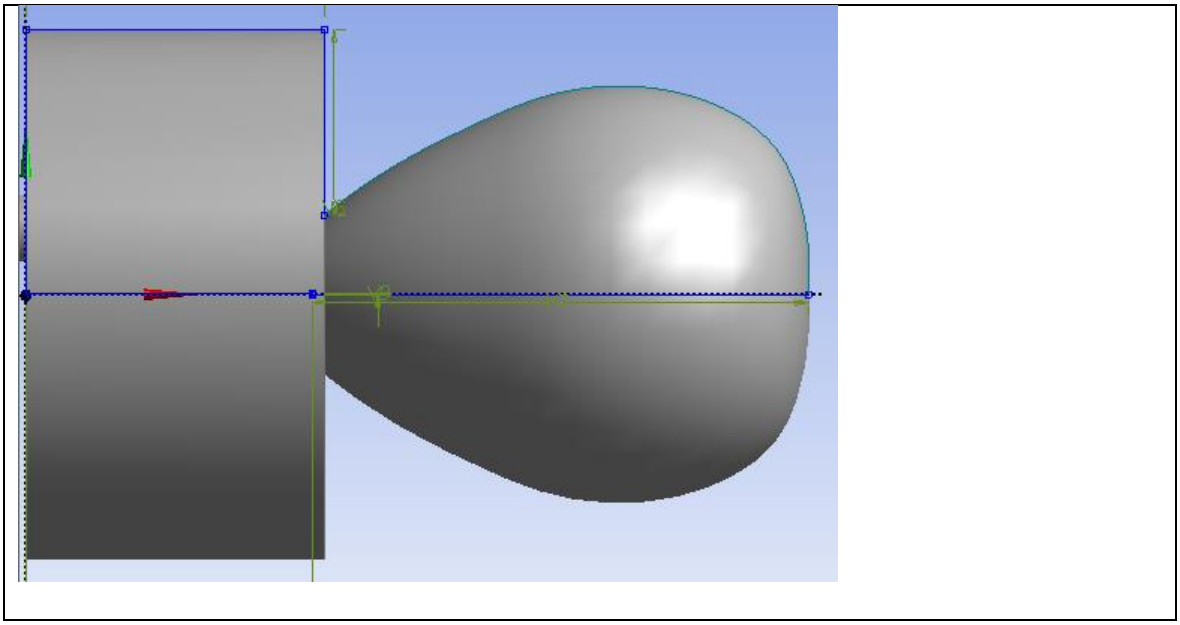

Figure 3.35: Computational domain at t= 900 seconds (15 minutes)

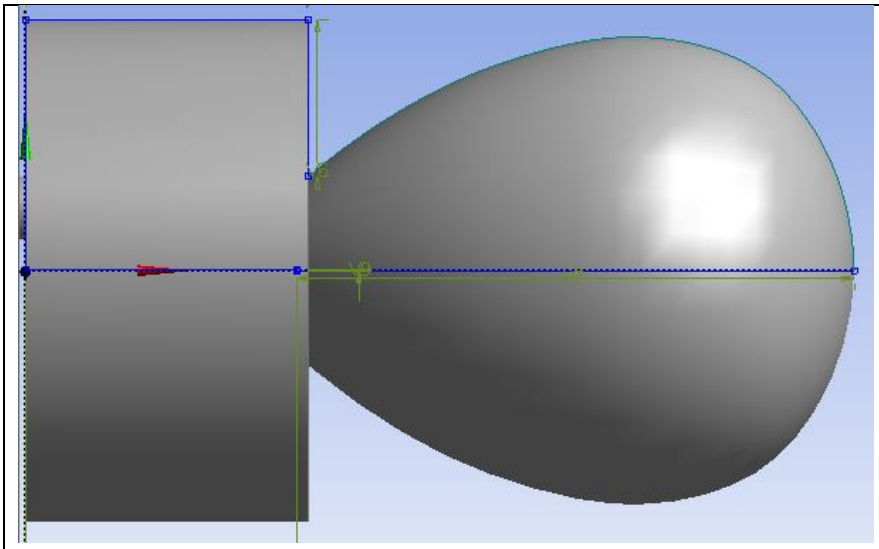

Figure 3.36: Computational domain at t= 1200 seconds (20 minutes)

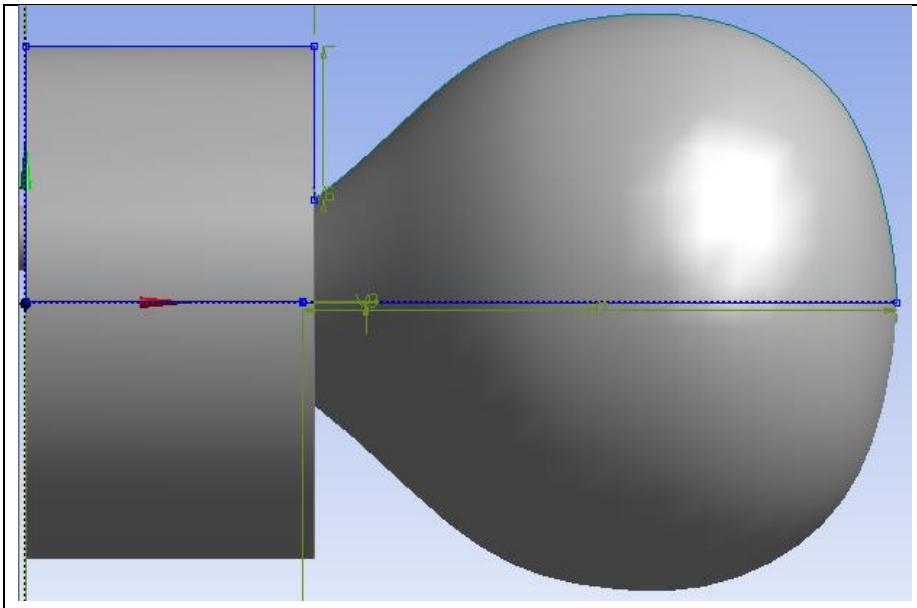

Figure 3.37: Computational domain at t= 1500 seconds (25 minutes)

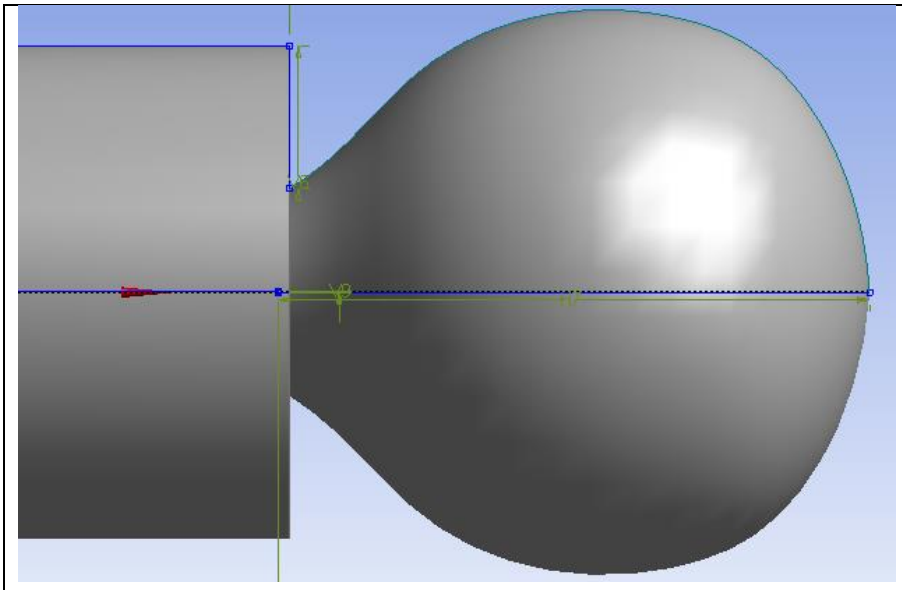

Figure 3.38: Computational domain at t= 1800 seconds (30 minutes)

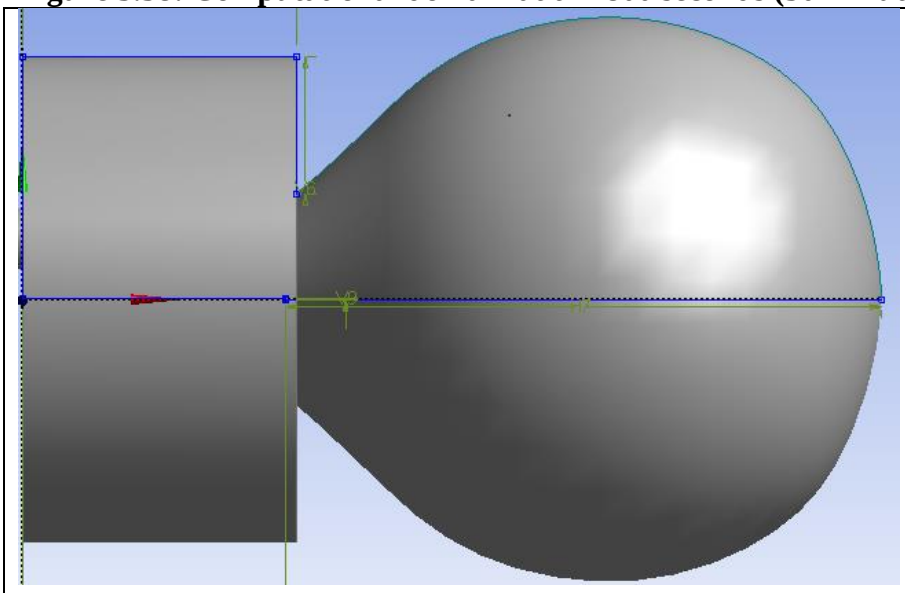

Figure 3.39: Computational domain at t=2100 seconds (35 minutes)

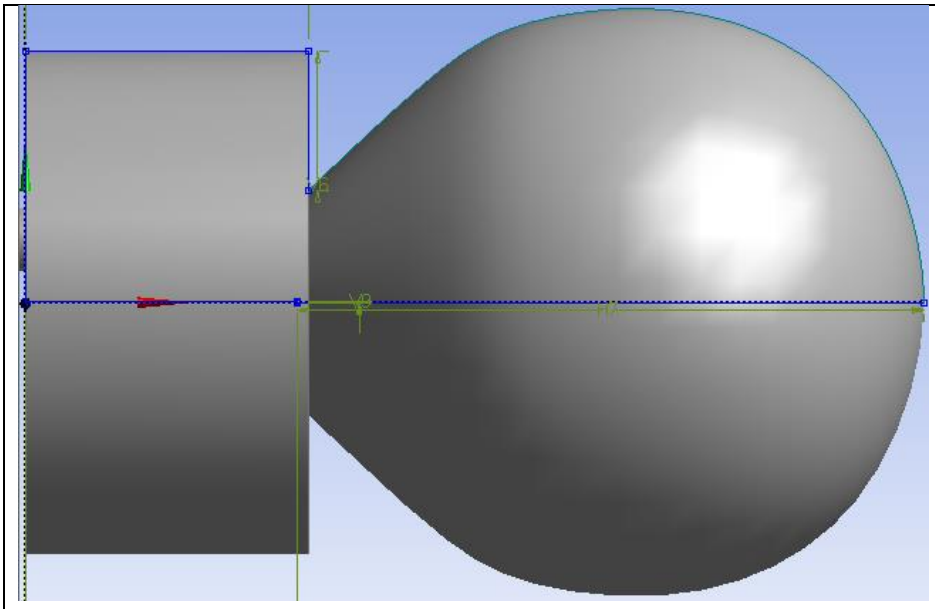

Figure 3.40: Computational domain at t=2400 seconds (40 minutes)

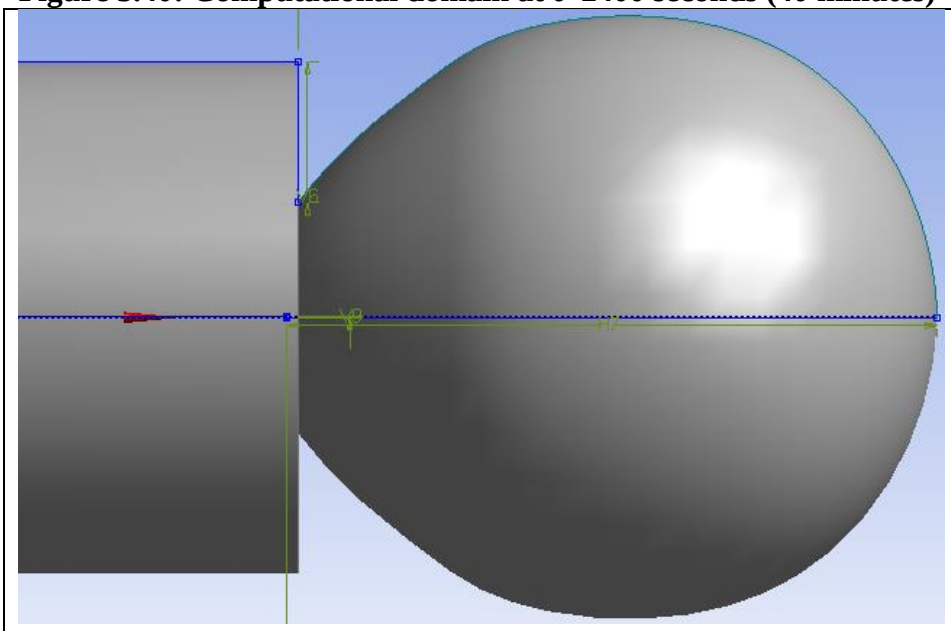

Figure 3.41: Computational domain at t=2700 seconds (45 minutes)

3.9 COMPUTATIONAL TIME

The time limiting step in the entire simulation is the turbulent jet impingement flow computation. Considering a serial simulation on a single CPU with one ANSYS Fluent license, it takes at least 90 minutes to run a 10-seconds round of turbulent jet impingement flow including the geometry design and result processing. In theory, using parallel computing could cut the clock time in half or more. The reactive flow and dissolution computations could be completed in approximately 20 minutes for each time step. Overall each round of simulation for a single time step currently takes approximately 2 hours. The overall computational time could also be reduced if the simulation were used as a complement to experimental data, i.e. use experimental data end points (dissolution volume and length) as initial data for simulations, where the aim would be to investigate what happens beyond experimental limitations.

CHAPTER IV

SIMULATION RESULTS ANALYSIS

15 simulations were run using the CFD model described in Chapter III and the results are presented in this Chapter. A large portion of those results were obtained for model validation purposes and the others were run to observe trends and study the sensitivity of the model to some parameters.

4.1 MODEL VALIDATION

Table C in the Appendix C summarizes the simulation cases used in this work; specific simulation time stamps are used to compare experimental and simulation results, as listed in Table 4.1 and 4.2, respectively. The focus is on the interstitial velocities less than or equal to 1.5cm/min, which are more likely to be considered for field applications. Figures 4.1 and 4.2 are plots of the tabulated data, which enable us to observe the similarities in trends.

Table 4.1: Experimental results considered for model validation taken from Ndonhong et al. (2017)

Experiment Number	Rock type	Jetting velocity (ft/sec)	Initial interstitial velocity (cm/min)	Permeability (md)	Porosity (%)	Jetting time (min)	PVbt	Axial length stimulated (in)
1	Indiana Limestone	107	0	5.4	15	20	12.4	2.1
2			0.14	2.4	14	20	2.1	9
3			0.17	2.1	14	16.3	1.1	16
4			0.21	10.7	16	17.6	1.3	16
5			0.74	6.9	15	14.4	1.9	16
6			0.89	5	10	8.1	1.9	16
7			1.55	6.1	14	5	1.0	16
8		200	0.09	2.1	14	20	4.8	7.6
9			0.33	9.6	16	10.4	2	16
10			1.22	4.4	14	5.7	1.4	16
11			1.65	3.8	14	4.1	1.3	16

Table 4.2: Summary of simulation results used to compare to experimental work, assuming a permeability of 5mD and 15% porosity

Simulation Number	Jetting velocity (ft/sec)	Flow weighting (%)	Simulation time (min)	Volume of Dissolution Structure (cm^3)	PVbt from Dissolved volume	Axial length stimulated (in)
1	107	0.01	20	85.2	13	2
2		0.1	20	70.8	2.5	9.5
3		0.15	20	71.5	2	12
4		0.2	15	95.4	2	16
5		0.75	12	95.4	2.5	16
6		1	10	81	1.7	16
7		1.5	7	35	0.5	16
9	200	0.1	20	131.1	5.5	8
10		0.5	12	81	1.7	16
11		1	6	42.9	0.9	16
12		1.5	5	42.9	0.9	16

When comparing Table 4.1 and 4.2, the results are in good agreement. Nonetheless, for experiments where acid breakthrough was not observed (experiments 1, 2 and 9) the values for pore volume to breakthrough (PVbt) and axial length stimulated obtained numerically are consistently larger than the values obtained experimentally. The simulation consistently overpredicts the dissolution volume and acid volume consumed for low interstitial velocities at both jetting velocities. The larger simulated volumes at low interstitial velocity, where large cavities and small wormholes are expected from experiments, may be explained by be the larger size of wormholes in the numerical simulations. The minimum wormhole diameter was set at 0.1 inches due to convergence constraints; the calculations were numerically unstable and could not proceed with smaller wormhole diameters. On the other hand, for high interstitial velocity or for experiments with an axial length of stimulation equal to 16" (equivalent to acid breakthrough) the numerical values are consistently lower than the experimental values. It could be due to the end effects observed experimentally, where the acid would "rush" to exit the core as it gets closer to breakthrough. That effect was not accounted for in the simulations. It is important to note that for the simulations the points in Table 4.2 and Figure 4.1 and 4.2 correspond to values obtained after a specific time, the simulation did not end at those values, generally the dissolution structure grew further as the time was incremented. The specific times were selected to compare with experimental results only. In the field, acid would be jetted for a fixed preset time.

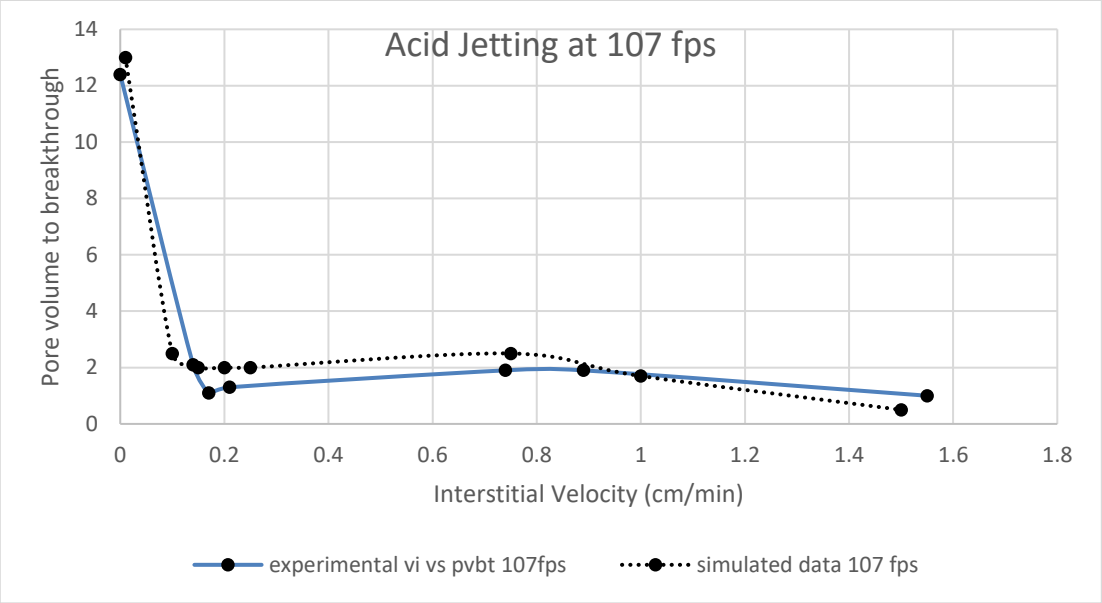

Figure 4.1: Comparing experimental and simulation results for jetting velocities of 107 ft/s.

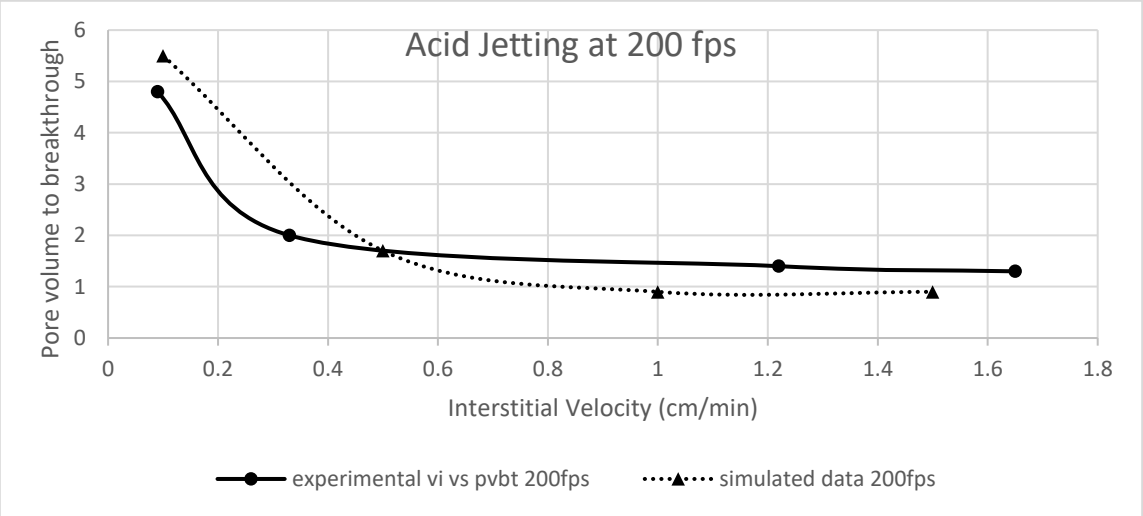

Figure 4.2: Comparing experimental and simulation results for jetting velocities of 200 ft/s.

Figure 4.3 shows what the computational space looks like after 12 minutes of acid jetting with no flux. In this case, there is no apparent wormhole growth and only the cavity is generated from the location of impingement. It can be compared to Figure 3.8 to observe how the geometry changes during a simulation.

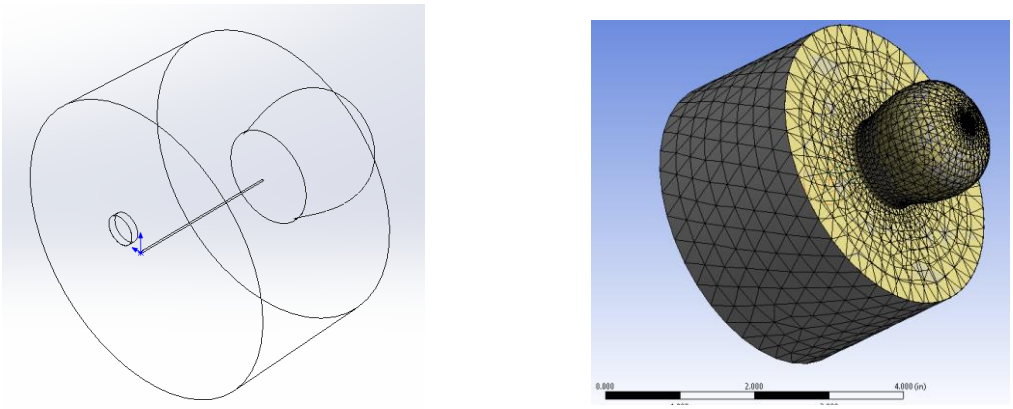

Figure 4.3: Computational space after acid jetting, v_{jet}=107ft/sec (32.6 m/s), v_i=0cm/min, t=12min, trimetric view (center), mesh (right)

Figure 4.4 displays a comparison of the velocity contour from ANSYS Fluent 15 after an initial simulation and a core picture after experimental acid jetting. It shows a similarity in appearance, confirming the strong correlation between the velocity distribution at the rock/fluid interface and the dissolution structure shape. Figure 4.5 shows velocity contours in two different planes at the beginning of a jetting simulation and a close-up of the new geometry after one round of simulation (t=10s) where it can be observed that the largest velocity on the interface is at the midpoint of that surface,

hence justifying the growth of the cavity and wormhole around that point, which was also observed experimentally. (Holland, 2014; Beckham et al., 2015; Ndonhong et al., 2017)

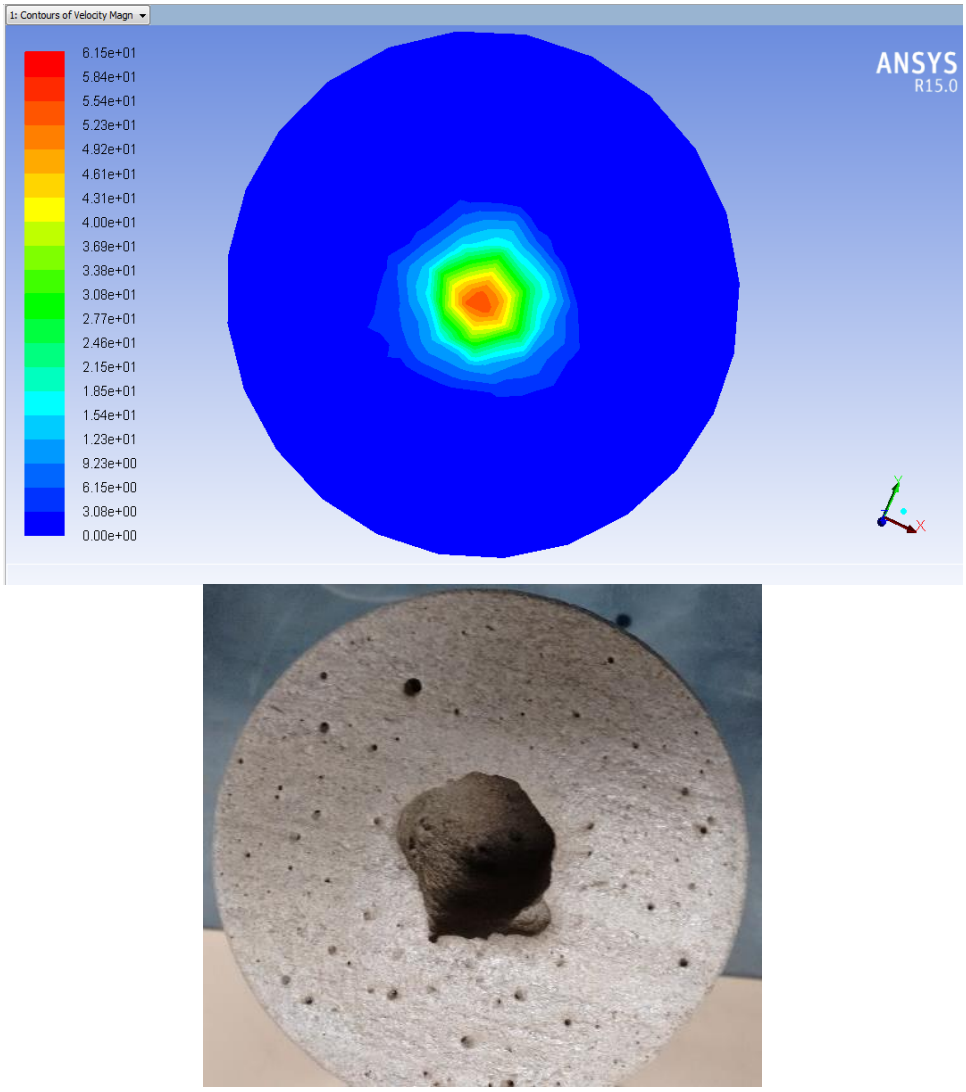

Figure 4.4: Velocity distribution compared with apparent dissolution structure: plane projection of impingement surface for a 200 ft/sec jet (61 m/s) (Top); Jetting inlet surface after an acid jetting experiment at 200 ft/sec (Bottom)

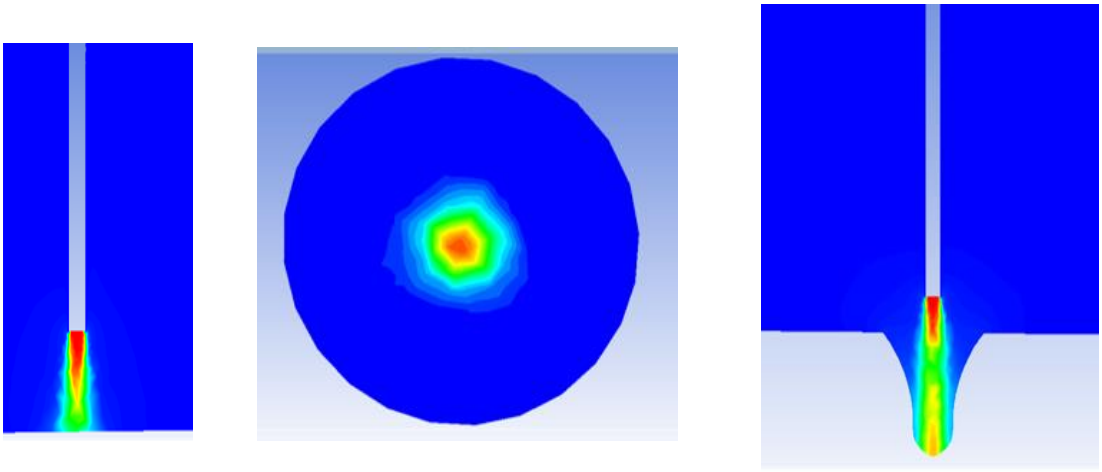

Figure 4.5: Velocity distribution during a (z-direction) jetting simulation with ANSYS Fluent 15 at 200 ft/sec: xz-plane projection, t=0 s (Left); Porous media and fluid interface (// to xy-plane) (Center), t=0 s; xz-plane projection, t=10 s (Right)

Figure 4.6 shows a visual comparison of experimental and simulation results with no flux at 107 ft/s (32.6 m/s), corresponding to experiment 1 and simulation 1 in Table 4.1 and 4.2, respectively.

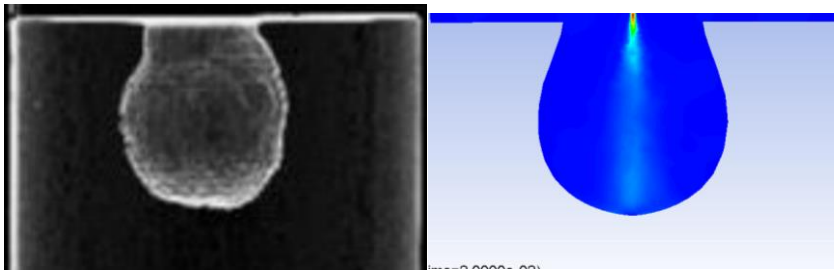

Figure 4.6: Visual comparison of cavities from experimental acid jetting and simulation results at 107 ft/sec and no acid flux: CT scan of cavity formed in a core after 20 minutes of experimental acid jet (Left); Front view of cavity in computational space after 20 minutes of simulated acid jetting (Right).

4.2 EFFECT OF JETTING VELOCITY

The turbulent jet self-similarity property is verified, as observed in Figure 4.7, where the velocity contours look identical in proportion and the most noticeable effect is the increase in turbulence intensity (the Reynolds number grows proportionally with the jetting velocity). This property could explain the observation by Holland (2014) that larger cavities were created with larger jetting velocities for similar injection times. It is important to note that these two dissolutions were not achieved at the same time, it took 10 seconds (equivalent to one simulation round) for the 200 ft/sec jetting velocity case, meanwhile it took 20 seconds for the 107 ft/sec jetting velocity case.

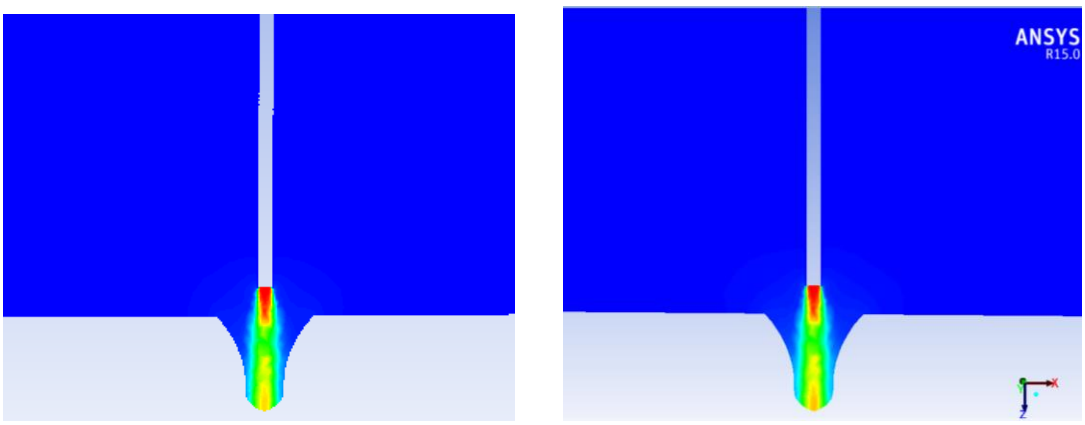

Figure 4.7: Velocity distribution during acid jetting: Axial plane projection of velocity contour for a 107 ft/sec jet (Left); Axial plane projection of velocity contour for a 200 ft/sec (61 m/s) jet (Right).

4.3 EFFECT OF INTERSTITIAL VELOCITY

The presence of interstitial velocity (or flux through the core) makes it a case of a turbulent jet in a co-flow instead of a jet in stagnant flow (for the case of no flux). The axial velocity will thus be increased, also leading to the formation of wormholes, and a more efficient axial dissolution as observed in Table 4.2 and Figure 4.8. The cavities appear more extended axially and thinner radially, as the interstitial velocity is increased. A similar observation was made in the experimental study, where the cavities in cases of larger interstitial velocities ended up looking similar to fat wormholes. (Ndonhong, 2017)

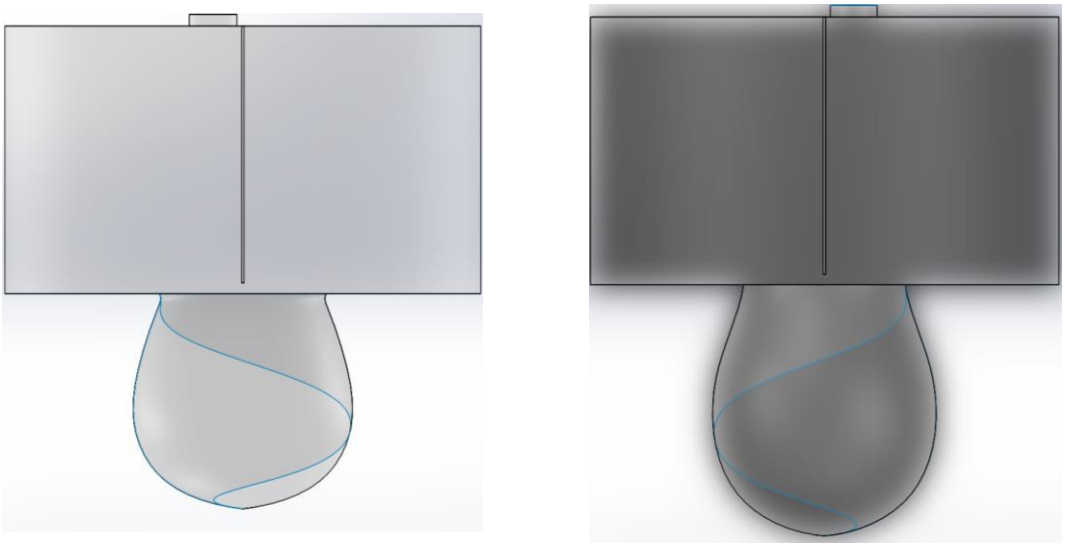

Figure 4.8: Front view of computational space. (Left) simulation 1 after 20 minutes of simulated acid jetting at 10.7 ft/sec and no acid flux; (Right) simulation 2 after 20 minutes of simulated acid jetting 10.7 ft/sec and $v_i = 1.4\ cm/min$.

4.4 RESULTS FOR LONGER JETTING TIMES

A major benefit of the simulations is the fact that the once the model is validated, the applications are no longer constrained by the laboratory limits. Experiments had to be run for 20 minutes or until acid breakthrough, to avoid core collapse as the cavity grew larger. In this work, simulations were allowed to run for up to 30 minutes of continuous acid jetting, without restrictions on axial length or radius. It enabled further observations of jet self-similarity and decrease in the effect of the jet as the standoff distance became larger.

4.5 CAVITY GROWTH

For the initial creation phase in the zone of flow establishment where the standoff distance is less than 6.2 nozzle diameters, as defined in the theory section, the cavity is growing fast. Past that phase, the cavity growth rate appears to decay with time, as the standoff distance increases, equivalent to a decreased impingement velocity and wall jet effect. This effect is more obvious for the cases of no flux. Figures 4.9 and 4.10 respectively show the cavity depth and cavity volume as a function of time for various jetting velocities. Figures 4.11 and 4.12 respectively show the approximate rates (gradients) of cavity depth growth and cavity volume growth as a function of time for various jetting velocities.

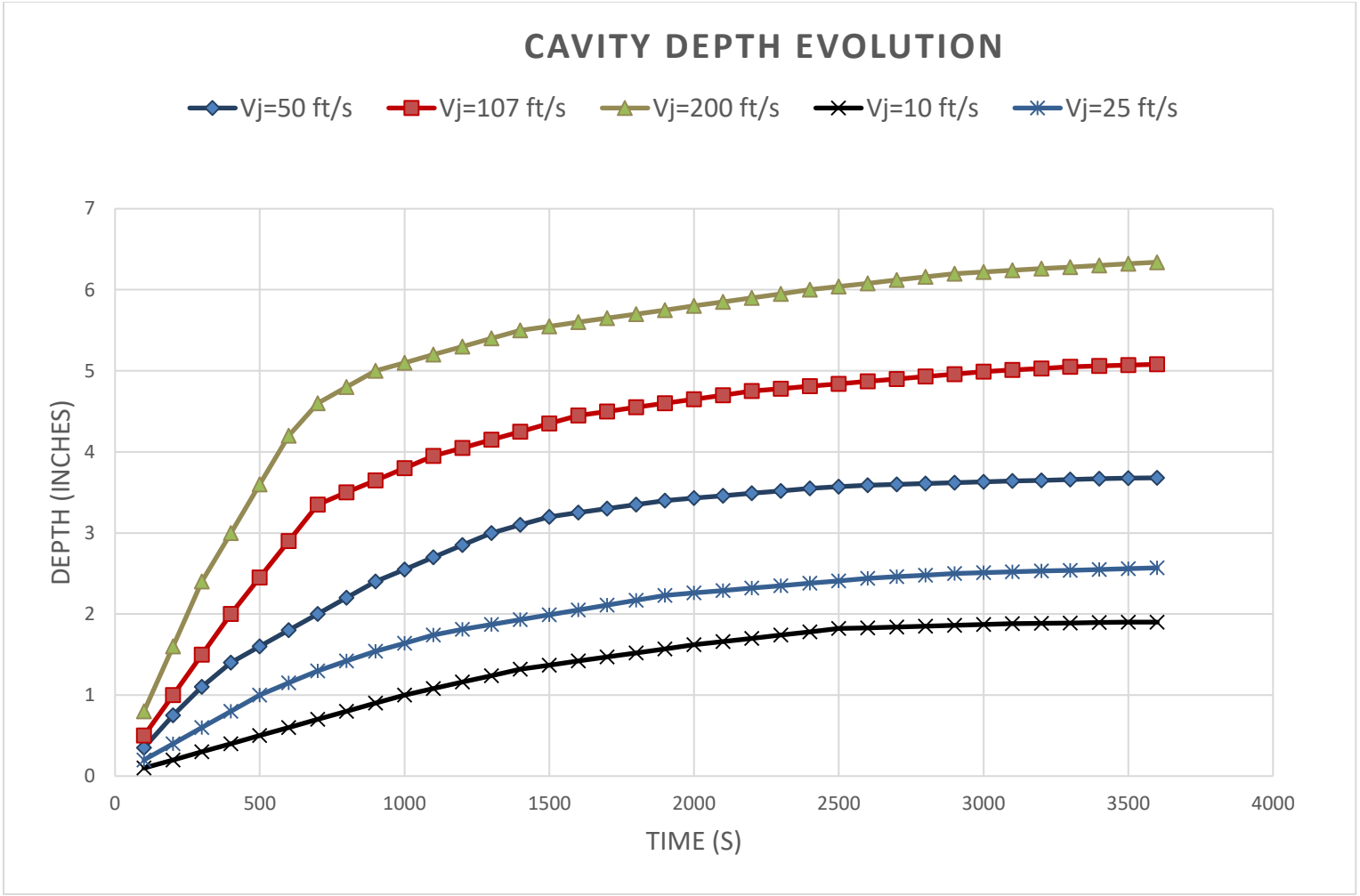

Figure 4.9: Simulated cavity depth vs time for various jetting velocities for no acid flux

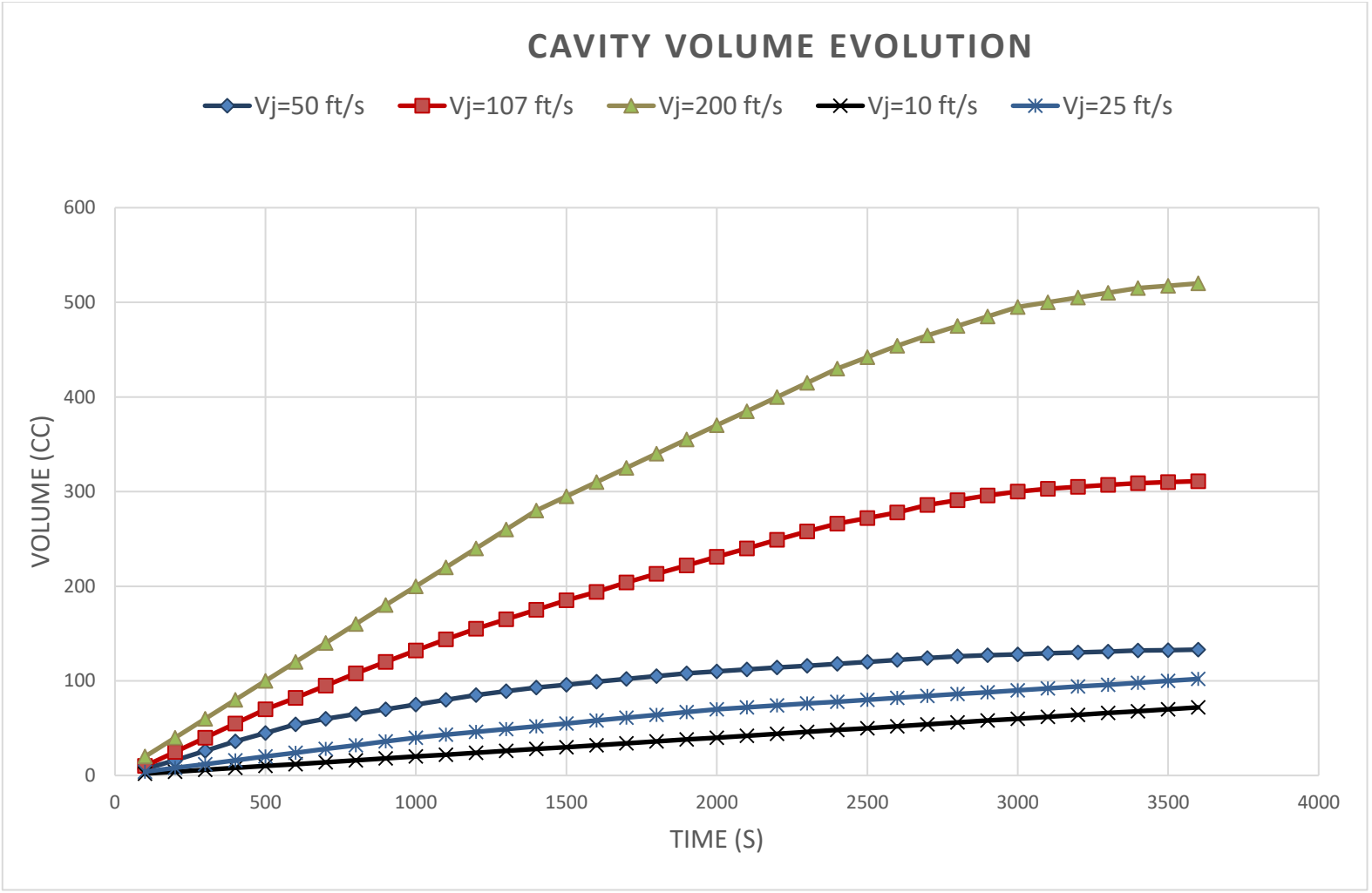

Figure 4.10: Simulated cavity volume vs time for various jetting velocities for no acid flux

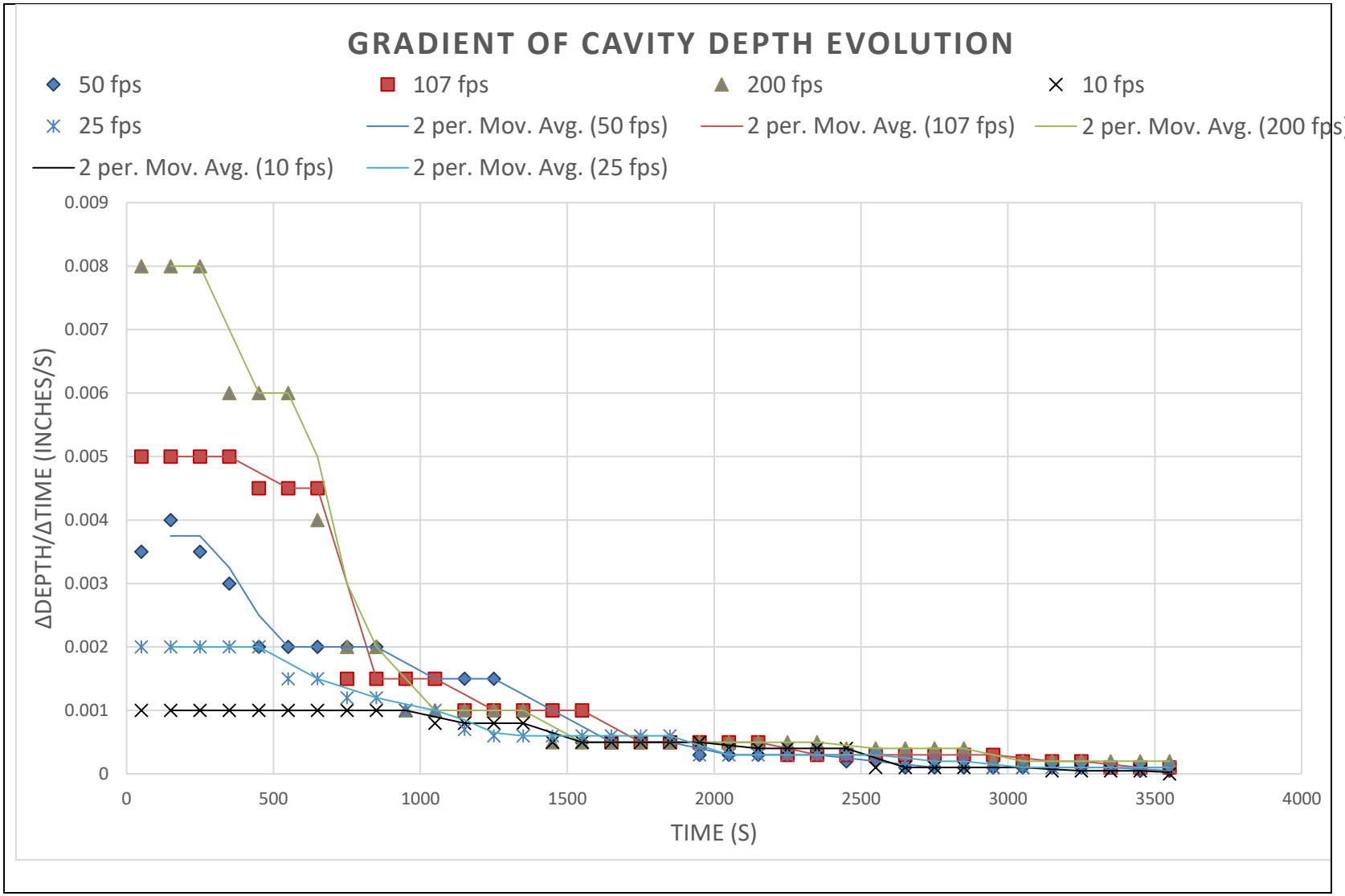

Figure 4.11: Calculated gradient of cavity depth vs time for various jetting velocities for no acid flux through the core

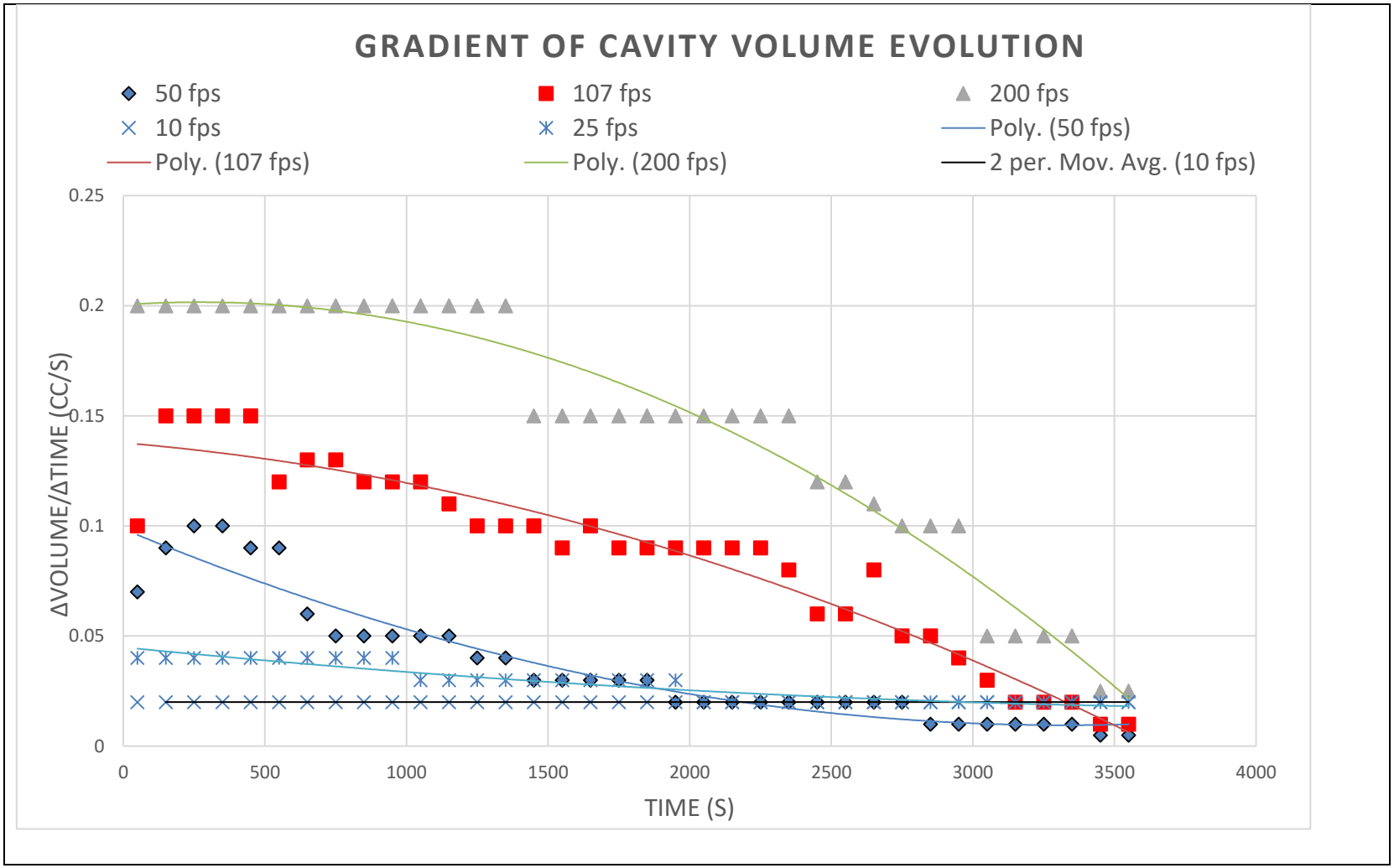

Figure 4.12: Calculated gradient of cavity volume vs time for various jetting velocities for no acid flux through the core

It is important to note that the turbulence intensity is greatly reduced as the standoff distance decreases for lower jetting velocities, it therefore leads to a reduced impingement intensity, a smaller entrainment, and hence a notable decrease in cavity growth rate and size through time These plots both indicate an initial strong dissolution for the cavity initiation and early growth, The cavity grows in all three dimensions, which is indicated by the increased gradients in the volume plot in Figure 4.12 compared to gradients in the depth plot in Figure 4.11. Generally, the cavity growth rate decreases with time, that decrease is observed more pronounced for higher jetting velocities.

4.6 JETTING EFFECT ON WORMHOLE GROWTH

The rock dissolution model, correctly predicts that at conditions of no flux through the core ($v_i = 0\ cm/min$) there is no apparent wormhole growth. As acid is allowed to flow slowly through the core ($v_i \neq 0$), in the early times, when the axial standoff distance is still relatively small ($d < 10\ d_{nozzle}$), the wormhole tip velocity is almost proportional to the peak velocity from the velocity distribution at the rock/acid interface velocity, the wormhole growth rate would therefore decrease almost proportionally to the impingement velocity. This model also correctly predicts the added effect of interstitial velocity to the system. The jetting effect would be stronger near the jet source and would be reduced as the rock is eroded, augmenting the standoff distance between the jet source and the fluid/rock interface.

In general, from the model's observations, acid jetting creates a localized region of high pressure and high equivalent fluid velocity, along the jet's centerline. When fluid

is allowed to flow through the rock, the additional acid flux from the large eddies in the jet (issuing from the entrainment, impingement, and recirculation from the wall jet) would enhance the wormhole growth. That enhancement would decrease with time, due to two simultaneous factors. The first one is the reduction in wormhole tip velocity due to the increase in the distance between the wormhole tip and the jet source. The second factor is the increase of the standoff distance which leads to the impingement of a more dissipated jet and consequently smaller velocities and a smaller turbulence. Figure 4.13 shows the computational domain when the wormhole and the cavity are growing concurrently, at high interstitial velocity, we can notice the faster wormhole growth rate at the expense of cavity growth rate.

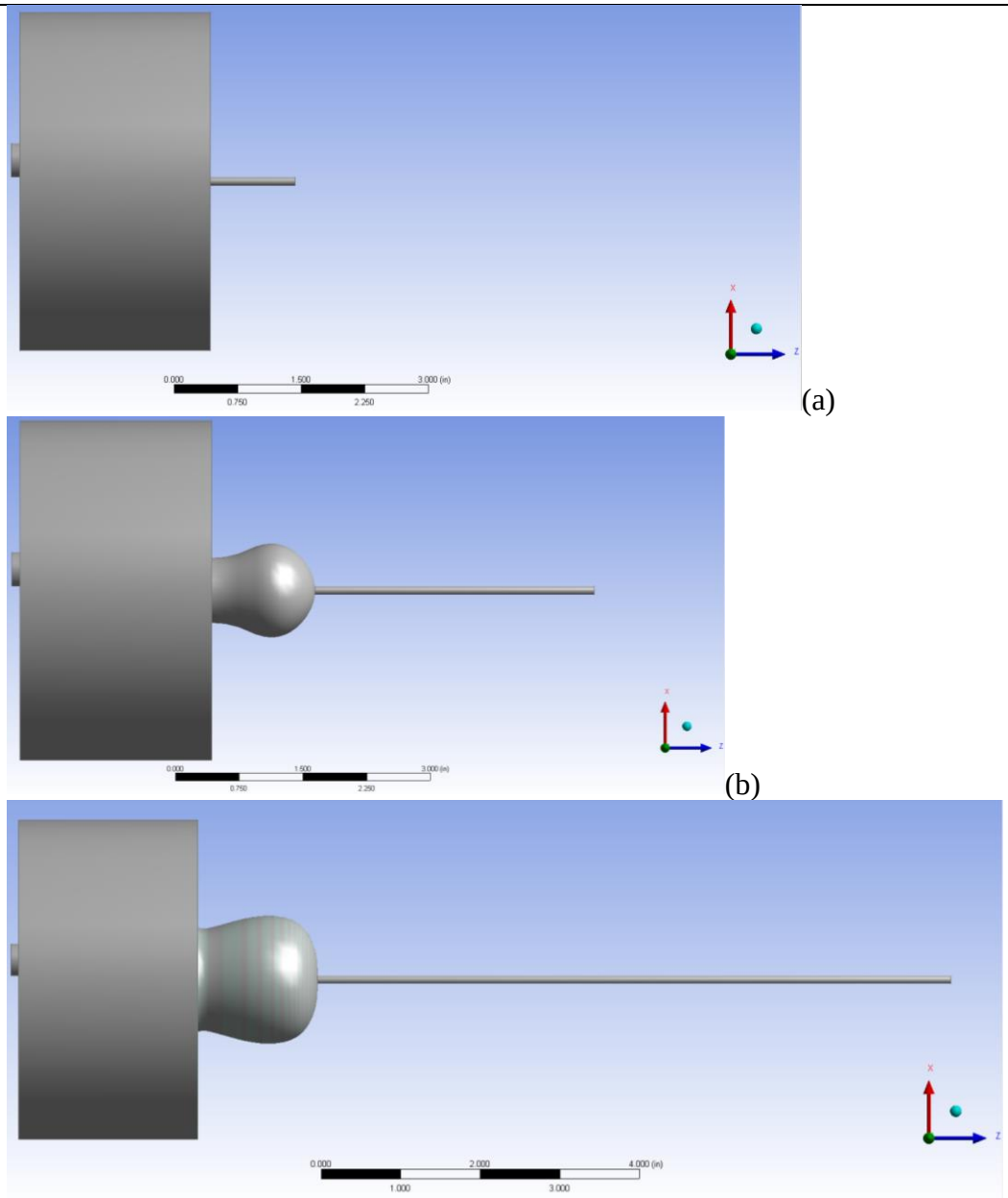

Figure 4.13: Wormhole and cavity simultaneous growth at high interstitial velocity. (a) wormhole propagation starts first due to the high interstitial velocity, (b) cavity and wormhole are both growing, (c) cavity growth rate is considerably reduced whereas wormhole keeps propagating fast.

4.7 OPTIMIZATION OF ACID JETTING

The optimization of acid jetting would impact the design process, it is recommended that for any new conceptual design, that a preliminary small-scale design be implemented in a laboratory, which will thus be followed by extensive simulation scenarios to establish the most favorable optimization scheme and finalize the design.

CFD simulation could be used to scan several alternative designs and determine the most beneficial. Unfortunately, there are too many possible design variations and uncertainty in input data which make achieving a true optimum solution highly improbable. Therefore, the goal of the optimization effort will not be to establish the universal true best design, but instead to establish a testing methodology to ensure successful acid jetting processes.

As presented earlier, acid jetting would accomplish two goals: the stimulation of the formation via the propagation of wormholes and efficient acid placement via the formation of the cavities. The success of an acid jetting job is thus a combination of two factors: first is the stimulation extent or how far in the formation did the wormhole reach and second is the benefit from the acid placement induced by the cavity volume acting like a pocket containing the injected acid.

The simplest approach to optimization would therefore be to define the acid injection and dissolution geometry through design parameters with assigned weights. The objective function, F, will therefore be defined as:

$$F = \alpha_1 W + \alpha_2 P,$$
$$\alpha_1 + \alpha_2 = 1 \; and \; \alpha_1 > \alpha_2 > 0 \tag{4.1}$$

where α_1 and α_2 are weights, W is the wormhole efficiency which is a measure of the extent and rate of the wormhole propagation in the formation, and P is the acid placement efficiency which is a measure of the cavity size and shape.

α_1=0 corresponds to a case where the process depends solely on the wormholing effect. In such a case, acid jetting would not present major benefits compared to conventional matrix acidizing, as the pore volumes of acid spent for a simulation with acid jetting are considerably larger than the pores volumes of acid spent for a matrix acidizing stimulation job of the same extent.

$\alpha_1 \leq \alpha_2$ corresponds to a case where the acid placement objective outweighs or equals the wormhole efficiency objective, which is a distant goal from the original and main motivation for acid jetting of carbonate formations.

Following the definition of such objective function, the formation properties would determine the weights α_1 and α_2. For example, for formations with high permeability or homogeneous porosity distributions, acid placement may be a considerable objective, whereas for heterogenous formations the goal may be more oriented towards the efficient propagation of wormholes beyond the damage zone.

CHAPTER V

UPSCALING EXPERIMENTAL ACID JETTING AND FURTHER STUDIES

5.1 OBJECTIVE AND DESIGN

A large scale experimental acid jetting project is in progress, to investigate radial acid jetting and the dissolution structures at larger scales. A cubic block of indiana limestone would have a wellbore drilled from its core. A concentric liner with a small diameter hole would be installed inside the wellbore to represent a limited entry liner with the hole as the jet nozzle. Initially the fluid would be allowed to flow freely in the annular space, with no imposed flux through the core, as a worse case scenario. Some simulations were attempted in order to get an idea of the pressure and velocity distribution from the impigement with that configuration.

5.2 METHODOLOGY

For the radial jetting case , the computational domain is the region between the two concentric cylinders made of the liner and the rock surface as indicated in Figure 45. The 4mm ID nozzle is in the inner cylinder and is centered at z=12in, in the midplane of the block. The dissolution would be happening at the rock surface (the outer cylinder). In order to speed up the calculations, the computational domain could be sectioned in 2, thus reduced to a half cylinder, by assuming planar symmetry across the vertical nozzle

midsection. For the simulation 16, with properties listed in Table C, the jet velocity is set at 150 ft/s, with no acid flux through the core.

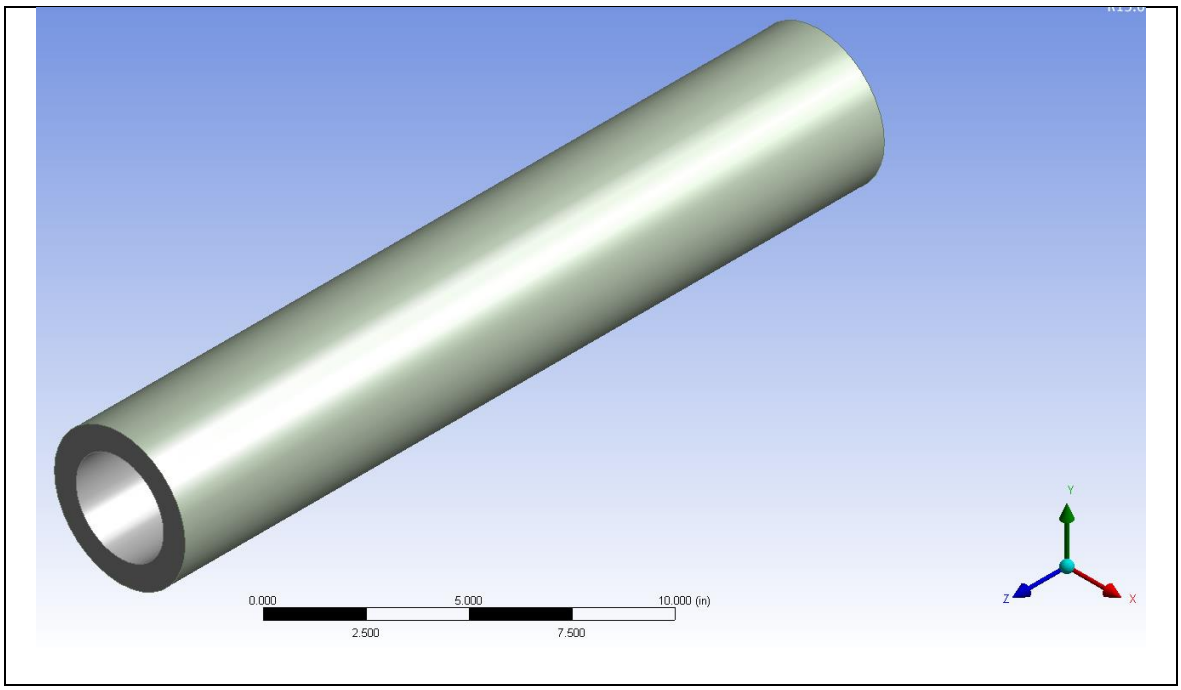

Figure 5.1: Computational domain for the radial acid jetting case

5.3 CFD OF UPSCALED EXPERIMENTS

The flow now is considered radial, with the dissipation in the tangential direction. The previous CFD considerations from the linear acid jetting still apply, except that the initial impingement surface is concave, which would affect the wall jet geometry and the shape of the subsequent large eddies. The modifications of the

geometry also become more cumbersome as the structure has to be drawn from a non-flat surface, and the revolve feature, which used to be a simplifying tool in the geometry design, can no longer be used.

5.4 PRELIMINARY RESULTS

Figure 5.2 shows preliminary results for the radial velocity distribution during a 5-minute simulation of acid jetting on the xy plane at z=12 in. The cavity growth can be observed as well as the changes in radial velocity distribution as the cavity grows. The dissolution is still localized around the impingement location, despite the larger surface area available for dissolution, even when including gravity considerations. It therefore indicates that acid jetting has high acid placement capabilities, a highly sought-after property for the acid stimulation of long horizontal wells in carbonate formations.

Observing the impingement pressure evolution can help understand the dissolution mechanism during this process. Initially, at the desired jetting velocity of 150 ft/sec and with the current design, the impingement pressure nears 40psi initially at the core of the impingement surface. This extra pressure could push acid inside the pores on the rock's surface and initiate wormholes. Looking at Figure 5.3, which represents a smoothed curve of the evolution of the impingement pressure with time, we observe that the pressure initially decreases very slowly during the dissolution, indicating an initial quasi-continuous cavity growth while initiating wormholes. This effect would potentially lead to the cavity outgrowing the wormholes, as no other pressure is applied to system to sustain the wormhole propagation. Later, the cavity growth considerably

slows down as the cavity becomes of similar magnitude as the original fluid volume (between the two concentric cylinders). With this setup considered for longer times, the acid erosion will be spread out across the entire exposed rock surface, regardless of the (impingement) pressure, and a compact dissolution would be observed on all exposed rock surfaces. It will therefore be expected to observe a considerable increase in the entire wellbore diameter by the end of the stimulation.

5.5 FURTHER STUDIES

The model could be improved in several ways. For example, coupling the turbulent impinging flow model with a different acidizing model, to account for the rock's heterogeneity, would enable a better study of the wormhole initiation, competition and branching with a random distribution of porosity and permeability. Further refinement could also be achieved with some modifications in the initial model assumptions to investigate their impact on the simulation outcome.

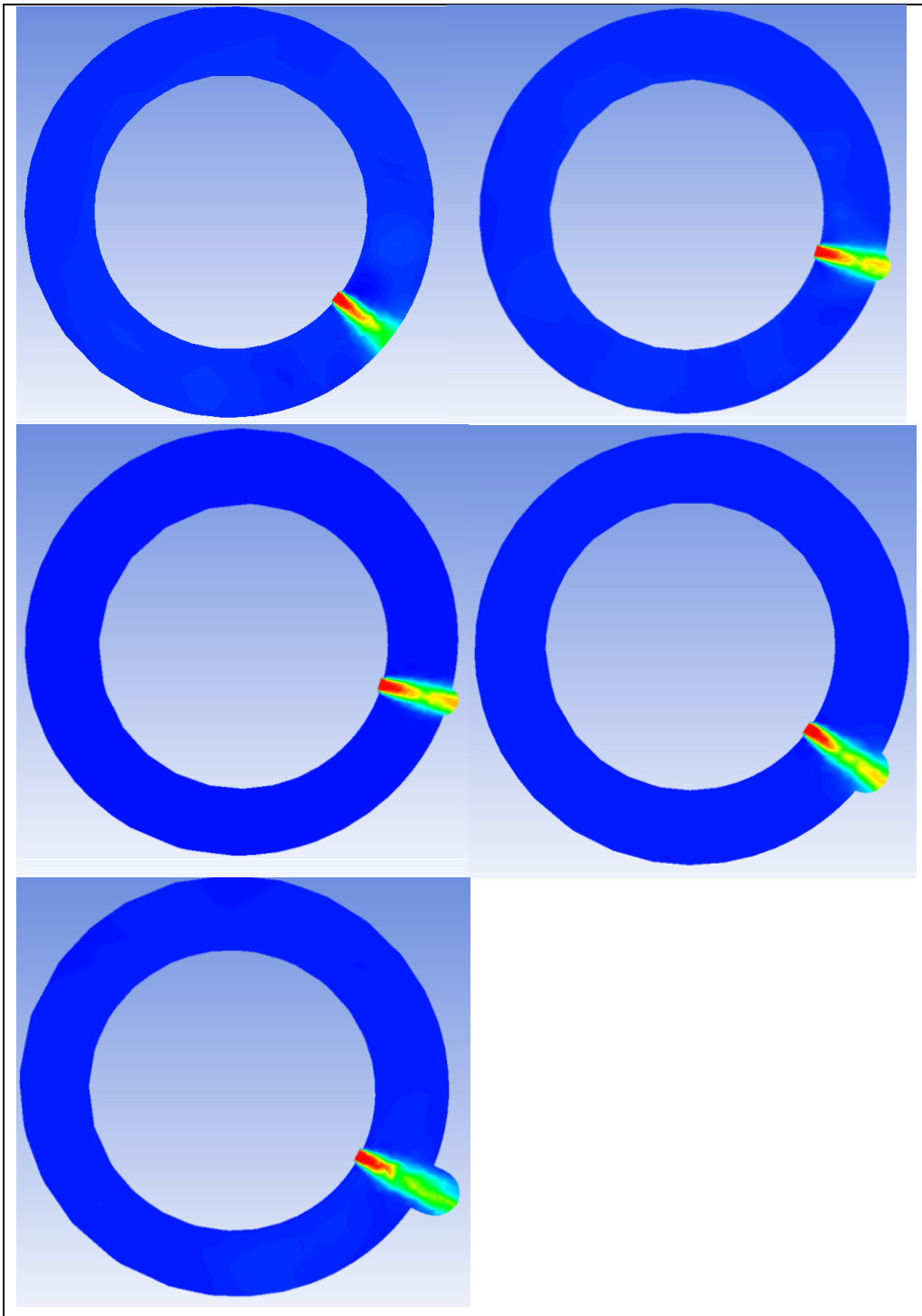

Figure 5.2: Evolution of dissolution during large scale jetting simulation

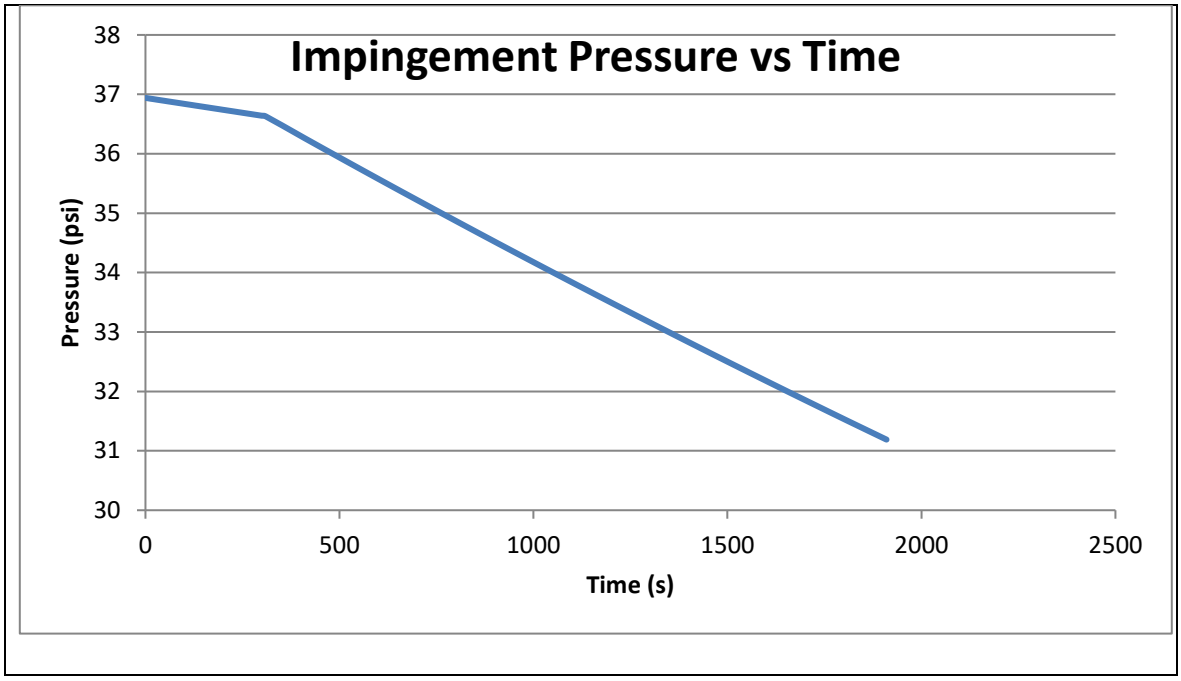

Figure 5.3: Smoothed Impingement Pressure vs Time during simulation of large-scale jetting experiment

CHAPTER VI

SUMMARY AND CONCLUSIONS

Acid jetting, is a process where turbulent impinging jets of hydrochloric acid encounter limestone carbonate formations under controlled pressure. This process is proving to be a positive stimulation method for those formations. A computational fluid dynamics model was developed and presented to provide a theoretical understanding of the process and improve the predictability of acid jetting from the fundamental of transport phenomena. The model was used to replicate and predict the outcome of acid jetting in an experimental setting. The following conclusions were reached:

- Acid jetting is a transient process, which leads to an initial turbulence-induced dissolution structure regardless of the flux through the rock. The bulb-shaped structure is a result of the initial dissolution at the impingement location followed by the wall jet erosion.
- The velocity decays as the standoff distance from the jet nozzle increases, in a self-similar manner. This observation has two implications. Firstly, cavity axial depth would be larger for larger jetting velocity for similar jetting times. Secondly a decreasing cavity growth is expected and observed in the axial direction past the cavity initial creation phase in the zone of flow establishment.

- The simulated results follow similar trends as the experimental results, where higher volumes of acid are consumed at low fluxes and faster stimulation is achieved at high fluxes.
- The model consistently slightly overestimates the dissolution at low fluxes, possibly due to the wormhole size constraints and generic definition of the porous medium.
- The model consistently underestimates the dissolution at high fluxes, as it only account for the propagation of one straight wormhole and not the branched wormholes observed experimentally. The model also does not account for the end effects observed experimentally.
- The simulation allows to study the effect of acid jetting for longer jetting time beyond the experimental limitations
- The jet effect increases the wormhole tip velocity, that increase gets smaller as the standoff distance increases during acid jetting.
- The model correctly predicts that the stronger effect of the jet appears to be localized in the near-field and decreases as the standoff distance is increased.
- Preliminary results of the large-scale experimental acid jetting simulations indicate that acid jetting has positive acid placement capabilities, a highly sought-after property for the acid stimulation of long horizontal wells in carbonate formations.

REFERENCES

Al-Harthy, S., Bustos, O.A., Samuel, M. et al. 2009. Options for High-Temperature Well Stimulation. *Oilfield Review,* **20** (4):52-62

Ashforth-Frost, S., and Jambunathan, K. 1996. Effect of Nozzle Geometry and Semi-Confinement on the Potential Core of a Turbulent Axisymmetric Free Jet, *Int. Com. Heat Mass Transf.*, **23**: 155–162

Ashforth-Frost, S., Jambunathan, K., and Whitney, C. F. 1997. Velocity and Turbulence Characteristics of a Semi-Confined Orthogonally Impinging Slot Jet, *Exp. Therm. Fluid Sci.*, **14**: 60–67

Ashkanani, F., Sharma Shankar, S., Moudi Fahad, A. et al. 2012. First Successful Rigless Acid Tunneling Job in Mauddud Carbonate Reservoir in Raudhatain Field, North Kuwait. Paper SPE-151564-MS presented at the SPE International Symposium and Exhibition on Formation Damage Control, 15-17 February, Lafayette, Louisiana, USA. https://doi.org/10.2118/151564-MS

Bardina, J., Ferziger, J. H., and Reynolds, W. C. 1980. Improved Subgrid Scale Models for Large Eddy Simulation, AIAA Paper no. 80-1357, 1–10

Beaubert, F., and Viazzo, S. 2003. Large Eddy Simulations of Plane Turbulent Impinging Jets at Moderate Reynolds Numbers, *Int. J. Heat Fluid Flow* **24**: 512–519

Beckham, R.E., Schuchart, C.E., and Buecler, S.R. 2015. Impact of Acid Jetting on Carbonate Stimulation. Presented at the International Petroleum Technology Conference held in Doha, Qatar, 6-9 December.

Belostrino, E., 2016. Experimental Study of Multi-Stage Acid Jetting in Carbonate Rocks. Texas A&M University, Masters of Science Thesis

Buijse, M.A. and Glasbergen, G. 2005. A semiempirical Model to Calculate Wormhole Growth in Carbonate Acidizing. Paper SPE 96892 presented at the Annual Technical Conference and Exhibition, Dallas, Texas, 9-12 October

Chung, Y. M., and Luo, K. H. 2002. Unsteady Heat Transfer Analysis of an Impinging Jet, *J. Heat Transf.*, **124**: 1039–1048

Cooper, D.; Jackson, D.C.; Launder, B.E.; Liao, G.X. 1993. Impinging jet studies for turbulence model assessment-I. Flow-field experiments. *Int. J. Heat Mass Transf.* **36:** 2675–2684

Cushman-Roisin, B. 2013. Turbulent Jets. Environmental Transport and Fate Class Notes. Thayer School of Engineering. Darmouth College

Cziesla, T., Biswas, G., Chattopadhyay, H., and Mitra, N. K. 2001. Large-Eddy Simulation of Flow and Heat Transfer in an Impinging Slot Jet, *Int. J. Heat Fluid Flow*, **22:** 500–508

Daccord, G., Touboul, E., and Lenormand, R.1989. Carbonate Acidizing: Toward a Quantitative Model of the Wormholing Phenomenon. *SPE Prod. Eng.* **4**(1):63-68

De Langhe, C., Bigda, J., Lodefier, K., and Dick, E. 2008. One-Equation RG Hybrid RANS/LES Computation of a Turbulent Impinging Jet, *J. Turbul.*, **9 (**16):1–19

de Lemos, M.J.S. 2006. *Turbulence in Porous Media Modeling and Applications*, first edition. San Diego, California: Elsevier

de Lemos, M. J. S. 2012. *Turbulent Impinging Jets into Porous Materials*, Springer Briefs in Computational Mechanics, DOI: 10.1007/978-3-642-28276-8_4

Deen, W.M. 2012. Transport in Turbulent Flow. In *Analysis of Transport Phenomena*, second edition Chapt. 13: 491—524. New York, New York: Oxford University Press.

Dewan A., Dutta, R., and Srinivasan, B. 2012. Recent Trends in Computation of Turbulent Jet Impingement Heat Transfer, *Heat Transf. Eng.*, **33**(4–5):447–460. DOI: 10.1080/01457632.2012.614154

Eckert, E.R.G., Sakamoto, H., and Simon, T.W. 2001. The Heat /Mass Transfer Analogy Factor, Nu/Sh, for Boundary Layers on Turbine Blade Profiles. *Int. J. Heat Mass Transf.*, **44**: 1223-1233

Fredd, C.N. 2000. Dynamic Model of Wormhole Formation Demonstrates Conditions for Effective Skin Reduction During Carbonate Matrix Acidizing. Paper SPE 59537 presented at the SPE Permian Basin Oil and Gas Recovery Conference, Midland, Texas, 21-23 March

Fredd and Fogler, 1999. Optimum Conditions for Wormhole Formation in Carbonate Porous Media: Influence of Transport and Reaction. *SPE J.*, **4** (3): 196-205

Frick, T., Kurmayr, M., and Economides, M.J. 1994. An Improved Modeling of Fractal Patterns in Matrix Acidizing and Their Impact on Well Performance. *SPE Prod. Op.*, **9** (1):61-68

Furui, K., Burton, R., Burhead, D.et al. 2012. A Comprehensive Model of High-Rate Matrix-Acid Stimulation for Long Horizontal Wells in Carbonate Reservoirs: Part I—Scaling Up Core-Level Acid Wormholing to Field Treatments. *SPE J.*, **17**(1): 271-279

Gardon, R., and Akfirat, J. C. 1965. The Role of Turbulence in Determining the Heat-Transfer Characteristics of Impinging Jets, *Int. J. Heat Mass* **8**: 1261–1272

Gdanski, R. 1999. A Fundamentally New Model of Acid Wormholing in Carbonates. Paper SPE 54719, presented at the SPE European Formation Damage Conference, The Hague, Netherlands 31 May-1 June.

Germano, M., Piomelli, U., Moin, P., and Cabot, W. H. 1991. A Dynamic Subgrid-Scale Eddy Viscosity Model, *Phys. Fluids A*, **3**(7): 1760–1765

Golfier, F., Zarcone, C., Bazin, B. et al. 2002. On the Ability of a Darcy-Scale Method Model to Capture Wormhole Formation During the Dissolution of a Porous Medium. *J. Fluid Mech*., 457, 213.

Goldstein, R. J., and Timmers, J. F. 1982. Visualization of Heat Transfer from Arrays of Impinging Jets, *Int. J. Heat Mass Transf.*, **25**: 1857–1868.

Hadziabdic, M., and Hanjalic, K. 2008. Vortical Structures and Heat Transfer in a Round Impinging Jet, *J. Fluid Mech.*, **596**: 221–260

Hallqvist, T. 2006. Large-eddy simulation of impinging jets with heat transfer, PhD Thesis, Royal Institute of Technology, Department of Mechanics, Sweden

Hanjalic, K. and Launder, B. 2011. *Modelling Turbulence in Engineering and the Environment Second-Moment Routes to Closure*. Cambridge University Press.

Hansen, J.H., and Neverdeen, N. 2002. Controlled Acid Jet (CAJ) Technique for Effective Single Operation Stimulation of 14,000+ ft Long Reservoir Sections. Paper SPE-78318-MS presented at the European Petroleum Conference, 29-31 October, Aberdeen, United Kingdom. https://doi.org/10.2118/78318-MS

Hattori, H., and Nagano, Y. 2004. Direct Numerical Simulation of Turbulent Heat Transfer in Plane Impinging Jet, *Int. J. Heat Fluid Flow*, **25**: 749–758

Hoefner, M.L. and Fogler, H.S. 1988. Pore Evolution and Channel Formation During Flow and Reaction in Porous Media. *AIChE J*. **34** (1): 45-54.

Holland, C.C. 2014. Experimental High Velocity Aid Jetting in Limestone Carbonates. *Master of Science*. Texas A&M University, College Station, Texas

Huang, T., Hill, A.D., and Schechter, R.S.1997. Reaction Rate and Fluid Loss: The Keys to Wormhole Initiation and Propagation in Carbonate Acidizing. Paper SPE 37312 presented at the International Symposium on Oilfield Chemistry, Houston, Texas, 18-21 February.

Huber, A. M., and Viskanta, R. 1994. Effect of Jet–Jet Spacing on Convective Heat Transfer to Confined, Impinging Arrays of Axisymmetric Air Jets, *Int. J. Heat Mass Transf.* **37**: 2859–2869

Hung, K.M., Hill, A.D., and Sepehrnoori, K. 1989. A Mechanistic Model of Wormhole Growth in Carbonate Matrix Acidizing and Acid Fracturing. *JPT* **41** (1):59-66.

Icardi, M., Gavi, E., Marchisio, et al. 2011. Validation of LES Predictions for Turbulent Flow in a Confined Impinging Jet Reactor. *Appl. Mathem. Model.* **35**(4): 1591-1602 https://doi.org/10.1016/j.apm.2010.09.035

Jambunathan, K., Lai, E., Moss, M.A. and Button, B.L. 1992. A review of heat transfer data for single circular jet impingement. *Int. J. Heat Fluid Flow* **13**: 106–115.

Johnson, A., Eslinger, D., and Larsen, H.1998. An Abrasive Jetting Scale Removal System. Paper SPE-46026-MS presented at the SPE/ICoTA Coiled Tubing Roundtable, 15-16 March, Houston, Texas. https://doi.org/10.2118/46026-MS.

Kalia, N. and Balakotaiah, V. 2007. Modeling and Analysis of Wormhole Formation in Reactive Dissolution of Carbonate Rocks. *Chem. Eng. Sci.* **62** (4):919-928.

Kendouch A.A. 1998. Theory of stagnation heat and mass transfer to fluid jets impinging normally on solid surfaces. *Chem. Eng. Process.* **37:** 223-228

Kim S.E. 2004. Large eddy simulation using unstructured meshes and dynamic sub grid-scale turbulence models. Technical Report AIAA-2004-2548, American Institute of Aeronautics and Astronautics, 34th Fluid Dynamics Conference and Exhibit, June

Kofoed, S.S., Marketz, F., Krabbenhoeft, J. 2012. Slotted Liner for Continuously Acid Jetting Stimulation. Paper SPE -151405-MS presented at the IADC/SPE Drilling Conference and Exhibition, 6-8 March, San Diego, California, USA. https://doi.org/10.2118/151405-MS

Kubacki, S., and Dick, E. 2009. Convective Heat Transfer Prediction for an Axisymmetric Jet Impinging Onto a Flat Plate with an Improved k–ω Model, *J. Computational Applied Math.*, **234**: 2327–2335

Knowles, K., and Myszko, M. 1998. Turbulence Measurements in Radial Wall-Jets, *Experimental Thermal and Fluid Science*, **17:** 71–78

Le Song, G., and Prud'homme, M. 2007. Prediction of Coherent Vortices in an Impinging Jet with Unsteady Averaging and a Simple Turbulence Model, *Int. J. Heat Fluid Flow*, **28**: 1125–1135

Lee, J.H.W. and Chu, V.H. 2003. *Turbulent Jets and Plumes a Lagrangian Approach*. Norwell, Massachusetts: Kluwer Academic Publishing.

Liu,T., and Sullivan, J. P. 1996. Heat Transfer and Flow Structure in an Excited Circular Impinging Jet, *Int. J. Heat Mass Transf.*, **39**: 3695–3706.

Liu, X., Ormond, A. et al., 1997. A Geochemical Reaction-Transport Simulator for Matrix Acidizing Analysis and Design. *J. Petro. Sci. Eng.*, **17**(1-2): 181-196.

Livescu, S. and Craig, S. 2017. New Insights on Coiled Tubing Acid Tunneling Stimulation in Carbonate Reservoirs. SPE Paper 188294 presented at the Abu Dhabi International Petroleum Exhibition and Conference held in Abu Dhabi, UAE, 13-16 November.

Lockheed Martin. 1968. *Los Angeles*, Sunset-Lane, Menlo Park, California

Lodato, G., Vervisch, L., and Domingo, P. 2009. A Compressible Wall-Adapting Similarity Mixed Model for Large-Eddy Simulation of Impinging Round Jet, *Phys. Fluids*, **21:** 1–21

Lytle, D., and Webb, B. W. 1994 Air Jet Impingement Heat Transfer at Low Nozzle-Plate Spacings, *Int. J. Heat Mass Transf.*, **37**:1687–1697

Maheshwari, P., Ratnakar, R. R., Kalia, N., and Balakotaiah, V. 2012. 3-D Simulation and Analysis of Reactive Dissolution and Wormhole Formation in Carbonate Rocks. Chemical Engineering Science.

Marin, C., Nunez, M. S., Duque, E.D. et al. 2013. Enhanced Jetting Tool Integrated with Sand/Well Vacuuming Technology Optimizes Cleaning and Stimulation for Heavy-Oil Wells. Paper SPE-163923-MS presented at the SPE/ICoTA Coiled Tubing & Well Intervention Conference & Exhibition, 26-27 March, The Woodlands, Texas, USA. https://doi.org/10.2118/163923-MS

Martin, H. 1997. Heat and mass transfer between impinging gas jets and solid surfaces. *Adv. Heat Transf.* **13**: 1–60.

McDuff, D., Jackson, S., Shuchart, C., et al., 2010. Understanding Wormholes in Carbonates: Unprecedented Experimental Scale and 3D Visualization. *JPT* **64** (10):78-81.

Mogensen, K., and Hansen, J. H. 2007. "A Dynamic Model for High-Rate Acid Stimulation of Very Long Horizontal Wells." Paper SPE 110135 presented at the Annual Technical Conference and Exhibition, 11-14 November, Anaheim, California, U.S.A.

Nagendra S.V.H., Bhagavanulu D.V.S., and Nanda P. 2017. Computational Study of Three-Dimensional Wall Jet on Concave Surface. *Fluid Mech. and Fluid Power – Contemporary Research. Lecture Notes in Mechanical Engineering* 529-538. Springer, New Delhi. https://doi.org/10.1007/978-81-322-2743-4_51

Nasr-El-Din, H.A., Al-Otaibi, M.B., and Altameimi, Y.M. 2005. Wellbore Cleanup by Water Jetting and Enzyme Treatment in MRC Wells: Case Histories. Paper SPE-97427-MS presented at the SPE/IADC Middle East Drilling Technology

Conference and Exhibition, 12-14 September, Dubai, United Arab Emirates http://dx.doi.org/10.2118/97427-MS.

Ndonhong, V., Belostrino, E., Zhu, D. et al. 2017. Acid Jetting in Carbonate Rocks: An Experimental Study. Paper SPE-180113-PA *SPE Prod. & Op.* July. https://doi.org/10.2118/180113-PA.

Nicoud, F., and Ducros, F. 1999. Subgrid-Scale Modeling Based on the Square of the Velocity Gradient Tensor, *Flow Turbulence and Combustion*, **62:** 183–200

Nishino, K., Samada, M., Kasuya, K. and Torii, K. 1996. Turbulence statistics in the stagnation region of an axisymmetric impinging jet flow, *Int. J. Heat Fluid Flow*, **17:** 193–201

Obot, N. T. Majumdar, A. S., and Douglas, W. J. M. 1982. Effect of Semi-Confinement on Impingement Heat Transfer, *Proc. 7th Int. Heat Transf. Conf.*, **3:** 395–400

O'Donovan, T. S. 2005. *Fluid Flow and Heat Transfer of an Impinging Air Jet, Ph.D. thesis*, Trinity College, Department of Mechanical and Manufacturing Engineering, Dublin

Olsson, M., and Fuchs, L. 1998. Large Eddy Simulations of a Forced Semiconfined Circular Impinging Jet, *Physics of Fluids*, **10:** 476–486

Panga, M., Ziauddin, M., Gandikota, R., and Balakotaiah, V. 2004. A New Model for Predicting Wormhole Structure and Formation in Acid Stimulation of Carbonates. Paper SPE 86517 presented at the SPE International Symposium and Exhibition on Formation Damage Control, Lafayette, Louisiana, 18-20 February.

Pekarek, J. L., Lowe, D. K. and Huitt, J. L. 1963. Hydraulic Jetting – Some Theoretical and Experimental Results. Paper SPE 421.

Polat, S., Huang, B., Majumdar, A. S., and Douglas, W. J. M. 1989. Numerical Flow and Heat Transfer Under Impinging Jets: A Review, *Annual Review of Heat Transfer*, **2:** 157–197

Pope, S.B. 2000. *Turbulent Flows*. Cambridge University Press.

Popiel, C. O., and Trass O. 1991. Visualization of a Free and Impinging Round Jet, *Exp. Therm. Fluid Sci.*, **4**: 253–264

Rajes, S., Shuchart, C.E., and Grubert, M.A. 2014. Advanced Completion and Stimulation Design Model for Maximum Reservoir Contact Wells. Paper SPE-171800-MS presented at the Abu Dhabi International Petroleum Exhibition and Conference, 10-13 November, Abu Dhabi, UAE. https://doi.org/10.2118/171800-MS

Rhea, S., Bini, M., Fairweather, M., and Jones, W. P. 2009. RANS Modeling and LES of a Single-Phase, Impinging Plane Jet, *Computers & Chem. Eng.*, **33**(8): 1344–1353

Ridner, D., Frick, T., Zhu, D. et al. 2018. Influence of Transport Conditions on Optimal Injection Rate for Acid Jetting in Carbonate Reservoirs. Paper SPE-189546-MS Presented at the SPE International Conference and Exhibition on Formation Damage Control, 7-9 February, Lafayette, Louisiana, USA. https://doi.org/10.2118/189546-MS

Ries, F., Li, Y., Riβmann, M., et al. 2018. "Database of Near-Wall Turbulent Flow Properties of a Jet Impinging on a Solid Surface under Different Inclination Angles" *Fluids*, **3**(1): 5; doi:10.3390/fluids3010005

Ritchie, B., Abbasy, I., Pitts, M.J., et al. 2008. Challenges in Completing Long Horizontal Wells Selectively. Paper SPE -116541-MS presented at the SPE Asia Pacific Oil and Gas Conference and Exhibition, 20-22 October, Perth, Australia. https://doi.org/10.2118/116541-MS

Robertson, P.R. 2005.The Design a Validation of an Impinging Jet Test Facility. Master of Science Thesis. Mechanical Engineering Department, Baylor University.

Sagaut, P. 2001. *Large Eddy Simulation for Incompressible Flows an Introduction*. Scientific Computation, Springer.

Satake, S., and Kunugi, T. 1998. Direct Numerical Simulation of an Impinging Jet into Parallel Disks, *Int. J. of Num. Methods Heat Fluid Flow*, **8:** 768–780

Schechter, R.S. and Gidley, J. L.1969. The Change in Pore Size Distribution from Surface Reactions in Porous Media. *AIChE J.*, **15**(3): 339-350.

Schlichting, H. 1979. *Boundary Layer Theory*, 7th edition, McGraw-Hill, New York.

Shadlesky, P. S. 1983. Stagnation Point Heat Transfer for Jet Impingement to a Plane Surface, *AIAA J.*, **21:** 1214–1215

Siddiqui, M. A. A., Sharma, S. S., Al-Ajmi, M. F. et al. 2013. "Enhancement of Oil Production from an Old Well in Thin Carbonate Reservoir through Acid Tunneling - A Case Study" Paper SPE 164876 presented at the EAGE Annual Conference & Exhibition incorporating SPE Europec, 10-13 June, London, UK

Smagorinsky, J. 1963. General Circulation Experiments with the Primitive Equations. 1. The Basic Experiment, *Monthly Weather Review*, **91:** 99–164

Stanley, R., Portman, L.N., Diaz, J.D. et al. 2010. Global Application of Coiled-Tubing Acid Tunneling Yields Effective Carbonate Stimulation. Paper SPE-135604-MS presented at the SPE Annual Technical Conference and Exhibition, 19-22 September, Florence, Italy. https://doi.org/10.2118/135604-MS

Tata, V. 2016. http://viscosity-hydrochloric-acid.blogspot.com/2016/01/3-acidizing-limestones-dolomite-and.html, Retrieved 04/01/2017

Tawfek, A. A. 1996. Heat Transfer and Pressure Distributions of an Impinging Jet on a Flat Surface, *Heat Mass Transf.* **32:** 49–54

Tsubokura, M., Kobayashi, T., Taniguchi, N., and Jones, W. P. 2003. A Numerical Study on the Eddy Structures of Impinging Jets Excited at the Inlet, *Int. J. Heat Fluid Flow*, **24:** 500–511

Tsujimoto, K., Ishikura, T., Shakouchi, T., and Ando, T. 2009 Direct Numerical Simulation of Active-Controlled Impinging Jets, *J. Fluid Sci. Tech.* 4(2):279–291

Tummers, M.J.; Jacobse, J.; Voorbrood, S.G.J. 2011. Turbulent flow in the near field of a round impinging jet. *Int. J. Heat Mass Transf.* **54**: 4939–4948.

Uddin, N. 2008 *Turbulence Modeling of Complex Flows in CFD, Ph.D. thesis*, Universtat Stuttgart, Institute of Aerospace Thermodynamics, Stuttgart, Germany

Uddin, N.; Neumann, A.O.; Weigand, B. 2013. LES simulations of an impinging jet: On the origin of the second peak in the Nusselt number distribution. *Int. J. Heat Mass Transf.* **57;**356–368.

Viskanta, R. 1993. Heat transfer to impinging isothermal gas and flame jets. *Exp. Therm. Fluid Sci.* **6:** 106–115.

Voke, P. R., and Gao, S. 1998 Numerical Study of Heat Transfer from an Impinging Jet, *Int. J. Heat Mass Transf.*, **41**:671–680

Wang, Y., Hill, A.D. and Schechter, R.S. 1993. The Optimum Injection Rate for Matrix Acidizing of Carbonate Formations. SPE Paper 26578 presented at the SPE Annual Technical Conference and Exhibition, Houston, Texas, 3-6 October.

Wasserman, S. https://www.engineering.com. Choosing the Right Turbulence Model for Your CFD Simulation https://www.engineering.com/DesignSoftware/DesignSoftwareArticles/ArticleID/13743/Choosing-the-Right-Turbulence-Model-for-Your-CFD-Simulation.aspx(accessed 05 January 2017)

Wilke, R. and Sesterhenn, J. 2015. Numerical Simulation of Impinging Jets. In *High Performance Computing in Science and Engineering '14*; Springer: Cham, Switzerland; 275–287.

Wilcox, D. C. 2006. *Turbulence Modeling for CFD*, third edition., DCW Industries, La Canada, California

Okoboji, S., Kasagi, N., and Hirata, M. 1983. Transport Phenomena at the Stagnation Region of a Two-Dimensional Impinging *Jet, Trans. JSME B,* **49**: 1029–1039

Yu, M., Chen, L., Jin, H., and Fan, J. 2005. Large Eddy Simulation of Coherent Structure of Impinging Jet, *J. Therm. Sci.*, **14** (2): 150–155

Zuckerman, N. and Lior, N. 2006. Jet impingement heat transfer: Physics, correlations, and numerical modeling. *Adv. Heat Transf.* **39:** 565–631

APPENDIX A

EXPERIMENTAL RESULTS

Table A.1: Experimental Results Used for Model Validation

Exp. No	Rock Type	Vjet (ft/s)	Initial vi (cm/min)	Core T(°F)	k(md)	ϕ (%)	PV_{bt}	Tjet(min)	Acid consumed (mL)	Core Weight Change (g)	Axial Length Stimulated (in)	Acid PV per inch stimulated axially
1	Indiana Lime stone	107	0	70	5.4	15	12.4	20	828.1	217	**2.1**	5.78
2		107	0.14	70	2.4	14	2.1	20	542.5	142	9.01	0.23
3		107	0.17	70	2.1	14	1.1	16.3	515.0	135	16.0	0.07
4		107	0.21	70	10.7	16	1.3	17.6	669.0	178	16.0	0.08
5		107	0.24	70	10.5	14	7.2	20	1066.0	284	4.6	1.54
6*		107*	0.24*	180*	7*	16*	2.0*	20*	472.4*	247*	7.6	0.26
7		107	0.74	70	6.9	15	1.9	14.4	897.4	212	16.0	0.12
8		107	0.89	70	5	10	1.9	8.1	619.4	155	16.0	0.12
9		107	1.55	70	6.1	14	1.0	5	473.6	124	16.0	0.07
10		150	0.14	70	4.5	15	1.8	20	853.5	225	3.9	0.45
11		150	0.2	70	5.9	14	2.6	20.2	929.3	247	11.5	0.22
12		150	0.79	70	2.1	13	3.3	7.4	1389.8	358	16.0	0.21
13		150	1.53	70	2.9	13	1.6	5.2	708.5	184	16.0	0.10
14		200	0.09	70	2.1	14	4.8	20	1059.6	277	7.6	0.63
15		200	0.09	180	3.2	15	13.1	20	1984.1	527	4.8	2.76
16		200	0.33	70	9.6	16	2.0	10.4	1028.1	274	16.0	0.13
17		200	1.22	70	4.4	14	1.4	5.7	634.5	166	16.0	0.09
18		200	1.65	70	3.8	14	1.3	4.1	591.1	139	16.0	0.08
19	Winter set Lime stone	107	0.11	70	0.7	23	3.0	20.1	1082.3	318	7.4	0.41
20		107	0.11	70	1	23	3.4	20.2	587.9	170	3.8	0.89
21		107	0.38	70	1.2	21	2.7	13			16.0	0.17
22		107	0.48	70	1.5	19	2.4	13.8			16.0	0.15
23		200	0.33	70	0.8	22	2.9	9.6	1913.3	467	12.2	0.23

*Experiment performed using 28 wt.% HC

APPENDIX B

ANSYS FLUENT 15 GENERAL SETTINGS FOR SIMULATIONS

Table B.1: General ANSYS Fluent parameters for simulations

Solver option	3D, double precision
	Transient, pressure-based, absolute velocity formulation
Model	Turbulent flow, large eddy simulation, Smagorinsky-Lilly dynamic model
Material fluid	Water, Hydrochloric Acid (user-defined)
Cell zone conditions	Treat all solid zones as fluid
Boundary conditions:	Jet nozzle tip: velocity inlet, requires initial jet velocity and gauge pressure
	Nozzle walls: non-slip, stationary wall
	Recycle outlet: Outlet vent, pressure outlet
	Bulk fluid: hydrochloric acid at 15 wt.% and 25^{o}C
	Interface fluid/rock surface: outflow, requires flow rate weighting value
Solution methods	SIMPLE algorithm, Bounded second order implicit transient formulation
Solution controls	Under-relaxation factors 0.4 for pressure and 0.6 for momentum
Solution monitors	Residuals for continuity, velocity in x, y and z directions
Calculation	Time step size: 0.1 seconds
	Number of time steps: 0 initially, to help reach a stable initial condition, followed by 1 to observe convergence then 99 more steps to reach the 10 second interval
	Max iteration per tie step: 500

APPENDIX C

SUMMARY OF SIMULATION CASES USED

Table C.1: Summary of Simulation Cases Used

Simulation Number	Jetting velocity (ft/sec)	Flow weighting (%)	Permeability (md)	Porosity (%)	Simulation time (min)
1	107	0.01	5	15	0-60
2		0.1	5	15	0-30
3		0.2	5	15	0-30
4		0.25	5	15	0-30
5		0.75	5	15	0-30
6		1	5	15	0-30
7		1.5	5	15	0-30
8	200	0.01	5	15	0-60
9		0.1	5	15	0-30
10		0.5	5	15	0-30
11		1	5	15	0-30
12		1.5	5	15	0-30
13	50	0.01	5	15	0-60
14	25	0.01	5	15	0-60
15	10	0.01	5	15	0-60
16*	150	0.01	5	15	0-5

*This simulation was using the upscaled experimental geometry

APPENDIX D

ESTIMATION OF FLOW RATE WEIGHTING FRACTION

$$f = \frac{q_{in}}{q_{total}} \approx \frac{v_i * A_{core} * \phi}{v_{jet} * A_{nozzle}} = \frac{v_i * \phi}{v_{jet}} * \left(\frac{d_{core}}{d_{nozzle}}\right)^2$$

For current experimental setup:

$$core\ diameter = 4\ in.$$

$$nozzle\ diameter = 0.0225\ in.$$

For ϕ= 15%, v_i=1 cm/min and v_{jet}=107 ft/sec,

$$\boldsymbol{f \approx 2.43\%}$$

APPENDIX E

ESTIMATION OF PVBT

D_{core}: 4 in (10.16 cm)

L_{core}: 16 in (40.64 cm)

Core bulk volume: 201 in^3 (3295 cm^3)

Calcite grain density: 2.71 g/cm^3

For experiment number 3,

Core dry weight: 7462.9 g

Saturated core weight: 7938.0 g

Axial stimulated length: 16 in

The average porosity is computed as:

$$V_{core} = 3295\ cm^3 \tag{B.1}$$

$$V_{pore} = \frac{M_{saturated} - M_{dry}}{\rho_{brine}} = \frac{(7938 - 7462.9)g}{\frac{1g}{cm^3}} = 475.1\ cm^3 \tag{B.2}$$

$$\phi = \frac{V_{pore}}{V_{core}} \times 100\% = 14.41\% \tag{B.3}$$

After the experiment:

$$Core\ weight\ after\ jetting\ =\ 7802.8\ g \tag{B.4}$$

$$Matrix\ volume\ dissolved = \left(m_{saturated} - m_{post-jetting}\right) * \frac{1-\phi}{\rho_{calcite}} = 42.70\ cm^3 \tag{B.5}$$

$$Acid\ volume\ consumed = \frac{Matrix\ volume\ dissolved}{\mathrm{X}_{14}} = 515\ cm^3 \tag{B.6}$$

$$PVbt = \frac{V_{acid}}{V_{pore}} * \frac{L_{core}}{axial\ stimulated\ length} = 1.084 \tag{B.7}$$

APPENDIX F

ANSYS FLUENT 15 INITIAL SETUP TUTORIAL

1- Open a new ANSYS workbench session

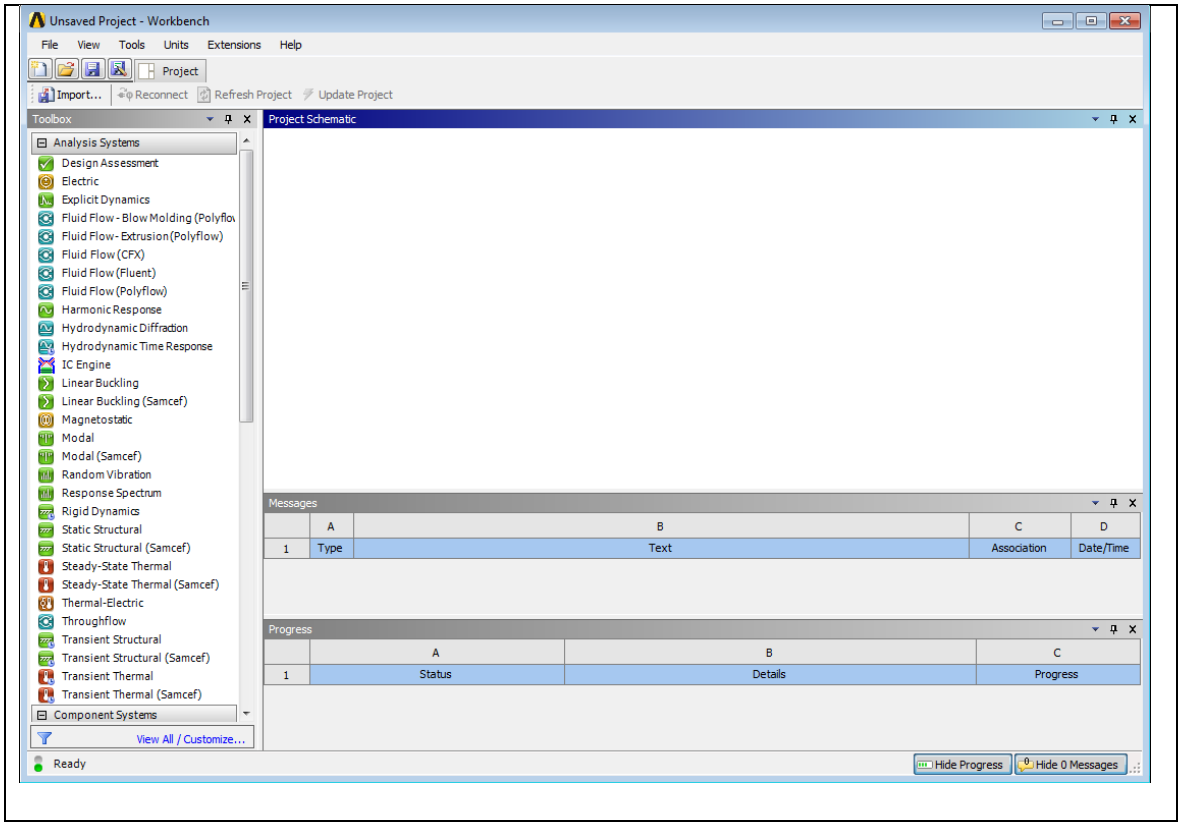

Figure F.1: ANSYS 15 workbench interface

2- Select Fluid Flow (Fluent): Left click on Fluent then drag to the white workbench and release click once red rectangle appears.

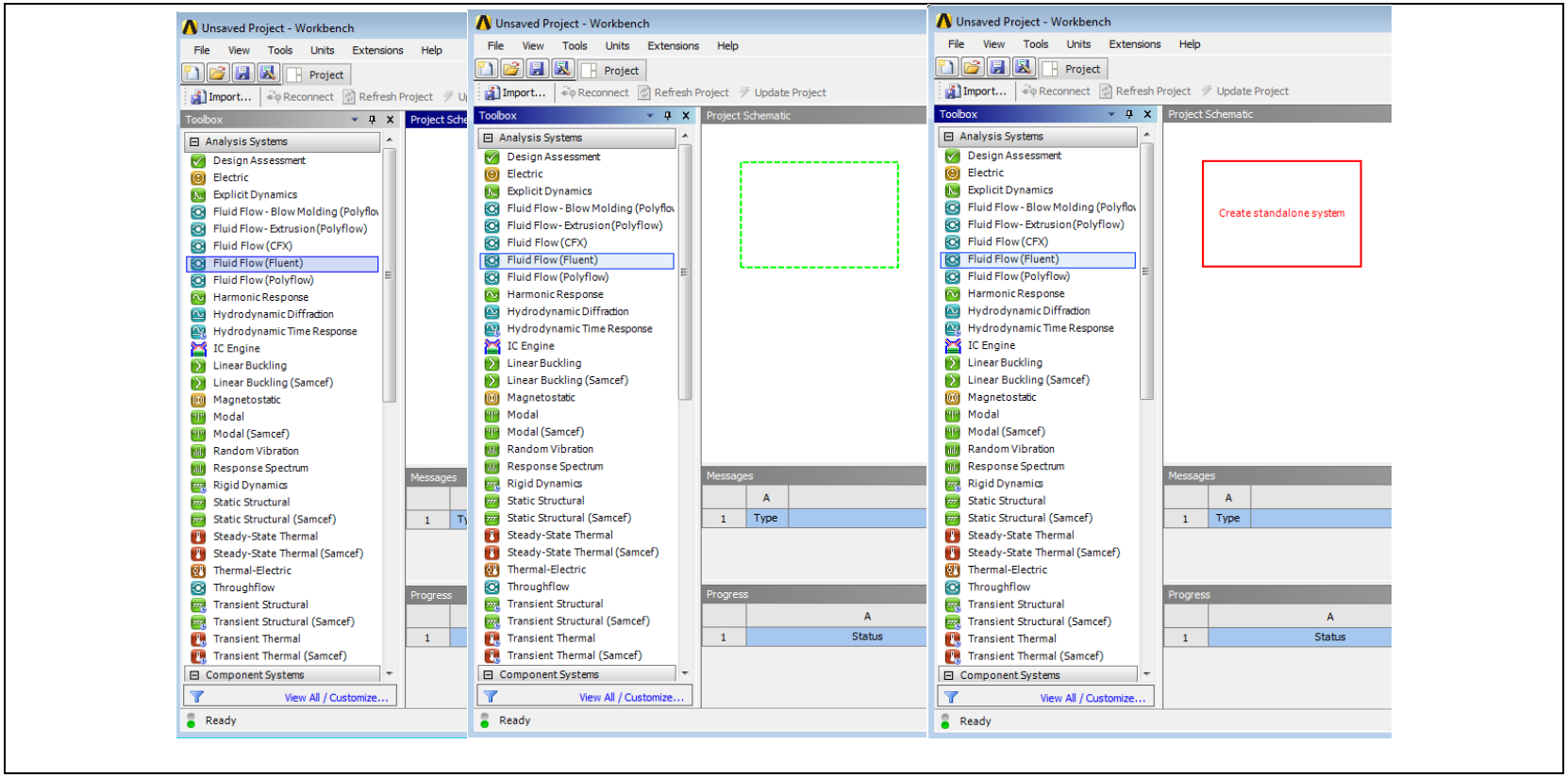

Figure F.2: How to open a new Fluid Flow (Fluent) system in ANSYS 15 Workbench interface

3- Name the new Fluent system

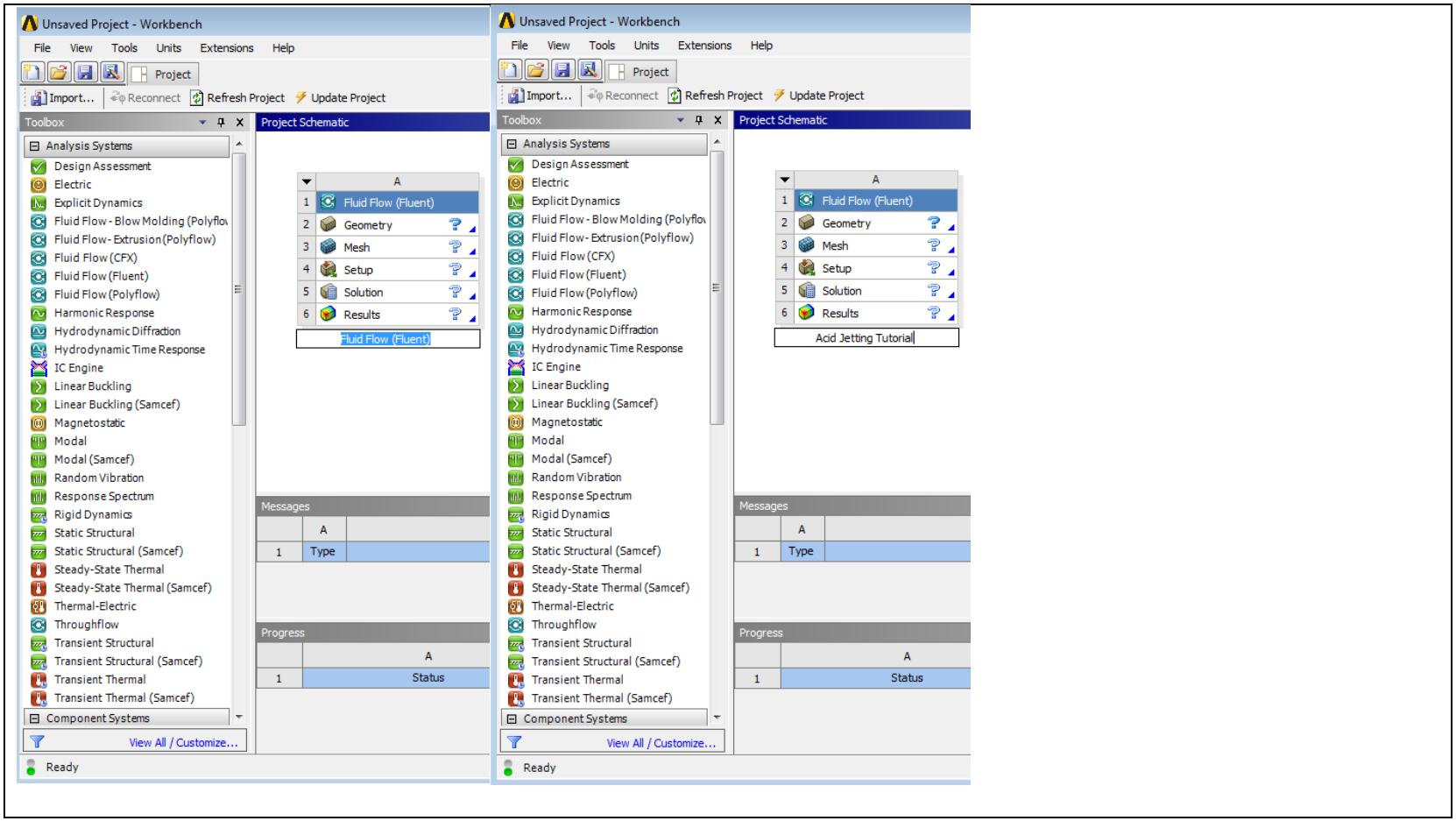

Figure F.3: Naming the new Fluent system

4- Open a Design modeler interface to build a new geometry as indicated from left to right: right click on “Geometry”, then left click on “New Geometry”

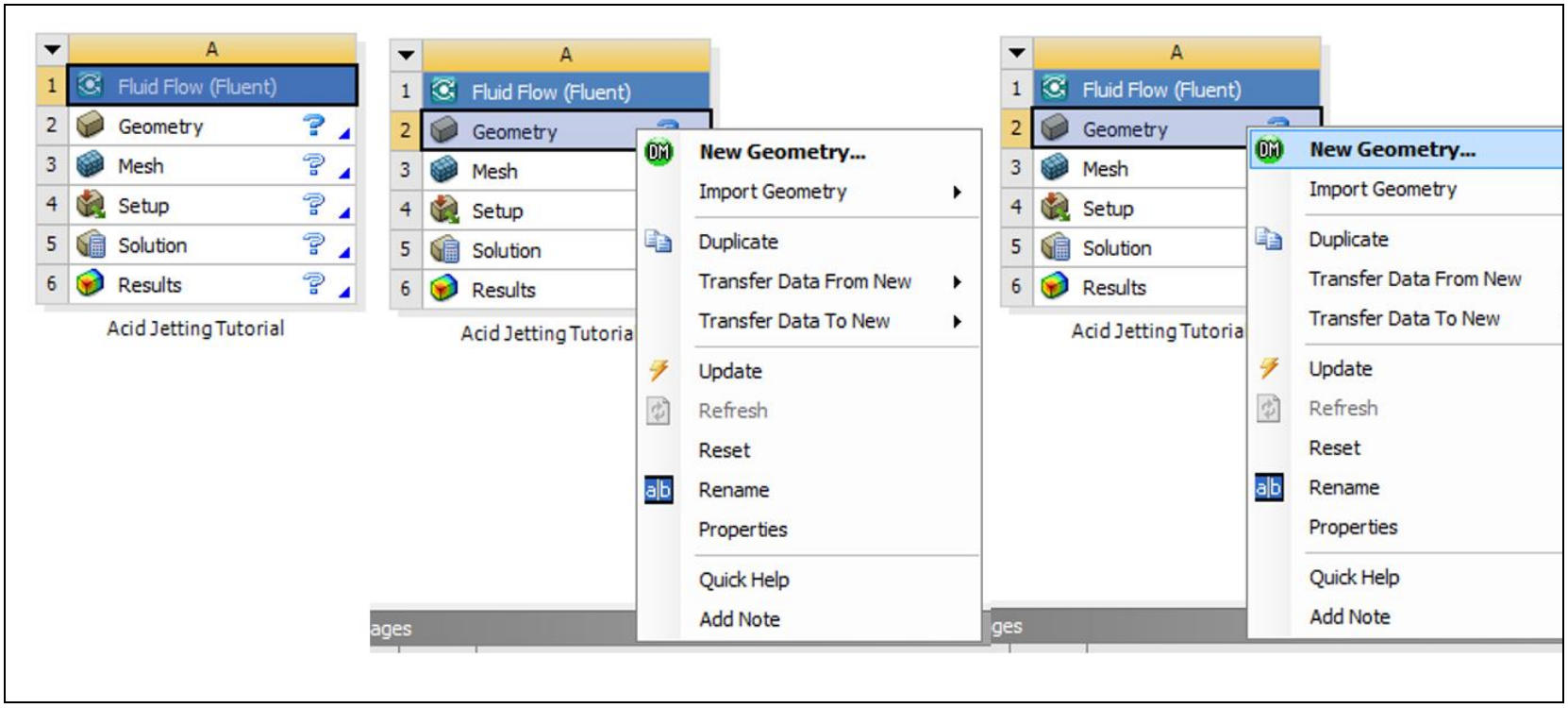

Figure F.4: Opening Design Modeler interface to build a new geometry

5- A new “Design Modeler” window opens

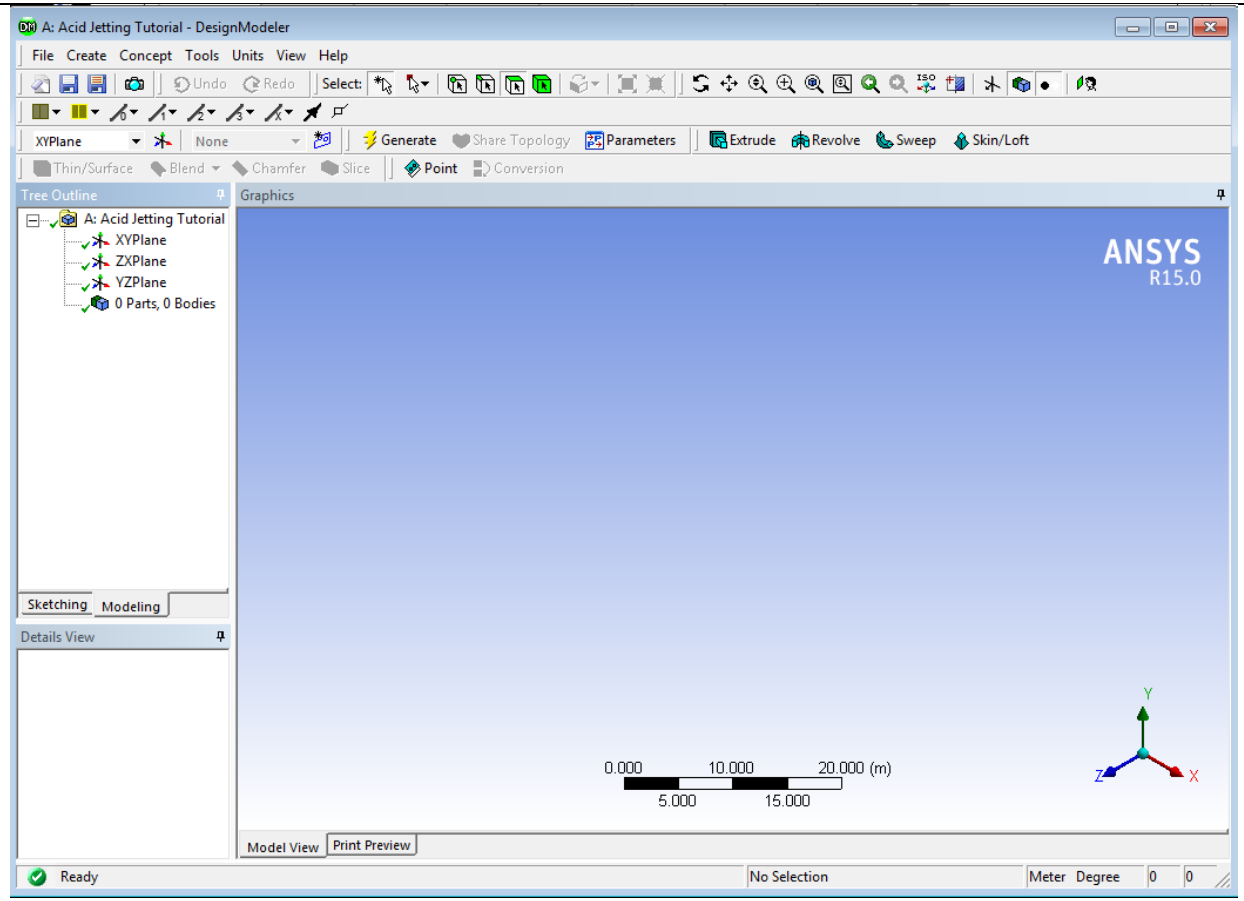

Figure F.5: Design Modeler interface

6- Select the plane to draw the 2D figure: right-click on the “ZX Plane” option then left-click on the “Look at” option.

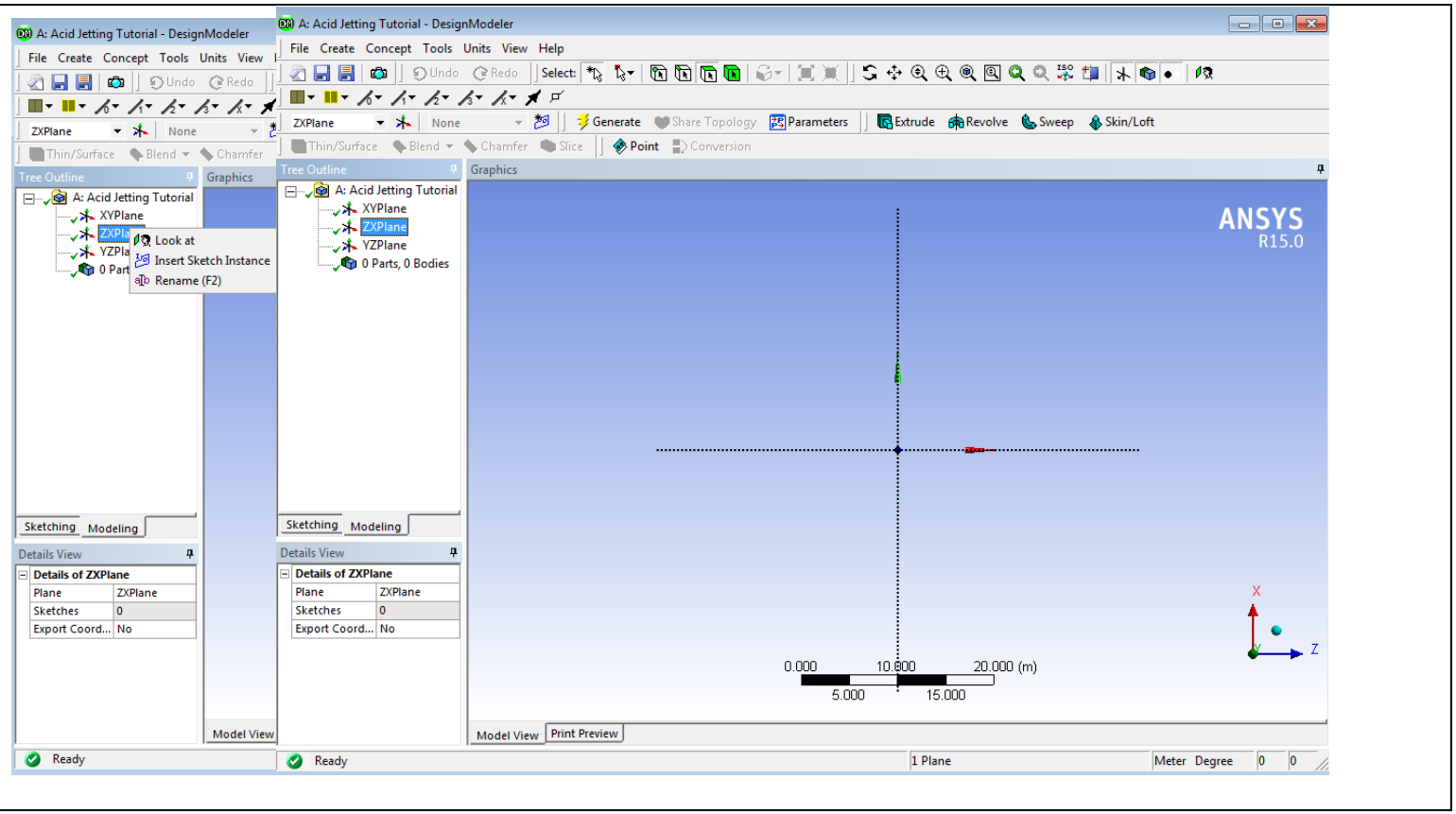

Figure F.6: Select ZX-Plane to draw the 2D Geometry

7- Select the appropriate system of units: left-click on the “Unit” option then left-click “Inch”.

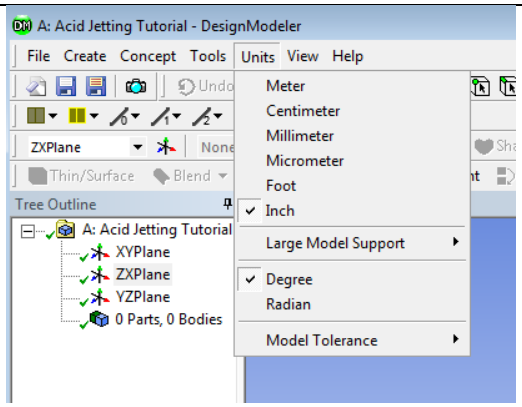

Figure F.7: Select the appropriate system of units

8- Switch to sketch mode by a left-click on “Sketching”, then left-click on “Polyline” from the “Draw” menu.

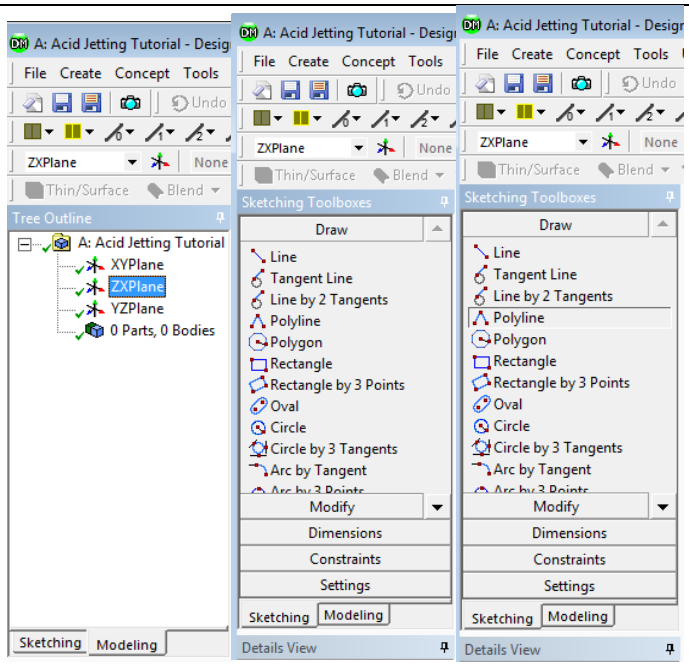

Figure F.8: Select the appropriate parameters to draw a polyline

9- Draw the polyline: a) right-bound horizontal segment from the x-axis, b) downward vertical segment coincident on z-axis, c) horizontal segment on z-axis, followed by upward vertical segment, d) left-bound horizontal segment coincident with x-axis, e) downward vertical segment on x-axis, f) right-click and select “Closed End” to have a coincident initial and final point.

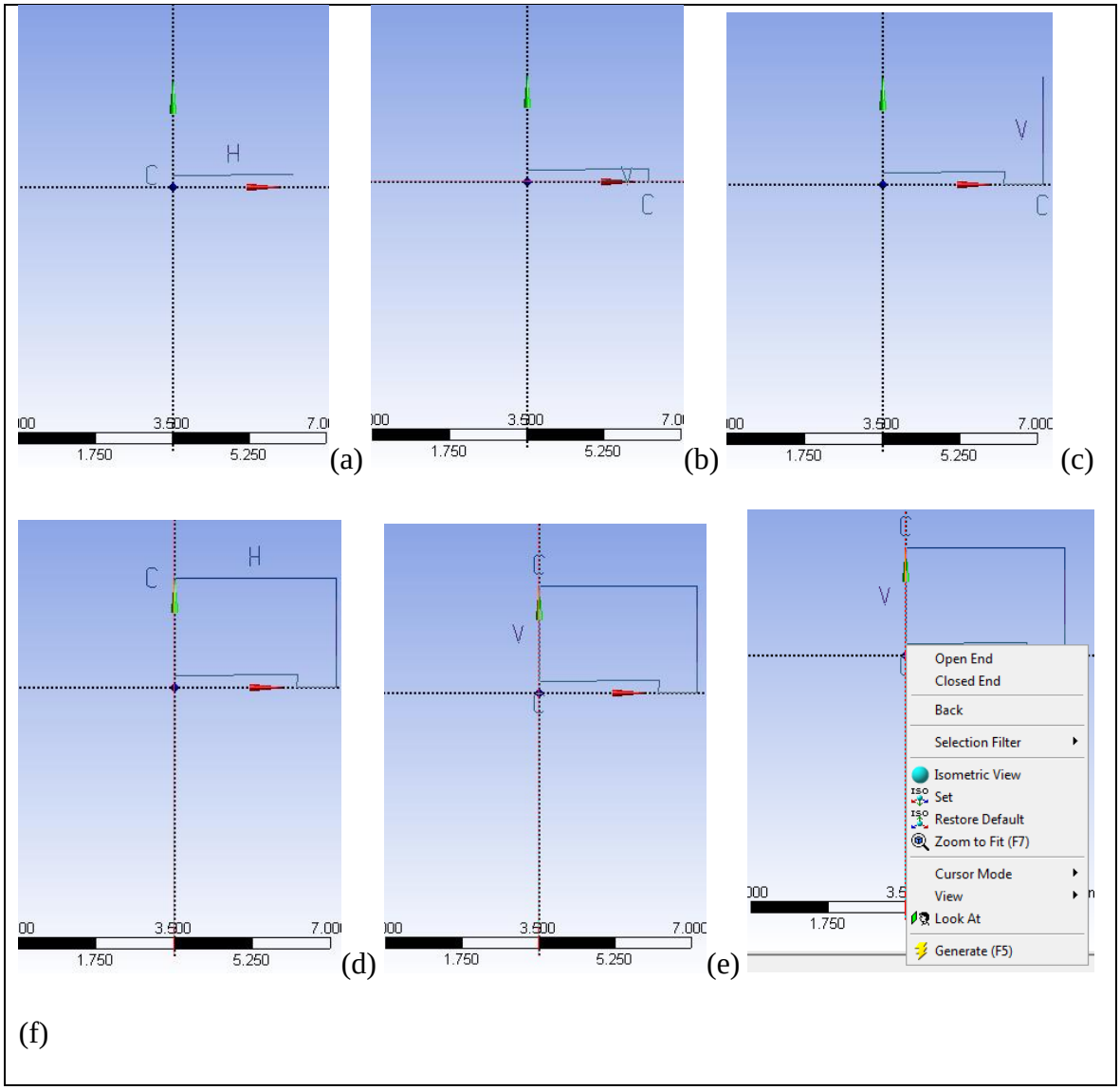

Figure F.9: Drawing the polyline

10- Set the polyline to the right dimensions: with the polyline completed, select “Dimensions” tab to assign dimensions to the plot.

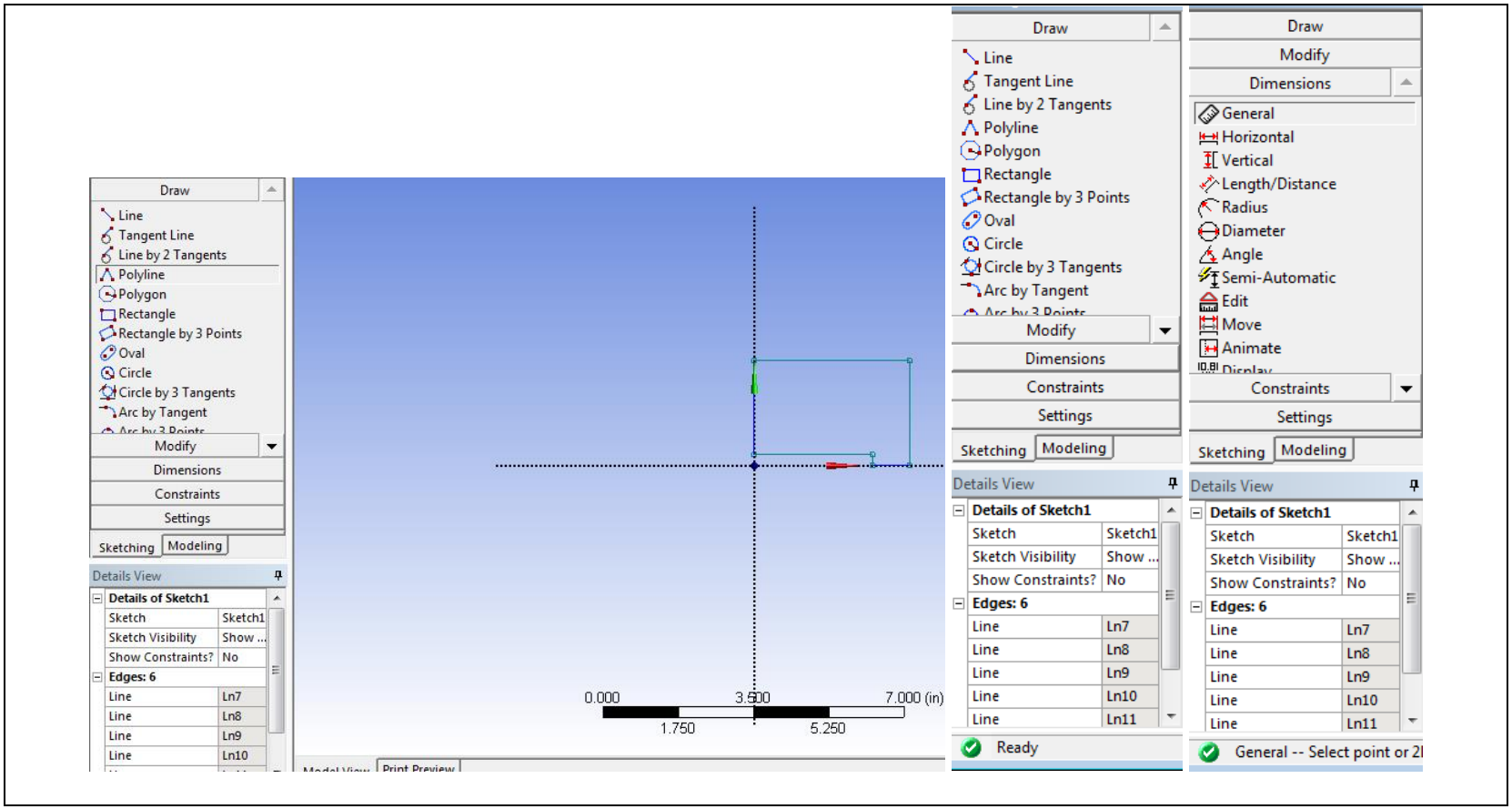

Figure F.10: Go to the “Dimensions” tab to enter the appropriate dimensions

11- Assign dimensions to 2 of the 3 vertical segments, and 2 of the 3 horizontal segments since directions are already prescribed.

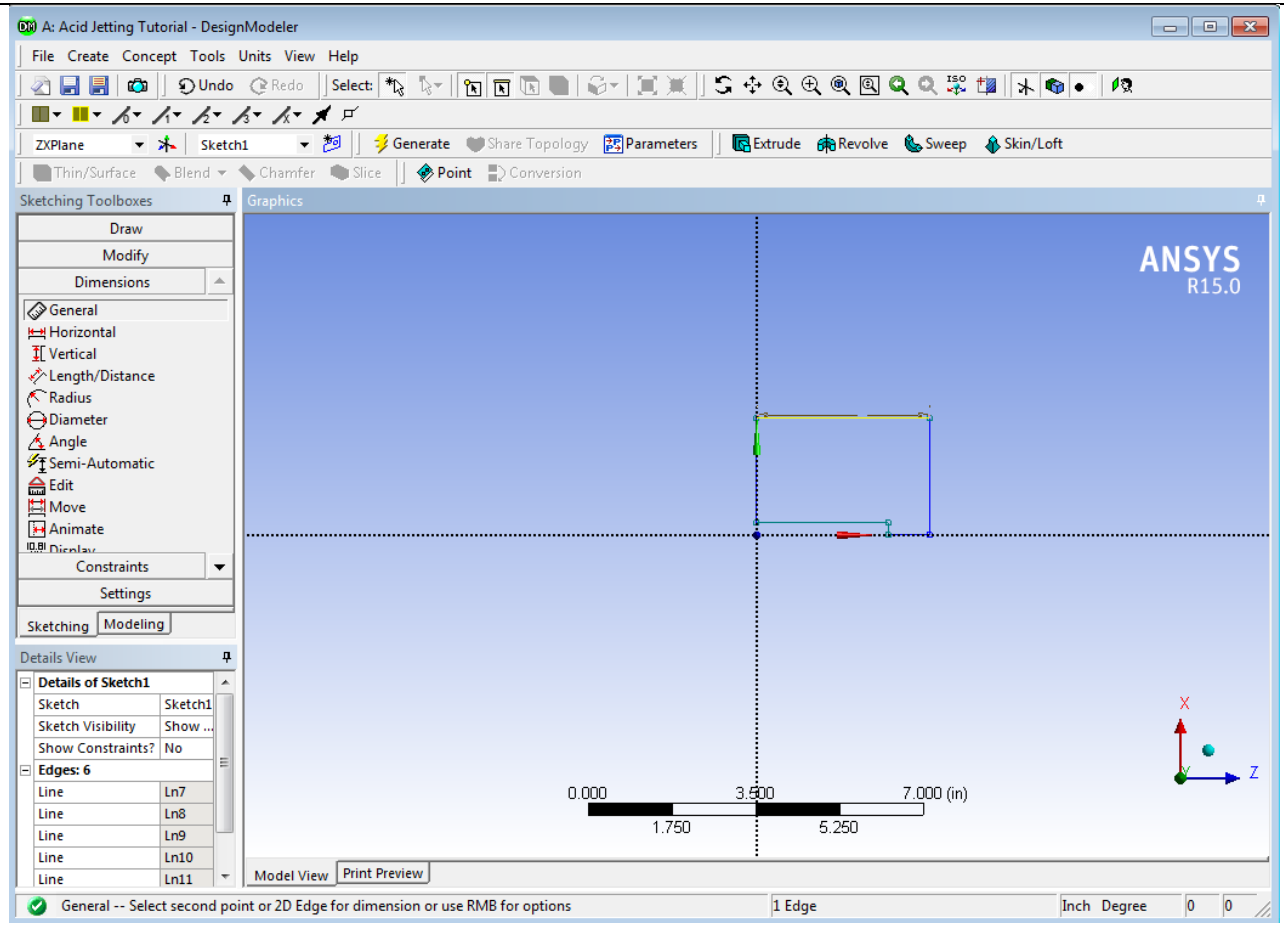

Figure F.11: Assigning dimensions to polyline segments: selecting first segment

Assigning length values to 2 of the 3 horizontal segments, H1 and H2: (a) The current value of H1 is displayed, (b) H1 is indicated on the plot, (c) the new length value is entered, (d) H1 is set and H2 is selected and becomes a yellow line, (e) H2 length is entered, (f) plot is shown with all the horizontal segments constrained.

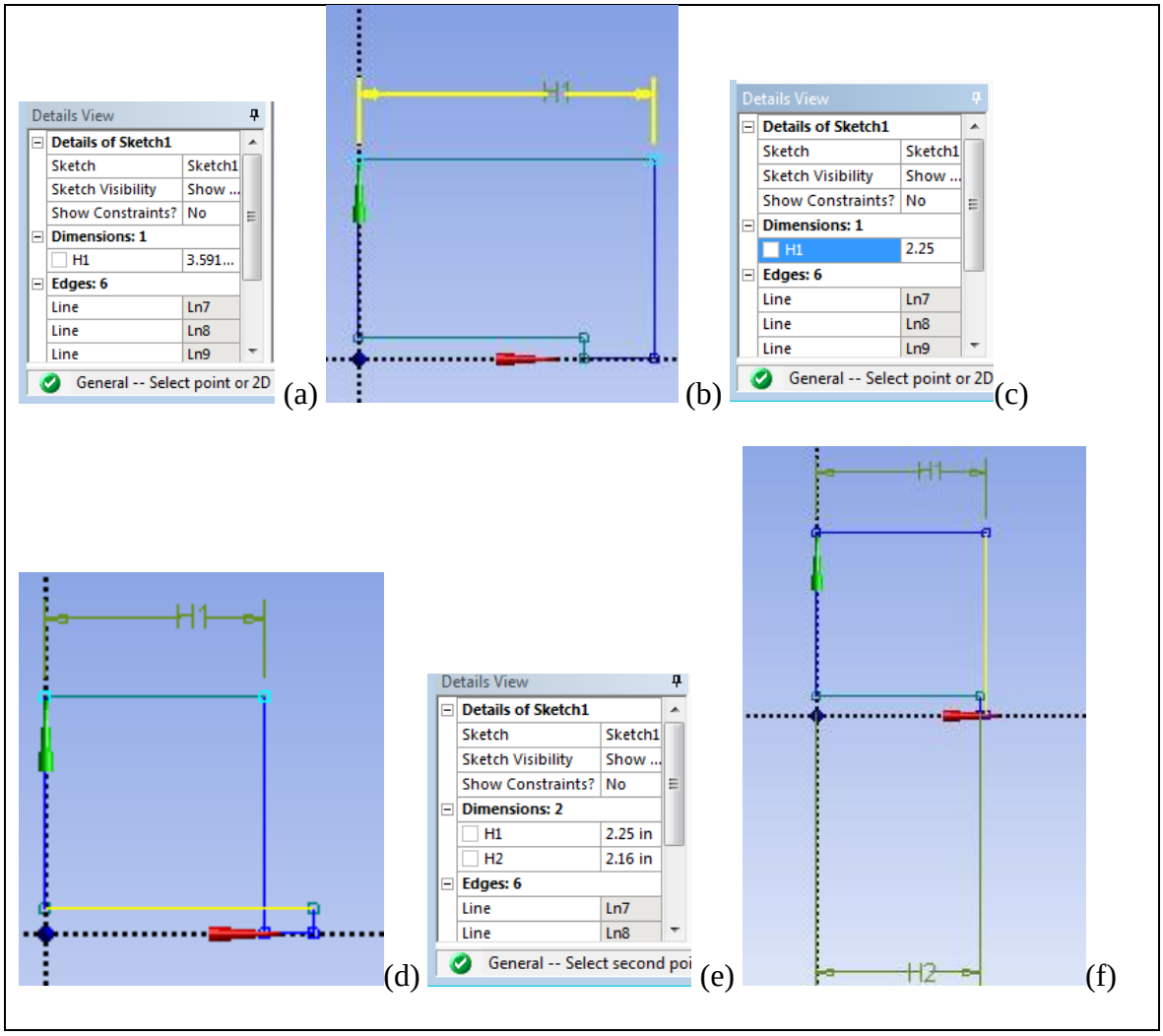

Figure F.12: Assigning horizontal length values to the 2D

Assigning length values to 2 of the 3 vertical segments, V4 and V5: (a) V4 is indicated on the plot, (b) the new length value is entered, (c) V5 is selected and is shown in yellow, (d) V5 length is entered, (e) plot is shown with all the horizontal and vertical segments constrained.

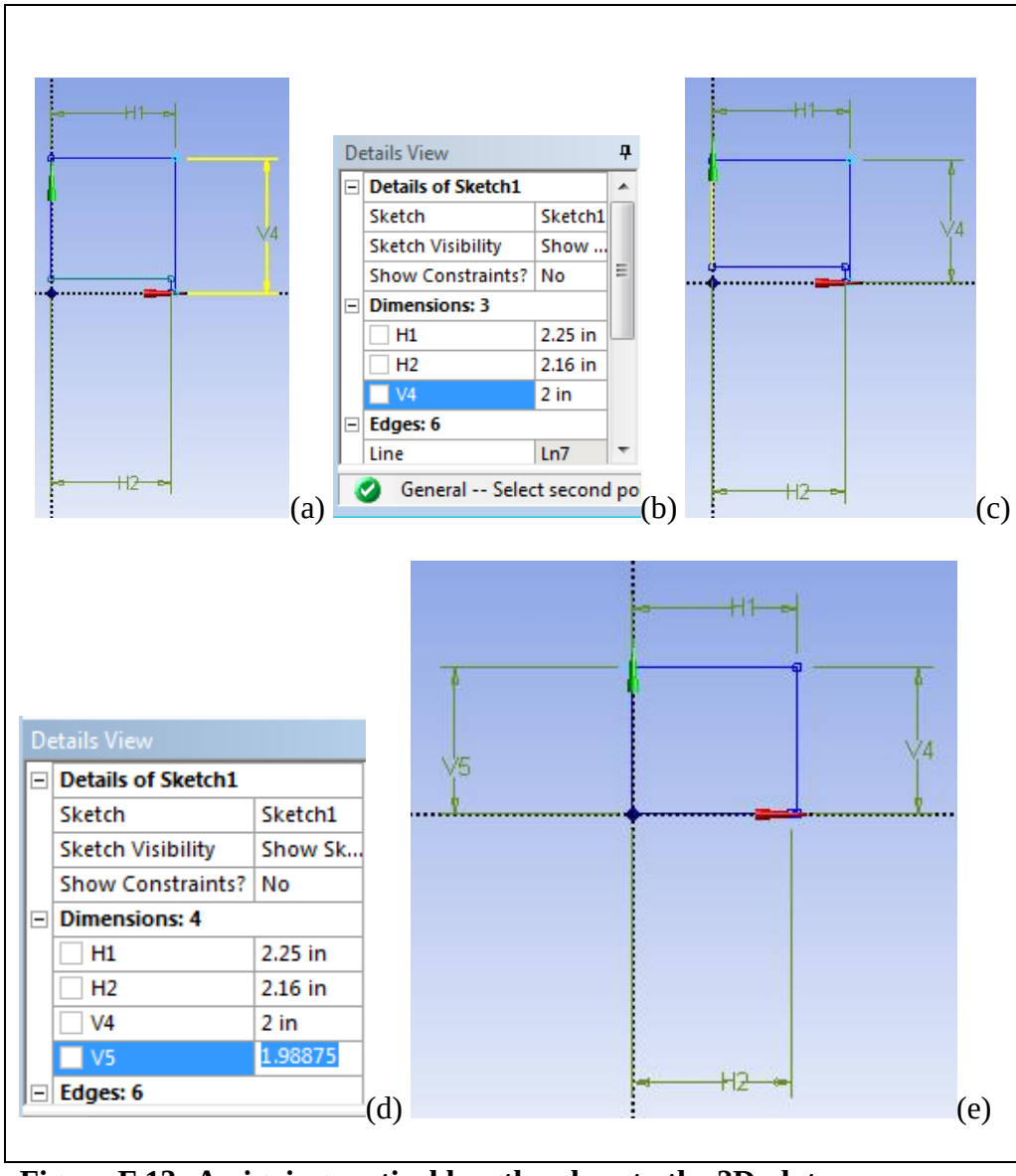

Figure F.13: Assigning vertical length values to the 2D plot

12- Apply a 360 degree revolve on the 2D sketch with a left click on the “Revolve” feature. If the sketch was already highlighted, it will automatically be considered as the geometry for the Revolve creation.

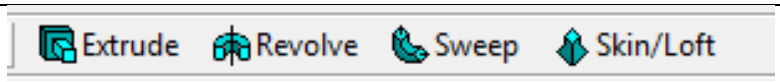

Figure F.14: Panel where the “Revolve” feature is selected

(b) Left-click on “Apply” then (c) left-click in the box in yellow adjacent to Axis to select the axis of revolution (d) In the plot area click on the z-axis then left-click on “Apply”

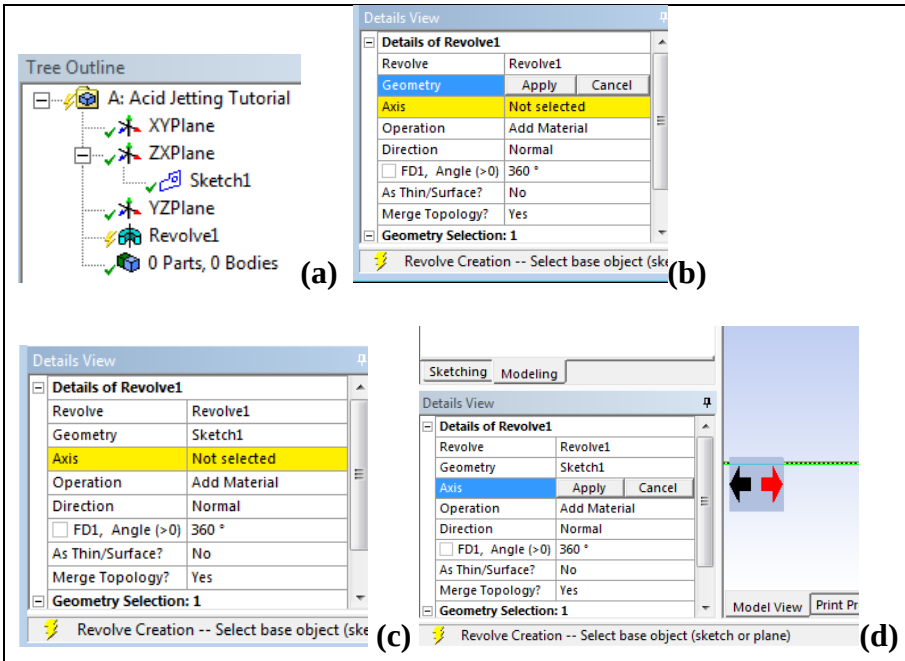

Figure F.15: Details of Revolve feature

In the top panel click on the “Generate” option.

Figure F.16: Top panel where the “Generate” feature is found to validate a design description

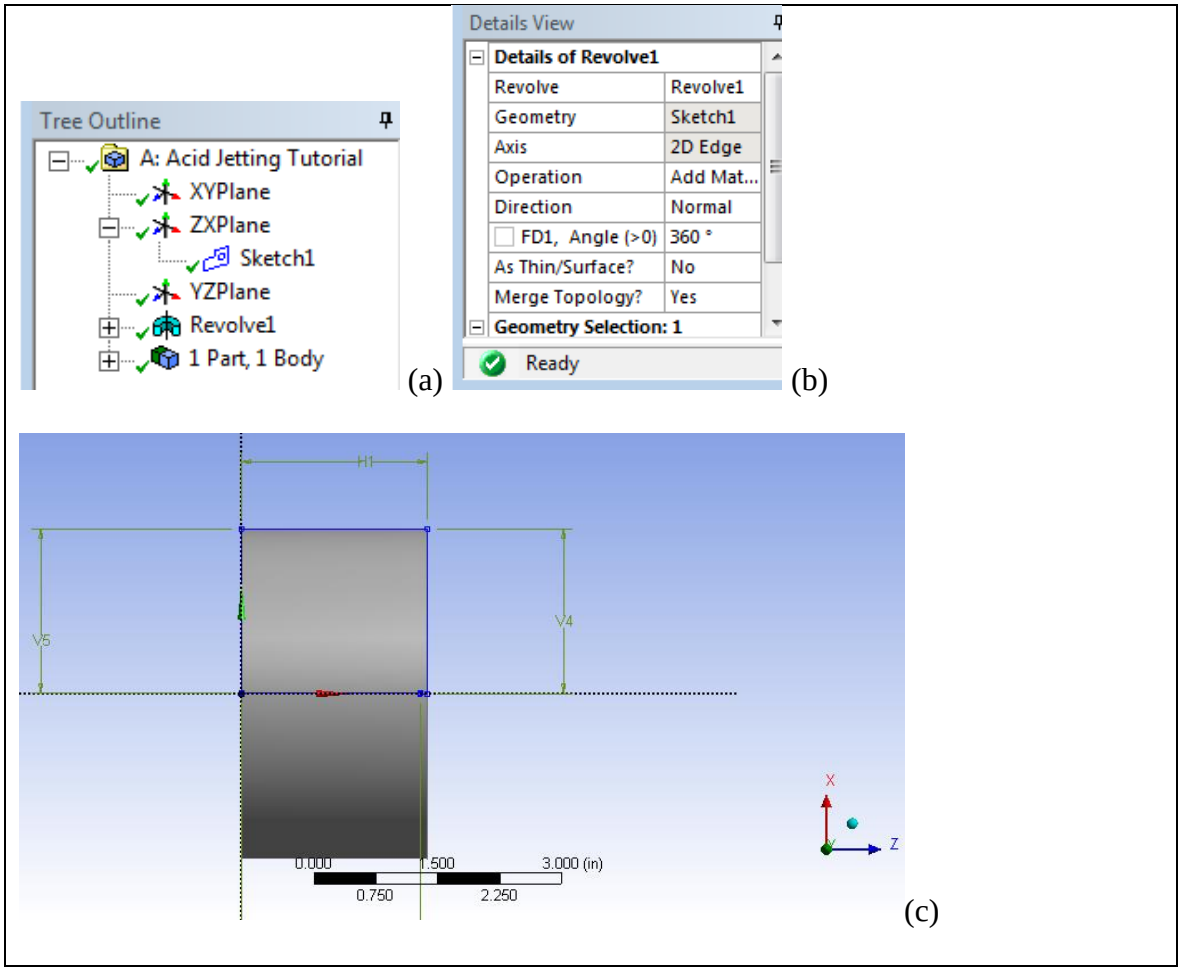

Figure F. 17: Resulting Geometry after “generating” the Revolve feature on 2D sketch

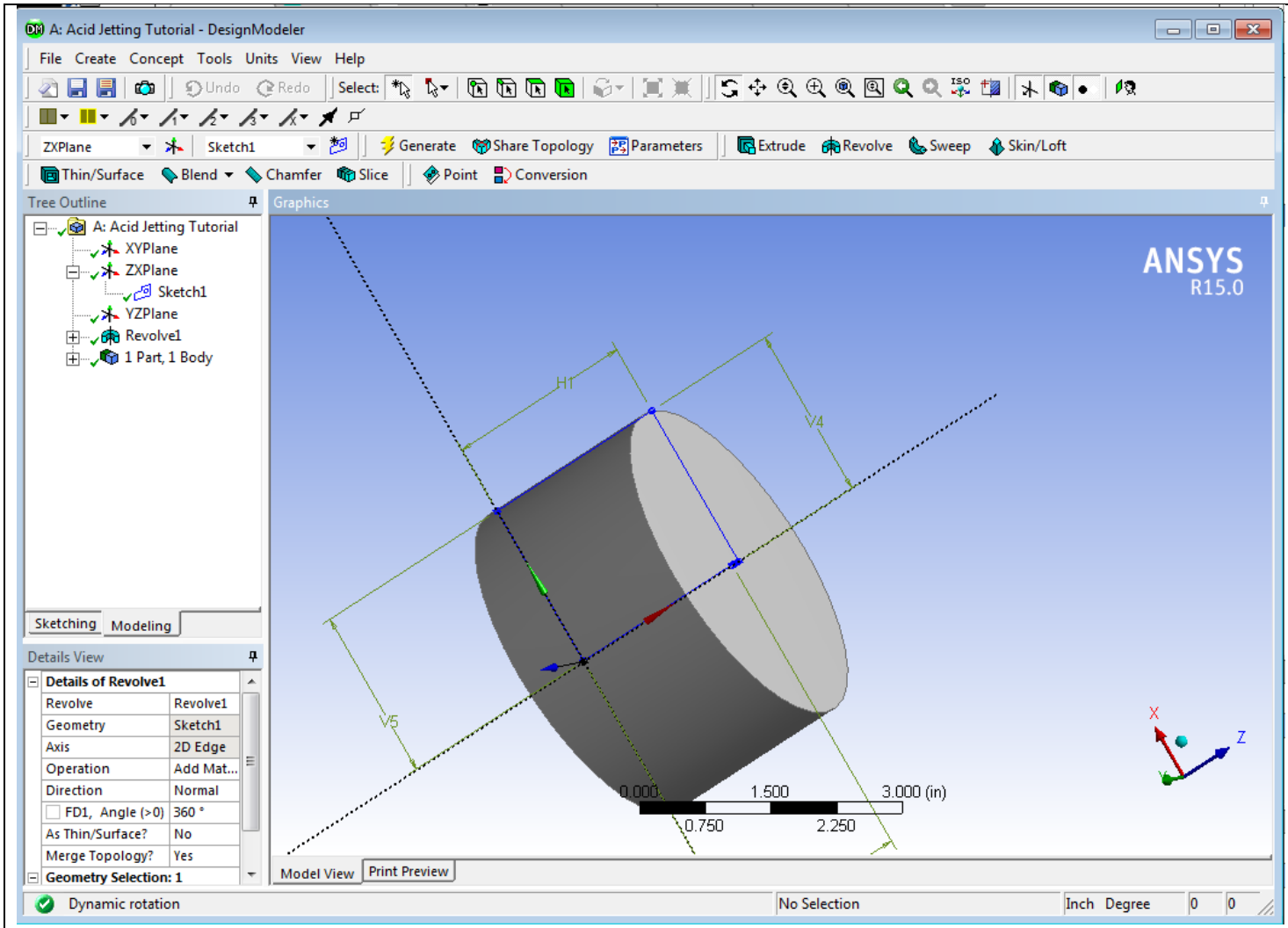

Figure F.18: 3D view of cylindrical geometry

13- Add a cylinder on the inlet face to represent the Recycle outlet: (a) left-click on “Create” from top toolbar, (b) left-click on “Primitive” then left-click on “Cylinder”, (c) and (d) enter cylinder geometry information, a 0.1 inches high (in negative z-direction), quarter inch diameter cylinder centered on (x,y)=(0.5, 0.5) with a face on the xy-plane (z=0 origin coordinate), select generate to create the additional 3D geometry

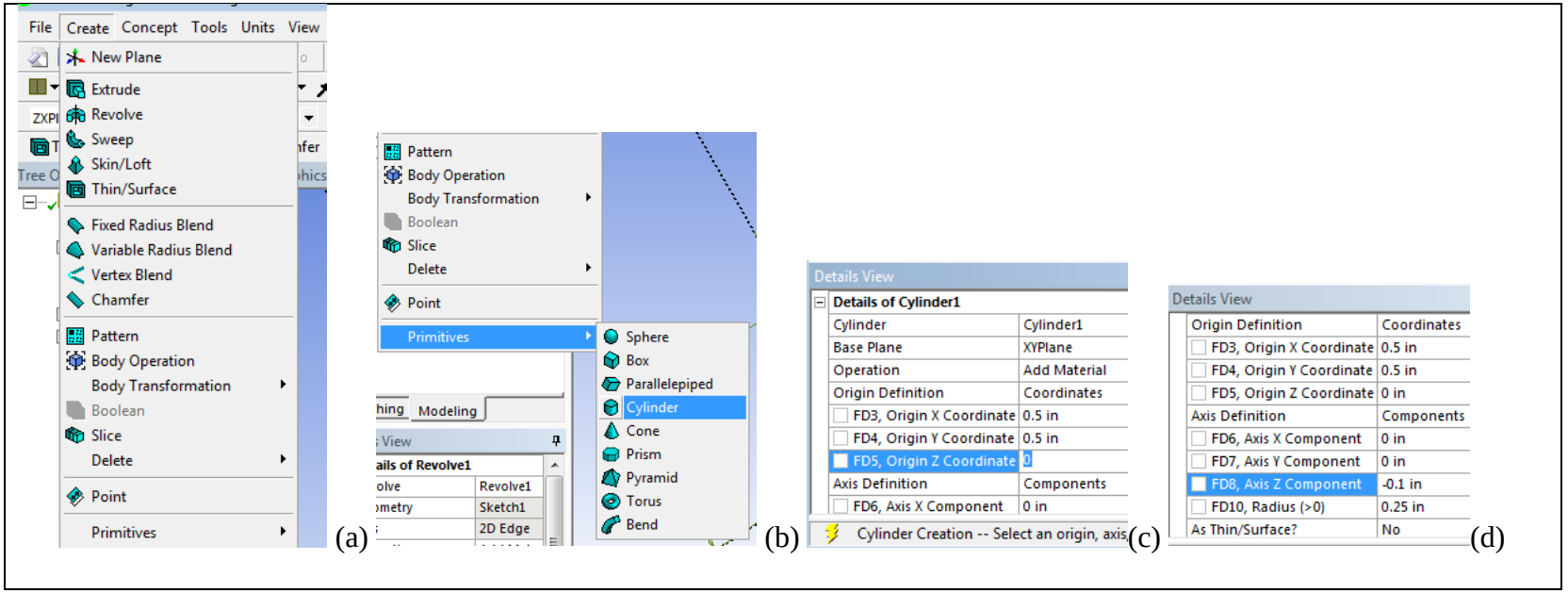

Figure F.19: Adding the recycle outlet geometry to main cylindrical geometry

The final geometry: (a) tree outline indicating the two 3D geometries making the solid body, (b) Trimetric view of 3D geometry

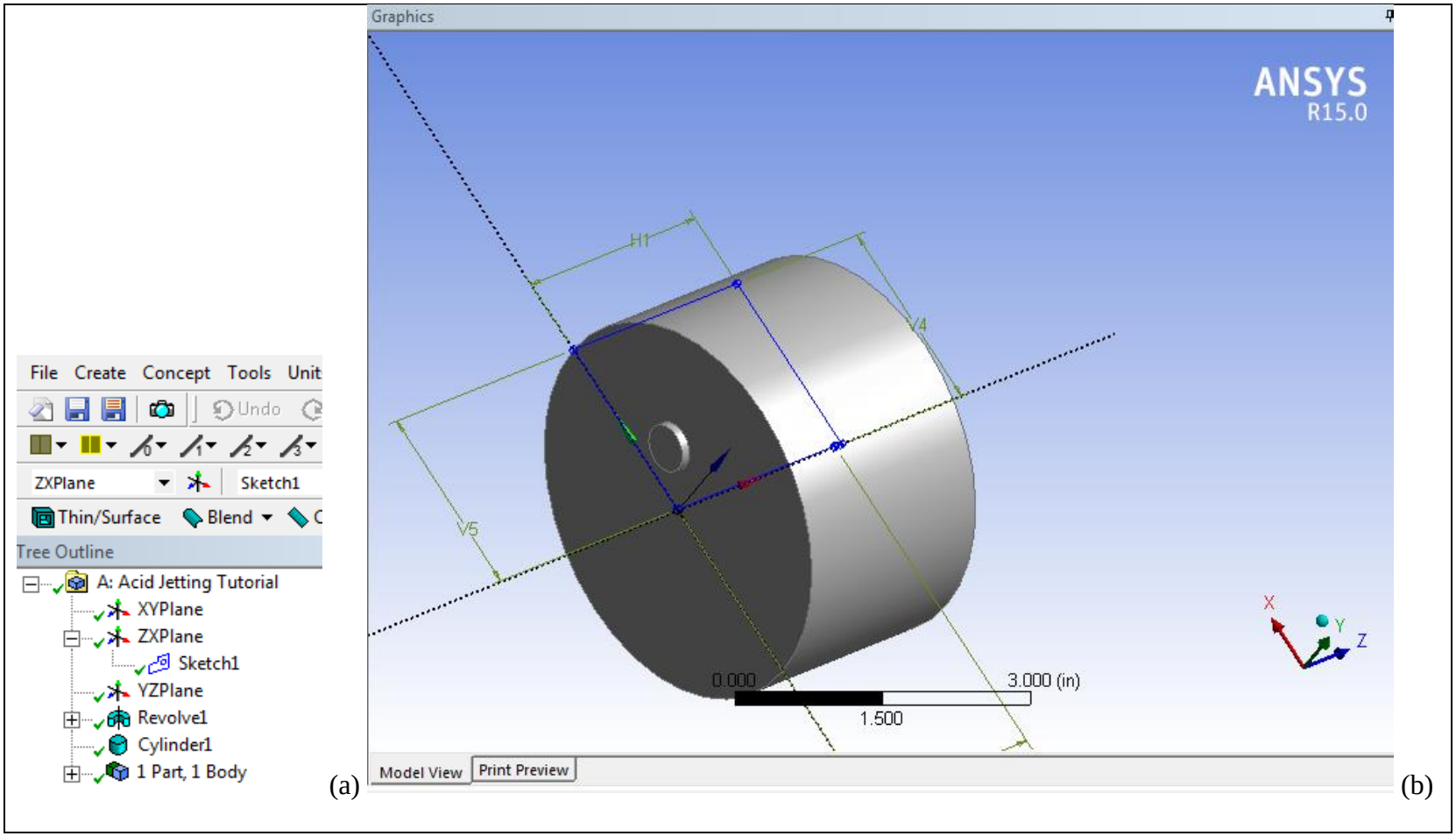

Figure F.20: Final 3D Geometry

14- Selecting and defining specific surfaces: (a) Left click on “Concept” in top toolbar, (b) Left-click on “Surfaces From Faces,” (c)select face with left-click, here the top surface of recycle outlet is selected, (d) Left-click on apply, (e) display once the face has been selected, (f) in tree outline, surface is listed as “SurfFromFaces2,”, right-click on it then select “Generate,” (g) Rename surface as “RecycleOutlet,” (h) Repeat procedure for new surface (j) surface is selected as shown, it is the nozzle tip surface which will as the fluid inlet (k) surface is generated hen renamed as “Inlet” and a new surface from face is created, (i) the nozzle wall is selected, then surface is generated and renamed as “NozzleWall,” (m) a fourth and last surface is selected, (n) surface is generated then renamed as “Outlet,” (o) the three outline after all the surfaces have been generated.

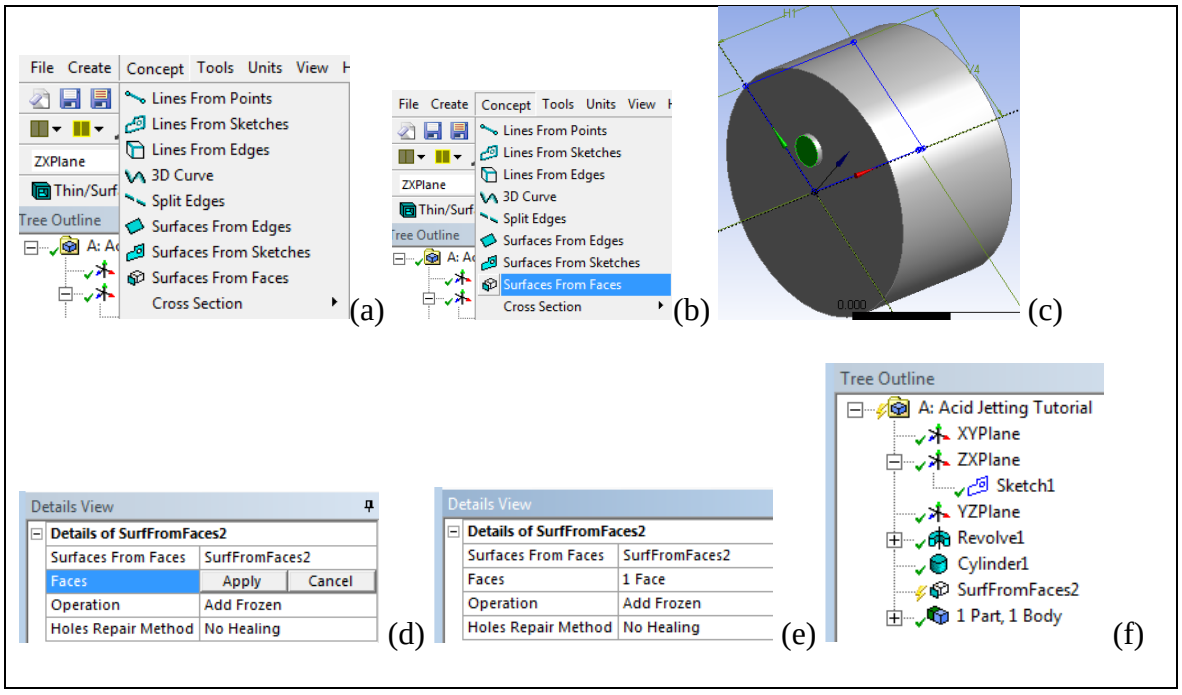

Figure F.21: Selecting and generating specific surfaces from faces: inlet, outlets and walls

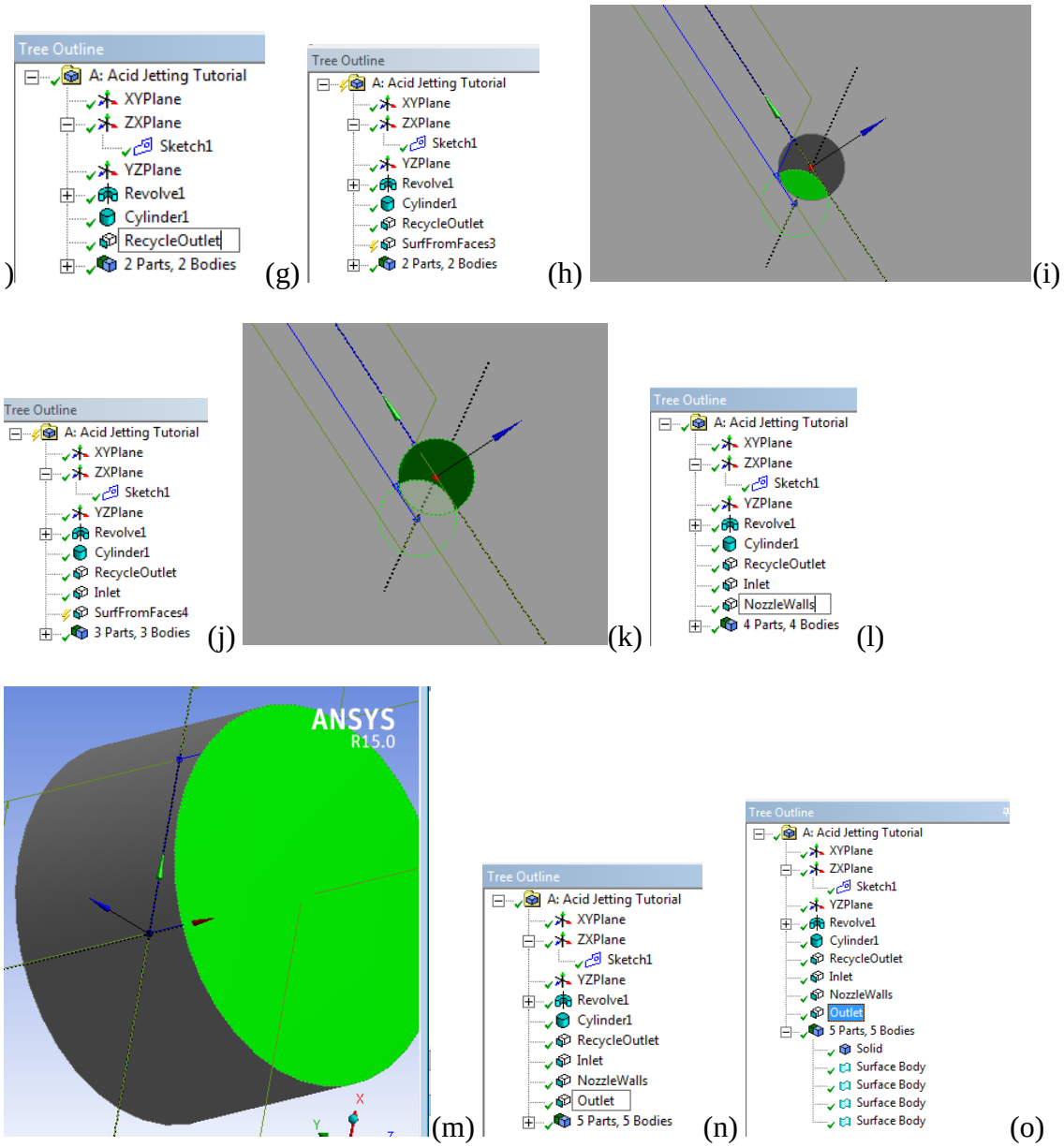

Figure F.21 (continued)

14- Meshing follows the Geometry (a)Double click on “Mesh,” (b) initial interface in the Meshing platform.

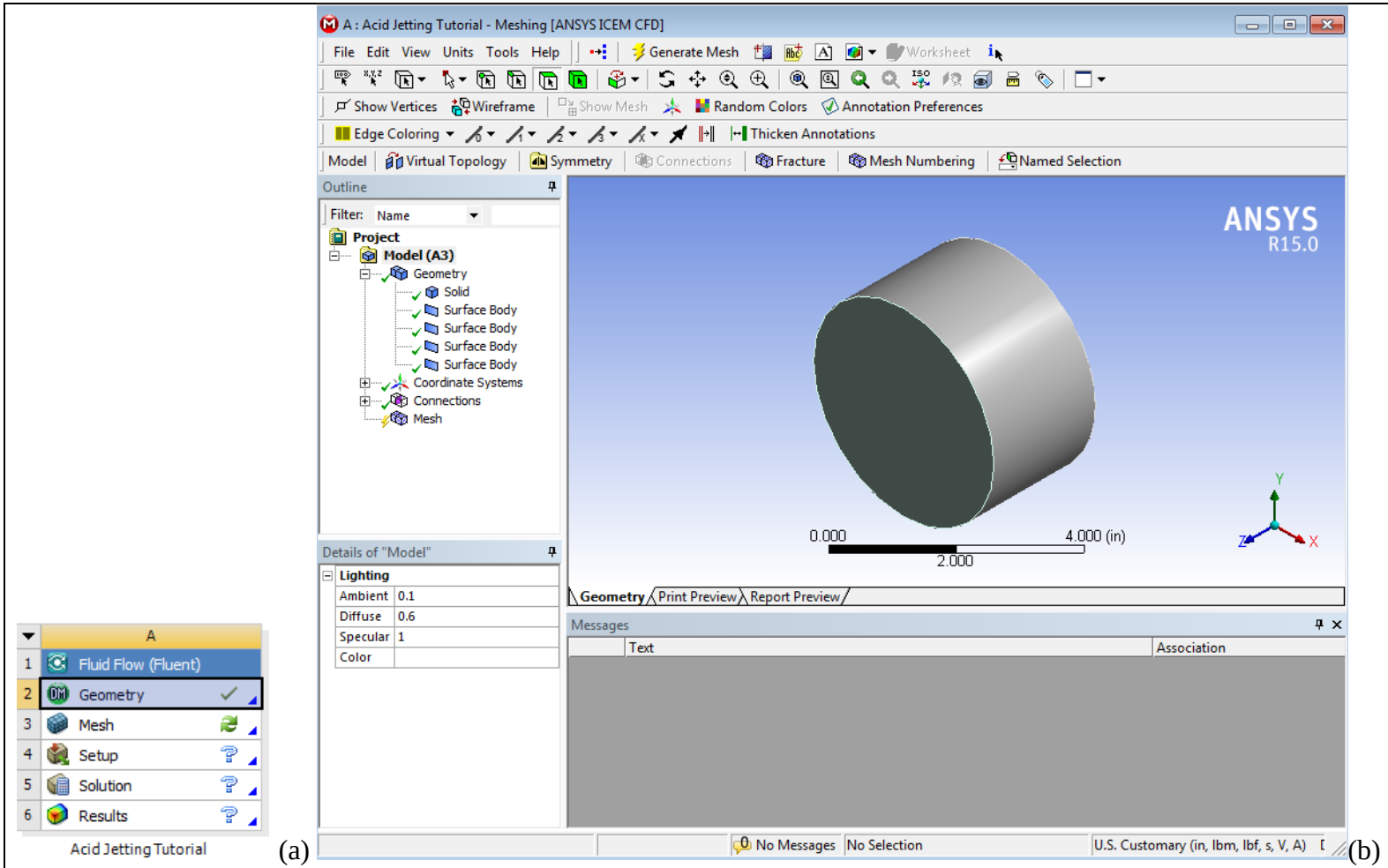

Figure F.22: Switching to Meshing mode

Left-click on “Mesh” under the “Outline” toolbar and (a) check if the default conditions apply to the desired meshing, otherwise modify as needed, (b) left-click on “Generate Mesh” in the top toolbar.

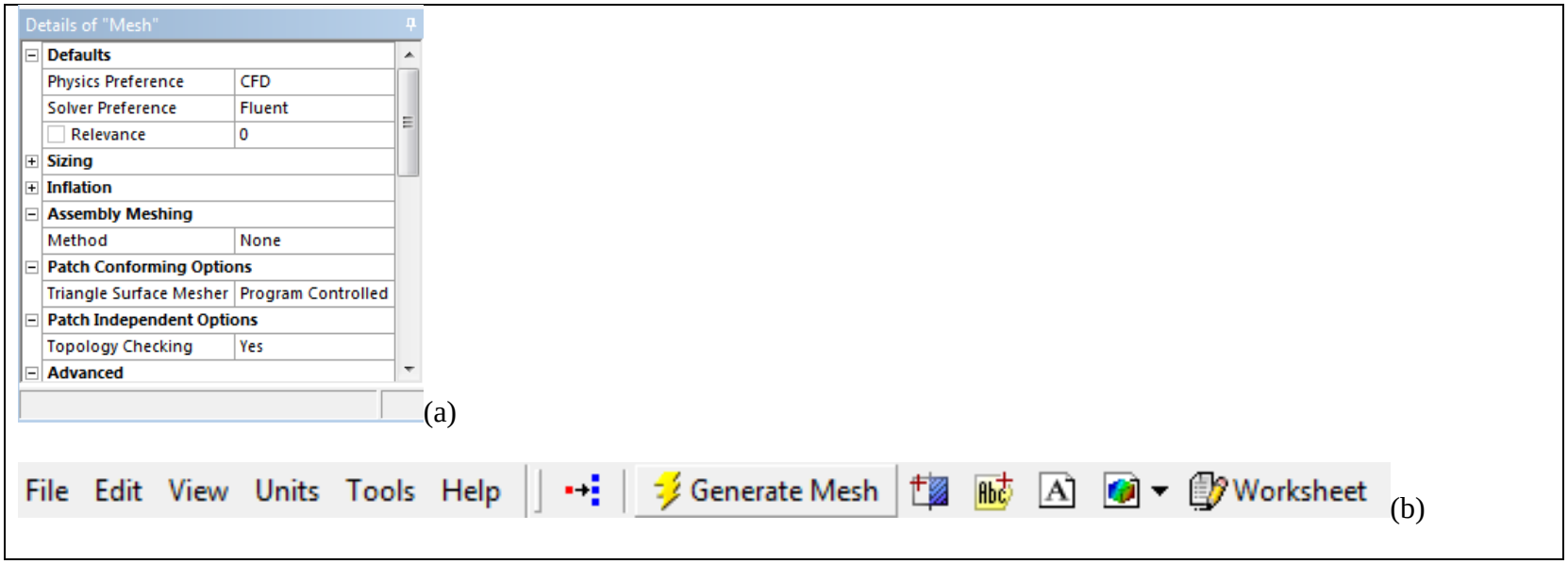

Figure F.23: Steps to generate mesh

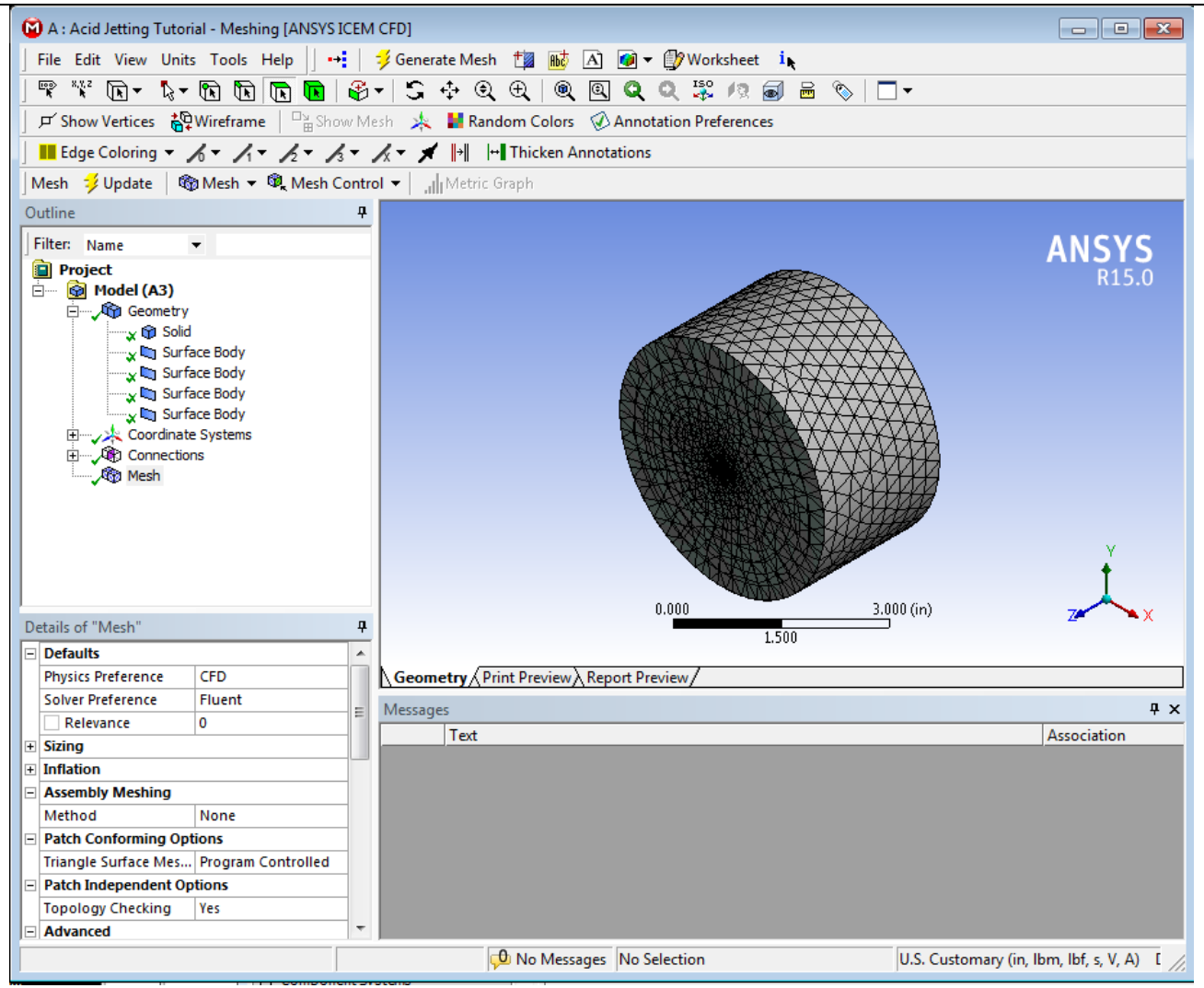

Figure F.24: Trimetric view of mesh generated

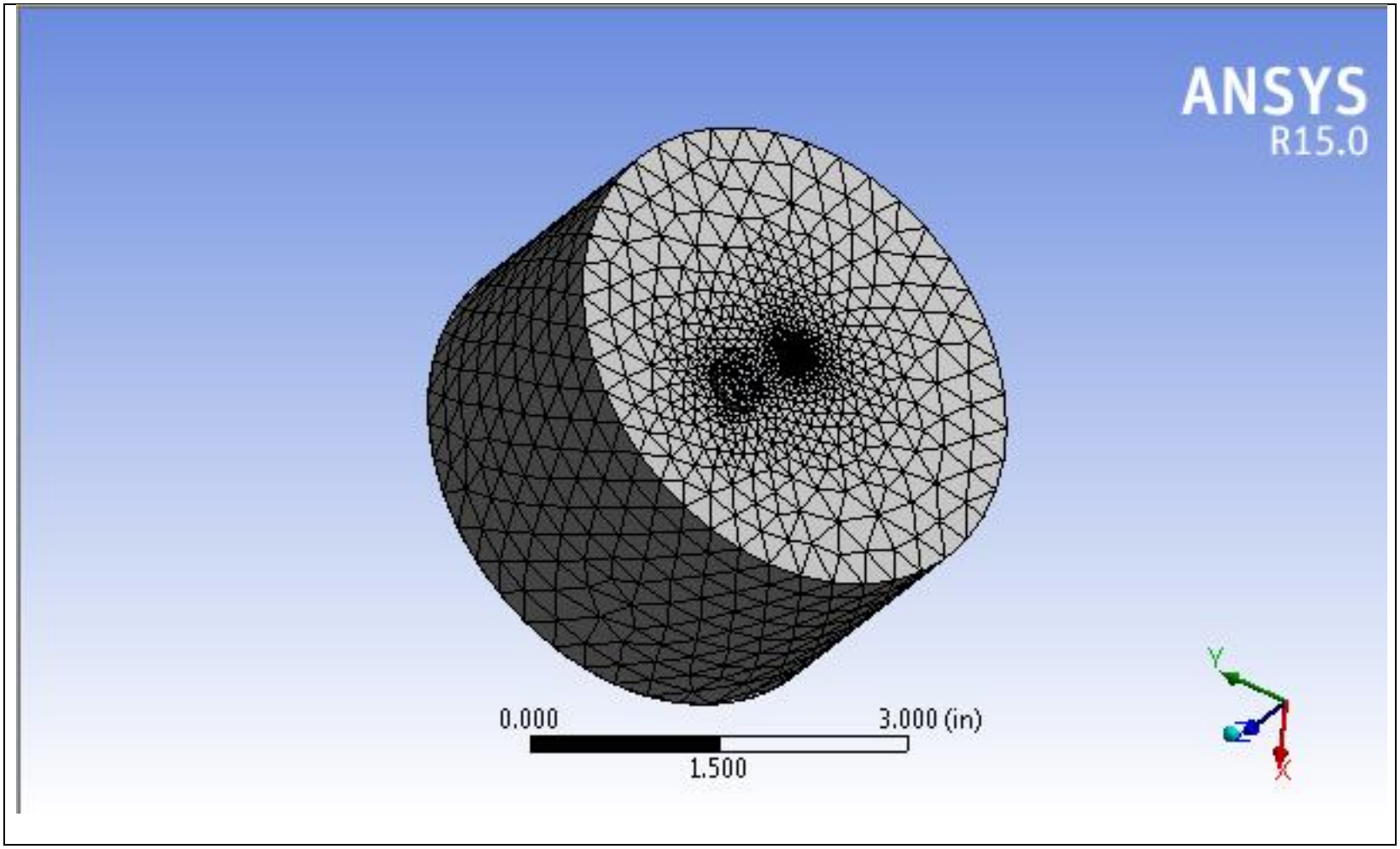

Figure F.25: Reverse trimetric view of mesh showing the mesh refining near the nozzle (inlet) and recycle outlet

15- After the meshing, the ANSYS Fluent setup starts: (a) Double left-click on “Setup” (b) Select “Double Precision,” to increase numerical accuracy, and “Serial” processing if using one CPU and one ANSYS license. System will automatically 3D geometry and proceed with a 3D solver

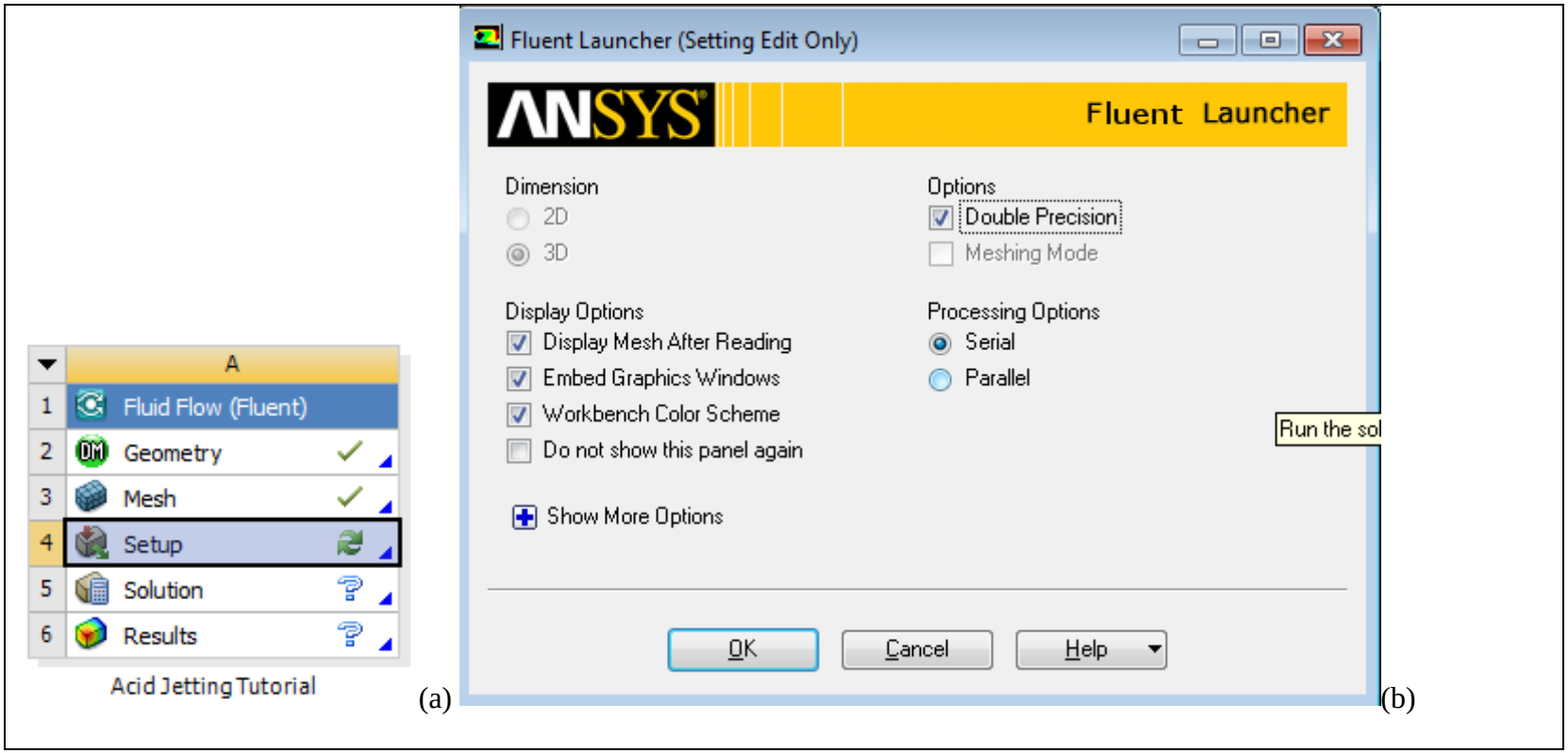

Figure F.26: Starting a new ANSYS Fluent setup session

16- (a) Graphical User Interface (GUI), showing workflow list, (b) geometry, mesh and plots section, (c) Text User Interface (TUI) to monitor progress, check for error messages and serve as a textual command line

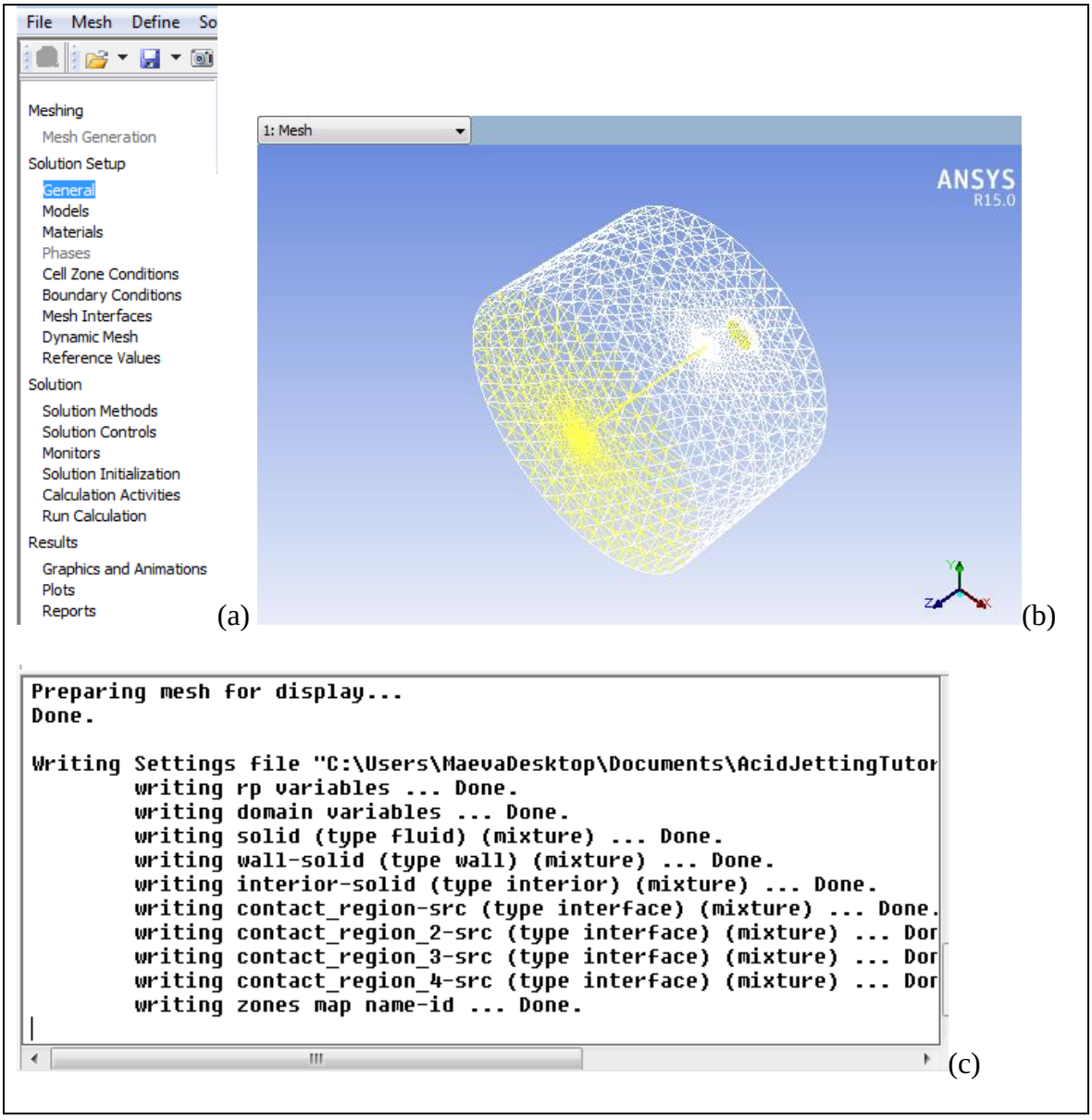

Figure F.27: Interface components in ANSYS Fluent 15

17- Scale mesh by selecting “in” under both “View Length Unit In” and “Mesh Was Created In”. (a) before selection, (b) after selection

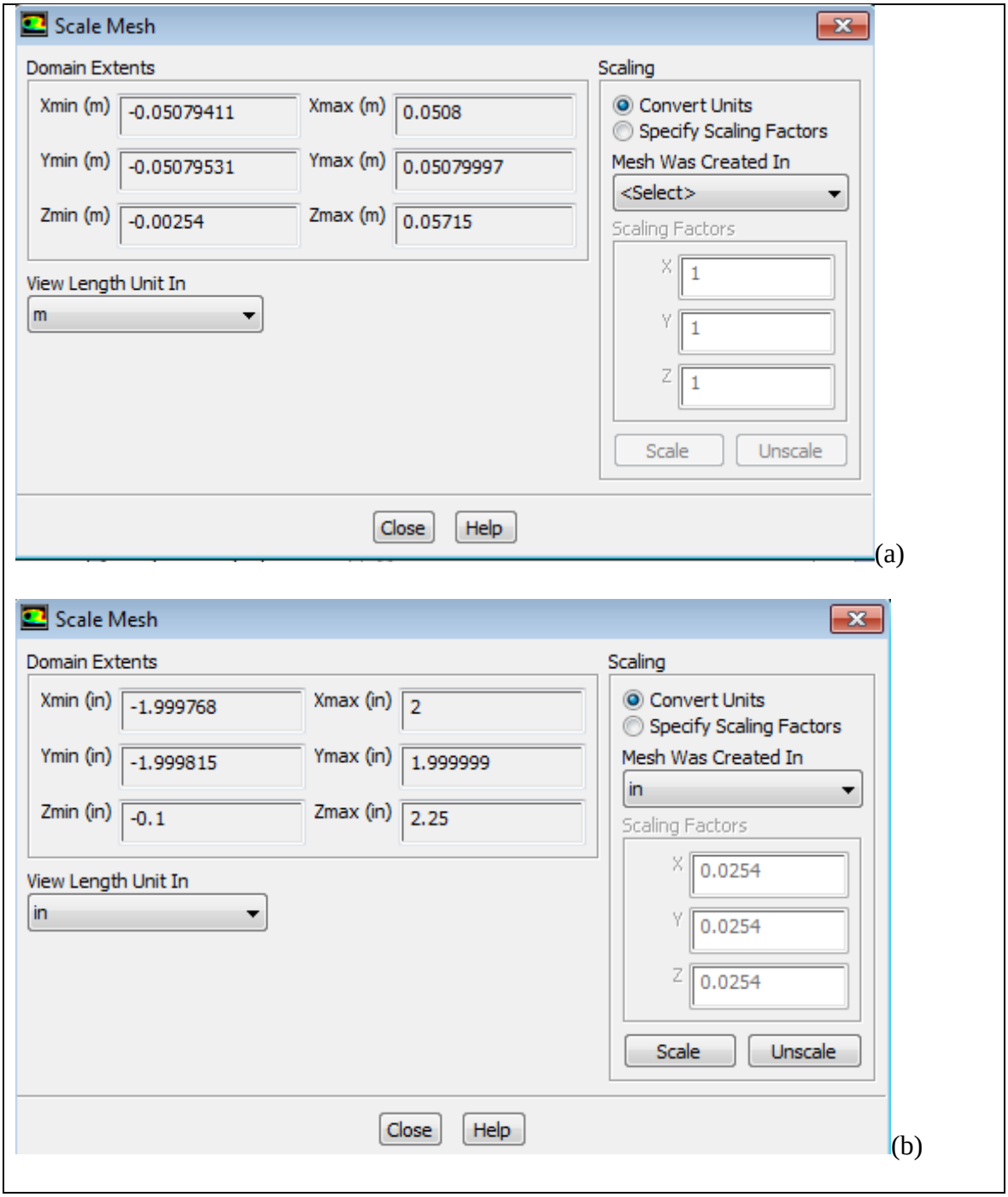

Figure F.28: Scaling Mesh

18- Selecting the turbulence model: (a) Left-click on “Models” then left-click on “Viscous – Laminar,” (b) initial view of viscous model list (c) left-click on “Large Eddy Simulation (LES),” (d) Left-click to check “Dynamic Stress” under “LES Model Options,” (e) Message to provide guidelines for correct solver and how to set it up.

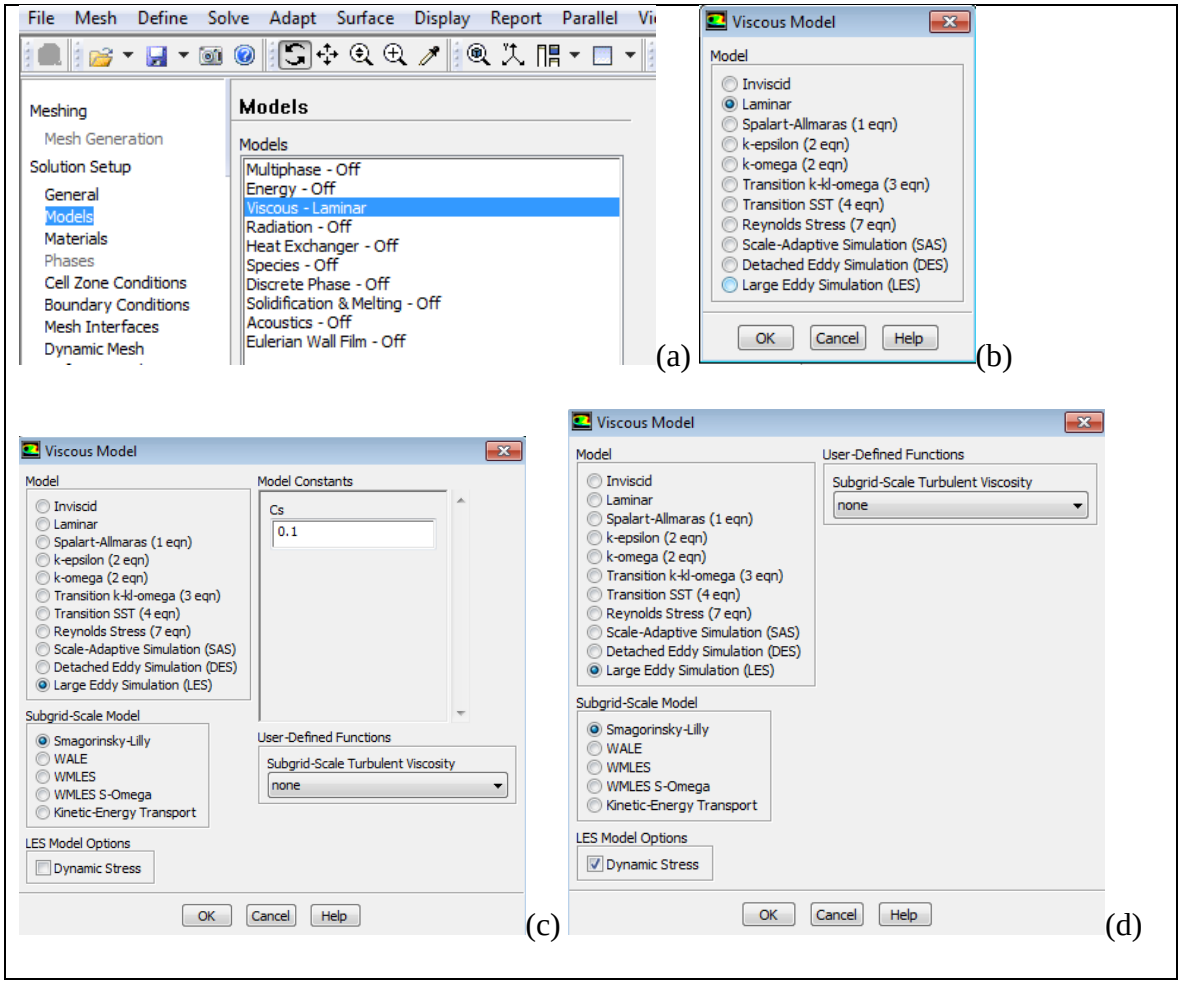

Figure F.29: Selecting the Dynamic Smagorinsky-Lilly model

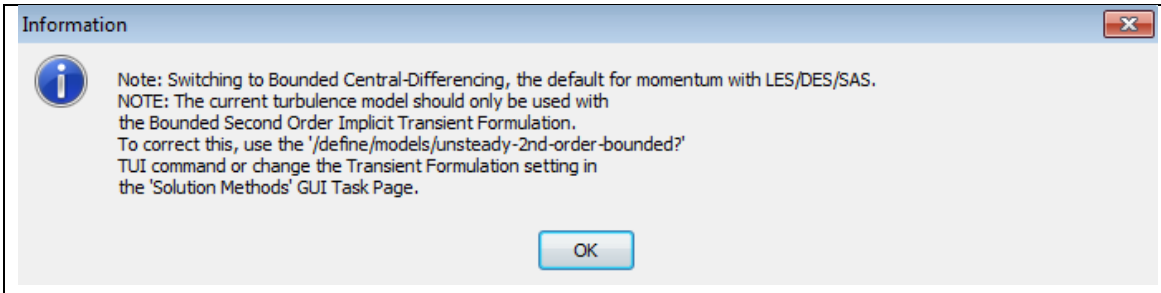

(e)

Figure F.29 (continued)

19- Adding materials: (a) Left-click on “Materials,” in step list then left-click on “Create/Edit” (b) left click on “Fluent Database” (c) in “Fluent Fluid Material” search for “water liquid” then click on “Copy”, then look for “hydrogen chloride” and click “copy”, for HCl the density and visocity will have to be manually entered. Under material type, select solid and under “Fluent Fluid Material” select “Calcium Carbonate” and click on copy, then close “Fluent database material”s window and “Create/edit Materials” window

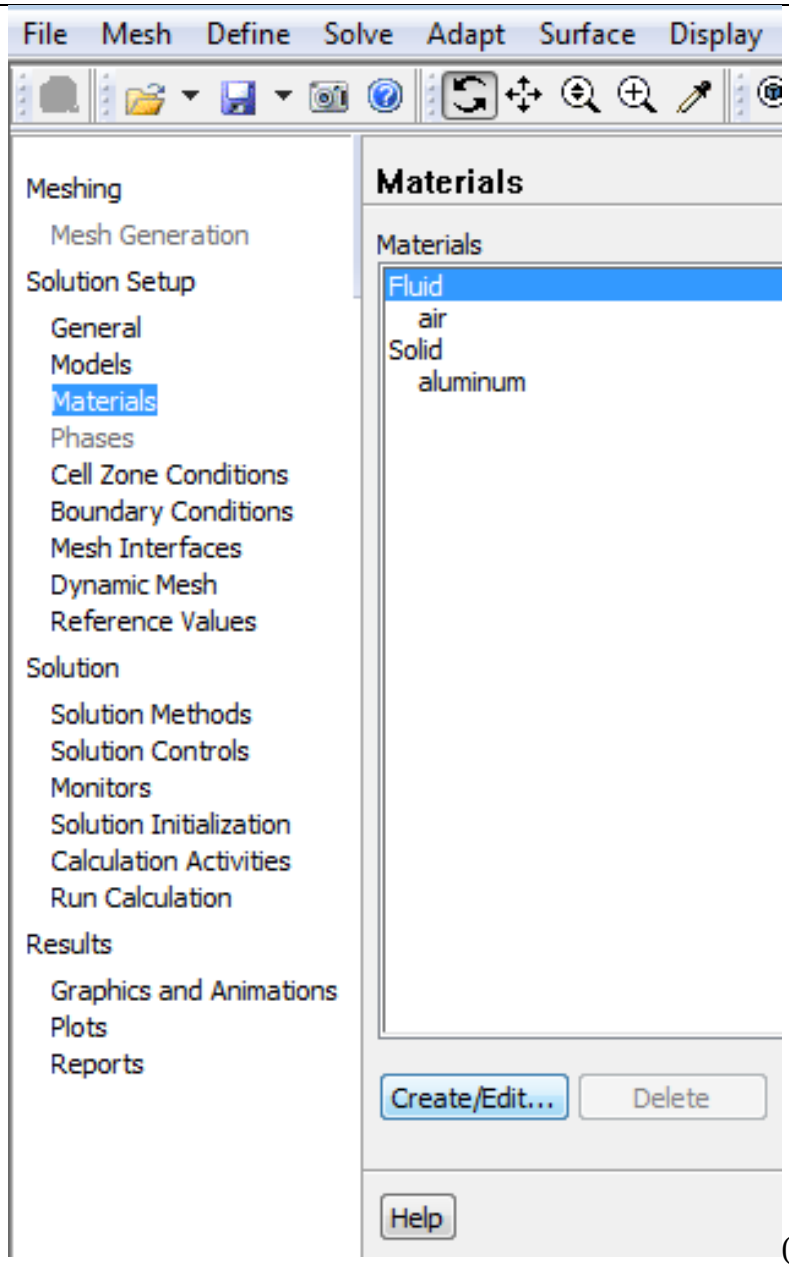

(a)

Figure F.30: Add materials to system: water, HCl and calcite

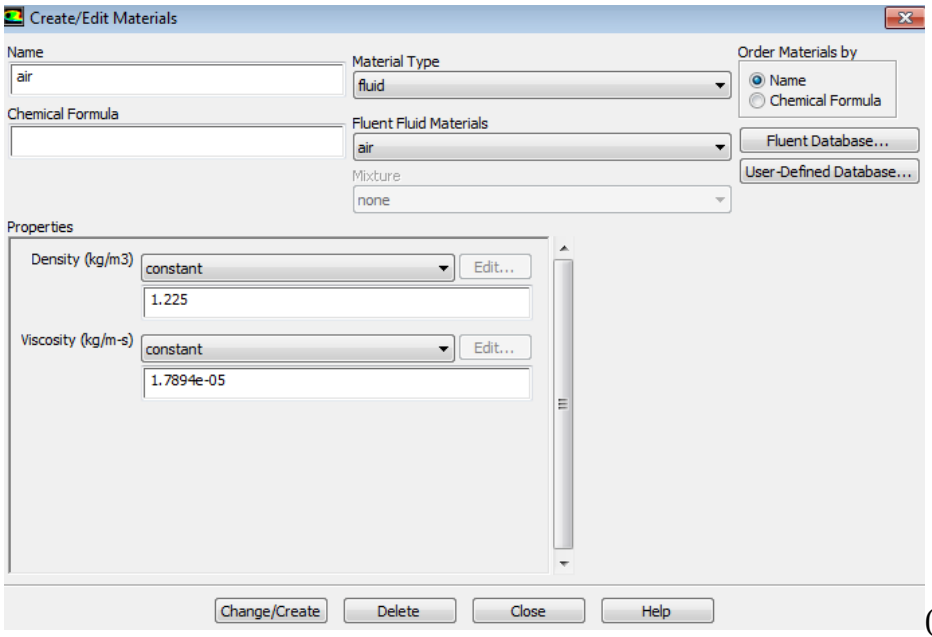

(b)

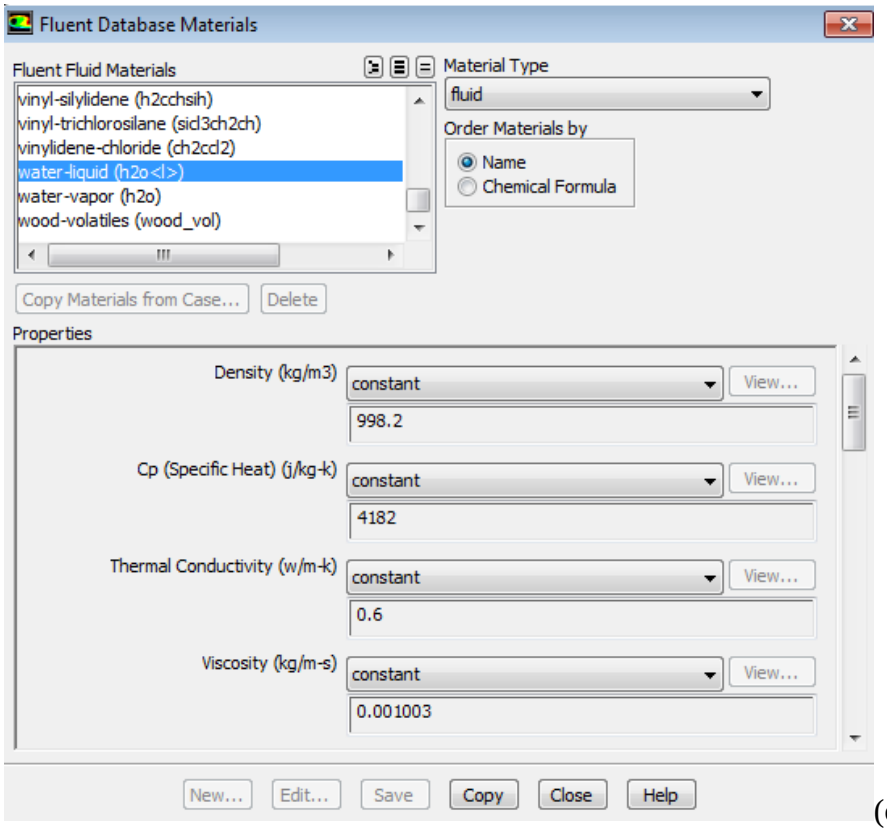

(c)

Figure F.30 (continued)

20- Set computational domain as liquid: (a) Click on Cell Zone Condition, then change type to fluid and click on Edit, (b) change material name to “water-liquid” then click on “OK”

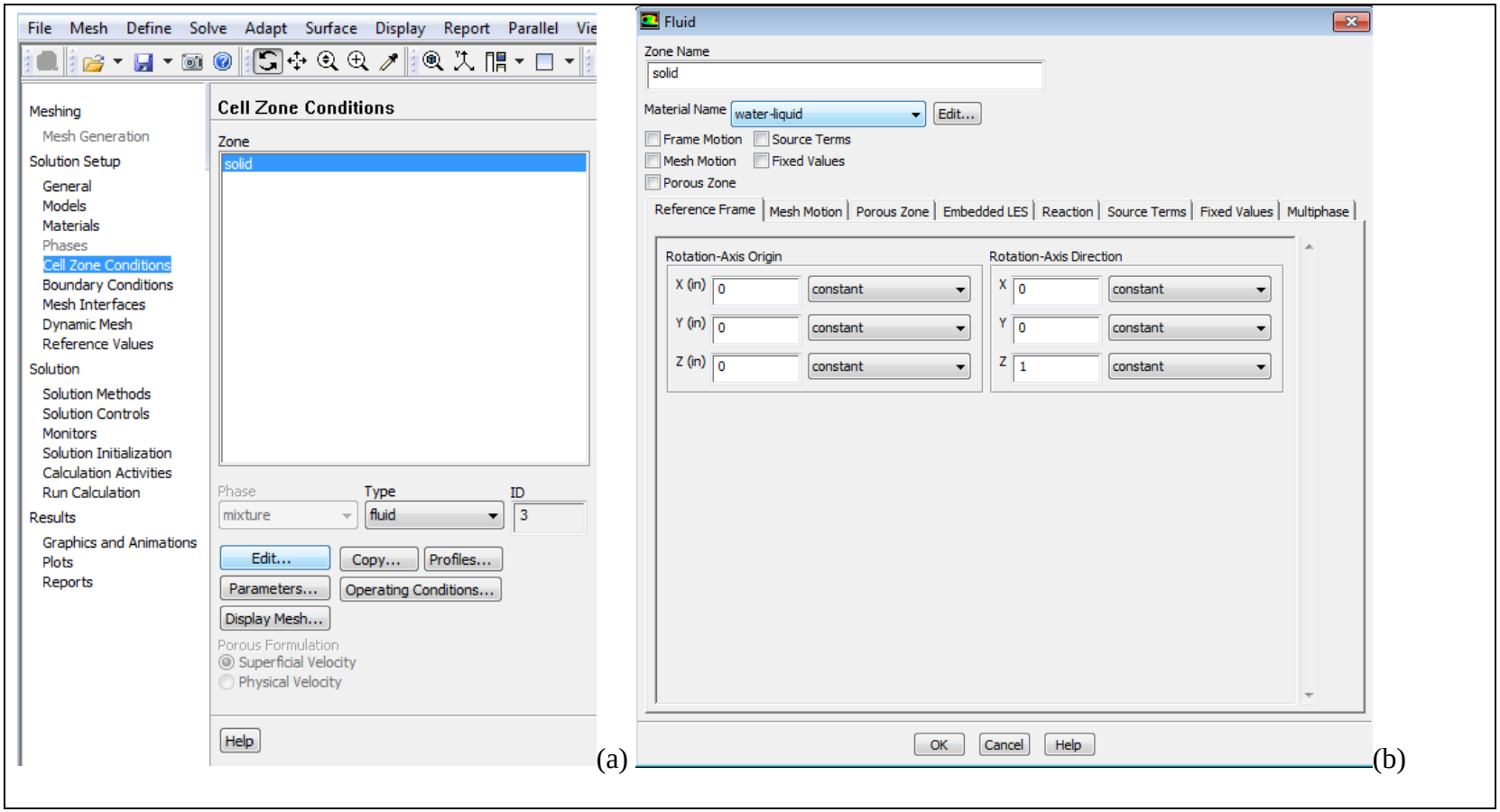

Figure F.31: Setting computational domain as liquid water

21- Setting boundary conditions: (a) left-click on “Boundary Conditions” select first zone under “Zone,” and select “outlet-vent” under “Type” (b) left-click on “Yes,” (c) rename zone as “outlet_vent,” and set gauge pressure at 0, (d) display after “outlet_vent” boundary condition setup, (e) set inlet conditions, (f) set nozzle walls conditions, (g) and (h)set outlet conditions, (i) display after all the boundary conditions have been set

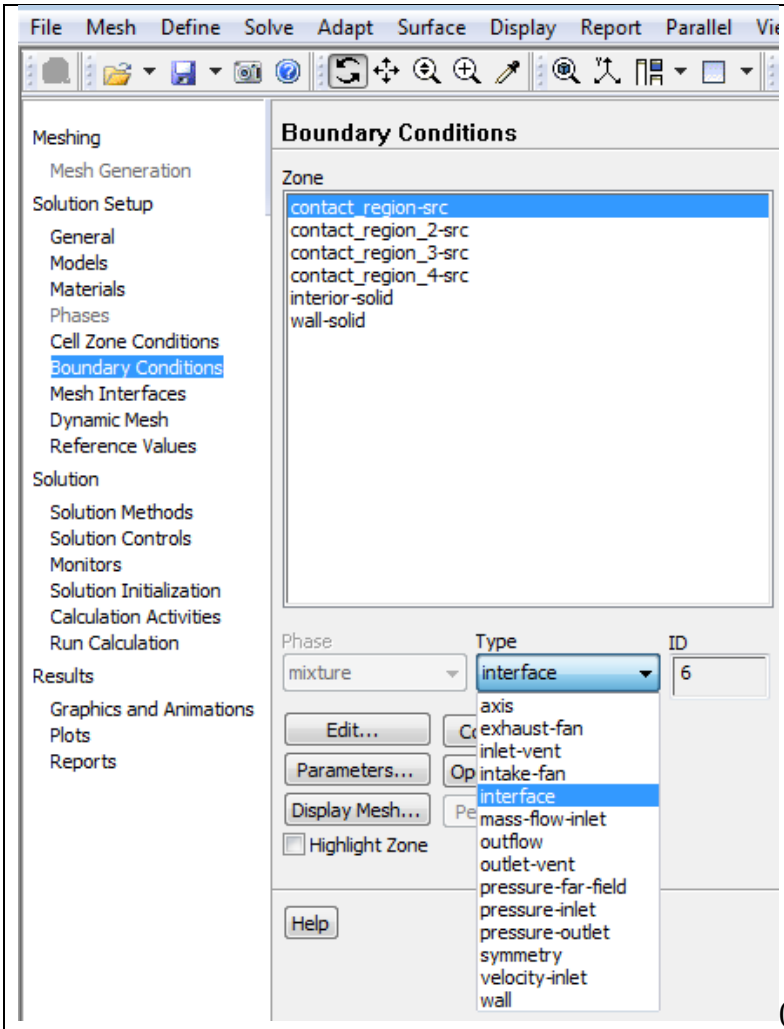

(a)

Figure F.32: Setting boundary conditions

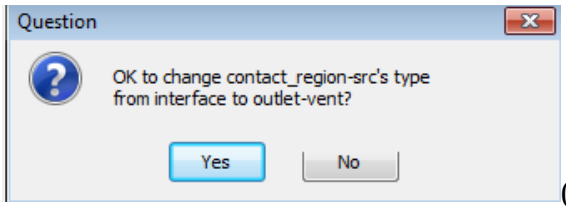

(b)

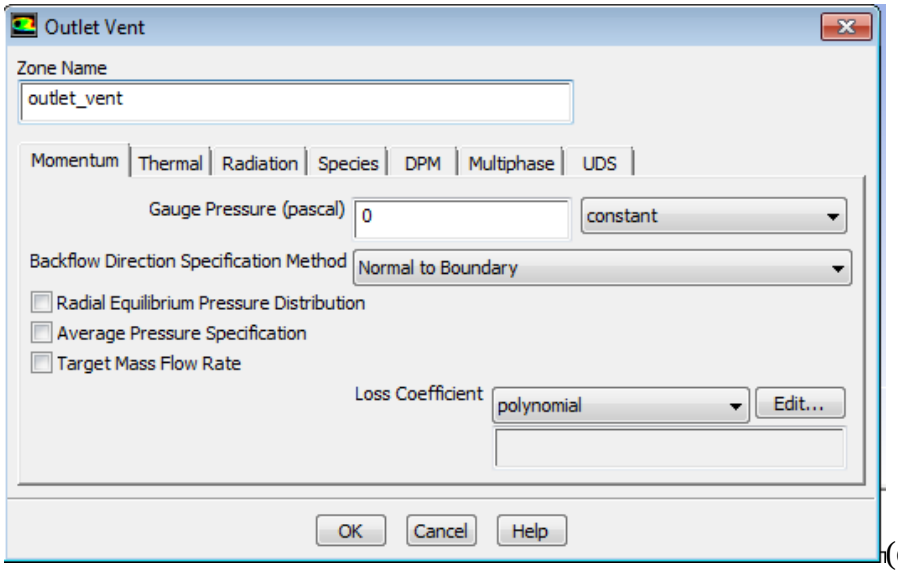

(c)

Figure F.32 (continued)

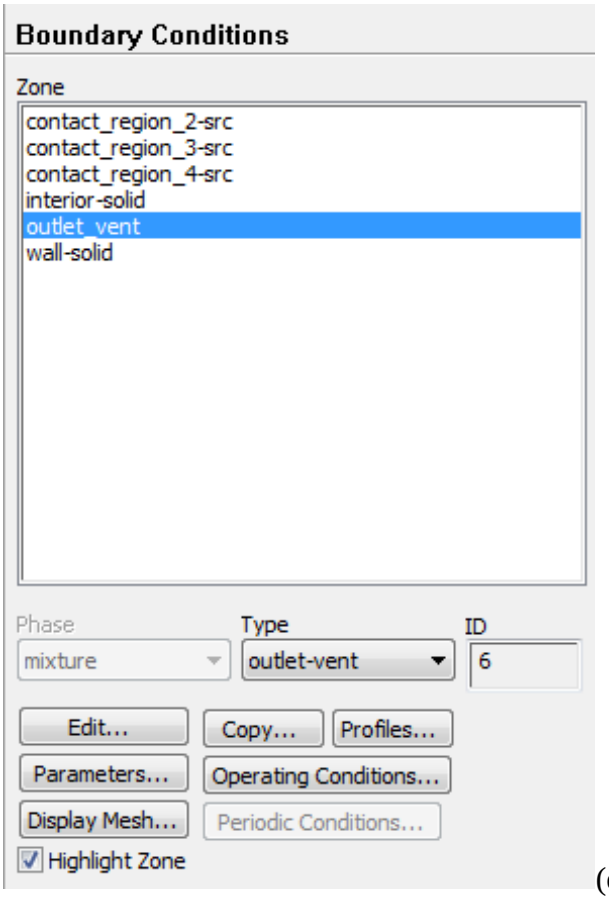

(d)

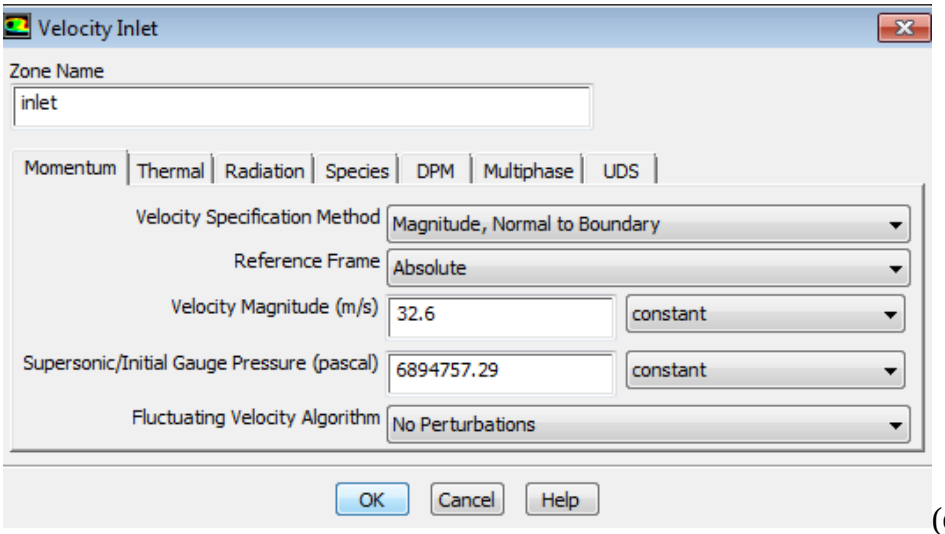

(e)

Figure F.32 (continued)

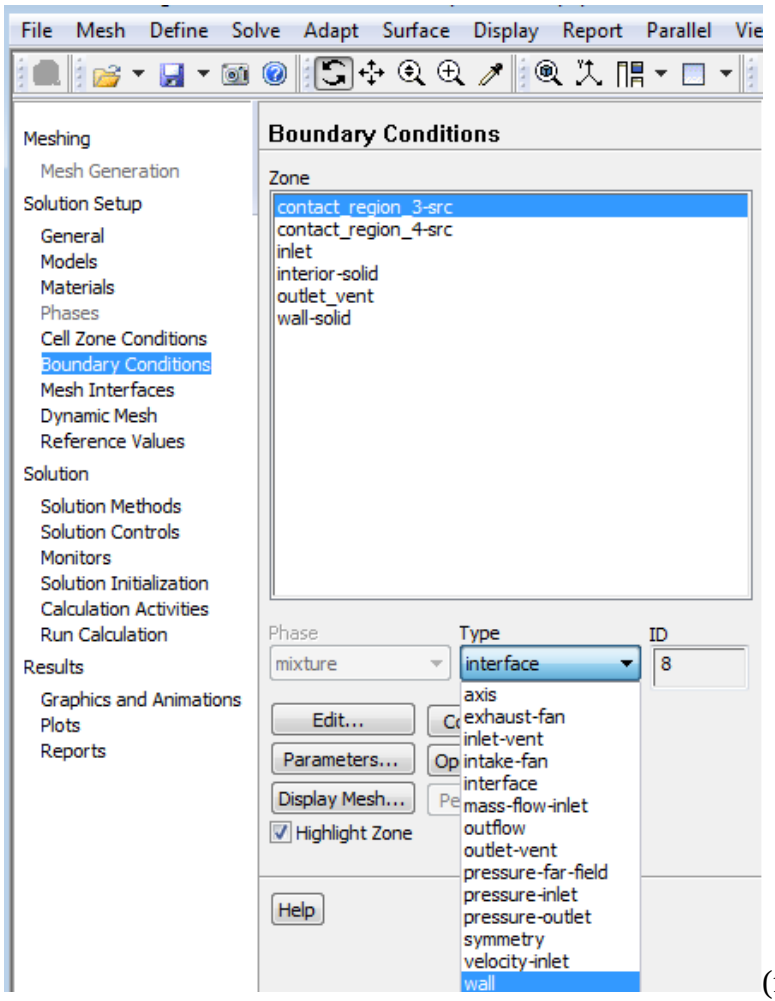

(f)

Figure F.32 (continued)

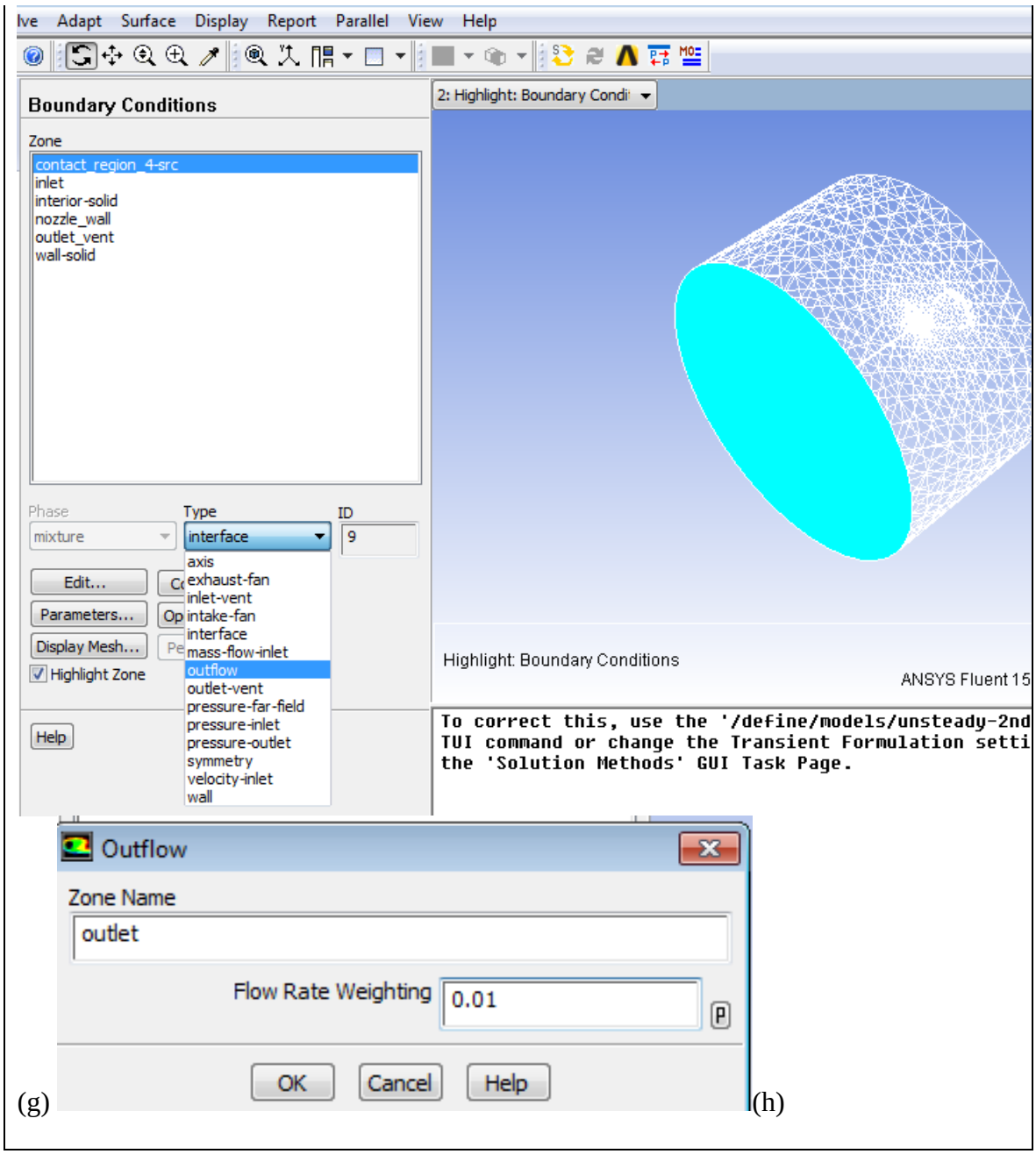

Figure F.32 (continued)

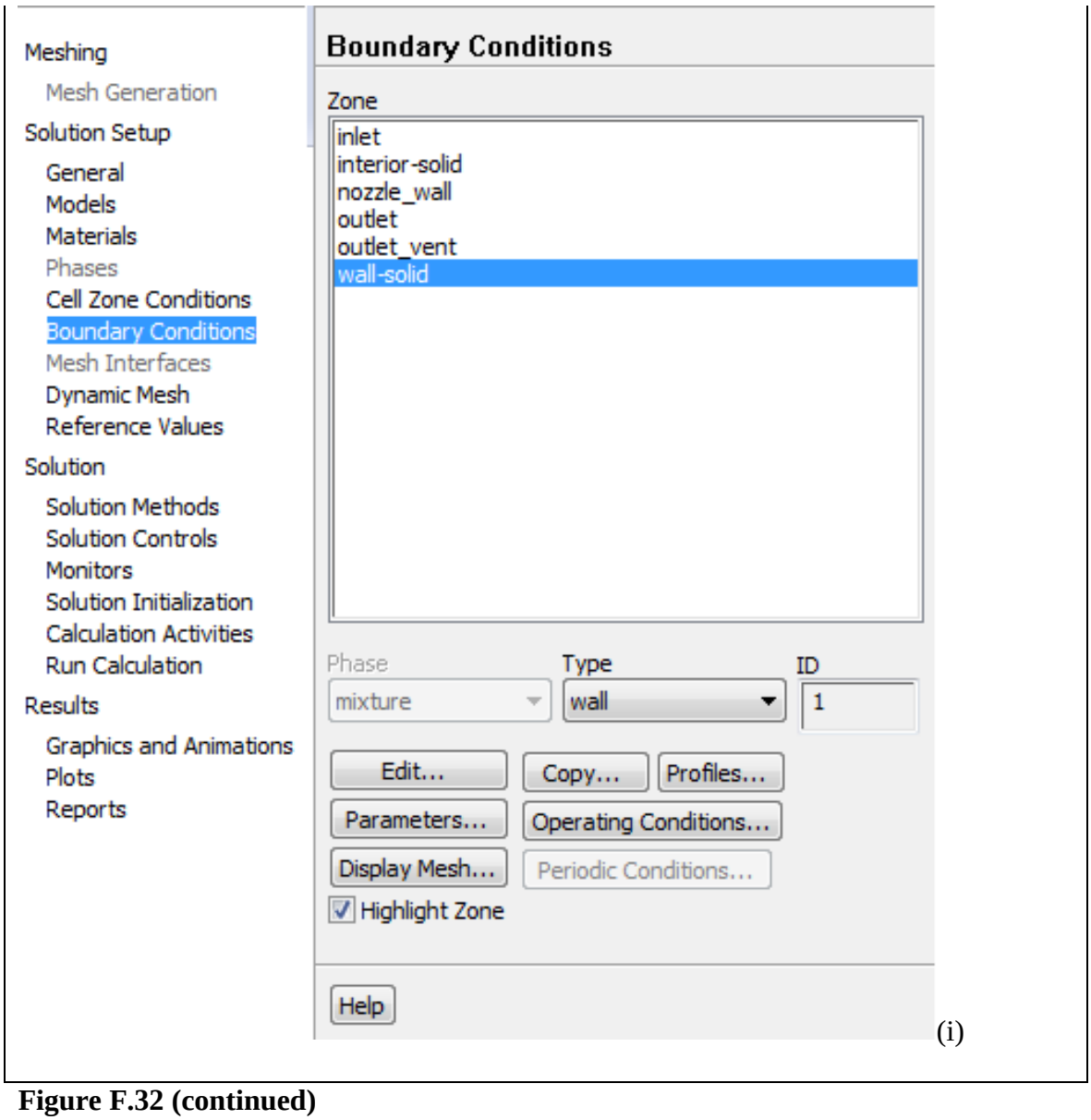

(i)

Figure F.32 (continued)

22- Setting reference values for computations: under compute from: select “inlet”

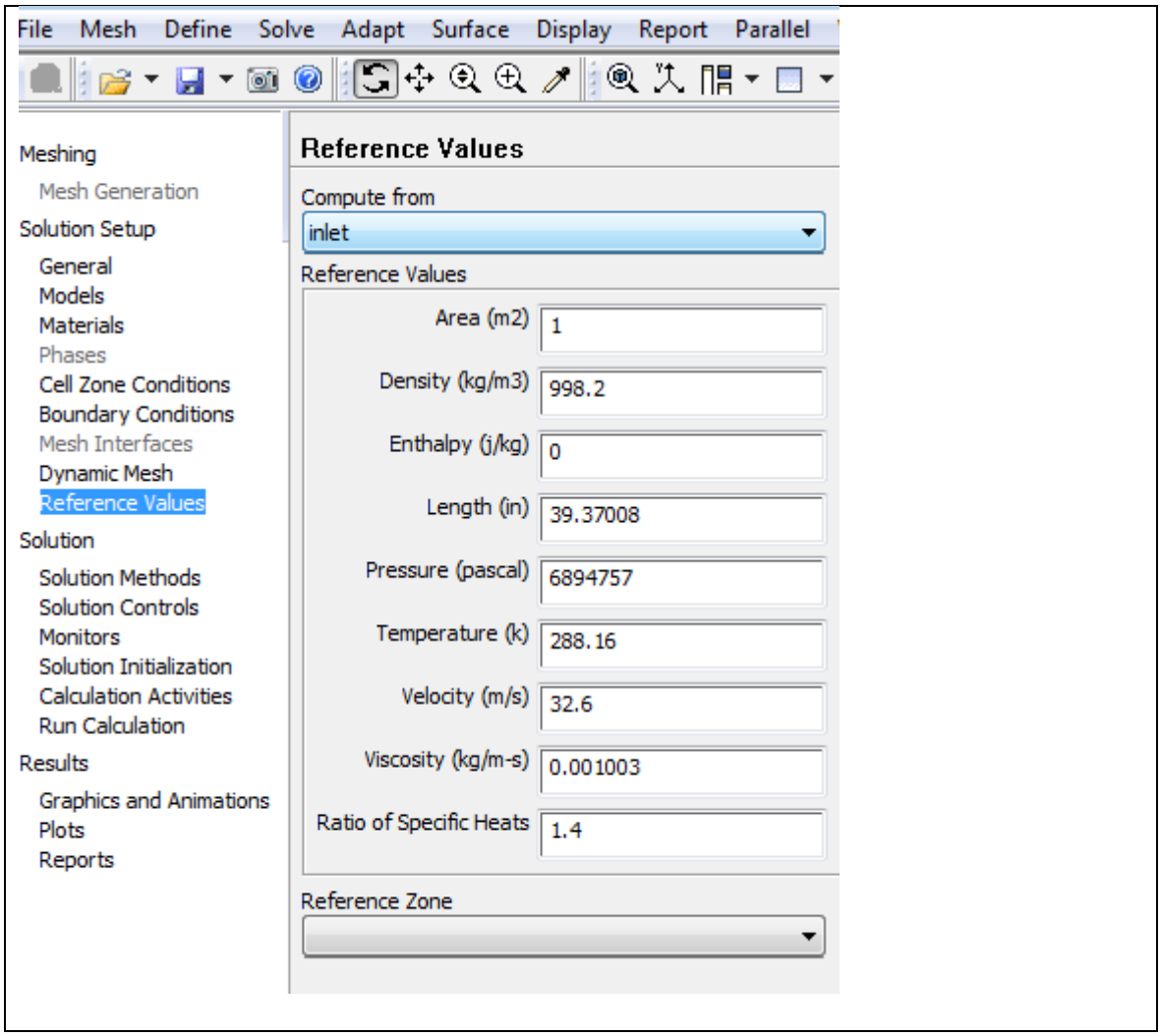

Figure F.33: Setting reference values for computations

23- Setting Solvers (a) standard display, (b) Under transient Formulation, switch to “Bounded Second Order Implicit”

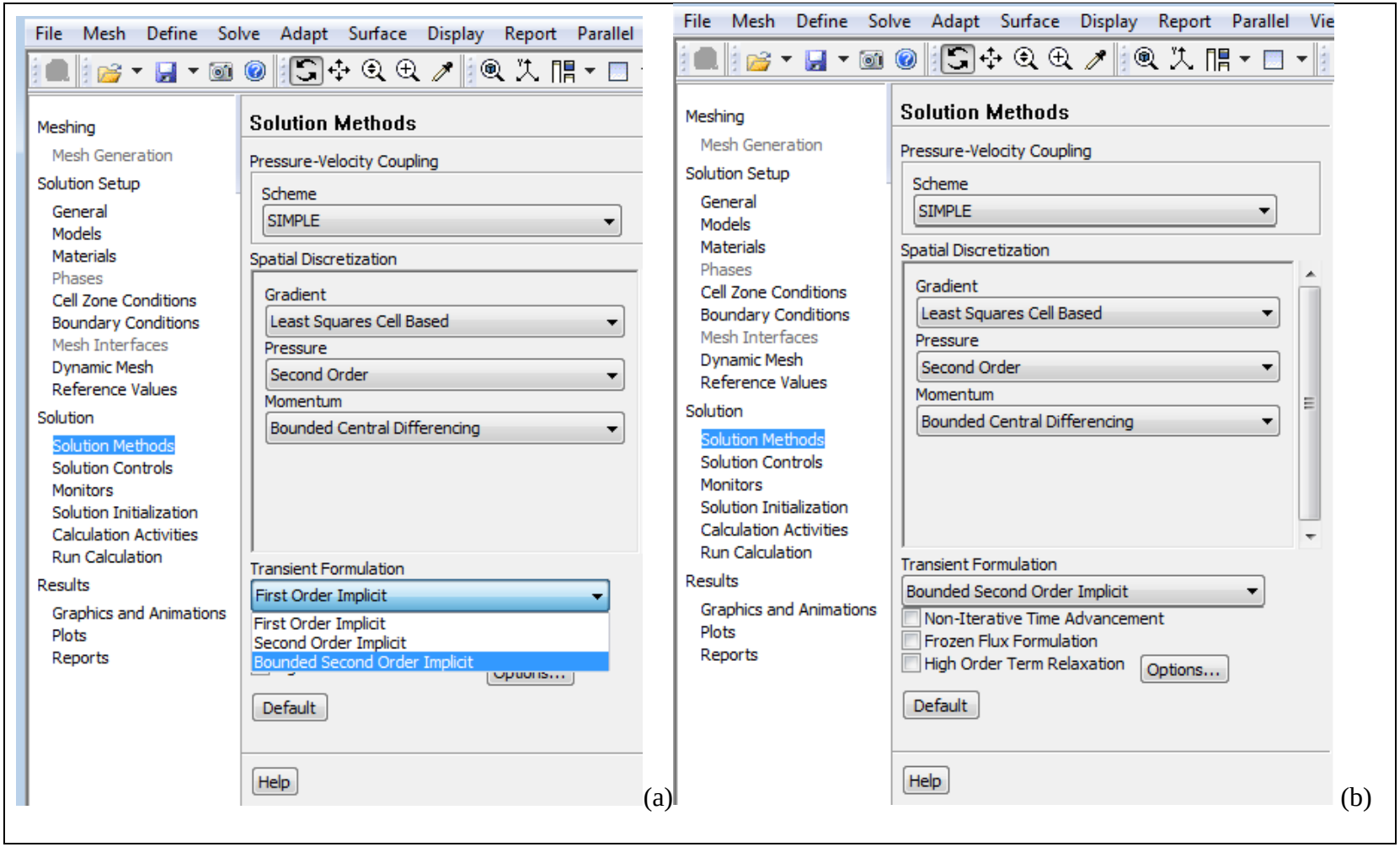

Figure F.34: Setting solvers

24- Setting Under-Relaxation Factors: enter 0.4 for pressure and 0.6 for momentum

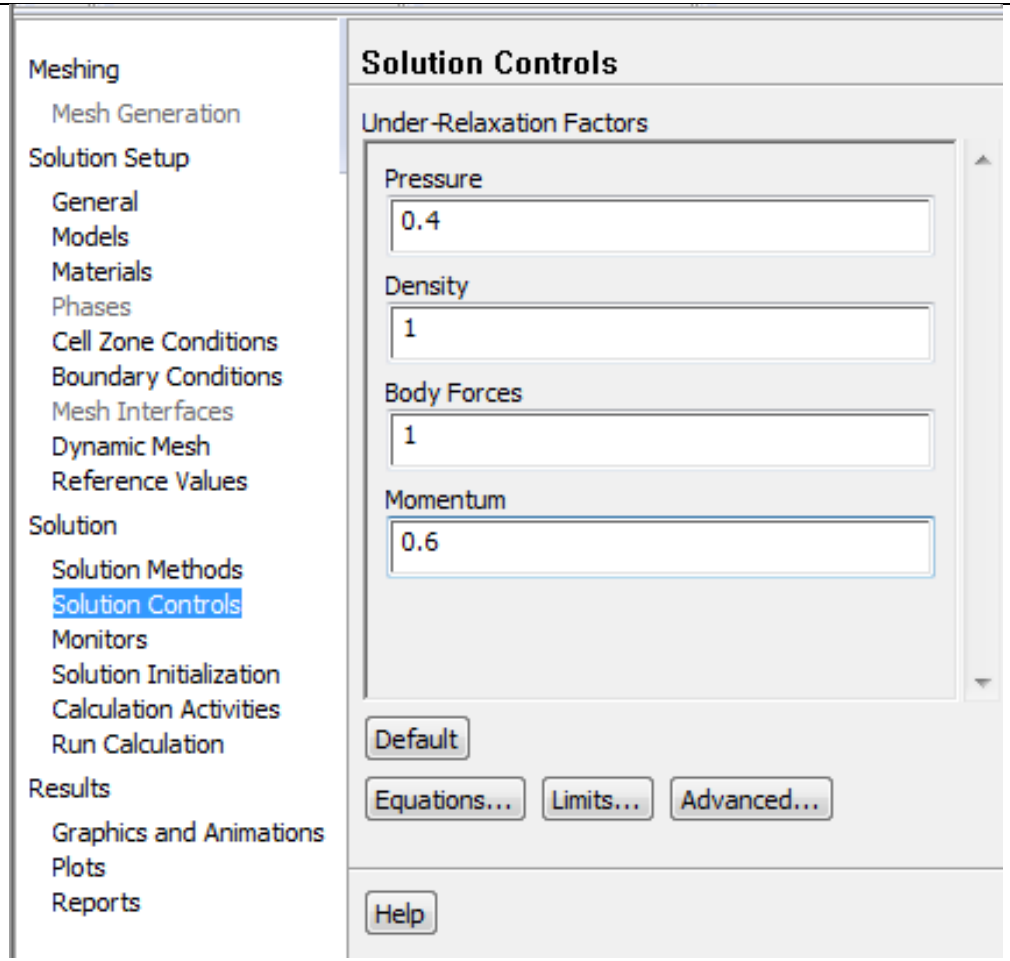

Figure F.35: Setting under relaxation factors

25- Initialize the solution: (a) left-click on “Solution Initialization” (b) Select “inlet” under “Compute from” then left-click on initialize

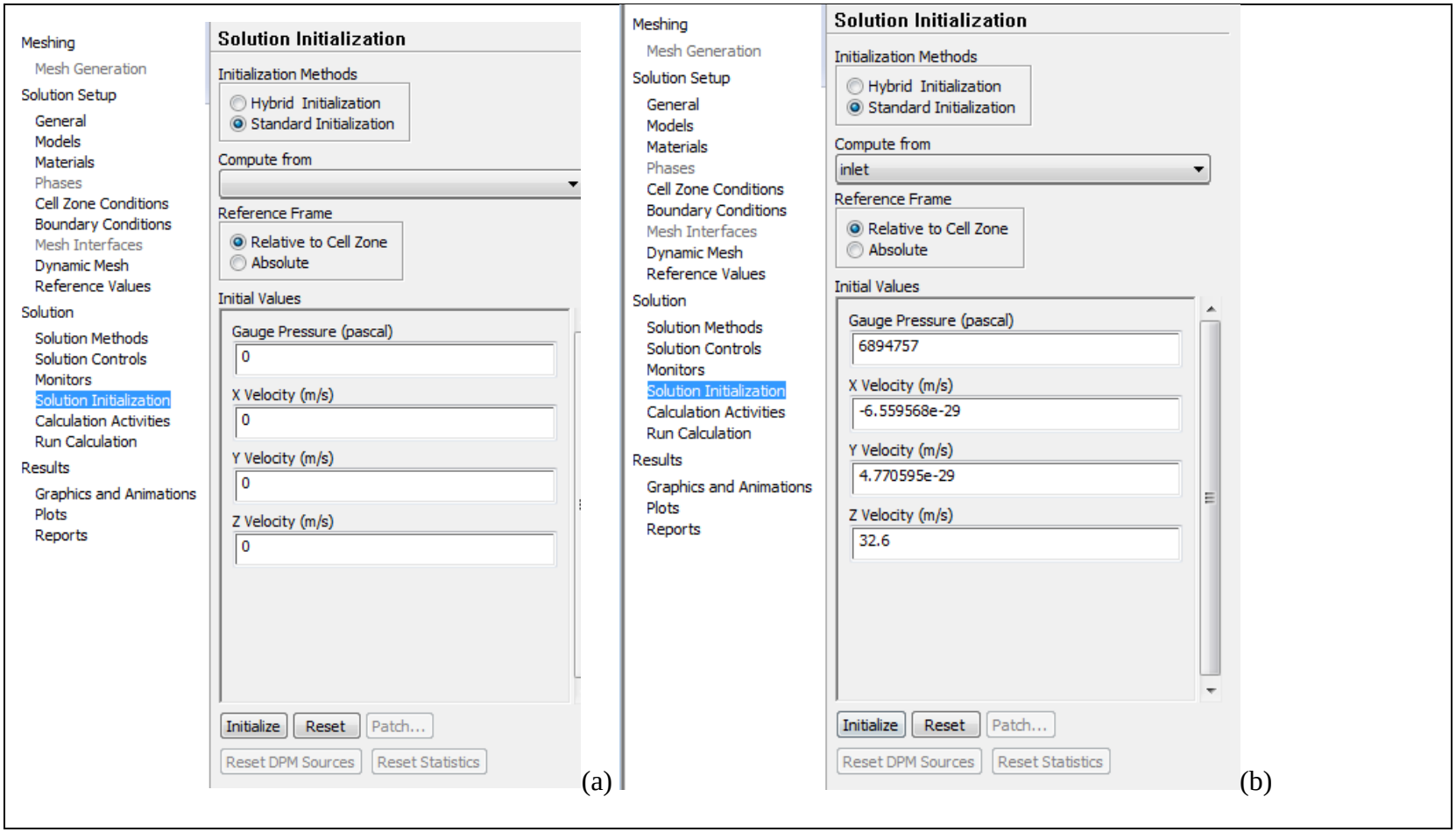

Figure F.36: Initializing the solution

26- Check the mesh prior to running the calculations: (a) left-click on “check,” (b)TUI indicates that the mesh check is complete.

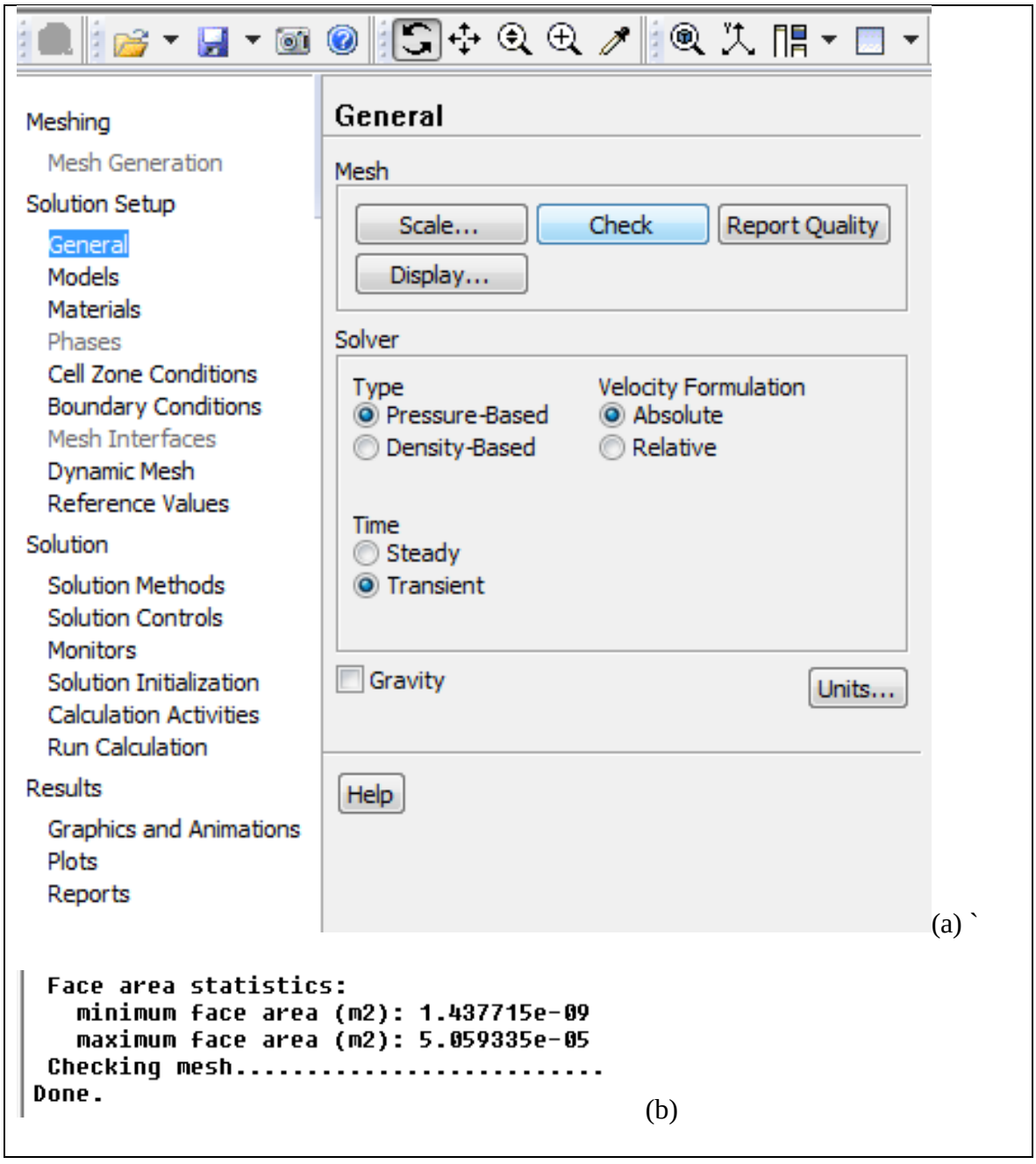

Figure F.37: Checking mesh prior to calculations

27- Setting autosave parameters: (a) display when selecting “Calculation activities” (b) add 1 under “Autosave Every (Time Steps)

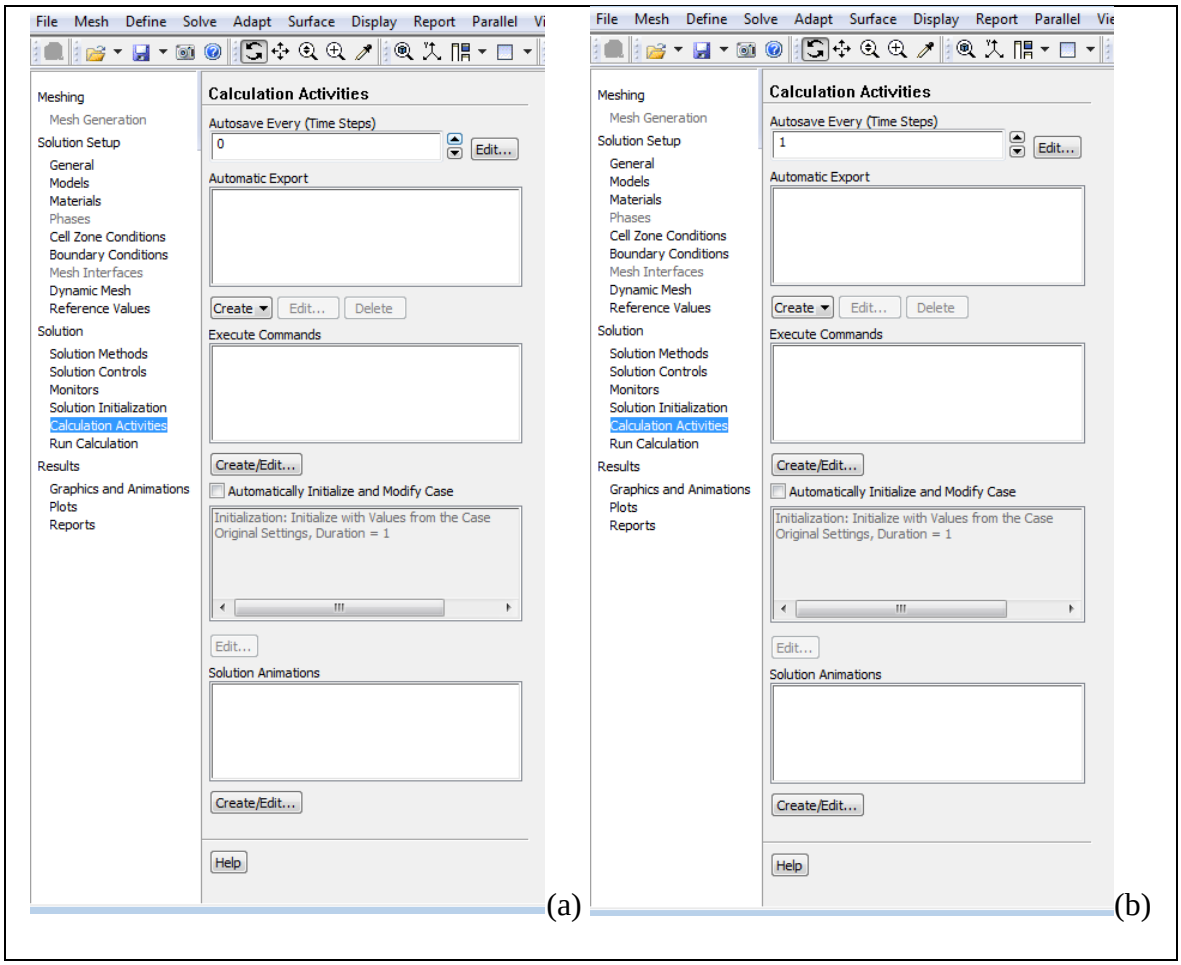

Figure F.38: Setting autosave parameters

28- Running calculations: starting at t=0s, first simulation is set at 500 iterations per time step, for 0 timestep, and a timestep size of 0.01sec, next iteration is at 1 timestep, followed by 99 timestep, both at 500 iterations

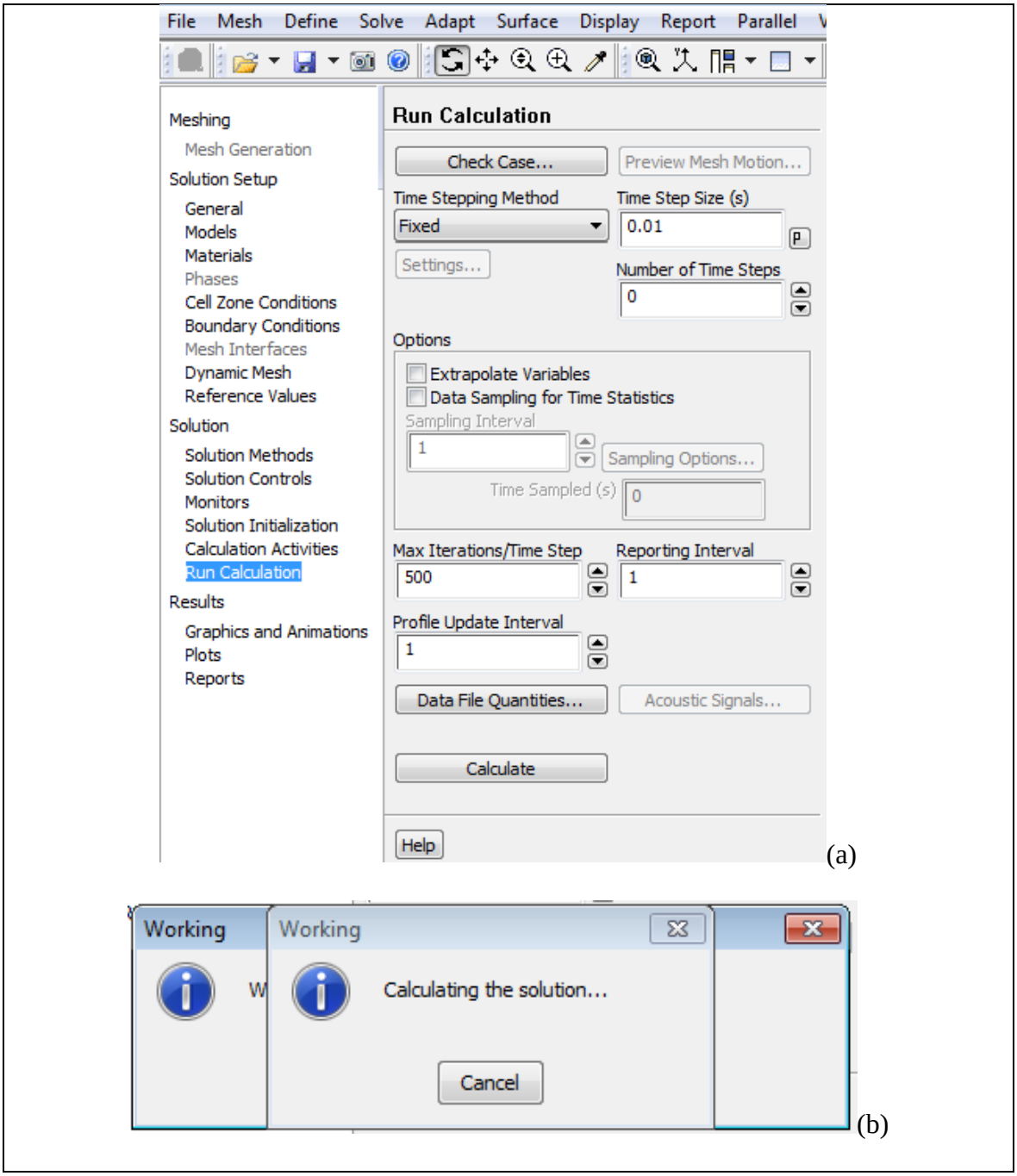

Figure F.39: Running initial calculations

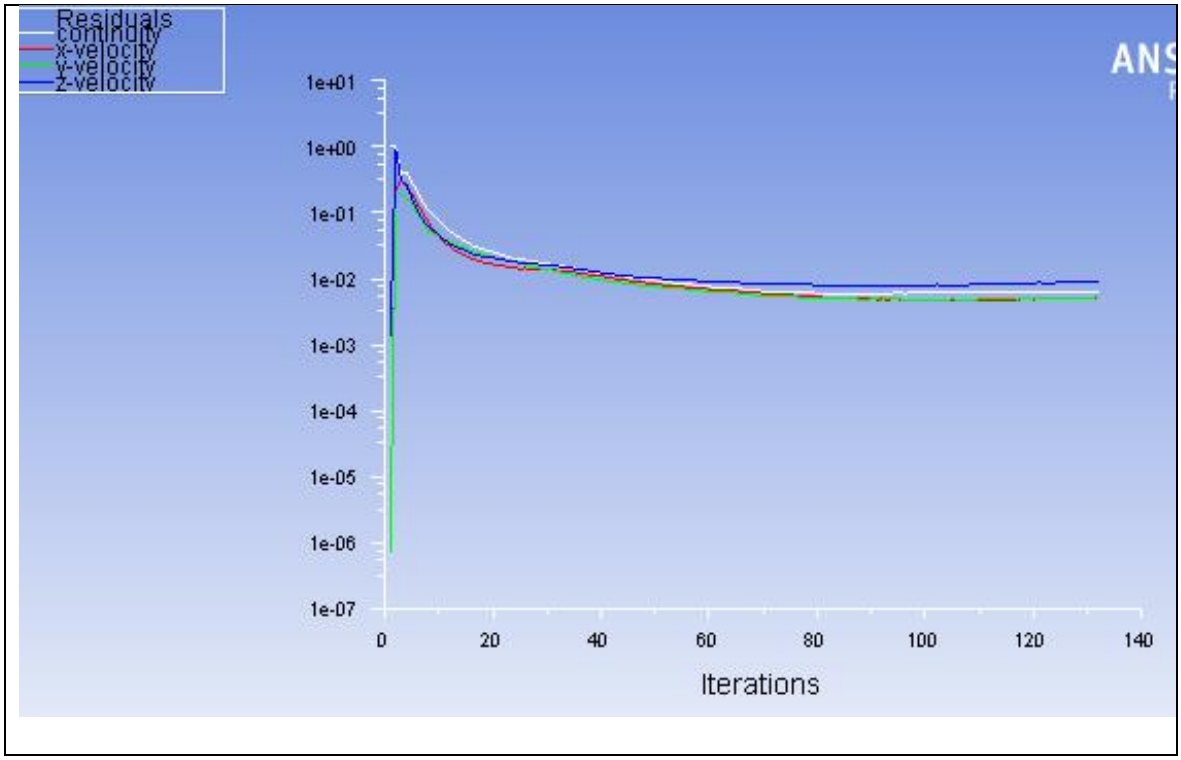

Figure F.40: Residual monitoring during initial calculations

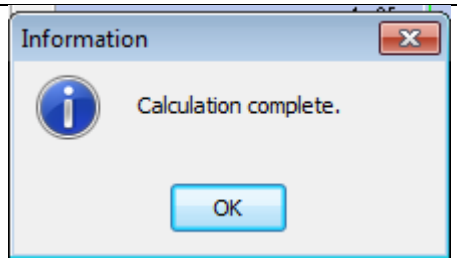

Figure F.41: Display indicating calculation completion

29- Increase number of time steps to 1.

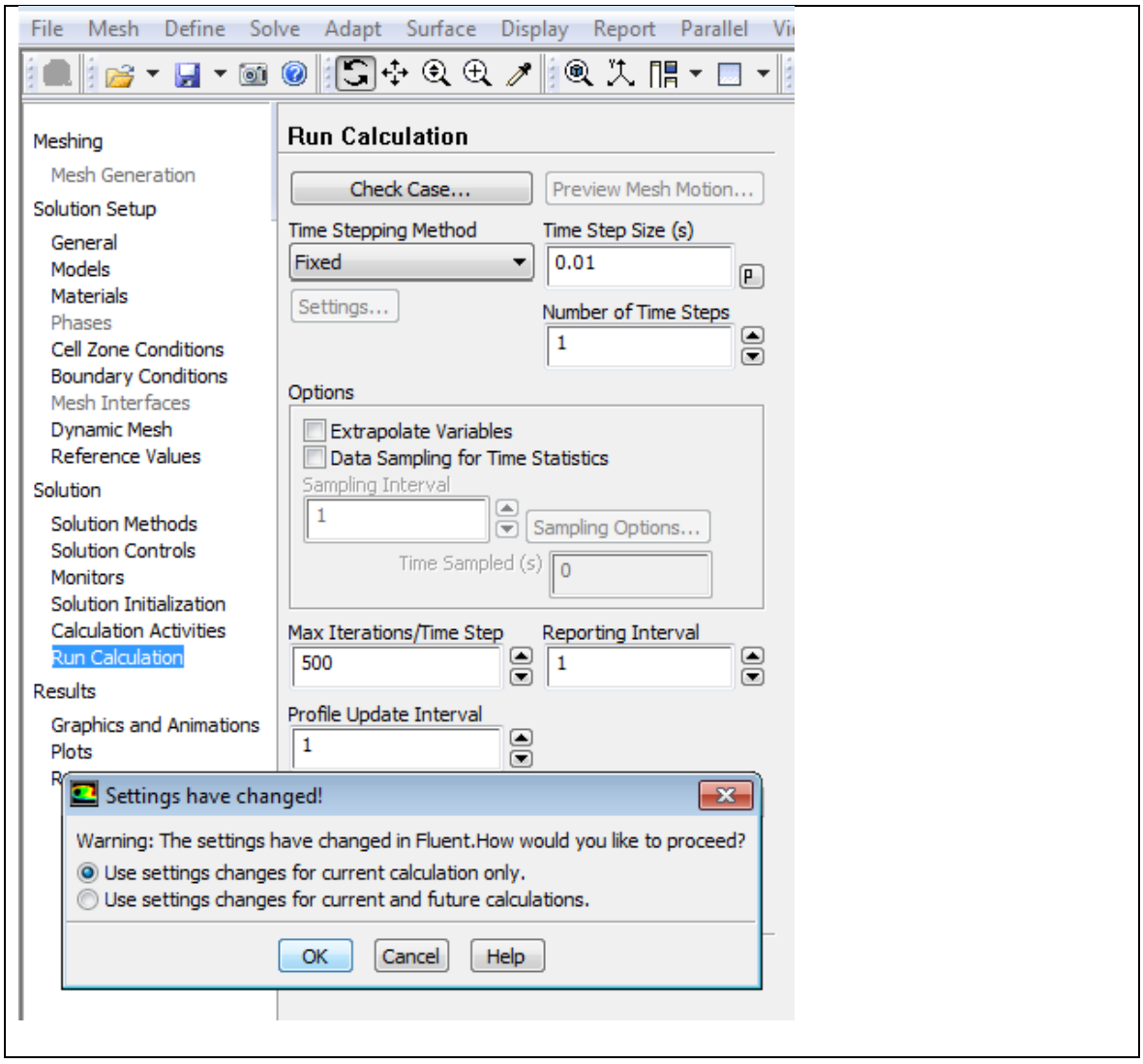

Figure F.42: Running calculation with non-zero steps

30- Scaled residuals view during simulation

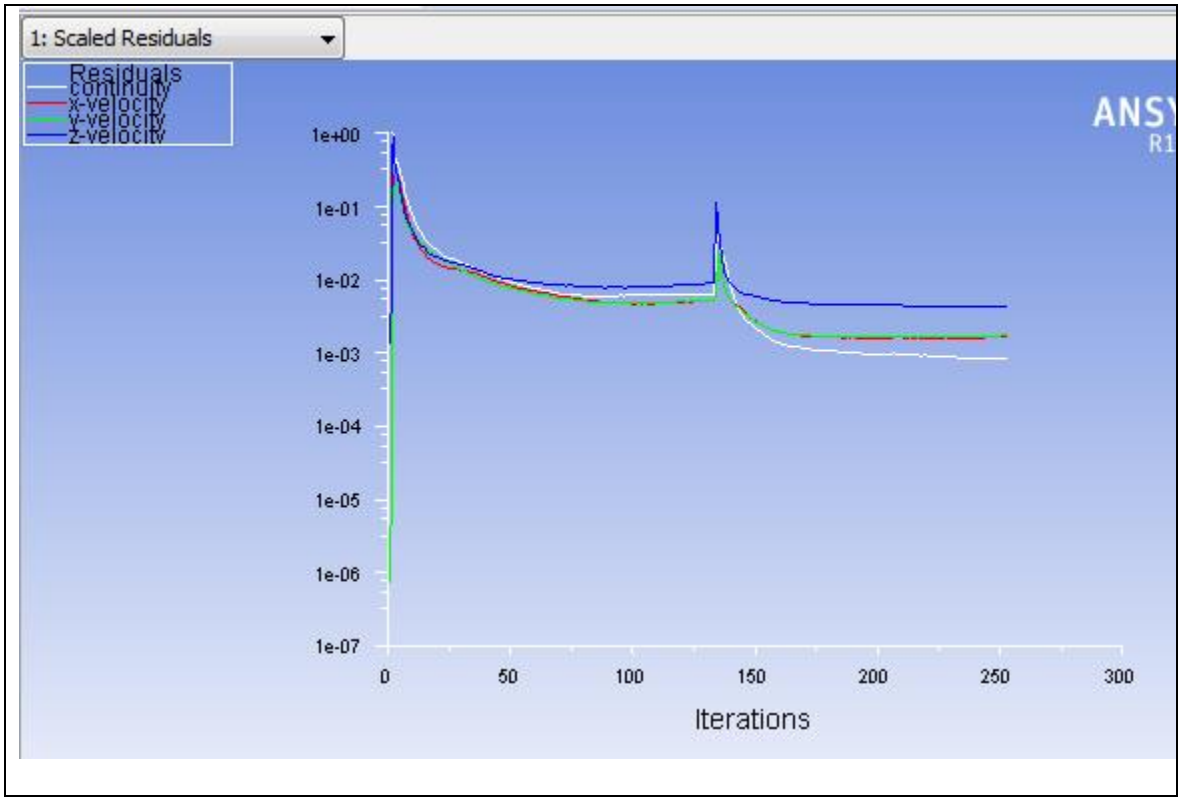

Figure F.43: Scaled residuals plots during computations

31- (a) Under “Graphic and Animation” select “Contours” then left-click on “Set Up,”

(b) Contour selection display

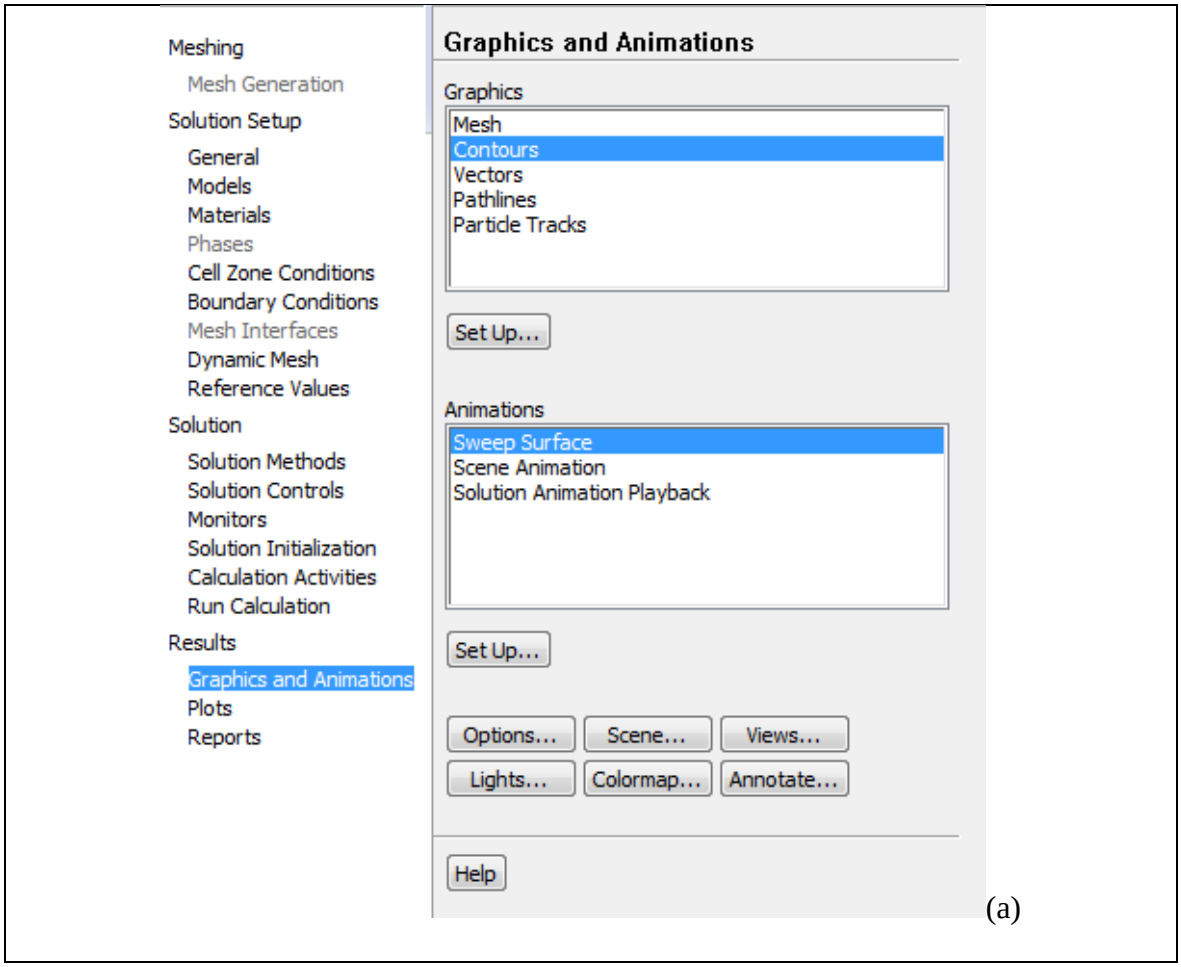

(a)

Figure F.44: Setting up contours

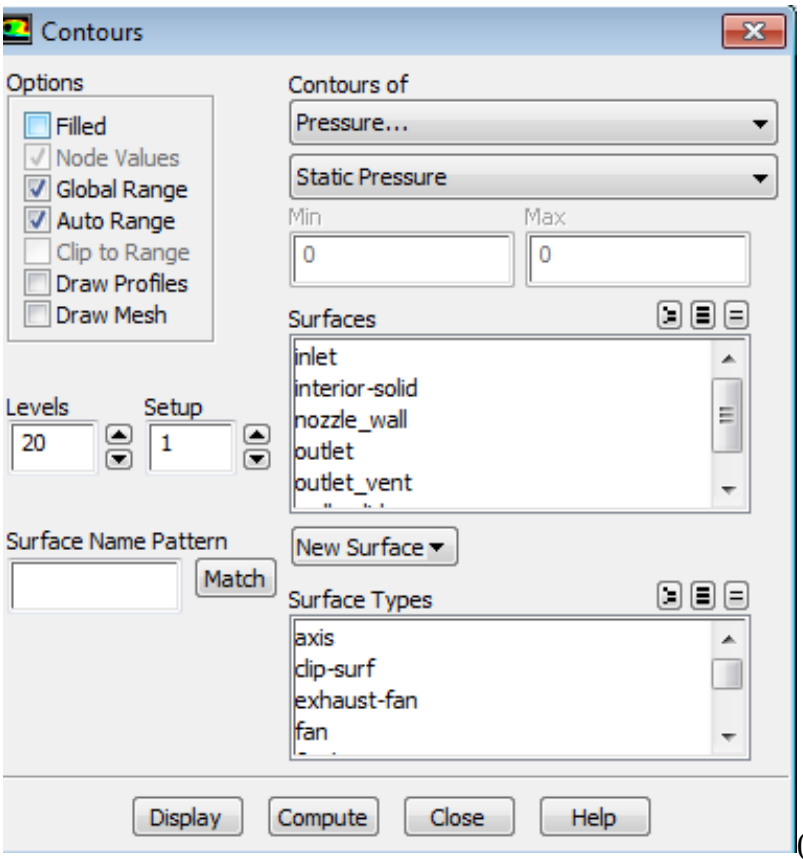

(b)

Figure F.44 (continued)

32- Building plane yz: (a) Left-click on “New-surface”, select “Plane,” (b) Display for plane definition, (c) select “Point and normal,” enter point (0, 0, 0) for (x0, y0, z0) and enter (1, 0,0) for (ix, iy, iz) corresponding to Normal vector.

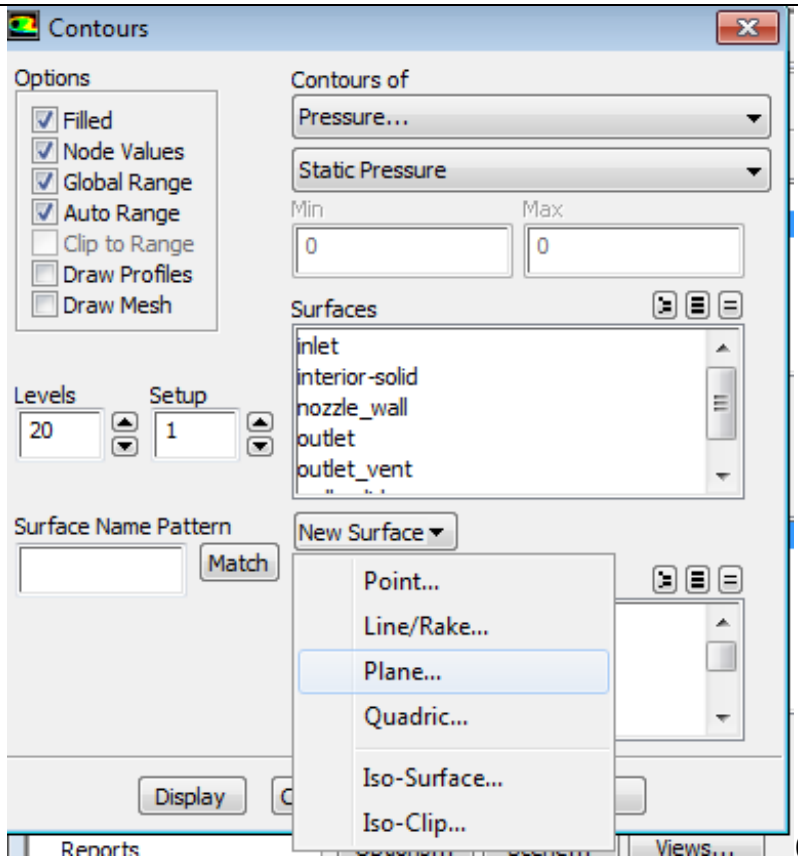

(a)

Figure F.45: Defining plane YZ

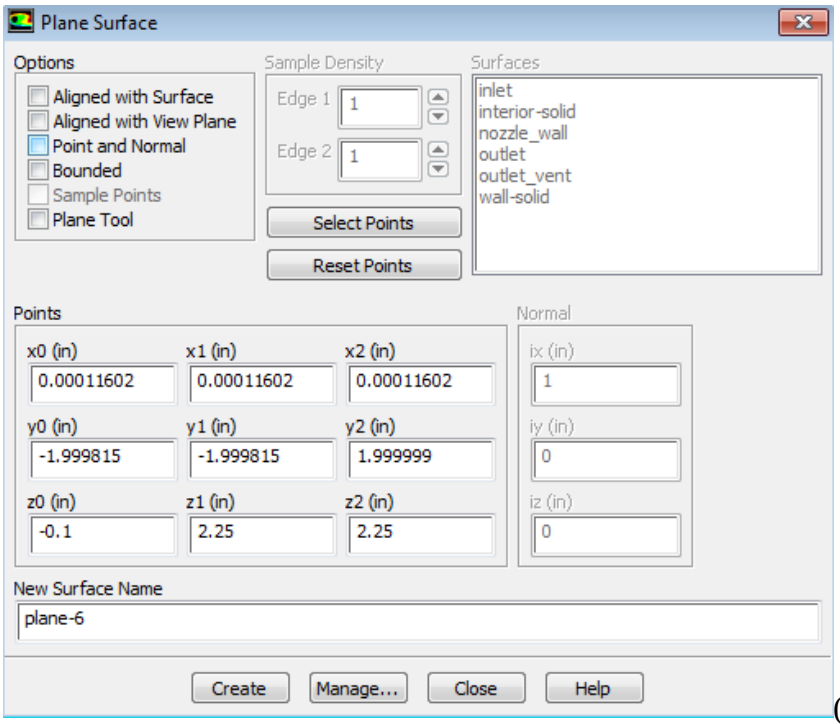

(b)

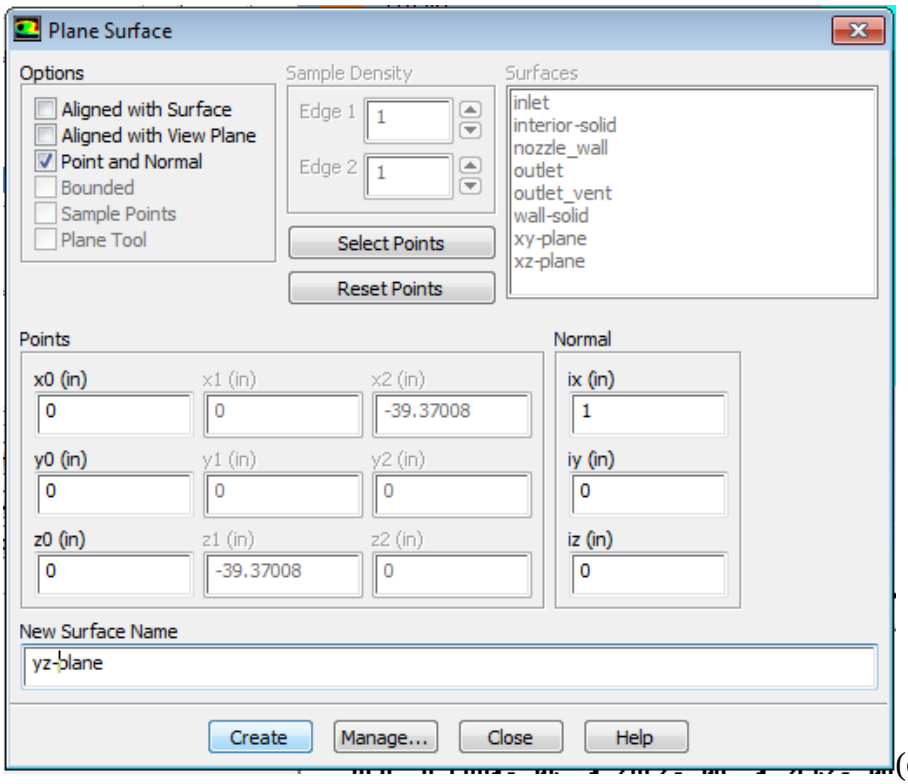

(c)

Figure F.45 (continued)

33- After the planes are created, (a) select the plane/surface where the contour should be drawn on, then left-click on “Display” (b) Contour (c) refine the plot by increasing the “Levels” from the initial 20 to 100, (d) new contour with refined levels

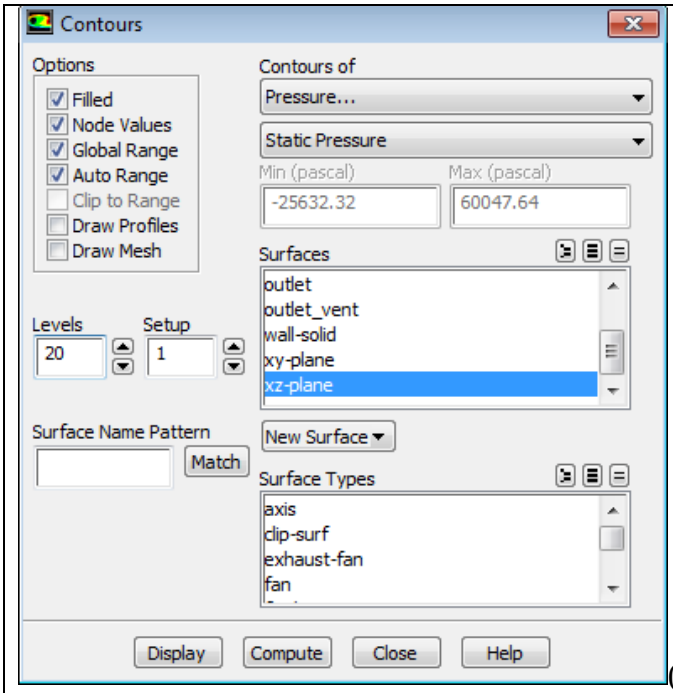

(a)

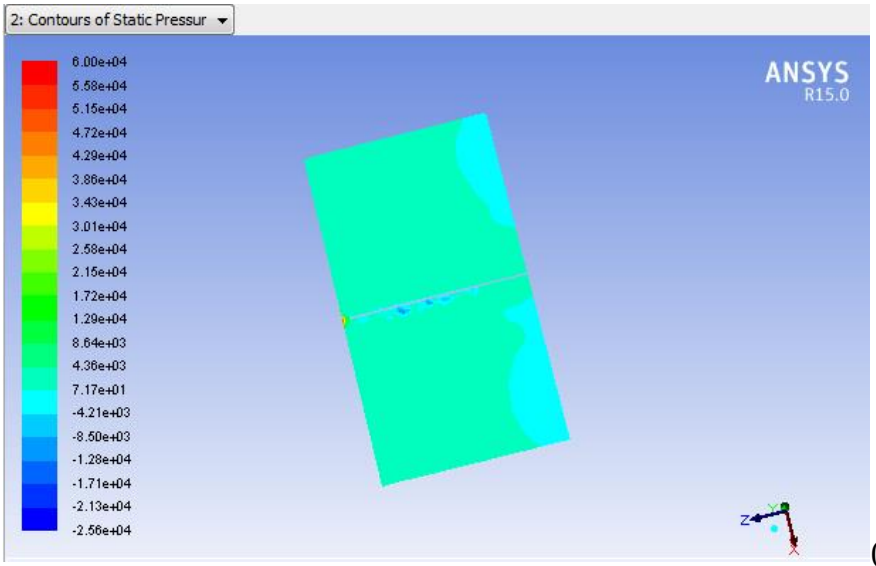

(b)

Figure F.46: Displaying properties contour

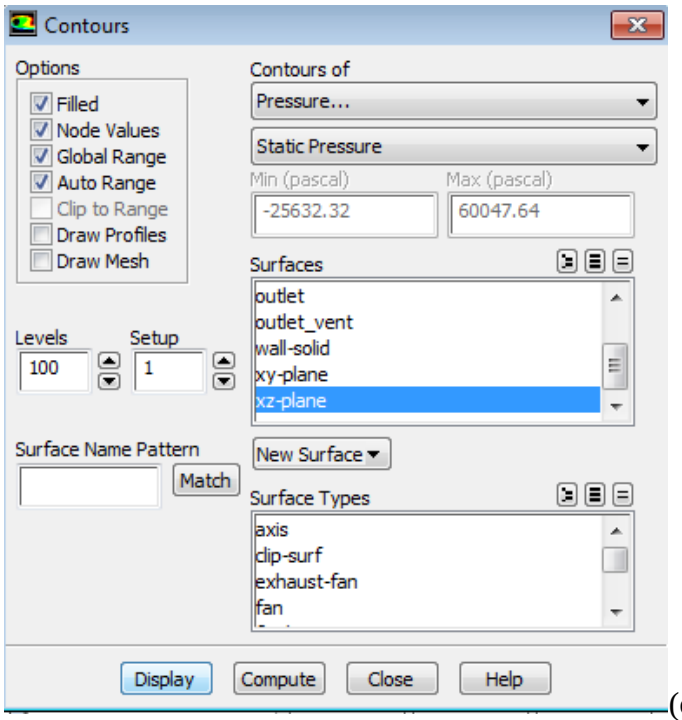

(c)

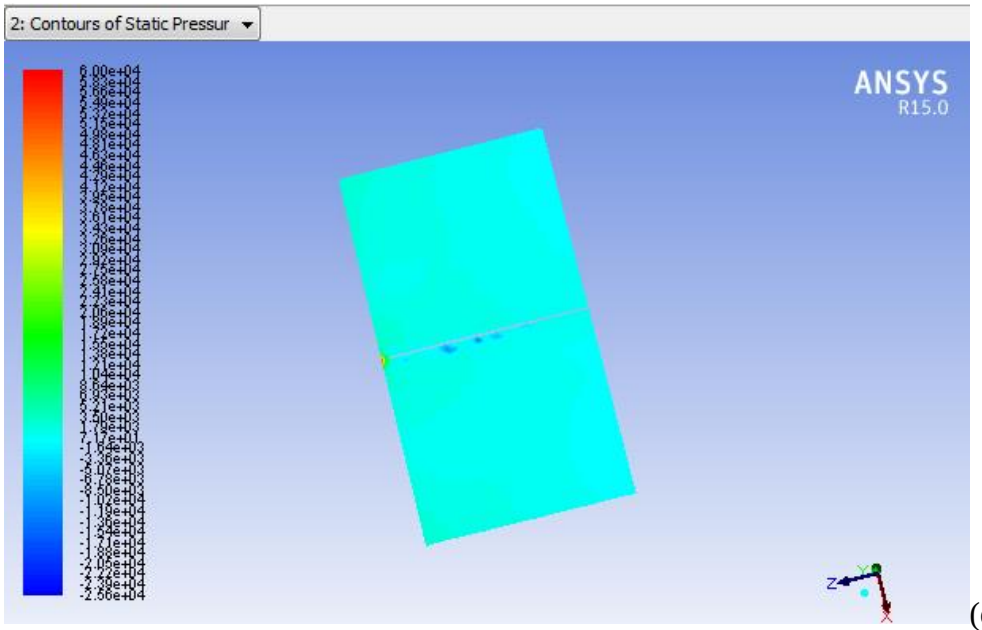

(d)

Figure F.46 (continued)

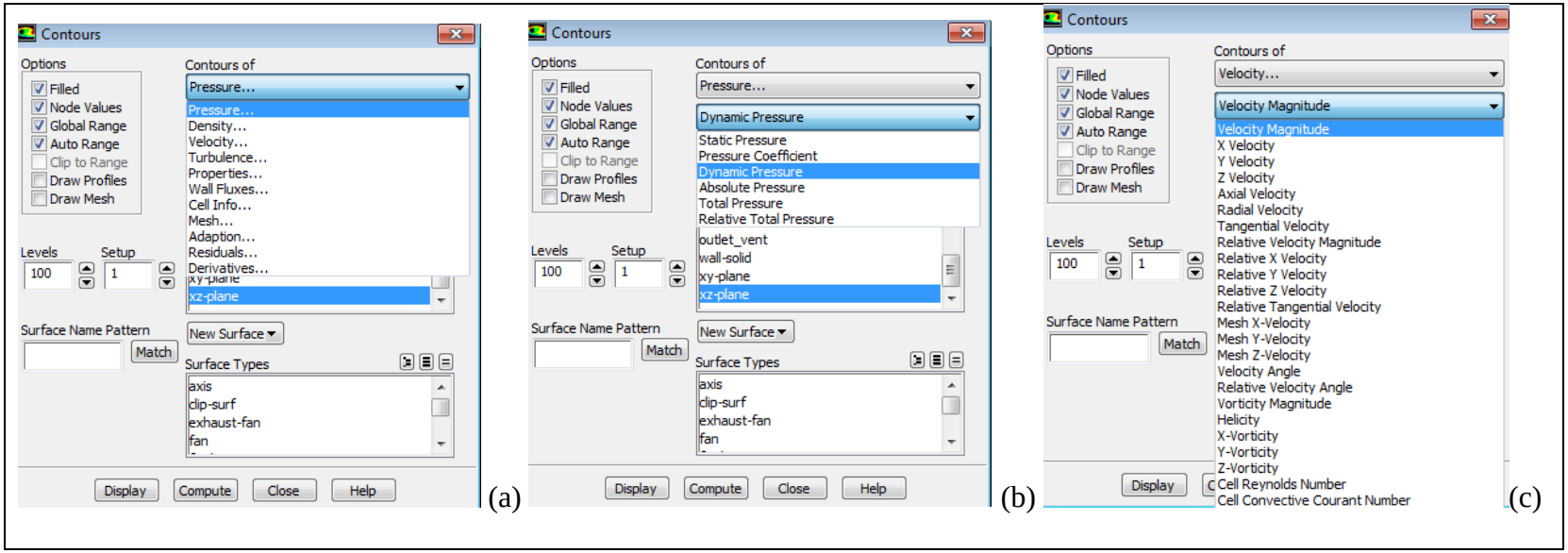

Figure F.47: (a)Physical properties available for contour plots, (b)types of pressure contours and (c) types of velocity contours

34- (a)Under Plots, select XY Plot then left-click on “Set-Up,” (b) and (c)Left-click on write to file to save file to an external file, when unchecked it will just plot the file within the ANSYS Fluent plot window. (d) select velocity then velocity magnitude, (e) select plane for node and property values

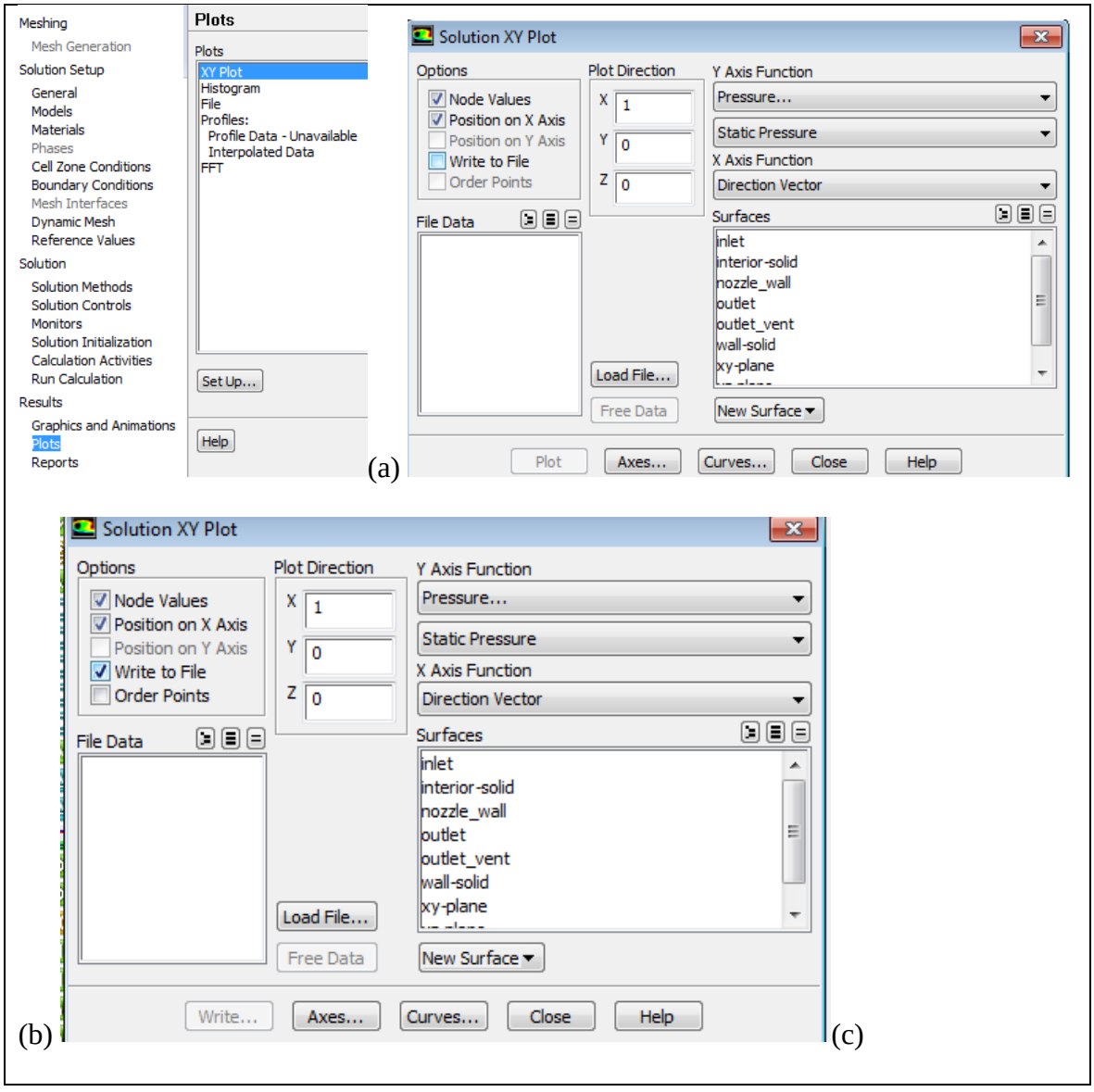

Figure F.48: Creating an axial velocity vs node position XY plot

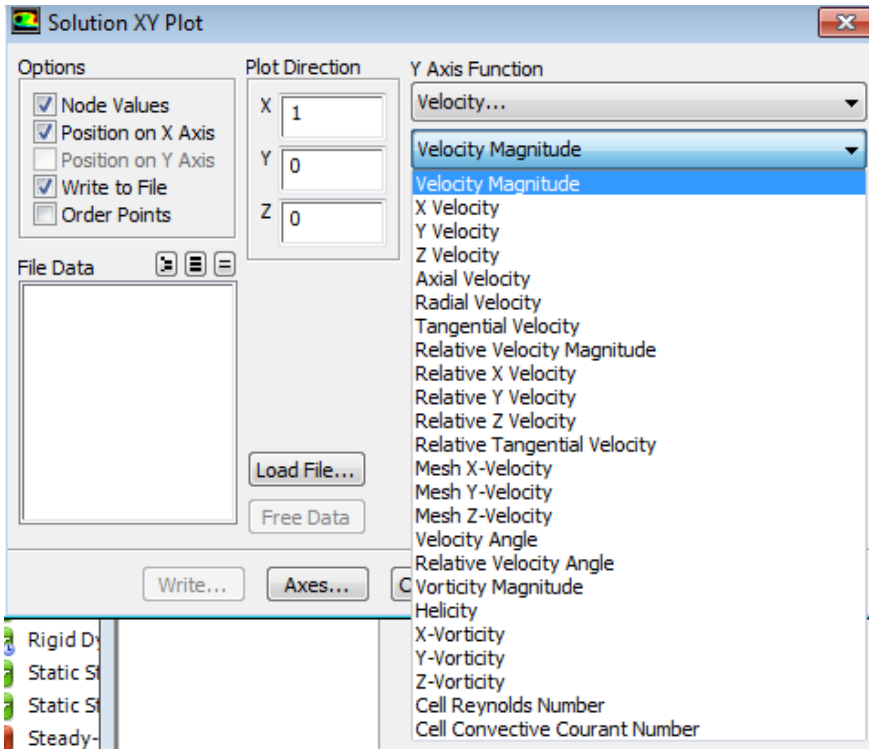

(d)

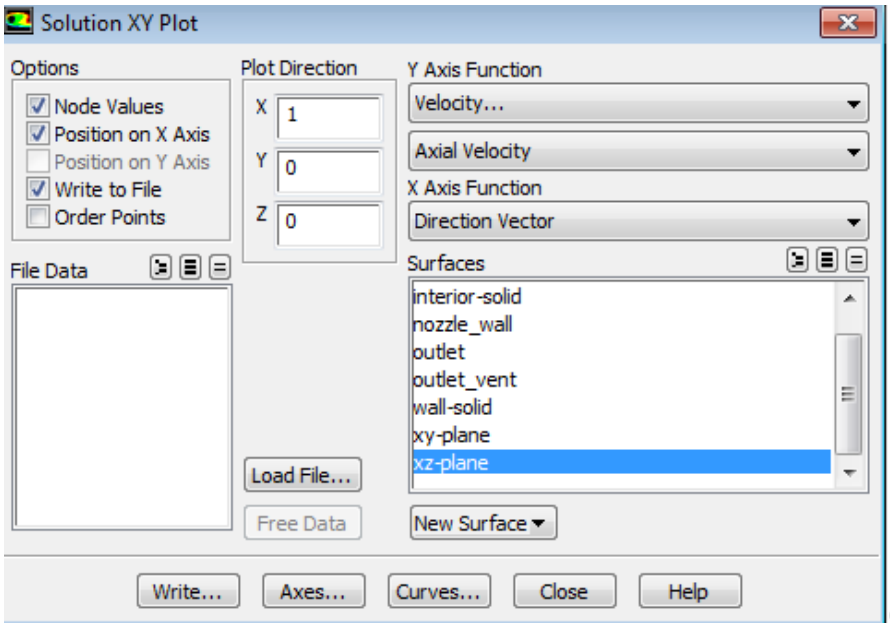

(e)

Figure F.48 (continued)

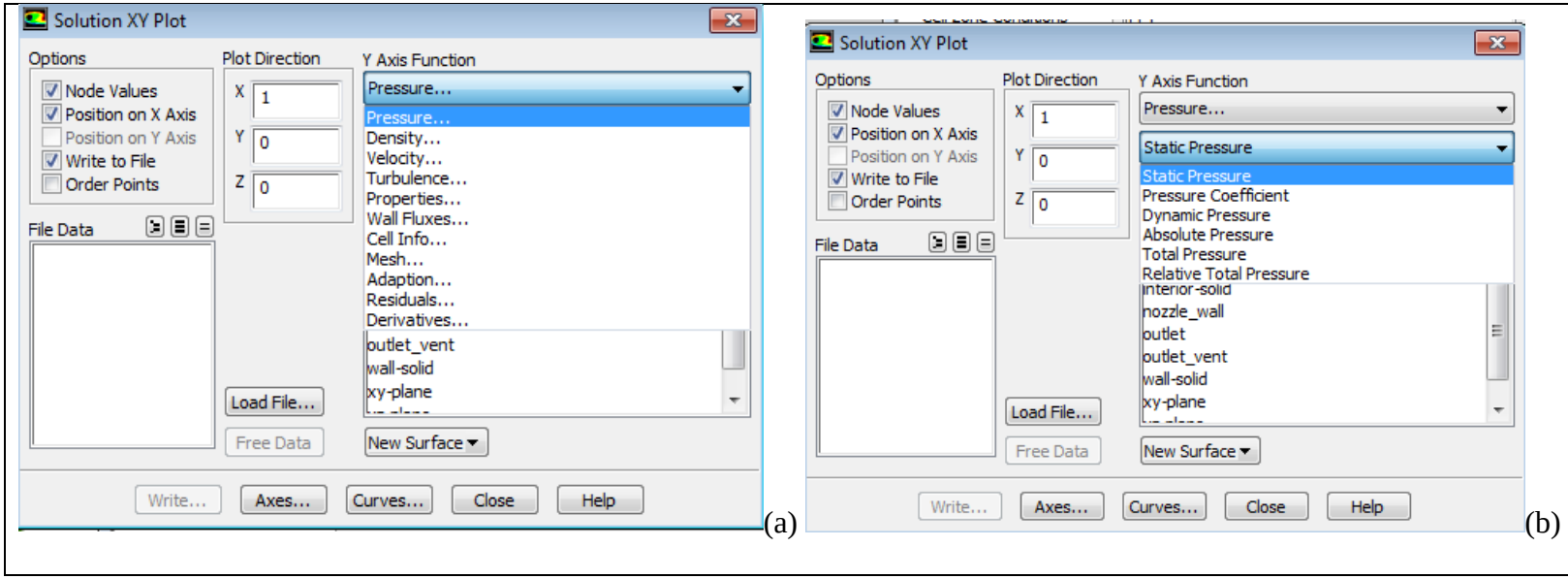

Figure F.49: (a)Physical Properties available for XY plots in ANSYS Fluent 15: (b) Pressure components available for XY plots in ANSYS Fluent 15

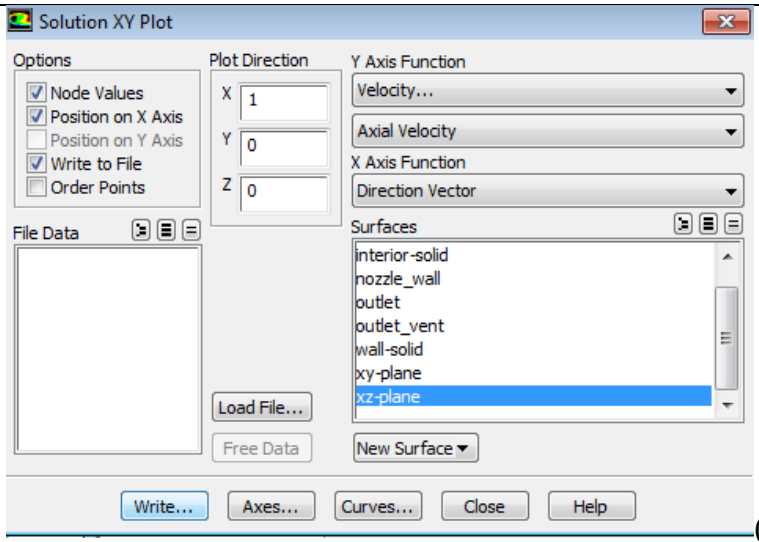

(a)

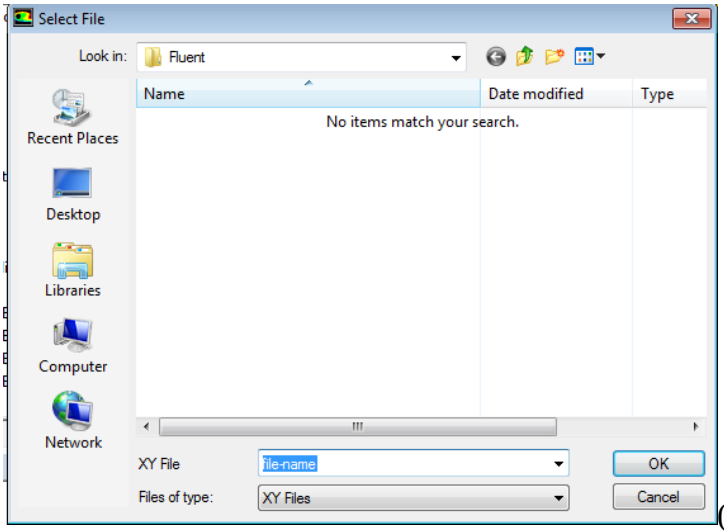

(b)

Figure F.50: Saving an XY plot in txt format

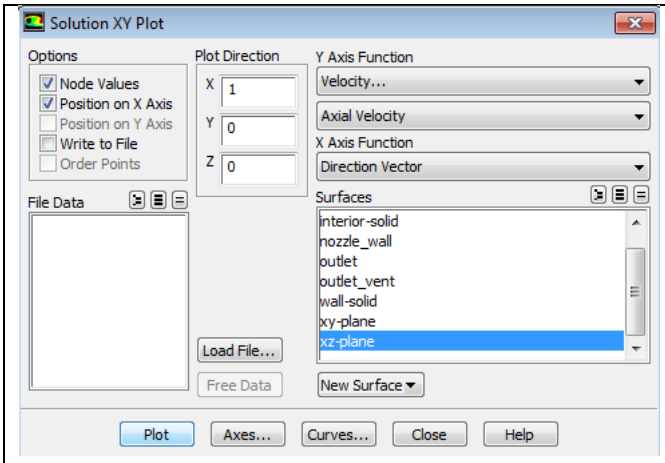

(a)

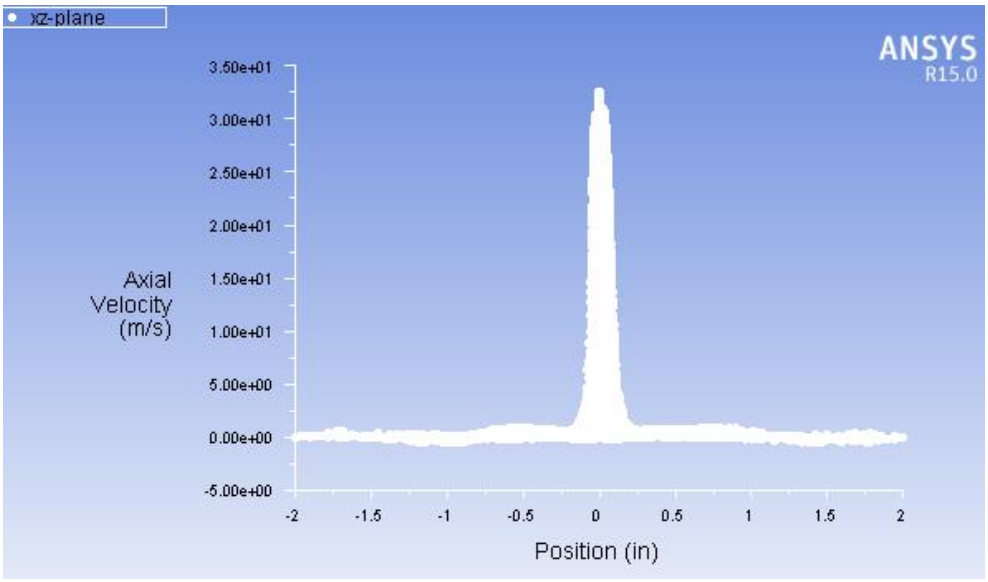

(b)

Figure F.51: XY-plot of axial velocity vs node position

35- Update geometry after simulation: After generating the dissolution data, with considerable dissolution values, a new turbulent jet impingement flow simulation is started. (a) Setting new ANSYS Fluent simulation by duplicating the previous workflow, right-click on “Fluid Flow (Fluent)” then left-click on “Duplicate.” (b) Right-click on Geometry of new model workflow, and left-click on Edit Geometry

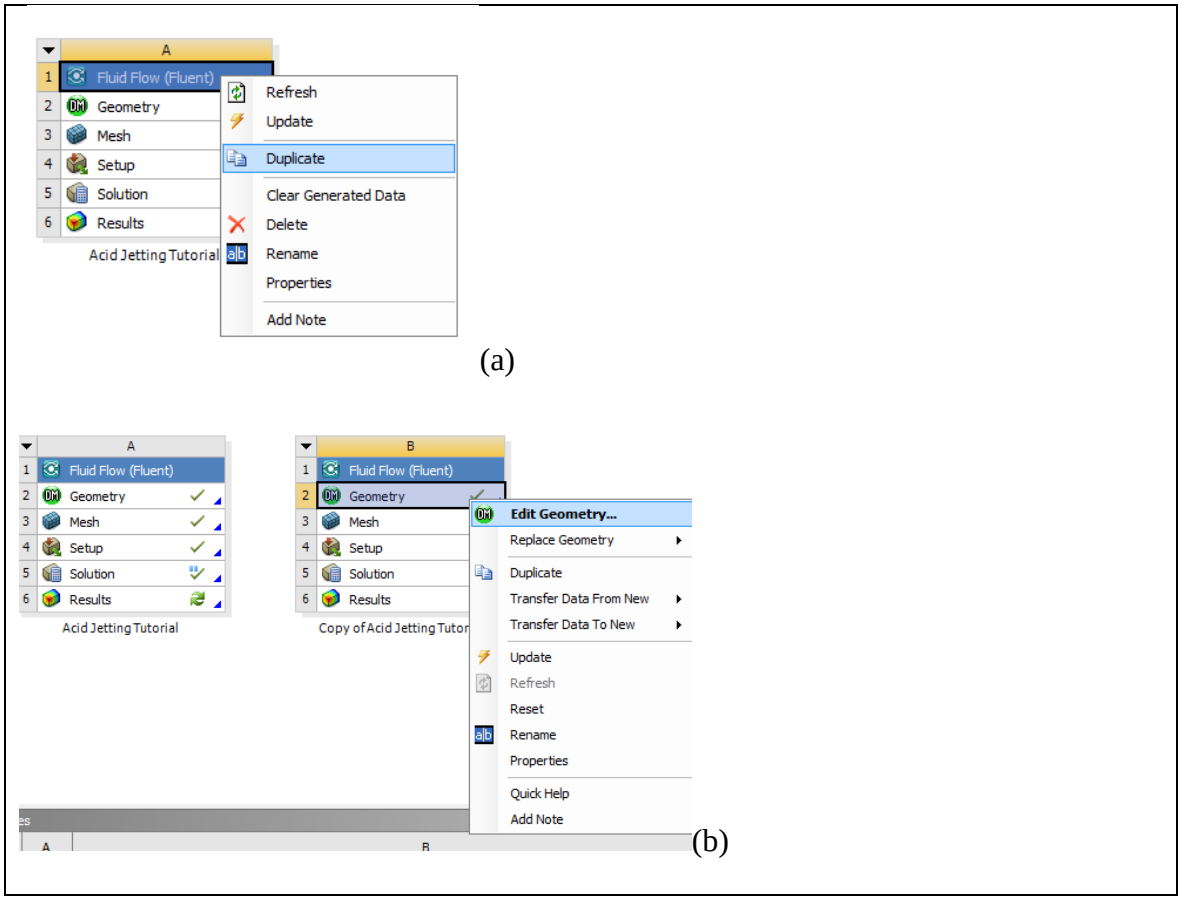

Figure F.52: Setting new ANSYS Fluent turbulent jet impingement model from previous setup

Delete outlet surface in order to redraw it, it will be the only surface changing on the entire geometry. (a) right-click on “Outlet” then select Delete

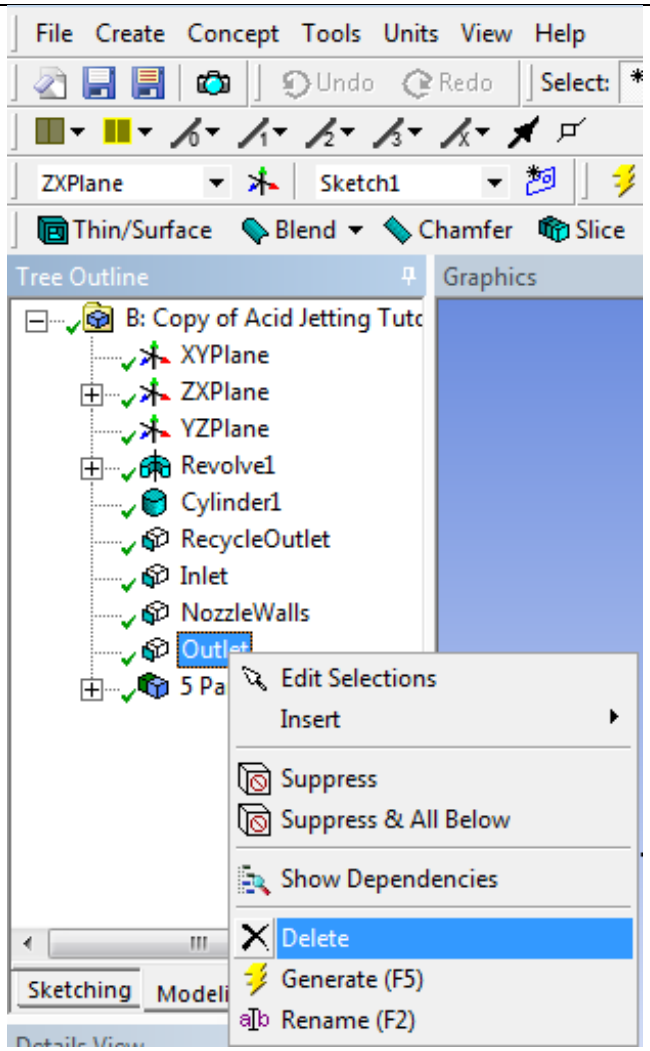

Figure F.53: Deleting previous outlet surface to redraw it for new geometry

(a) Under “sketching” menu, select “Modify” then select “Split at Select.” (b) current 2D geometry, (c) close up of 2D Geometry where the geometry modification would occur. (d) click on any portion of the east vertical line, the portion below the point will turn red and the top part will remain blue. (e) select “cut” (f) right click on red segment then (g) select delete

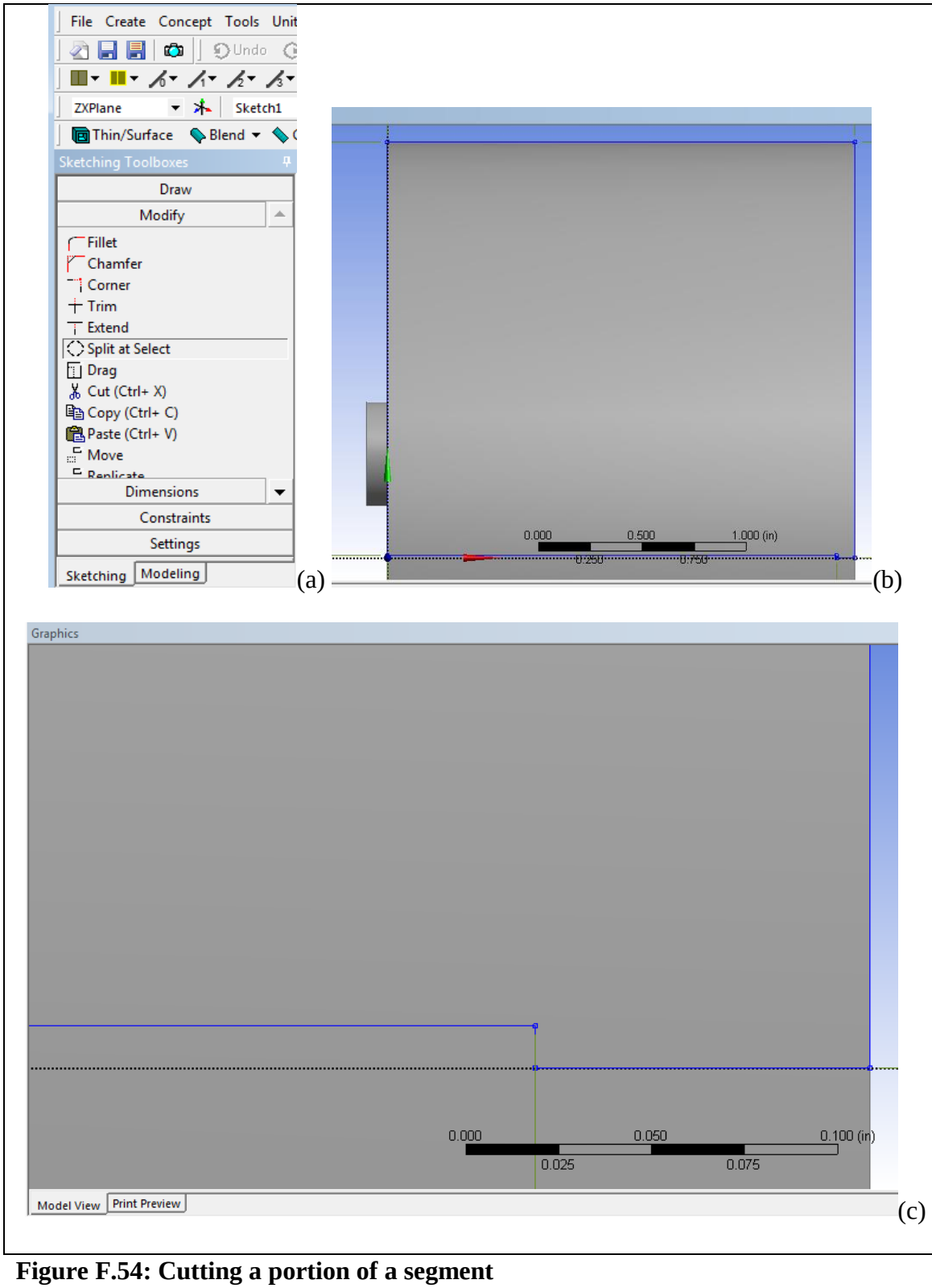

Figure F.54: Cutting a portion of a segment

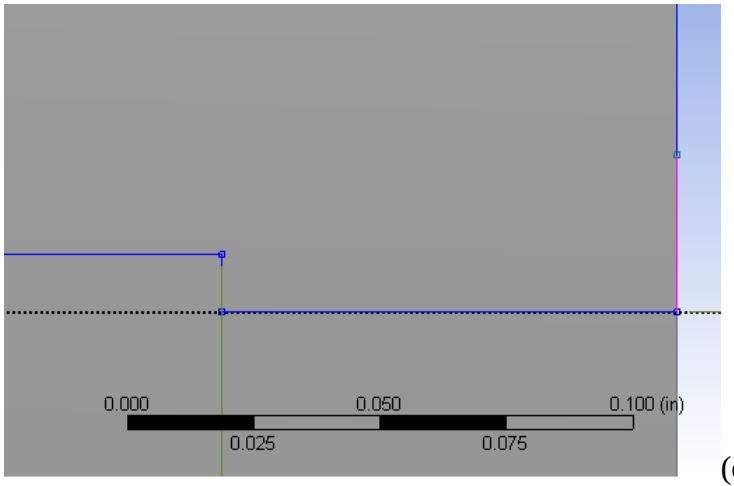

(d)

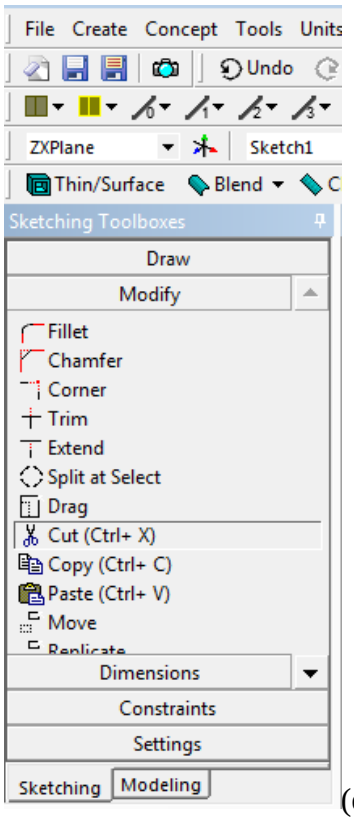

(e)

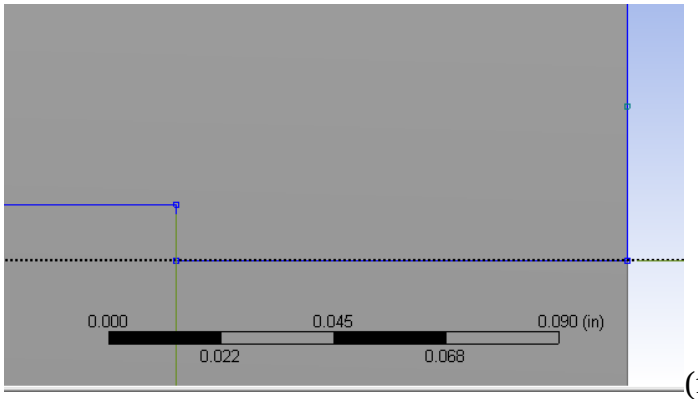

(f)

Figure F.54 (continued)

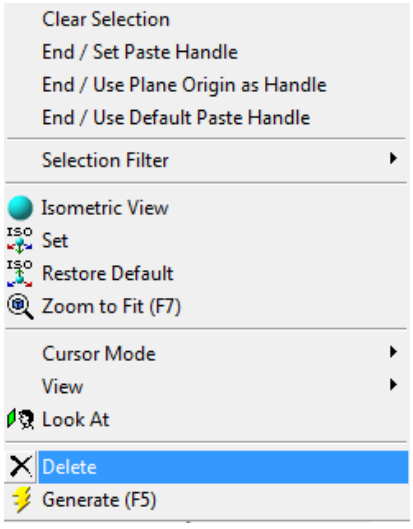

(g)

Figure F.54 (continued)

Incorporating results from dissolution model: Dissolution data indicates furthest axial dissolution of 0.2 inches on the centerline ((a) and (b)segment H6 is extended to .011 inches from the initial standoff distance of 0.09 inches) and furthest radial dissolution of 0.2 inches away from the centerline ((c) and (d) segment V7 is reduced to 1.98 inches), (e)select spline under “sketching” ad “draw”, (f) Draw spline connecting the points as indicated by dissolution results. (g) under constraints, select coincident to have the spline end points match the connected segments end points, (h)generate new revolve feature including the geometry modifications

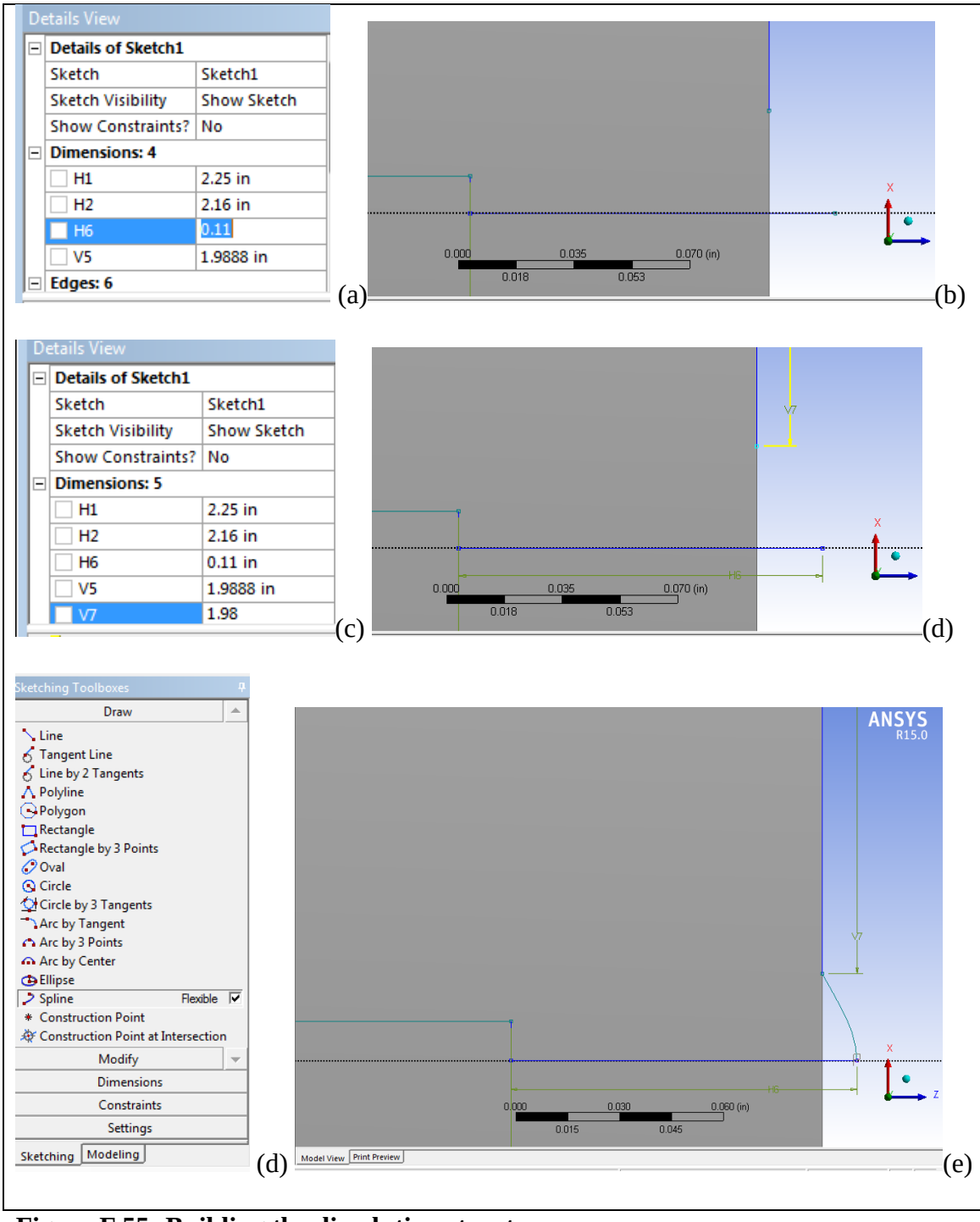

Figure F.55: Building the dissolution structure

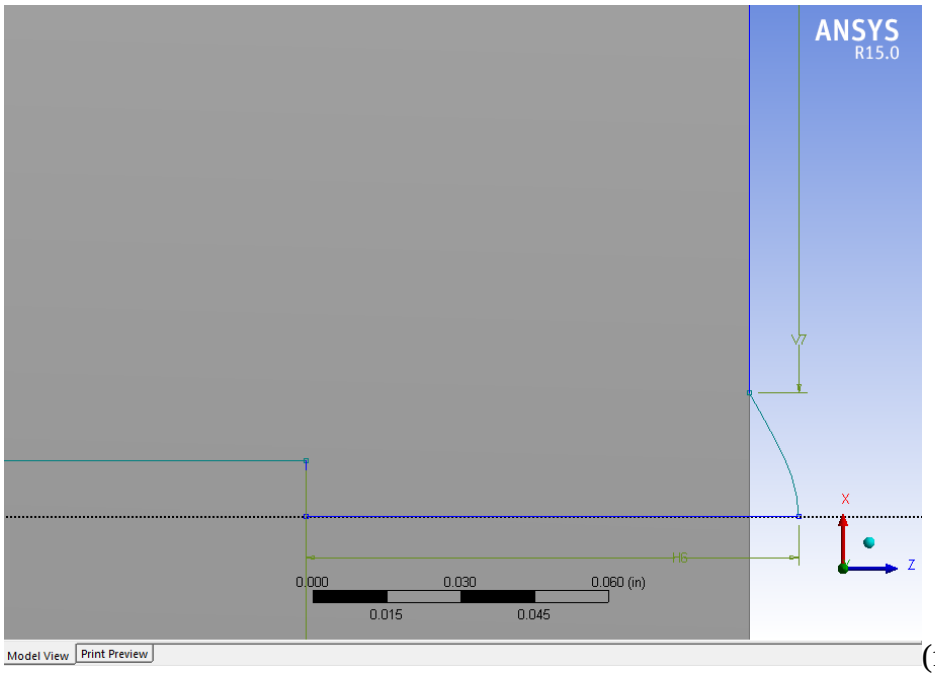

(f)

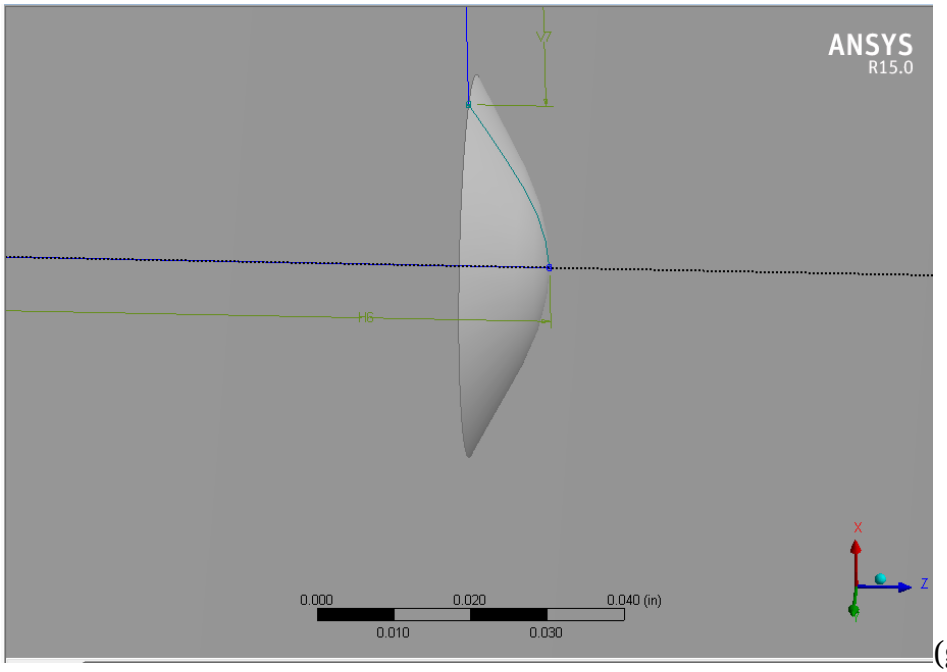

(g)

Figure F.55 (continued)

37-Rebuild the new outlet surface including the dissolution structure.

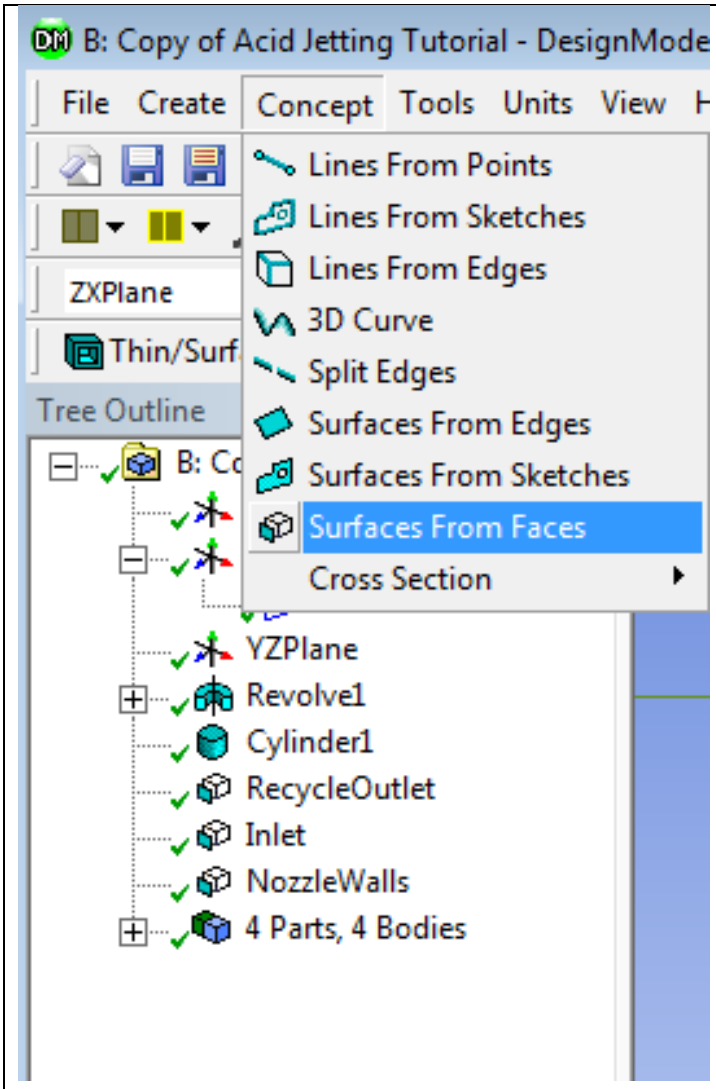

Figure F.56: Rebuild new outlet surface

38- Mesh new geometry: (a)Right-click on “Mesh” then Left-click on “Update.” (c) Display once the meshing is completed.

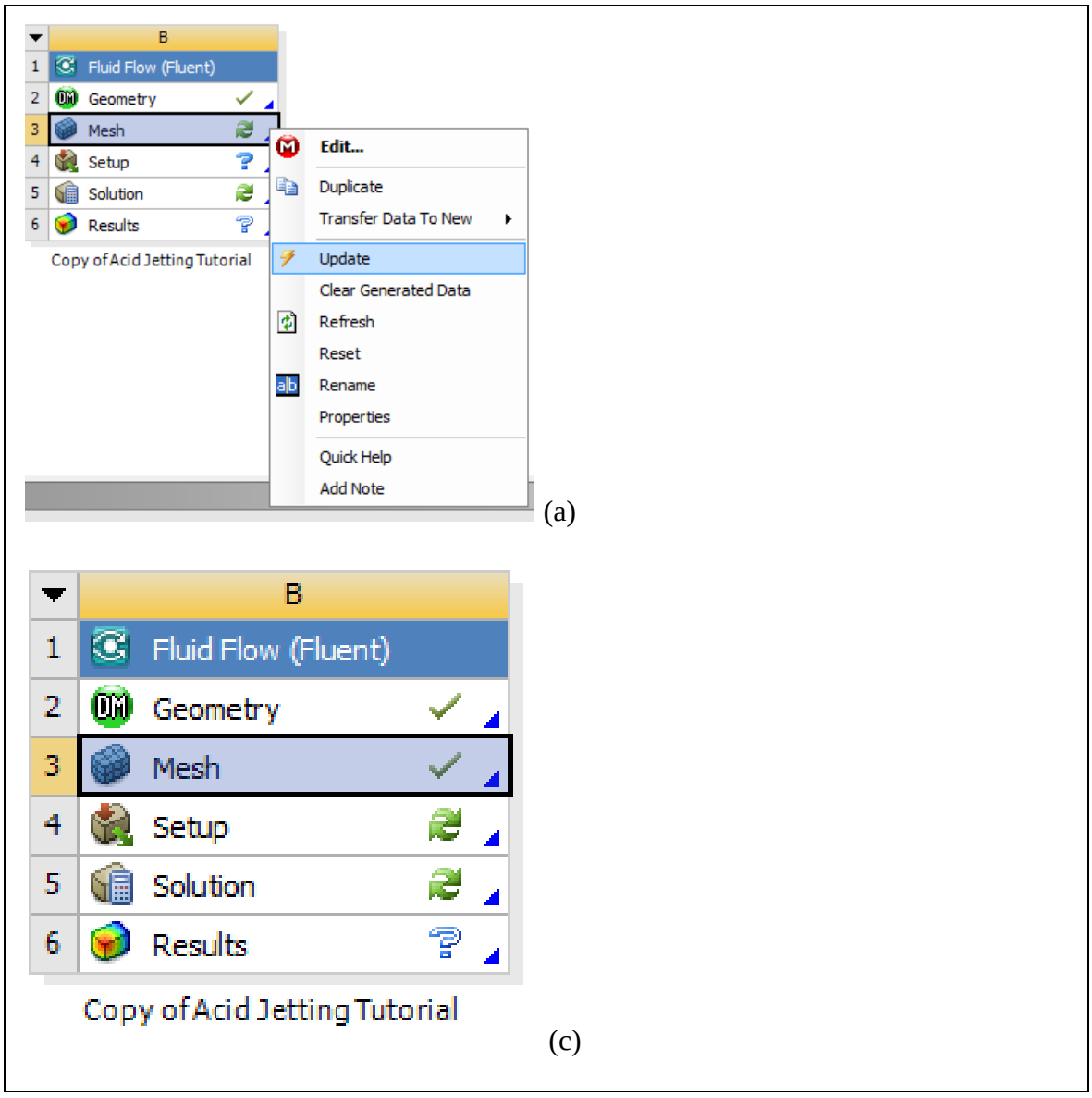

Figure F.57: Meshing of new geometry

39-Running a new Fluent session: (a) Right-click on “Setup” then left-click on “Edit”, (b) Select “Yes” to use the updated geometry for the new simulation

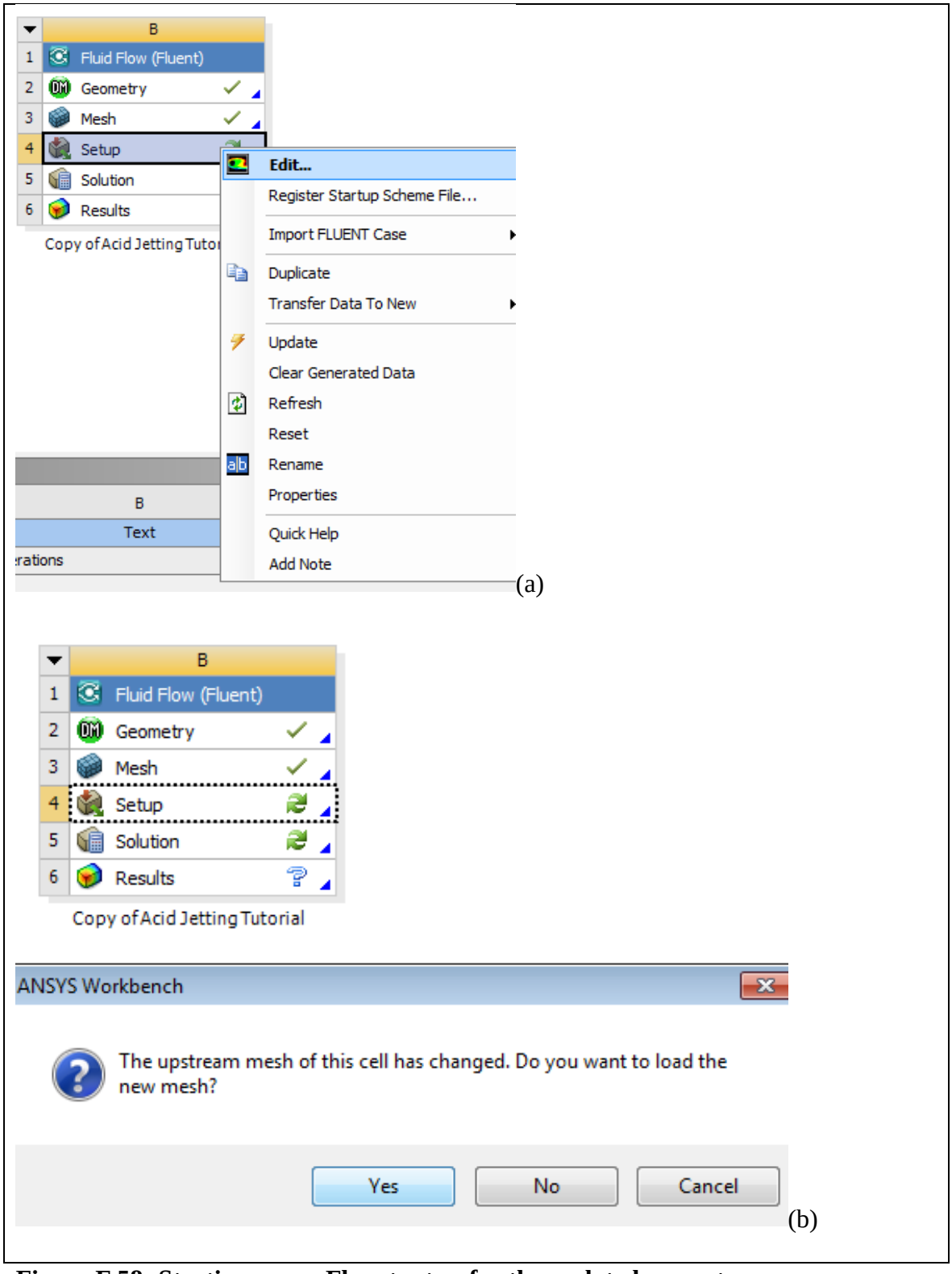

Figure F.58: Starting a new Fluent setup for the updated geometry